The Effect of Particle Properties on Fluidized Bed Hydrodynamics and Entrainment

by

Suren Sookai

A dissertation submitted in fulfilment of the academic requirements
for the degree of Master of Science in Engineering
in the School of Chemical Engineering at the
University of Kwazulu-Natal, Durban, South Africa

December 2007

DECLARATION

The research presented in this dissertation was carried out by Suren Sookai under the supervision of Professor M. Carsky from the University of Kwazulu-Natal, Durban, South Africa.

Portions of this work have been submitted, accepted and published in the proceedings of the Industrial Fluidization South Africa Conference, 2005 (IFSA 2005).

I, Suren Sookai, declare that this dissertation, unless otherwise indicated as a reference, is my own work and it has not been submitted, in whole or in part, to any other university for degree purposes.

Signature: 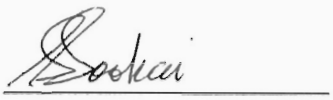

Name: SUREN SOOKAI

Date: 16 APRIL 2008

To my wife
Sunitha

ABSTRACT

This study focuses on the effect that particle properties (size, density and shape) have on fluidized bed hydrodynamics and entrainment rate. The experimental work was carried out using two Plexiglas columns having internal diameters of 0.05 m and 0.14 m respectively and a total height of 6 m from the gas distributor. The particle density was in the range 1300 to 4600 kg/m^3, the Sauter mean diameter was in the range 23 to 60 μm and the fines content (% < 22 μm) was in the range 1 to 29 %. Particle shapes, which ranged from angular to spherical, were characterized by image analysis of SEM photographs. Air was used, as the fluidizing gas and the superficial velocity was kept constant at 0.38 m/s in the 0.05 m column. In the 0.14 m column it was varied in the range 0 to 0.8 m/s. The dense-phase voidage, bubble fraction and entrainment rate of the powders were measured at ambient conditions. In general it was found that the bubble fraction and entrainment rate increased with an increase in the superficial gas velocity. The dense phase voidage was found to increase with an increase in the fines content of the powder and it was only a weak function of the superficial gas velocity. Most importantly, it was found that angular-shaped particles had a higher dense phase voidage, a lower bubble fraction and a lower entrainment rate when compared to spherical-shaped particles having similar particle density and size. Possible reasons for the lower entrainment rate for the angular-shaped particles are given.

The measured dense phase voidage, bubble fraction and entrainment flux was compared with predictions from published correlations and it was found that none of the correlations provided a good fit to the data obtained in this work and that different correlations predicted widely different entrainment rates for the same system. It is therefore recommended that literature correlations should be used with caution in the absence of experimental data. Empirical correlations for the dense phase voidage and bubble fraction are developed.

ACKNOWLEDGEMENTS

My heartfelt thanks and appreciation are extended to Professor Milan Carsky from the University of Kwazulu-Natal for his guidance and suggestions during the course of this project. Special thanks also go out to Fiona Higginson from the University of Kwazulu-Natal for all her administrative assistance; Terry Shingles for encouraging me to pursue this degree; Willem Erasmus for sharing and allowing me to use some of his work on particle shape characterization; Simon Baloyi and Alfred Zulu for assistance with the experimental work and the many hours of inspiring discussions and debate; J.P Botha and Paulus Khiba for equipment set-up and maintenance, Tracy Bromfield, Johan Labuschagne and team for the preparation of some of the powders used in this work; Nadim Shaik, Paul Smit, Martin Keyser and Theo Chronis for their assistance and support.

I would also like to acknowledge the sacrifices made by my family and the love and support I received from them during this time.

Finally, this work would not have been possible without the love, support, encouragement and motivation provided by my dear wife Sunitha Sookai. Her self-sacrificing spirit was evident throughout this project and for this I will remain eternally grateful.

CONTENTS

LIST OF FIGURES

LIST OF TABLES

LIST OF SYMBOLS

A	cross-sectional area of column	$[m^2]$
A_0	area of distributor plate per hole	$[m^2]$
Ar	Archimedes number defined by: $Ar = d_p^3 \rho_g (\rho_p - \rho_g) g / \mu^2$	[-]
B	constant used in eq. 2-141	[-]
b	parameter defined by eq. 2-103	[-]
b_0, b_1	constants used in eq. 2-97	[-]
B_1, B_2	constants used in eq. 2-21	[-]
C_1, C_2	constants used in eq. 2-24	[-]
C_D	drag coefficient	[-]
D	column internal diameter	[m]
d_{50},d_m	median particle diameter	[m]
d_a	diameter of a sphere having the same projected area as the particle	[m]
d_A	Sieve diameter of particle	[m]
d_{b0}	initial bubble diameter	[m]
d_{be}	diameter of a sphere having the same volume as the bubble	[m]
d_{bc}^*	maximum stable bubble size	[m]
d_{bf}	frontal diameter of bubbles in a fluidized bed	[m]
d_{bm}	mean bubble diameter defined by eq. 2-85	[m]
d_F	Feret diameter	[m]
D_f	fractal dimension defined by eq. 2-13	[-]
D_h	column hydraulic diameter	[m]
d_p	average particle size	[m]
d_p^*	dimensionless particle size defined by eq. 2-130	[-]
d_{pi}	particle size of fraction i	[m]
d_s	diameter of a sphere having the same surface area as the particle	[m]
d_{sv}	diameter of a sphere having the same surface area to volume ratio as the particle	[m]
d_v	diameter of a sphere having the same volume as the particle	[m]
E_∞	total entrainment flux above TDH	$[kg/m^2.s]$
E_0	entrainment flux at the bed surface	$[kg/m^2.s]$
E_h	entrainment flux a height h above the bed surface	$[kg/m^2.s]$
$E_{i\infty}$	entrainment flux of particles of size d_{pi} above TDH	$[kg/m^2.s]$
E_{mb}	modulus of elasticity at minimum bubbling conditions	[Pa]

F_{22}	mass fraction of particles whose size is less than 22 microns	[-]
F_{45}	mass fraction of particles whose size is less than 45 microns	[-]
F_d	drag force	[N]
F_{da}	drag force per projection area used in eq. 2-151	[Pa]
F_g	gravity force minus buoyancy force per projection area of particle, used in eq. 2-151	[Pa]
F_i	Entrainment rate of particles of size d_{pi}	[kg/s]
	fluidization regimes	[m/s]
f_s	slug frequency	[s^{-1}]
F_T	total entrainment rate	[kg/s]
g	acceleration due to gravity = 9.81	[m/s^2]
h	height above the bed surface	[m]
H_1	height over which ΔPbd is measured	[m]
H_{bed}	average height of the fluidized bed	[m]
H_d	height of the dense phase	[m]
H_{fb}	maximum bed height below which the bed will be freely bubbling	[m]
H_{fbd}	freeboard height	[m]
H_{mb}	bed height at minimum bubbling conditions	[m]
H_{mf}	bed height at minimum fluidization conditions	[m]
H_{ms}	minimum bed height for stable slugging	[m]
H_o	settled bed height established two minutes after the gas supply is shut off	[m]
j	constant used in eq. 2-49	[-]
k	constant used in eq. 2-62	[-]
k_1	constant used in eq. 2-112	[-]
K_1	parameter used in eq. 6-3	[-]
K_2	parameter used in eq. 6-4	[-]
$K^*_{i,\infty}$	elutriation rate constant above TDH for particles of size d_{pi}	[$kg/m^2.s$]
L_s	slug length	[m]
M	gas molecular weight	[kg/kmol]
m	parameter used in eq. 6-4	[-]
n	index used in eq. 2-34	[-]
N_o	Total number of orifices in a gas distributor	[-]
N_T	number of bed diameters between the rear of a leading slug and the nose of a trailing one	[-]
P	operating pressure	[kPa]

Q_b	visible bubble volume flow rate	[m^3/s]
R	entrainment intensity used in eq. 2-149	[-]
r	parameter used in eq. 6-3	[-]
Re	Reynolds number defined by: $Re = D\rho_g U/\mu$	[-]
Re_c	Reynolds number defined by: $Re_c = d_p\rho_g U_c/\mu$	[-]
Re_{mf}	Reynolds number defined by: $Re_{mf} = d_p\rho_g U_{mf}/\mu$	[-]
Re_p	Reynolds number defined by: $Re_p = d_p\rho_g U/\mu$	[-]
Re_t	Reynolds number defined by: $Re_t = d_p\rho_g U_t/\mu$	[-]
R_g	gas constant = 8.314	[kJ/kmol.K]
S	slope of the line obtained from a plot of particle perimeter versus step length	[-]
S_p	Particle surface area	[m^2]
T	temperature	[K]
t	time	[s]
T_b	fluidized bed temperature	[°C]
U	superficial gas velocity	[m/s]
U^*	dimensionless particle velocity defined by eq. 2-131	[-]
U_b	rise velocity of bubbles in a fluidized bed	[m/s]
$\overline{U_b}$	height average bubble rise velocity	[m/s]
U_{br}	rise velocity of a single bubble	[m/s]
U_c	transition gas velocity between bubbling and turbulent	
U_{cf}	minimum gas velocity for complete fluidization	[m/s]
U_d	gas velocity in the dense phase	[m/s]
U_k	gas velocity at which the standard deviation of the differential bed pressure fluctuations stabilize	[m/s]
U_{mb}	gas velocity at minimum bubbling conditions	[m/s]
U_{mf}	minimum fluidization velocity	[m/s]
U_{ms}	minimum gas velocity required for slugging to occur	[m/s]
U_r	relative velocity between particle and gas	[m/s]
U_s	slug rise velocity	[m/s]
U_t	terminal velocity	[m/s]
U_{ti}	terminal velocity of particle with size d_{pi}	[m/s]
V	volume occupied by powder	[m3]
V_b	total volume of the bubbles in a fluidized bed	[m^3]
V_{bed}	total volume of the fluidized bed	[m^3]
V_d	total volume of the dense phase in a fluidized bed	[m^3]

V_d	total volume of the dense phase	[m^3]
V_g	volume of gas in the fluidized bed	[m^3]
V_{gd}	volume of gas in the dense phase	[m^3]
V_p	particle volume	[m^3]
V_{pore}	specific particle pore volume	[m^3/kg]
w	mass of powder	[kg]
w_p	particle mass	[kg]
x	constant used in eq. 2-82	[-]
X_{bi}	mass fraction of particles with size d_{pi} in the bed	[-]
X_i	weight fraction of particle size dpi	[-]
Y	constant used in eq. 2-100	[-]
z	height above the gas distributor	[m]
z*	height above the gas distributor at which bubbles attain a maximum stable size	[m]
z_0	parameter dependent on gas distributor	[m]

Greek symbols

α	constant used in eq. 2-92	[-]
β	constant used in eq. 2-72	[-]
β_0	constant used in eq. 2-82	[-]
ΔP_1	pressure drop for bed density calculation in the 0.05 m internal diameter column	[Pa]
ΔP_2	pressure drop across the bed in the 0.05 m internal diameter column	[Pa]
ΔP_3	pressure drop for bed density calculation in the 0.14 m internal diameter column	[Pa]
ΔP_4	pressure drop across the bed in the 0.14 m internal diameter column	[Pa]
ΔP_{bd}	pressure drop used for bed density calculation	[Pa]
ε	overall bed voidage	[-]
ε_b	bubble fraction defined	[-]
ε_{bulk}	bulk voidage of powder	[-]
ε_d	dense phase voidage	[-]
ε_i	voidage in the freeboard used in eq. 2-144a	[-]
ε_{mb}	bed voidage at minimum bubbling conditions	[-]
ε_{mf}	bed voidage at minimum fluidization conditions	[-]

ε_{pore}	particle pore volume	[m^3]
$(1-\varepsilon)_H$	particle hold-up in the freeboard used in eq. 2-149	[-]
δ_{bed}	standard deviation of the bed pressure drop fluctuations	[kPa]
ρ_{bed}	bed density	[kg/m^3]
ρ_g	gas density	[kg/m^3]
$\rho_{g,20}$	gas density at a temperature of 20°C	[kg/m^3]
ρ_p	particle density	[kg/m^3]
ΔP_{bed}	pressure drop across the fluidized bed	[kPa]
$\rho_{bed,\,mf}$	bed density at minimum fluidization conditions	[kg/m^3]
ρ_{bulk}	bulk density of powder	[kg/m^3]
ρ_d	bed density of the dense phase	[kg/m^3]
ρ_e	effective gas density defined by eq. 2-142a	[kg/m^3]
ρ_i	solids concentration of size dpi at the gas exit	[kg/m^3]
ρ_m	density defined by eq. 2-37	[kg/m^3]
ρ_{sk}	particle skeletal density	[kg/m^3]
μ	gas viscosity	[kg/m.s]
μ_{20}	gas viscosity at a temperature of 20°C	[kg/m.s]
γ	parameter defined by eq. 2-36	[-]
η	constant used in eq. 2-136	[-]
λ	solid friction coefficient used in eq. 2-144b	[-]
φ	parameter defined by eq. 2-73	[-]
χ	particle circularity defined by eq. 2-10	[-]
ψ	Heywood shape factor (eq. 2-11)	[-]
ω	constant used in eq. 2-111	[-]
Φ	particle sphericity defined by eq. 2-9	[-]

Acronyms

APF	actual pressure fluctuations
ASTM	American Society for Testing and Materials
DPF	differential pressure fluctuations
FCC	Fluid Catalytic Cracking
IXRF	Integrated X-Ray Fluorescence
PC	pressure control
PSD	particle size distribution
SEM	Scanning Electron Microscope
TDH	transport disengagement height

1. INTRODUCTION

Fluidization of solid particles occurs when fluid is passed upwards through a bed of solids, which as a result of fluid-particle interactions is transformed into a fluid-like state. In this fluid-like state there is intimate fluid-solid contacting and when the fluid is a gas, excellent solids mixing is brought about by the stirring action of the gas bubbles which continually move the solids around. Hence, gas-solid fluidization has been extensively used for industrial applications, where the benefits of high heat and mass transfer rates, isothermal operation and ease of solids handling have been exploited, via chemical reactors. For example, fluidized bed reactors were first utilized on an industrial scale in 1922 for coal gasification applications (Kunii and Levenspiel 1991, p.15) and since then they have been used for various other applications such as fluid catalytic cracking, solids mixing, drying, coating of particles, minerals processing and Syngas conversion via the Fischer-Tropsch process.

However, like any other process a gas fluidized bed comes with its fair share of disadvantages. Although particle mixing is good in a fluidized bed, gas mixing is not and the flow of gas bubbles through the bed may lead to gas bypassing. This is especially problematic if high gas conversions are required. In addition, the complexity of the system makes it difficult to accurately predict the behaviour of the fluidized bed and hence, special and often costly development efforts for process scale-up are required. In many cases the advantages outweigh the disadvantages and fluidized beds therefore find wide and increasing application in many branches of the chemical and allied industries.

Motivated by the increased use of fluidized beds for industrial applications and the complexity associated with the modelling of such systems there has been an abundance of academic research carried out to develop a mechanistic understanding of fluidized beds. In the search for this fundamental understanding researchers have met with many stumbling blocks along the way and have had little success in certain areas. This has resulted in an overwhelming amount of empirical correlations that have been proposed to describe essential features of fluidized beds such as hydrodynamics and entrainment.

1.1. Motivation for research

In view of the many empirical and semi-empirical correlations that exist to predict the hydrodynamic and entrainment behaviour of fluidized beds the design engineer is often faced with a dilemma: which correlation is the most reliable to use. This can only be

answered by comparing experimental data of the system under consideration with literature correlations and the one that best suits the data can be used for further development work. Hence, the first motivating factor for this research was to determine how literature correlations that predict fluidized bed hydrodynamics and entrainment rate compare with experimental data when they are applied to systems other than those for which they were developed.

The second motivation was to address the often-neglected effect of particle shape on fluidized bed hydrodynamics and entrainment rate. The literature review revealed that there has been no systematic study on the effect of particle shape on, for example, the dense phase voidage, bubble fraction, bed expansion and entrainment rate. Fluidization research is mostly carried out with spherical particles such as fluid catalytic cracking catalyst or glass beads. It was therefore envisaged that research on the effect of particle shape on fluidization would be useful, both from an industrial and academic point of view.

A third motivation for this work was to gain greater insights into the effect of particle properties (shape, fines fraction, density, average particle size and Geldart (1973) powder classification) on fluidization behaviour in small diameter columns, which are typically used as pilot scale reactors in industry. Insufficient quantitative information was found in the literature on the effect of particle properties (for example, shape and size distribution) on the slugging regime of fluidization.

Finally, it is worth mentioning that the effect of particle properties on fluidization should never be underestimated. There are many examples in the literature where the effect of particle properties on fluidization have been, either neglected, or inappropriately quantified, with dire consequences. The classical example is that of the Brownsville reactors. The design of these fluidized bed reactors was based on data from a 4-inch pilot plant reactor, which was operated with a fine Geldart (1973) group A powder. For the commercial reactor a group B powder was specified without the proper testing and Squires (2005) reports that the commercial reactors failed to perform as advertised and that no one appreciated what a mistake it had been to replace the fine catalyst with a coarser group B powder. This is motivation enough to warrant a study on the effect of particle properties on fluidization.

1.2. Research objectives

The objective of this research was to study the effect that particle properties (size, density and shape) have on the dense phase voidage, bubble fraction, bed expansion and entrainment rate. Particular emphasis was given to the effect of particle shape since previous studies on

this subject are rare. The primary objective was also to study the effect of particle properties on their fluidization behaviour in small diameter columns. This is important because most industrial pilot plant reactors are small and typically operate in the slugging fluidization regime. Through this study it was envisaged that greater insights into the effect of particle properties on slugging beds could be obtained, which would facilitate better problem solving and process optimisation of pilot scale reactors. In addition it was also the objective of this study to compare experimental results with published correlations so as to determine their suitability when applied to systems other than those for which they were developed.

The general conclusion is that the stated primary objective "to gain greater insight into the effect of particle properties on slugging beds" was successfully achieved. Greater insight was also obtained on the impact of particle shape on dense phase voidage, bubble fraction and entrainment rate.

1.3. Dissertation outline

This dissertation begins with a literature review, which is provided in Chapter 2. It is the intention of this review to provide the state of the art with regards to particle characterization techniques; fluidization regimes, regime transitions and factors influencing regime transitions; entrainment and factors influencing entrainment. In particular, the effect of particle properties on these parameters is provided. The effect of gas properties, gas velocity, pressure and temperature are also provided for information purposes. The physical properties and Geldart (1973) classification of the powders used in this study are provided in Chapter 3 and this is followed by Chapter 4 and 5, where a description of the experimental equipment and experimental procedures are provided respectively. In Chapter 6 the experimental results are provided along with a discussion and comparison with literature correlations. The conclusions derived from the experimental results are provided in Chapter 7 and recommendations for future work are discussed in Chapter 8. Finally, detailed experimental results and sample calculations are provided in the Appendices.

2. LITERATURE SURVEY

2.1. Particle characterization

Having knowledge of the particle characteristics such as size, density and shape are prerequisites to understanding and explaining the fluidization behaviour of different powders. Intuitively, the particle shape would play a significant role in the complexity of the definition of the particle characteristics. For example, the characterization of particles that are spherical in shape is relatively simple as these particles can be uniquely and mathematically described in terms of size and shape. However, this is not true in the case of irregular or angular shaped particles since there are various, more complex ways to describe the particle size and shape. A review of some of the more common methods of defining the particle characteristics of irregular shaped particles is therefore provided.

2.1.1. Particle size, size distribution and measurement

According to Yang (2003a, p.1) "the particle size is one or more linear dimensions appropriately defined to characterize an individual particle." Hence, the linear dimension that appropriately describes a perfect spherical particle is the diameter of the sphere. For irregular particles there are many different linear dimensions that could be defined to appropriately characterise the particle, and most often, this does not imply a unique description of the particle and it will depend on the particle orientation. A list of twelve definitions for the particle size of irregular shaped particles has been provided by Allen (1981 cited by Geldart 1986a p.11). The reader is also referred to Yang (2003a, p.1-2) for particle size definitions. In view of the many definitions of particle size, both Geldart (1986a, p.11) and Yang (2003a, p.2) indicate that only the sieve diameter, volume diameter, surface diameter and surface-volume diameter are of interest for fluidized bed applications. The definitions of these particle sizes as well as the Feret diameter (commonly used in particle image analysis) are as follows:

Sieve diameter (d_A): The width of the minimum square aperture in the sieve screen through which the particle will pass.

Volume diameter (d_v): The diameter of a sphere having the same volume as the particle. If the particle volume is known the volume diameter can be calculated using equation 2-1.

$$d_v = \left(\frac{6V_p}{\pi} \right)^{1/3} \tag{2-1}$$

Surface diameter (d_s): The diameter of a sphere having the same surface area as the particle. If the particle surface area is known the surface diameter can be calculated using equation 2-2.

$$d_s = \left(\frac{S_p}{\pi} \right)^{1/2} \tag{2-2}$$

Surface-volume diameter (d_{sv}): The diameter of a sphere having the same external-surface-area-to-volume ratio as the particle. If the external surface area and the volume of the particle are known the surface-volume diameter can be calculated using equation 2-3.

$$d_{sv} = \left(\frac{6V_p}{S_p} \right) = \frac{d_v^3}{d_s^2} \tag{2-3}$$

Feret diameter (d_F): This is a statistical diameter representing the mean value of the distances between pairs of parallel tangents to a projected outline of the particle.

Both Geldart (1986a, p.11-12) and Yang (2003a, p.2) recommend that the surface volume diameter is the most relevant for fluidized beds. According to Geldart (1986a, p.12), this recommendation is based on the establishment that the external surface area of the powder per unit particle volume is "the most appropriate parameter for correlating the flow of fluids through packed beds." However, it is uncertain whether a similar study was carried out to show the relevance of the use of the surface-volume diameter to fluidized bed applications.

In industrial fluidized bed applications it is unusual to find powders consisting of exactly similar particles; rather, it is more probable that the powder will contain a distribution of particle sizes and shapes. The particle size distribution used could be chosen so as to achieve certain desired fluidization properties or it could be inherent to the powder manufacturing process. When using a powder having a distribution of particle sizes, a probability distribution and a cumulative distribution diagram can be used to represent the particle size distribution. The probability distribution diagram is obtained from a plot of the weight fraction (or percentage in a size range) against the average size of specific size ranges. The cumulative distribution diagram is constructed by plotting the weight percent of particles that

is less than or equal to a specific particle size for each particle size measured. These particle size distribution diagrams are illustrated in Figure 2-1.

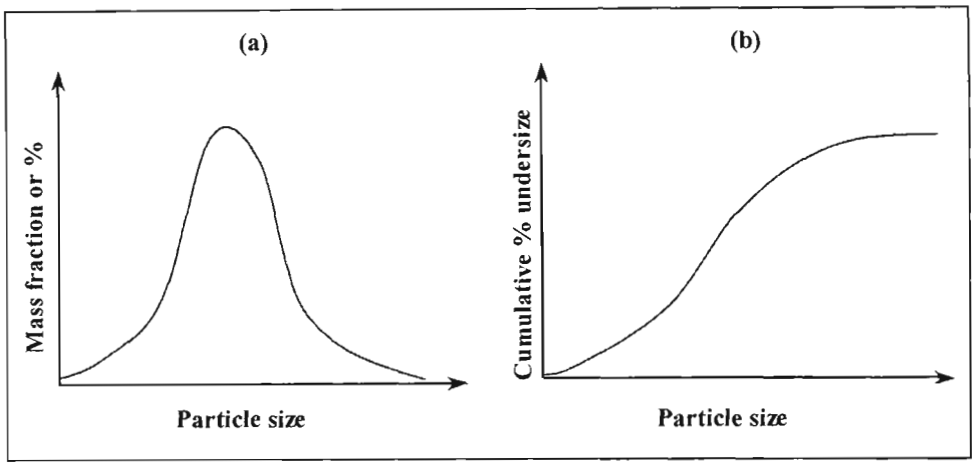

Figure 2-1: (a) Probability distribution and (b) Cumulative distribution of particle sizes.

The particle size distribution can be characterised by an appropriately averaged particle size. The most common average particle sizes are the median particle size and the surface-volume (or Sauter mean) particle size (for more definitions of average particle size refer to Yang 2003a, p.21-22). The surface-volume diameter and median particle diameter are obtained from the particle size distribution as follows:

Surface-volume diameter (d_{sv}): The surface volume diameter is obtained from the probability distribution of particle sizes and can be calculated using equation 2-4 and x_i and d_{pi} are obtained as illustrated in Figure 2-2 (a).

$$d_{sv} = \frac{1}{\sum_i \frac{x_i}{d_{pi}}} \qquad (2\text{-}4)$$

Median diameter (d_m): The median particle size (also commonly referred to as d_{50}) is defined as that particle size for which fifty percent of the material is less than this size. It is conveniently obtained from the cumulative particle size distribution plot as shown in Figure 2-2 (b).

According to Geldart (1986a, p.14), the above definition of d_{sv} "gives proper emphasis to the important influence which small proportions of fines have", and it is always advisable to plot

both the probability and cumulative particle size distributions since it is more likely that abnormalities in the particle size distribution would show-up in the probability distribution diagram but not in the cumulative distribution diagram.

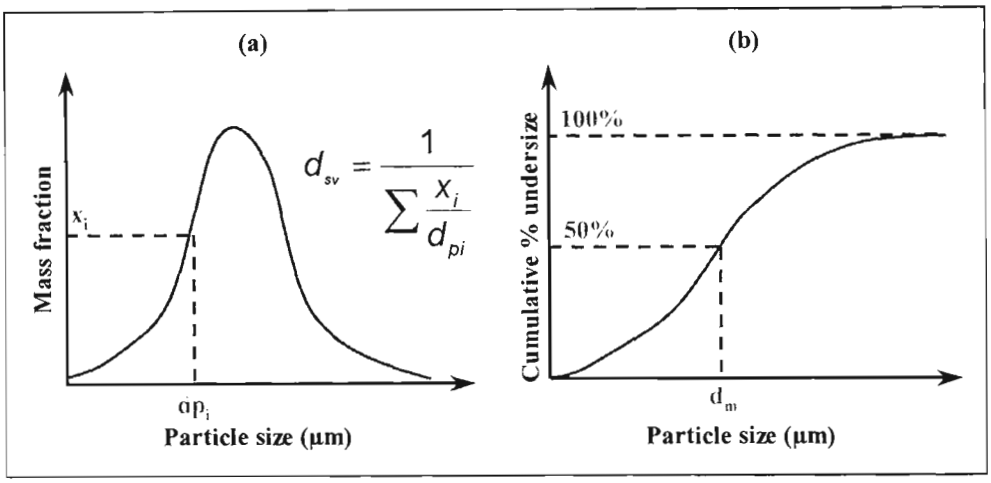

Figure 2-2: Calculation of (a) d_{sv} and (b) median particle size.

The use of d_{sv} for very wide or abnormal particle size distributions such as bi-modal or tri-modal, is not recommended since these "powders generally do not behave in a homogeneous way and cannot be characterised by a single number" (Geldart, 1986, p.14).

There are various methods and commercially available equipment for measurement of the particle size distribution of powders. These include sieve analysis, imaging techniques, gravity and centrifugal sedimentation, elutriation, cascade impaction, and resistivity and optical zone sensing techniques. The reader is referred to Yang (2003a, p.7-12), Allen (1975 cited by Yang 2003a), Kaye (1981 cited by Yang, 2003) and Ma *et al.* (2000) for more detailed information on these particle size measurement techniques.

There is no universally accepted particle size measurement technique or equipment that can be used for all types of particles. Most often, the results obtained from available particle size measurement equipment vary in accuracy depending on the particle properties, sample preparation and measurement principle employed. Hayakawa *et al.*. (1998) noted that different particle size distributions could be obtained even when the same sample was analysed on different commercially available equipment and they point out two reasons for this discrepancy, namely, sample preparation conditions and differences in the measurement principles. Based on their work with agglomerated powders of titanium dioxide, aluminium nitride and a mixture of titanium dioxide and barium titanate, Hayakawa *et al.* (1998)

showed that the dispersion medium and the de-agglomeration operation used during sample preparation had an effect on the particle size distribution as measured by different commercially available equipment. They found that the de-agglomeration operation with a mortar and pestle decreased the differences in the data among the measuring principles tested (laser diffraction and scattering, photo-sedimentation, X-ray sedimentation, light obscuration and electrical sensing zone).

Image analyses techniques are often time consuming since the analysis is carried out per particle. It is therefore expected that the particle size distribution obtained from this technique would depend on the sample size. Vigneau *et al.* (2000) carried out a study using starch granules and an image analysis technique to show that the number of particles used for the analysis affected the number-based particle size distribution obtained.

The particle shape and orientation is also expected to affect the particle size distribution. For example, in the simple sieve analysis, a needle shaped particle can either pass through the aperture on the sieve or be retained on the screen depending on the orientation of the particle (Yang 2003a, p.7). Naito *et al.* (1998) investigated the effect of particle shape on the particle size distribution measured with several types of commercial equipment (eight analyzers based on the laser diffraction and scattering principle, seven analyzers based on the photo-sedimentation principle, 3 analyzers based on the X-ray sedimentation principle, one analyzer based on the light obscuration principle and three analyzers based on the electrical sensing zone principle). They used spherical, flaky and rod-like shaped particles (aluminium oxide, barium titanate, boron nitride and silicon nitride whisker) in round robin tests. They used the results obtained from the electrical sensing zone principle as a basis for their comparisons since this technique yields the equivalent volume diameter, which is expected to be independent of particle shape. The conclusion drawn from this investigation was that the particle shape drastically influences the laser diffraction and scattering technique and the photo-sedimentation technique because of the preferential particle orientation along the shear flow. The influence of particle shape on the X-ray sedimentation technique is small because the transmittance intensity of X-rays is independent of the particle shape and its orientation. Similarly, the light attenuation technique also displayed a small effect of particle shape since the particles dispersed at random in the agitated sample suspension. The effect of particle shape on the photo-sedimentation technique was found to be large in the coarse-size range of the distribution.

In summary, it has been shown that for irregular-shaped particles there are various ways to define the particle size. Commercially available particle size analyzers can provide different particle size distribution results depending on the measurement principles, particle shape and

orientation, sample preparation and sample size. A universally accepted particle size analyzer does not exist unless particles which are close to spherical in shape are being analysed. Therefore, it is important to verify that the instrument being used is applicable for the degree of accuracy required. It is particularly important to ensure that the measurement technique used is not sensitive to particle shape when different shaped particles are being compared in terms of size distribution.

2.1.2. Particle density

In fluidization applications, three commonly used densities are generally used to characterize particles, namely, bulk density, particle density and skeleton density. The definitions of these densities are as follows:

Bulk density (ρ_{bulk}): The bulk density refers to the mass of an assemblage of particles divided by the volume it occupies. The volume that is used in the calculation of the bulk density includes the voids between the particles and voids within porous particles. This is illustrated in Figure 2-3 and the bulk density can be calculated using equation 2-5.

$$\rho_{bulk} = \frac{w}{V} \qquad (2\text{-}5)$$

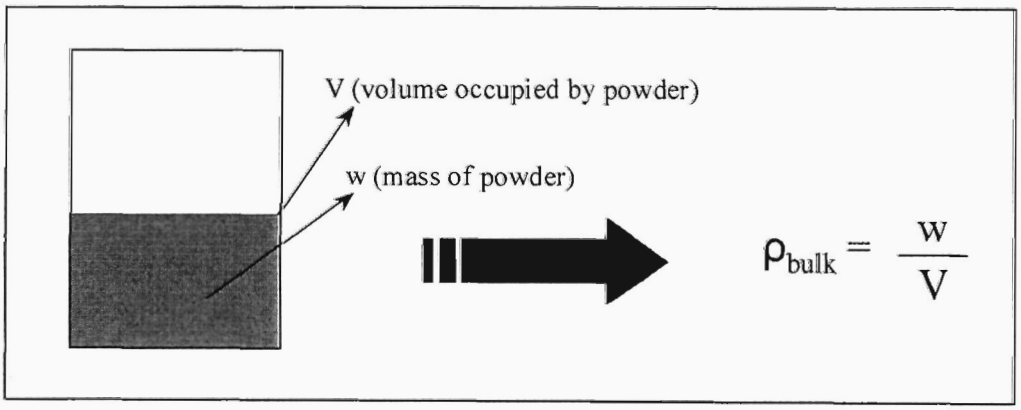

Figure 2-3: Definition of bulk density.

The bulk density of a powder is not unique as it depends on the packing structure of the powder in the given volume, the particle shape, the particle size and degree of compaction. Two types of bulk density have been used in the literature (Mohammadi and Harnby 1997; Abdullah and Geldart 1999), namely, the aerated bulk density and the tapped bulk density. The aerated bulk density is obtained under conditions where the dispersed powder is allowed

to freely settle under the influence of gravity. The tapped bulk density is obtained by physically tapping the container holding the powder. The tapped bulk density will obviously depend on the tapping procedure and standard equipment such as the Hosokawa powder tester and the Copley tap density volumeter (Abdullah and Geldart 1999) can be used to measure the tapped bulk density. Abdullah and Geldart (1999) also note that the Hosokawa powder tester provides more reliable results than the Copley volumeter as the powder weight can be more accurately measured on the former. Both Abdullah and Geldart (1999) and Mohammadi and Harnby (1997) indicate that the ratio of the aerated bulk density and tapped bulk density, which is termed the Hausner ratio, can be used as a measure of the flowability and cohesiveness of powders.

Particle density (ρ_p): The particle density is defined as the mass of a particle divided by its volume. In this case, the volume that is used for the particle density calculation is the volume that the particle would displace if its surface were nonporous. This volume is illustrated in Figure 2-4 by the hydrodynamic envelope around the particle and it therefore includes both open and closed pores in the case of porous particles. The particle density is therefore relevant to fluidized systems and can be called a "hydrodynamic" density since it is based on the shape and volume, which the flowing gas "sees" (Geldart 1986a, p. 17). The particle density can be calculated using equation 2-6.

$$\rho_p = \frac{w_p}{V_p} \tag{2-6}$$

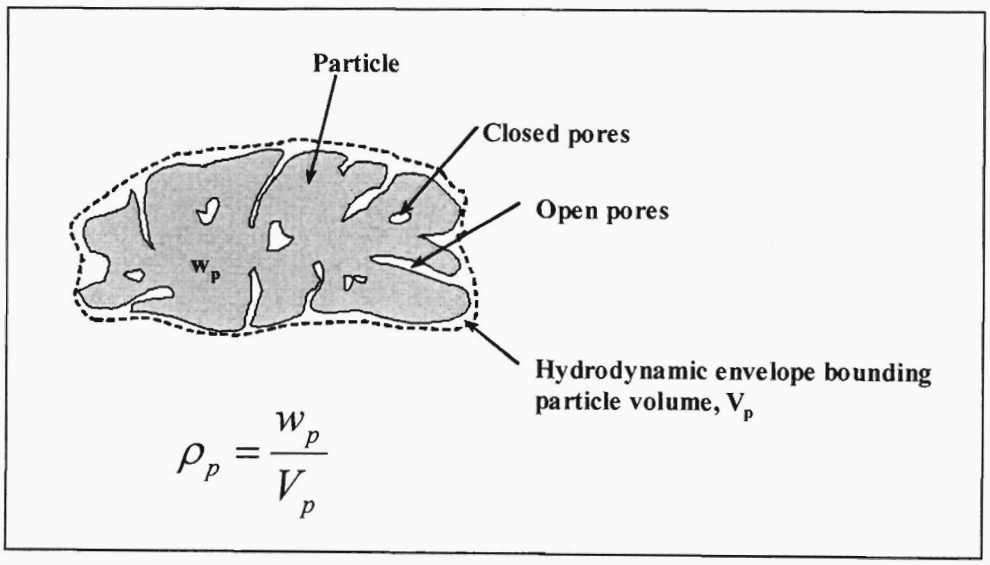

Figure 2-4: Definition of particle density.

Skeletal density (ρ_{sk}): The skeletal density is the density that the particle would have if it had no pores and is also referred to as the absolute or true density. It is obtained by dividing the mass of the particle by the skeletal volume of the particle. The skeletal volume includes the volume of closed pores but not open pores. For nonporous particles the particle density is exactly equal to the skeletal density.

Based on the above density definitions, the following relationships can be derived:

$$\rho_{bulk} = \rho_p (1 - \varepsilon_{bulk}) = \rho_{sk} (1 - \varepsilon_{pore})(1 - \varepsilon_{bulk}) \tag{2-7}$$

$$\rho_p = \frac{1}{V_{pore} + \frac{1}{\rho_{sk}}} \tag{2-8}$$

The skeletal density and open pore volume is normally measured using a gas or liquid pycnometer and/or a mercury porosimeter (eg. Naito *et al.* 1998; Silva and Miranda 2003). With these instruments, the volume of closed pores cannot be measured and therefore the skeletal density so obtained is based on a particle volume that includes the volume of closed pores. The particle density can be calculated using equation 2-8 once the open pore volume and skeletal densities have been measured using a pycnometer and/or a mercury porosimeter.

The particle density of porous particles can also be influenced by particle size since the smaller particles contain fewer pores than the larger ones, resulting in the smaller particles being denser than the larger particles.

2.1.3. Particle shape

Particle shape is expected to be one of the important particle properties that affect the aerodynamic or hydrodynamic behaviour of powders in fluidized beds. In reality particles can have an infinite number of shapes and these shapes can be dependant on the particle orientation. Therefore, it is no surprise that there has been very little success with characterization of particle shapes by a single parameter. The use of single empirical parameters for particle shape description has often been criticised in the literature largely because it is possible for particles with different shapes to have the same shape descriptor. The literature shows that particle shape analysis can be broadly classified into two categories, namely, behavioural analysis and image analysis (Goosen 1988 p. 9; Pickett *et al.* 1991).

In behavioural techniques, the shape of the particles is inferred from their behaviour when they are subjected to certain tests. According to Goosen (1988, p. 10) examples of behavioural techniques include the measurement of pressure drop through a packed bed of particles, the ability of particles to flow up an inclined rotating disc or cylinder and the ratio of particle sizes determined by two different methods. The latter is related to the well known sphericity shape factor and has been used quite extensively in the literature.

Wadell (1933 cited by Yang 2003a, p. 3) proposed the Sphericity and Circularity as particle shape descriptors, which are defined according to equations 2-9 and 2-10 respectively.

$$\Phi = \frac{\text{Surface area of a sphere having the same volume as the particle}}{\text{Actual surface area of the particle}} \qquad (2\text{-}9)$$

$$\chi = \frac{\text{Perimeter of a circle having the same cross-sectional area as the particle}}{\text{Actual perimeter of the particle cross-section}} \qquad (2\text{-}10)$$

By these definitions, the sphericity and circularity of a perfect sphere would be 1 and that of non-spherical particles would be less than 1. The difficulty with using these shape factors directly, arises from the fact that it makes use of the surface area and perimeter of the particles which is difficult to obtain. However, Wadell (1934 cited by Yang 2003a, p. 3) claimed that sphericity was useful for correlating the drag coefficient. On the other hand Isaacs and Thodos (1967 cited by Flemmer *et al.* 1993) showed that the concept of sphericity was not suitable when applied to the prediction of drag for a variety of smooth cylinders. Clark *et al.* (1989) also criticised the concept of sphericity as a particle shape descriptor because it requires knowledge of the particle surface area, which they claim, is generally indeterminate and it is influenced by the measurement technique. There is little mentioned in the literature on the practical application of using the circularity as a particle shape descriptor other than that it has the potential advantage of allowing correlation between flow behaviour and particle orientation (Cliff *et al.* 1978 cited by Yang 2003a, p. 4).

Despite the criticism associated with the use of the sphericity as a unique particle shape descriptor many researchers have used it to characterize the shape of particles in their studies. For example, Haider and Levenspiel (1989 cited by Yang 2003a, p. 16-17) present an equation for the drag coefficient of non-spherical particles in terms of the particle Reynolds number and sphericity. Luckos and den Hoed (2004) also used the sphericity to

characterise the shape of ilmenite and a titania slag and their measurements showed that the particle sphericity decreased with an increase in particle size.

The Heywood shape factor that was proposed by Heywood (1962 cited by Yang, 2003a, p. 5) is an empirical factor, which is based on the projected profile of the particle, and is calculated using equations 2-11 and 2-12.

$$\psi = \frac{V_p}{d_a^3} \tag{2-11}$$

$$d_a = \sqrt{\frac{4A_p}{\pi}} \tag{2-12}$$

The projected area diameter, d_a, refers to the diameter of a sphere having the same projected area as the particle. The Haywood shape factor also requires knowledge of the particle volume and projected area; hence it can be subject to the same criticism as for the sphericity factor. Clark *et al.* (1989) also points out that the particle's most stable position is required for computation of the Heywood shape factor and this is not always known.

The reader is referred to Bouwman *et al.* (2004) for more definitions of particle shape factors and their use in discriminating between the shapes of granules. Their conclusion was that the projection shape factor and the circularity worked well in distinguishing the differences in the shapes of their granules. They also introduce a roughness factor to characterise the surface roughness of the granules. Xie and Zhang (2001) have correlated the relationship between the Stokes shape factor and the sphericity. They propose that with this relationship the sphericity of non-spherical particles can be determined by settling experiments in the Stokes regime.

Modern techniques of particle shape characterization have focused mainly on computer-based image analysis. In image analysis, a two dimensional image or silhouette of the particle, which is obtained using a suitable microscope and camera, is examined by various methods. Clark (1986) reports that the early image analysis techniques measured simple proportions of the particle such as the aspect ratio, ratio of particle perimeter to diameter and the ratio of inscribed-to-circumscribed circles in the particle silhouette. Image analysis techniques have since evolved in sophistication resulting in 'unrolling' the particle silhouette to produce a Feret's signature (Kaye 1978 and Meloy 1978 cited by Clark 1986), which was then subjected, to Fourier analysis. Despite Fourier analysis being the most widely

documented of all image analysis techniques, it has been found to be ideally suited to the characterization of smooth, rounded particles. It has also been found that the application of Fourier analysis to very jagged or highly re-entrant silhouettes is not appropriate (Clark 1987; Hundal *et al.* 1997; Fong *et al.* 1979; Drolon *et al.* 2000).

Fractal analysis, as discussed by Clark (1986) is another method used in the analysis of particle images. This technique makes use of the fact that the perimeter of a particle silhouette is dependant on the magnitude of the step length used to measure it. Large step lengths do not take surface irregularities into account, whereas smaller step lengths do and hence the smaller the step length the larger the perimeter that is measured. The particle perimeter is then obtained as a function of the step length. By plotting the step lengths and corresponding perimeters on log scales, it has been found that a linear relationship (with negative slope) is obtained. If the slope of this linear relationship is S, then the fractal dimension D_f is defined by equation 2-13.

$$D_f = 1 - S \qquad (2\text{-}13)$$

When a two dimensional curve is examined, the fractal dimension has been found to assume values between 1 and 2 and for particle silhouettes the fractal dimensions are typically between 1.05 and 1.36 (Clark 1986).

Other techniques, which have a "fractal flavour" about them, are Pipers angular analysis (Clark 1986; Pickett *et al.* 1989) and Delta analysis as proposed by Clark and Meloy (1985 cited by Pickett *et al.* 1989). According to Clark (1986), "these two methods measure the local angular variation of the silhouette edge". A frequency plot of these angles is then used to infer the surface microstructure of the particle.

Fractal analysis on its own is more a measure of the surface roughness of a particle and therefore provides very little information on the macroscopic particle shape. Clark (1987) therefore proposed the concept of fractal harmonics or polygonal harmonics to describe the macroscopic shape of particles (see also Hurter and Clark 1987). This analysis is similar to the fractal analysis but instead of terminating the fractal analysis with an unequal step length, the fractal analysis is continued, traversing the silhouette edge repeatedly. Clark (1987) points out that as the step length is varied, different polygons are constructed. The first harmonic to arise consists of two diametrically opposed points (second order harmonic); the second harmonic to arise is a triangle (third order harmonic); the third harmonic is a rhombus (fourth order harmonic) and so on. Clark *et al.* (1989) used this method to study the relationship between polygonal harmonics and the drag coefficient for smooth river pebbles

and rough angular gravel. They found that the persistence of the second harmonic, which is related to the aspect ratio of an image, had the strongest effect on the drag coefficient of irregular particles. Flemmer *et al.* (1993) studied the effect of particle shape on the relationship between void fraction and superficial gas velocity. In this study, limestone, quartz, bottom ash and pea gravel were fluidized with water and the void fraction was measured as a function of superficial gas velocity. The shape of the solids used in this study was characterized using image analysis. The methods used for image analysis included aspect ratio, fractal dimension, Piper's angles and polygonal harmonic persistence. It was found that the persistence of the third harmonic provided the best fit for correlating the slope of a log (superficial velocity) versus log (void fraction) plot. Thus, it is clear, that image analysis based on the method of fractal harmonics is not universal, as different harmonic persistence's are required to describe different aspects of particle behaviour and it is not clear prior to experimentation which harmonic would be best suited to correlate the data.

Two-dimensional image analysis has also been used to provide three-dimensional particle shape descriptors by analysing the images of particle projections in three mutually perpendicular directions (Abou-Chakra *et al.* 2004). However, it appears that the method employed by Taylor *et al.* (2006) using X-ray computed tomography and spherical harmonics provides more promise for the three dimensional characterization of particles.

Finally, Zeidan *et al.* (2007) provide an analysis of the errors and accuracy associated with the use of image analysis techniques for determining particle properties. The main inaccuracies arise during the digitisation process where the particle image is represented by an array of pixels. These pixels are usually square in shape and give rise to jagged edges at the boundaries of the particle image. Accuracy can be improved by improving the image resolution.

In summary, it has been shown that there are a variety of behavioural and image analysis techniques that have been used to characterize the shape of particles. Some have been successful for the correlation of certain data while others are not. However, it is clear from this review that very little research has been carried out specifically to characterize particle shape as a means of explaining the differences in fluidization behaviour. The current work attempts to address this issue.

2.2. Powder classification based on fluidization behaviour

There are many practical incentives to be able to predict the fluidization behaviour of powders with minimum experimentation. For example, catalyst powders can be designed to have a certain particle density, size distribution and shape so as to display desirable fluidization properties. This can only be done successfully if the relationship between these particle properties and their fluidization behaviour is unambiguously known.

The well-known and most widely quoted powder classification system based on fluidization properties is that of Geldart (1973). According to this classification system, which is shown in Figure 2-5, powders are classified as being in either group A, B, C or D, depending on the difference between the particle and gas density (ρ_p-ρ_g), and the particle size (d_{sv}). Each group exhibits unique fluidization characteristics, which forms the basis for distinguishing between groups. This group classification can therefore be used to predict the general "package" of fluidization characteristics of a particular powder from knowledge of the particle and gas density and the particle size distribution. For example, if a powder falls in group C then it would be known that these powders are cohesive, difficult to fluidize and are prone to gas channelling.

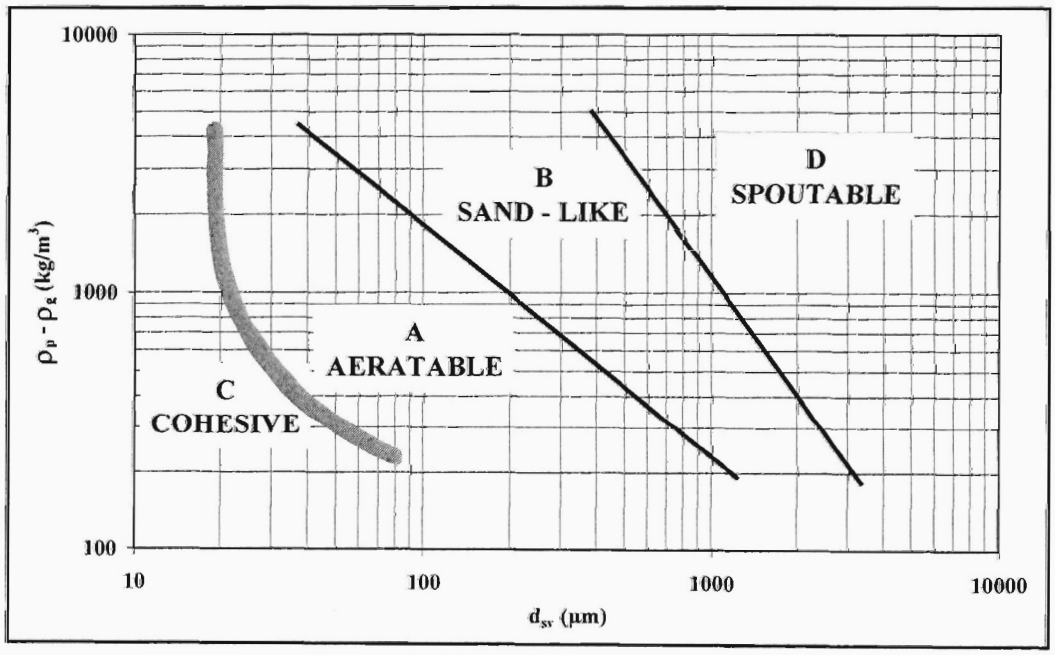

Figure 2-5: Geldart (1973) powder classification diagram.

However, if a powder has a group A classification, then it would be known that these powders display good fluidization properties, are easily aeratable, have a high dense phase

voidage and limited bubble growth. Further characteristic fluidization properties of the different groups are summarised in Table 2-1 (Geldart 1986b p.39) [**Note:** The meaning of the fluidization terms introduced here, such as minimum fluidization velocity, bubbling and slugging will be explained in the next section].

Table 2-1: Summary of fluidization characteristics of Geldart groups A, B, C and D powders.

Increasing particle size →				
Group	**C**	**A**	**B**	**D**
Typical solids	Flour, Cement	Cracking catalyst	Building sand, table salt	Crushed limestone, coffee beans
Most obvious characteristic	Cohesive, difficult to fluidize	Bubble free range of fluidization	Starts bubbling at minimum fluidization velocity	Coarse solids
Bed expansion	Low when bed channels, can be high when fluidized	High	Moderate	Low
De-aeration rate	Initially fast, exponential	Slow, linear	Fast	Fast
Bubble properties	No bubbles; Channels and cracks	Splitting/re-coalescence predominates; maximum size exists; large wake.	No limit on size	No known upper size; small wake
Solids mixing	Very low	High	Moderate	Low
Gas back-mixing	Very low	High	Moderate	Low
Slug properties	Solid slugs	Axisymmetric	Axisymmetric asymmetric	Horizontal voids, solid slugs, wall slugs
Spouting	No	No, except in very shallow beds	Shallow beds only	Yes, even in deep beds

Source: Geldart (1986b, p. 39)

The Geldart (1973) powder classification system is only applicable at ambient conditions when air is used as the fluidizing gas. It, therefore, has limited application to most industrial processes, which operate at high pressure and temperature with a range of gases other than air. Geldart (1973) did, however, mention that the boundary between groups A and B would shift to the right with an increase in operating pressure, to the extent that, group B powders would start to behave like group A powders. The other shortfall of the Geldart (1973) powder classification system is that it does not take the particle shape into account, and, as

will be shown in the current study, the particle shape has a significant effect on the fluidization behaviour of powders.

Molerus (1982 cited by Yang 2007) also provided a powder classification diagram similar to Geldart (1973) with the addition that it included the effects of inter-particle cohesion forces. Later, Grace (1986 cited by Yang 2007) proposed that the Geldart (1973) boundaries between groups A and B and between groups B and D could be better represented by equation 2-14 and 2-15 respectively, which could also be used for temperatures and pressures other than ambient and for gases other than air.

$$\text{Group A and B boundary: } Ar = 1.03 \times 10^{6} \left(\frac{\rho_p - \rho_g}{\rho_g} \right)^{-1.275} \tag{2-14}$$

$$\text{Group B and D boundary: } Ar = 1.45 \times 10^{5} \tag{2-15}$$

In equations 2-14 and 2-15, Ar is the Archimedes number and is defined by equation 2-16, where d_p is some average particle diameter; the use of d_{sv} is recommended by Yang (2003b, p.63).

$$Ar = \frac{d_p^3 \rho_g \left(\rho_p - \rho_g \right) g}{\mu^2} \tag{2-16}$$

Goosens (1998) also classified powders based on the Archimedes number. This classification was based on the hypothesis that the relative importance of laminar and turbulent phenomena governed the fluidization behaviour of powders. The powder groups were still based on Geldart (1973) groups A, B, C and D except that the boundaries between groups were different. Wang and Li (1995) proposed that the fluidization properties and the inter-particle forces of powders were governed by the surface properties of powders and in particular, the specific surface area. They, therefore, developed boundaries for Geldart (1973) groups A, B, C and D in terms of the specific surface area and showed that this technique could also be applied to mixtures of powders. Finally, Yang (2007) proposed a modification of the Geldart (1973) diagram to take into account operating conditions other than ambient and gases other than air. In the modified Geldart (1973) diagram the particle size (d_{sv}) is replaced by the Archimedes number and the density difference between the particle and gas is replaced by the dimensionless density or density ratio given in equation 2-17.

$$\text{Dimensionless density} = \left(\frac{\rho_p - \rho_g}{\rho_g} \right) \qquad (2\text{-}17)$$

Representing the group boundaries in terms of Archimedes number and dimensionless density has been shown to provide good agreement with the literature data (Yang 2007). Yang (2007) also acknowledges that the original Geldart (1973) boundary for group A and B is still valid in the modified diagram when extrapolated as it "remarkably explains the existing literature data better than any other proposed criteria".

2.3. Fluidization regimes and transitions

When gas is passed through a bed of particles, which is unrestrained at the upper surface, the particles experience a drag force. This drag force arises from the flow of gas past the particles and can be observed as a pressure drop across the bed. The particles remain stationary and in a packed bed regime as long as the drag force on the particles are less than the weight of the particles. As the gas velocity through the bed is increased, the drag force on the particles (and the pressure drop across the bed) increases until a point is reached whereby the drag force is in equilibrium with the weight of the particles. At this point the particles begin to move apart, the bed expands and the pressure drop across the bed is equal to the weight of the bed per unit area. The velocity at which this occurs is termed the minimum fluidization velocity and marks the transition from a packed bed to a fluidized bed.

A further increase in gas velocity sees the appearance of bubbles and the velocity at which this occurs is called the minimum bubbling velocity. In the region between the minimum fluidization velocity and minimum bubbling velocity, the fluidization regime is called the particulate regime.

At gas velocities in excess of the minimum bubbling velocity, the bed operates in the bubbling fluidization regime, which is characterized by an increase in gas hold-up, bed expansion, bubble growth, particle mixing and entrainment.

A further increase in the gas velocity sees a transition from the bubbling regime to the turbulent regime which is characterized by a break-down of well defined bubbles and further increases in the bed expansion, particle mixing and entrainment rate.

Finally, increasing the gas velocity further causes a transition from the turbulent regime to the transport regime. These fluidization regimes are shown schematically in Figure 2-6 along with typical trends of the bed voidage and density with an increase in gas velocity.

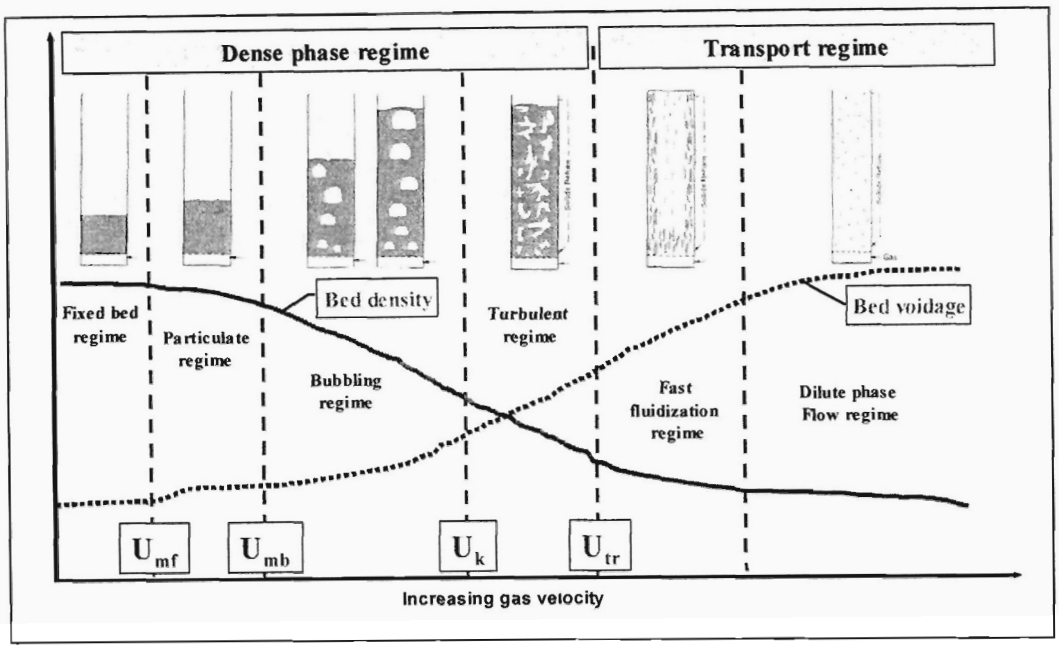

Figure 2-6: Overview of fluidization regimes.

The above provides a brief overview of the pertinent fluidization regimes that can occur in a fluidized bed. In the next sub-sections a closer look will be taken at each of these regimes along with a literature review on factors controlling the hydrodynamic behaviour of the different fluidization regimes and the fluidization regime transitions. Although this review should, strictly speaking, be focused on the effect of particle properties, the effect of pressure and temperature is included, in certain cases, for information purposes in view of its industrial significance.

2.3.1. Minimum fluidization velocity

The minimum fluidization velocity (U_{mf}), which is also referred to as the incipient fluidization velocity represents the velocity at which transition from a packed bed to a fluidized bed occurs. This phenomenon is best explained in terms of the bed pressure drop versus superficial gas velocity diagram shown in Figure 2-7. The curve ABCD represents a typical bed pressure drop versus gas velocity relationship that is observed if the gas velocity is increased from zero until the bed is fluidized while curve DCA indicates a typical bed pressure drop profile obtained if the gas velocity is decreased to zero.

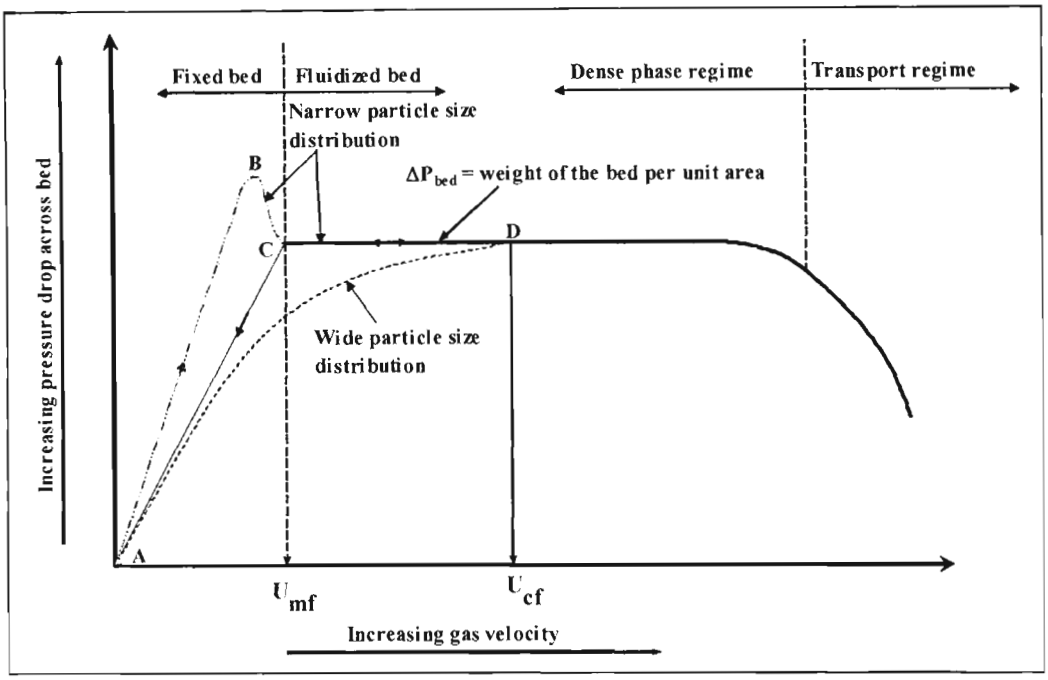

Figure 2-7: Bed pressure drop versus superficial gas velocity.

It is immediately apparent that in the case of increasing gas velocity (curve ABCD) the pressure drop across the bed is higher than the weight of the bed per unit area. This will typically occur if the bed is compacted or composed of very angular and cohesive particles. The higher than expected pressure drop occurs due to more energy being required to overcome these compaction and cohesive forces prior to fluidization. Above the incipient fluidization velocity the pressure drop across the bed does not change with gas velocity and is related to the particle and gas properties through equation 2-18.

$$\Delta P_{bed} = \frac{wg}{A} = (\rho_p - \rho_g)(1-\varepsilon)gH_{bed} \qquad (2\text{-}18)$$

2.3.1.1. Measurement of U_{mf}

For a bed containing a powder with a narrow particle size distribution U_{mf} is more distinct and well defined, and in this case U_{mf} is conventionally taken to be that velocity at which the packed bed pressure drop profile and the fluidized bed pressure drop intersect, as shown in Figure 2-7. For a powder with a wide particle size distribution, the different size fractions fluidize at different velocities and in this case the curve AD in Figure 2-7 is normally obtained. In this case Geldart (1986a, p. 22) makes mention of the minimum velocity of

complete fluidization (U_{cf}), which is defined as the minimum velocity required to fully support the bed of particles.

At minimum fluidization conditions the pressure drop across the bed should, theoretically, be equal to the weight of the bed per unit cross-sectional area. However, Yang (2003b p. 62) points out that in practice, the pressure drop across the bed is sometimes less than the weight of the bed per unit cross-sectional area because some of the particles are "supported by the wall owing to the less than perfect design of the gas distributor; to the finite dimension of the containing vessel; and to the possibility of channelling".

Felipe and Rocha (2007) have investigated the use of the Puncochar *et al.* (1985 cited by Felipe and Rocha 2007) method to measure the U_{mf} of sand, microcrystalline cellulose, FCC and alumina. This method is based on an analysis of the standard deviation of the pressure measurements (pressure measurements were made in the plenum and at different heights in the bed). The plenum chamber was shown to be the most appropriate location for obtaining the pressure signals at a sampling frequency of 100 Hz. The standard deviation of the pressure signals is plotted as a function of superficial gas velocity and through linear regression analysis the velocity at which the standard deviation of the pressure fluctuation is zero marks the minimum fluidization velocity.

2.3.1.2. Literature correlations for U_{mf}

There are various correlations available in the literature to calculate U_{mf} from the particle and gas properties. These are summarised in Yang (2003a, p.63). One of the classical methods makes use of the Ergun equation by equating the packed bed pressure drop to the weight of the bed per unit cross-sectional area at minimum fluidization conditions. The result according to Yang (2003a, p. 63) is given by equation 2-19.

$$Ar = 150\frac{(1-\varepsilon_{mf})}{\Phi^2\varepsilon_{mf}^3}Re_{mf} + 1.75\frac{1}{\Phi\varepsilon_{mf}^3}Re_{mf}^2 \qquad (2\text{-}19)$$

Re_{mf} is defined by equation 2-20.

$$Re_{mf} = \frac{d_{sv}U_{mf}\rho_g}{\mu} \qquad (2\text{-}20)$$

If it is assumed that ε_{mf} is independent of Re_{mf} then equation 2-18 can be also be written as shown in equation 2-21, where the constants B_1 and B_2 are given in equations 2-22 and 2-23 respectively.

$$B_1 Re_{mf}^2 + B_2 Re_{mf} = Ar \tag{2-21}$$

$$B_1 = \frac{1.75}{\Phi \varepsilon_{mf}^3} \tag{2-22}$$

$$B_2 = \frac{150(1-\varepsilon_{mf})}{\Phi^2 \varepsilon_{mf}^3} \tag{2-23}$$

By solving equation 2-21 for Re_{mf}, equations 2-24, 2-25 and 2-26 are obtained.

$$Re_{mf} = \sqrt{C_1^2 + C_2 Ar} - C_1 \tag{2-24}$$

$$C_1 = \frac{B_2}{2B_1} \tag{2-25}$$

$$C_2 = \frac{1}{B_1} \tag{2-26}$$

Most correlations are presented in terms of equation 2-24 with values for C_1 varying between 25.25 and 33.7 and values for C_2 varying between 0.0365 and 0.0651 (Yang 2003a p. 63). The famous Wen and Yu (1966 cited by Yang 2003a, p. 63) correlation for U_{mf} has $C_1 = 33.7$ and $C_2 = 0.0408$. These values of C_1 and C_2 are based on experimental data which showed that $1/\Phi\varepsilon_{mf}^3 \approx 14$ and $(1-\varepsilon_{mf})/\Phi^2\varepsilon_{mf}^3 \approx 11$. The resulting correlation is given in equation 2-27, although Dry *et al.* (1983) and Abrahamsen and Geldart (1980) quote the Wen and Yu correlation as given in Equation 2-28. On further analysis it was found that equation 2-27 is derived from quation 2-21, whereas equation 2-28 is obtained by removing the Re_{mf}^2 term in equation 2-21.

$$Re_{mf} = \sqrt{33.7^2 + 0.0408Ar} - 33.7 \tag{2-27}$$

$$U_{mf} = \frac{d_{sv}^2 g(\rho_p - \rho_g)}{1650\mu} \quad (2\text{-}28)$$

Xie and Geldart (1995) also found that the Carman-Kozeny packed-bed pressure drop equation could also be used to estimate U_{mf}. This relationship is given in equation 2-29.

$$U_{mf} = \frac{\varepsilon_{mf}^3 (\rho_p - \rho_g) g d_{sv}^2}{180\mu(1-\varepsilon_{mf})} \quad (2\text{-}29)$$

2.3.1.3. Factors influencing U_{mf}

The fact there is a wide variation in the values of C_1 and C_2, as shown in the previous section, indicates that the particle properties have a strong influence on U_{mf}. In order to use equations 2-19 and 2-29 to predict the effect of particle properties on U_{mf}, knowledge of ε_{mf} is required, which, according to Goosen (1988 p. 25) is also expected to be a function of particle properties. Generally, U_{mf} increases with an increase in particle size and particle density.

There has been little work showing the effect of particle shape on the minimum fluidization velocity. Lucas *et al.* (1986 cited by Goosen 1988 p.18) investigated the effect of particle shape on U_{mf} and found that the factor $(1-\varepsilon_{mf})/\Phi^2\varepsilon_{mf}^3$ ranged between 4 and 16, which indicates the strong influence which particle shape can have on U_{mf}. Goosen (1988 p. 101) showed that both U_{mf} and ε_{mf} of angular-shaped powders were greater than that of spherical-shaped particles.

The effect of pressure and temperature on the minimum fluidization velocity is summarised in Yates (1996). In general, it has been found that the effect of pressure on U_{mf} depends on the particle size. For Geldart group A materials, U_{mf} is not affected by pressure (Sidorenko and Rhodes 2004) while for Geldart groups B and D, U_{mf} decreases with increasing pressure. The effect of temperature on U_{mf} is not as straightforward since an increase in temperature causes a decrease in the gas density but an increase in the gas viscosity. The net effect of temperature on U_{mf} will, therefore, be dependant on the relative changes in gas density and gas viscosity. Xie and Geldart (1995) found that in the case of 68 μm FCC catalyst fluidized with air, the U_{mf} decreased with an increase in temperature. They also found that U_{mf} calculations based on the Carman-Kozeny equation (equation 2-29) provided excellent agreement with their data, especially with regards to predicting the effect of temperature on U_{mf}.

2.3.2. Minimum bubbling velocity

With fluidized beds containing fine powders, typically Geldart group A powders, the bed expands homogenously when the gas velocity is increased above U_{mf}. When a certain velocity is reached, called the minimum bubbling velocity (U_{mb}), gas bubbles appear in the bed. For group B and D powders bubbling occurs as soon as the bed is fluidized and in this case U_{mf} and U_{mb} are identical.

2.3.2.1. Literature correlations for U_{mb}

Abrahamsen and Geldart (1980) developed an empirical correlation for U_{mb} based on the results of experiments carried out on 48 gas-solid systems. The tests were carried out at ambient conditions in a 0.15 m internal diameter Plexiglas column with powders ranging in size (d_{sv}) from 21 to 71 μm and particle densities ranging from 1117 to 4600 kg/m^3. The particle shapes were not quantified but were qualitatively described as being spherical, rounded or angular. The fluidizing gas was in most cases air but some of the powders were also fluidized with helium, argon, carbon dioxide and dichlorodifluoromethane (Freon-12). The resulting correlation for U_{mb} is given in equation 2-30.

$$U_{mb} = \frac{2.07\exp(0.716F_{45})d_{sv}\rho_g^{0.06}}{\mu^{0.347}} \qquad (2\text{-}30)$$

2.3.2.2. Factors influencing U_{mb}

Simone and Harriott (1980 cited by Goosen 1988, p. 31) claimed that their measurement of U_{mb} did not show such a large effect of particle size and fines fraction as does equation 2-30. They also claim that $U_{mb} \propto d_{sv}^{0.6}$ and that the differences between their data and that of Abrahamsen and Geldart (1980) could be attributed to other powder properties such as shape, roughness and surface charge. Interestingly, equation 2-30 predicts that U_{mb} is independent of the particle density. Davies and Richardson (1966 cited by Goosen 1988, p.31) found that U_{mb} for irregular-shaped Poly Vinyl Chloride (PVC) was significantly higher than that of spherical-shaped Diakon particles.

The research carried out by Piepers *et al.* (1984) on the effect of pressure on fluidization behaviour showed that U_{mb} increases with an increase in pressure. They also showed that the increase in U_{mb} with an increase in pressure was strongly dependent on the type of gas used. For example, when hydrogen was used to fluidize the bed, the effect of pressure on U_{mb} was

only slight. However, when Argon was used to fluidize the bed, there was a significant increase in U_{mb} with pressure.

Xie and Geldart (1995) found that U_{mb} decreased with temperature and that equation 2-30 did not adequately predict the effect of temperature on U_{mb}. The correlation for U_{mb} was therefore modified to account for the effects of temperature and the modified correlation is given in equation 2-31.

$$U_{mb} = \frac{0.3\exp(0.716F_{45})d_{sv}\rho_g^{0.13}}{\mu^{0.5}} \qquad (2\text{-}31)$$

2.3.3. Particulate regime

The particulate regime, also referred to as the homogenous fluidization regime, exists when the gas velocity is between U_{mf} and U_{mb}. This regime only occurs with Geldart (1973) group A powders and is of significant industrial importance since it is a stable fluidization regime and the bed has the maximum density in this regime (as shown in Figure 2-6). Therefore, it is a desirable operating regime for applications where pressure recovery is required for powder circulation. For example, the particulate regime is an ideal operating regime for diplegs and standpipes. The disadvantage of this regime is that particle mixing and heat transfer is poor and the range of gas velocities over which this regime exists is fairly small. It is therefore not suitable for applications requiring good mixing and heat transfer and is not practical for industrial scale fluidized beds due to the low gas velocities and narrow range of operation.

According to Yates (1996) "fluidized beds are considered stable when operating in the uniformly expanded regime and to be become unstable at the point where bubbles first form". Theories relating to the stability of fluidized beds are a subject of controversy in the literature as there are two schools of thought. The one school subscribes to stability arising from inter-particle forces while the other school contends that hydrodynamic forces are the controlling factors of stability in fluidized beds.

The stability theory based on inter-particle forces assumes that the adhesion force between the particles (van der Waals forces) provides the bed an elasticity, which is characterised by the modulus E_{mb}. A criterion for stability is then given by equation 2-32 (Yates 1996).

$$\frac{\rho_p^3 d_{sv}^4 g^2}{\mu^2 E_{mb}} = \left[\frac{150(1-\varepsilon_{mb})}{\varepsilon_{mb}^2(3-2\varepsilon_{mb})}\right]^2 \qquad (2\text{-}32)$$

For stability (no bubbles) the left hand side of equation 2-32 must be less than the right hand side. Yates (1996) points out that this theories great weakness is that there is no way at present for calculating E_{mb} as it is presently obtained empirically from measurements of the voidage at minimum bubbling conditions.

The other stability theory, which claims that hydrodynamic forces controls stability in a fluidized bed, is based on the proposal of Wallis (1969 cited by Yates 1996), which has been explored further by Foscolo and Gibilaro (1984 cited by Yates 1996) and Gibilaro (1994 cited by Yates 1996). The "two-fluid" model assumes the fluidized bed to consist of two interpenetrating incompressible continua, the gas phase and the particle phase. The particle phase behaves like a fluid under the influence of gas-particle interactions (drag and buoyancy). Voidage disturbances in the bed then propagate either as dynamic or kinematic waves and stability arises if the velocity of the dynamic waves exceeds that of the kinematic waves. If the velocity of the kinematic waves exceeds that of the dynamic waves then bubbles are formed leading to an unstable condition. The stability criterion arising from this theory is given in equation 2-33.

$$\left[\frac{g d_{sv}\left(\rho_p-\rho_g\right)}{U_t^2\rho_p}\right]^{0.5} = 0.56n\left(1-\varepsilon_{mb}\right)^{0.5}\varepsilon_{mb}^{n-1} \qquad (2\text{-}33)$$

For stability (no bubbles) the left hand side of equation 2-33 must be less than the right hand side. In equation 2-33, n is the same index used in the Richardson-Zaki (1954 cited by Yates 1996) equation given in equation 2-34.

$$\frac{U}{U_t} = \varepsilon^n \qquad (2\text{-}34)$$

The index, n, is a function of Reynolds number and has been found to vary between 4.8 in the laminar regime to about 2.4 in the turbulent flow regime (Yates 1996). However, Abrahamson and Geldart (1980) warns that the Richardson-Zaki equation "was originally developed for solid-liquid systems, and although the form of the equation fits gas fluidization data, experimental values of n vary widely from system to system and are quite different from those in liquid fluidization".

Xie and Geldart (1995) conclude that both inter-particle forces and hydrodynamic forces influence the extent or stability of the particulate regime and that the controlling forces are dependant on the particle size. For very fine particles, belonging to group C, inter-particle

forces dominate whereas for larger group B particles the hydrodynamic forces dominate. For group A powders the situation is somewhat more complex but in general there will be a combined effect of inter-particle forces and hydrodynamic forces determining the stability of the particulate regime with the controlling forces being determined by the particle size.

Jean and Fan (1992 cited by Xie and Geldart 1995) developed a more complicated expression for the voidage at minimum bubbling conditions. This expression is given in equations 2-35, 2-36 and 2-37.

$$\left[\frac{gd_{sv}\left(\rho_p-\rho_g\right)}{U_t^2\rho_p}\right]^{0.5}=0.56n\left(1-\varepsilon_{mb}\right)^{0.5}\varepsilon_{mb}^{n-0.5}\gamma \tag{2-35}$$

$$\gamma=\frac{\left(\frac{\rho_m-\rho_g}{n}\right)\varepsilon_{mb}^{-0.5}}{\sqrt{\frac{\rho_p\rho_m-\rho_p^2\rho_g U_t^2\varepsilon_{mb}^{2n-1}}{3.2gd_{sv}\left(\rho_p-\rho_g\right)}}} \tag{2-36}$$

$$\rho_m=\left(1-\varepsilon_{mb}\right)\rho_g+\varepsilon_{mb}\rho_p \tag{2-37}$$

Xie and Geldart (1995) showed that for air fluidization of FCC at ambient conditions, equation 2-33 provides better agreement with the measured data than equation 2-35. However, equation 2-33 only provides good agreement with the measured data when the particle size is greater than 50 μm. For particle sizes less than 50 μm both equations 2-33 and 2-35 provide substantial over-predictions. The data of Xie and Geldart (1995) was combined with data of Abrahamsen (1980 cited by Xie and Geldart 1995) and Wong (1983 cited by Xie and Geldart 1995) to develop the correlation given in equation 2-38, which is valid for fluidization of FCC catalyst with air at ambient conditions.

$$\varepsilon_{mb}=0.09\rho_p^{0.212}\left(\frac{U_{mb}}{U_{mf}}\right)^{0.22} \tag{2-38}$$

Xie and Geldart (1995) have discussed the importance of the ratio U_{mb}/U_{mf} extensively, to the extent that they suggest it be called the Geldart number. They postulate that this ratio is related to the mechanical properties of the powder and powders having a higher ratio of U_{mb}/U_{mf} display better bed expansion in the particulate regime. Based on their experimental data they proposed that U_{mb}/U_{mf} could be calculated using equation 2-39.

$$\frac{U_{mb}}{U_{mf}} = \frac{2300\rho_g^{0.126}\mu^{0.523}\exp(0.716F_{45})}{d_{sv}^{0.8}g^{0.954}(\rho_p - \rho_g)^{0.934}} \quad (2\text{-}39)$$

Geldart (1973) used the ratio U_{mb}/U_{mf} to distinguish between group A and group B powders (for group A powders $U_{mb}/U_{mf} > 1$). The ratio U_{mb}/U_{mf} has been shown to increase with an increase in pressure (Rowe *et al.* 1983 cited by Yates 1996).

Abrahamsen and Geldart (1980) also showed that bed expansion at minimum bubbling conditions could be related to U_{mb}/U_{mf} by equation 2-40.

$$\frac{H_{mb}}{H_{mf}} = \left(\frac{U_{mb}}{U_{mf}}\right)^{0.22} \quad (2\text{-}40)$$

Based on their correlations for U_{mb} and U_{mf}, they developed equation 2-41, which can be used to predict the bed expansion at minimum bubbling conditions.

$$\frac{H_{mb}}{H_{mf}} = \frac{5.50\exp(0.158F_{45})\rho_g^{0.028}\mu^{0.115}}{d_{sv}^{0.176}g^{0.205}(\rho_p - \rho_g)^{0.205}} \quad (2\text{-}41)$$

However, Piepers *et al.* (1984) found that equation 2-41 did not provide good predictions for their data at high pressure and concluded that equation 2-41 underestimates the effect of gas density. Abrahamsen and Geldart (1980) also provided a general equation (equation 2-42) for predicting the bed voidage in the particulate regime.

$$\frac{\varepsilon^3(\rho_p - \rho_g)gd_{sv}^2}{\mu(1-\varepsilon)} = 210(U - U_{mf}) + \frac{\varepsilon_{mf}^3(\rho_p - \rho_g)gd_{sv}^2}{\mu(1-\varepsilon_{mf})} \quad (2\text{-}42)$$

The constant 210 in equation 2-42 was obtained by regression of their data to fit an equation based on the Carmen-Kozeny packed-bed pressure drop equation. There was considerable scatter in the data with angular particles showing more deviation than spherical particles. It is therefore believed that the particle shape also plays an important role in determining the bed voidage in the particulate regime and therefore no generalised correlation can be developed without accounting for the particle shape effects. Use of equation 2-42 requires knowledge of ε_{mf}, which can only be obtained experimentally. However Abrahamsen and Geldart (1980) suggest that ε_{mf} can be calculated from the aerated bulk density and they provide a procedure for measuring this.

2.3.4. Slugging regime

The bubbling fluidization regime exists when the gas velocity exceeds the minimum bubbling velocity. In this regime the type of bubbling fluidization, which results, is dependant on the size of the column containing the bed. In small diameter columns, the combination of bubble growth and wall effects leads to a phenomenon called slugging. In the slugging regime, gas slugs rise through the bed at regular intervals and because their size is close to the diameter of the column they divide the bed into alternate regions of dense and lean phase, as illustrated in Figure 2-8. The slugging fluidization regime is characterized by large pressure fluctuations, which correspond to the rise and fall of the dense phase. Baeyens and Geldart (1974) noted that variations of 5 – 10 % in the bed pressure drop or bed density is a strong indication of slugging. Since slugging occurs mainly in small diameter columns, bench scale and pilot scale reactors are more prone to slugging behaviour than large commercial fluidized bed reactors. Kunii and Levenspiel (1991, p. 430) warns that since the flow patterns are so different in bench and pilot scale reactors compared with commercial reactors, conversion data obtained from the pilot units should not be used directly for the design of the commercial units.

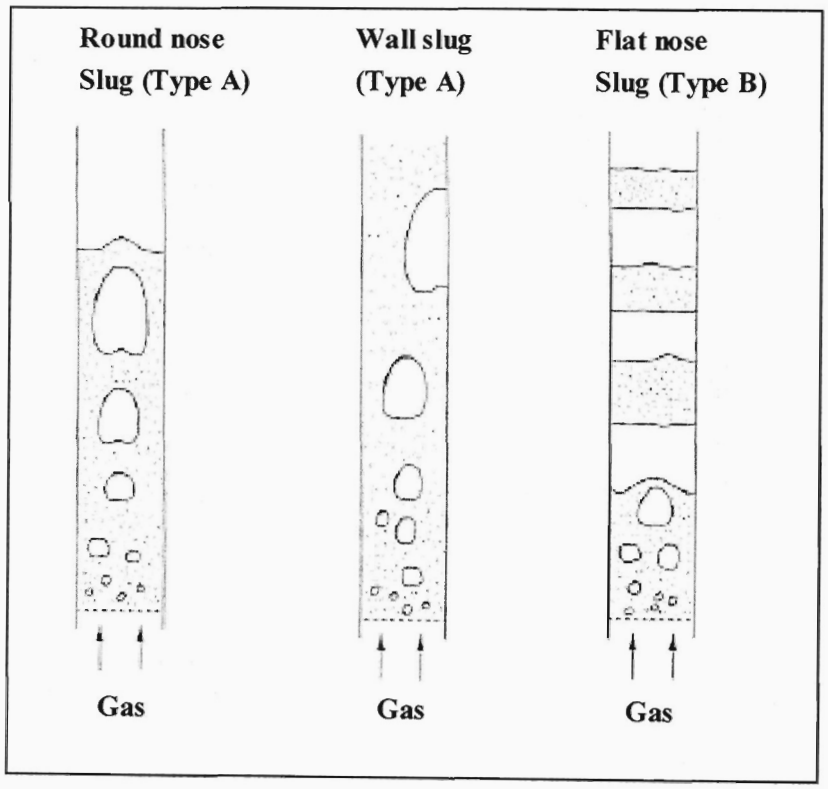

Figure 2-8: Different types of slugging fluidized beds.

2.3.4.1. Types of slugging

Yang (2003b p.75) indicates that there are generally two types of slugging fluidized beds. The first type, called Type A occurs with group A and B powders, and consists of axisymmetric or asymmetric round-nosed gas slugs with the solids flowing in the annulus region outside the gas slug and close to the column wall. Wall-slugs are also a variation of Type A slugs. The second type of slugging, called Type B occurs with cohesive particles and particles that are angular in shape. These slugs are square-nosed and occupy the complete cross-section of the column and the only way the solids can pass through the gas slugs is by raining down through the slugs. These two types of slugging beds are illustrated in Figure 2-8. Based on a modelling approach, Zhang and Yu (2002) found that the nature of the particle-wall interactions determines the type of slugs that are formed. For example, no-slip wall conditions led to the formation of round-nosed slugs while full-slip wall conditions resulted in square-nosed slugs.

Baeyens and Geldart (1974) proposed the existence of three zones in a slugging fluidized bed. Zone 1 occurs at the bottom of the bed, in the region just above the gas distributor, and is essentially a freely bubbling bed. Zone 2 occurs just above zone 1 and is the region where slugs start to form through bubble coalescence. Zone 3 occurs at the top portion of the bed where bubble coalescence is complete and fully developed slugs predominate.

2.3.4.2. Slugging criteria

According to Zhang and Yu (2002) the onset of slugging is dependant on many factors such as the bed geometry, particle properties, wall conditions and the superficial gas velocity. Clift (1986) identifies three conditions, which must be satisfied for a fluidized bed to be in the slugging regime. These are:

- The maximum stable bubble size must be greater than 0.6D
- The gas velocity must be above the minimum slugging velocity (U_{ms})
- The bed height must be above that required for minimum slugging (H_{ms})

The bubble size depends on the particle and gas properties and typically the coarser and denser the particles, the larger the bubble size. Group B and D powders have larger bubble sizes when compared to group A (Clift 1986 p.60), therefore, slugging is expected to be more pronounced with groups B and D powders. The literature that was reviewed did not

contain any information on the effect of particle shape on bubble size and slugging. Therefore, in the current study the effect of particle shape on slugging is investigated.

The minimum slugging velocity refers to that velocity at which stable slugging occurs in the bed. Choi *et al.* (2003) indicate that U_{ms} is normally determined from a plot of slug frequency versus gas velocity. U_{ms} is the velocity at which the slug frequency starts to stabilize and does not increase further with gas velocity. Stewart and Davidson (1967 cited by Yang 2003b p. 76) proposed that the minimum slugging velocity could be calculated using equation 2-43.

$$\frac{U - U_{mf}}{0.07\sqrt{gD}} > 1 \quad \text{for slugging to occur} \tag{2-43}$$

Baeyens and Geldart (1974) contend that equation 2-43 is valid provided the bed height is greater than 0.3 m. For bed heights below 0.3 m, they recommended that U_{ms} should be calculated using equation 2-44.

$$U_{ms} = U_{mf} + 0.07\sqrt{gD} + 1.6\times10^{-3}\left[60(100D)^{0.175} - 100H_{mf}\right]^2 \tag{2-44}$$

Baeyens and Geldart (1974) also found that there exists a minimum bed height for stable slugging (H_{ms}), which is a function of the column diameter. They recommend that H_{ms} can be calculated using equation 2-45. They also found that there exists a bed height below which the bed will be freely bubbling (H_{fb}) and they recommend that this height can be calculated using equation 2-46.

$$H_{ms} = 60(100D)^{0.175} \tag{2-45}$$

$$H_{fb} = \frac{100D - 2.51(100D)^{0.2}}{0.13(100D)^{0.47}} \tag{2-46}$$

Equations 2-44 to 2-46 have been modified from the original form so that SI units can be used.

2.3.4.3. Properties of slugs

According to Yang (2003b, p. 76-77) the slug length (L_s) and slug frequency (f_s) can be calculated using equations 2-47 and 2-48 respectively.

$$L_s = \frac{(U - U_{mf}) N_T \sqrt{D}}{0.35\sqrt{g}} \tag{2-47}$$

$$f_s = \frac{U - U_{mf}}{L_s} = \frac{0.35\sqrt{g}}{N_T \sqrt{D}} \tag{2-48}$$

The use of equations 2-47 and 2-48 are limited since the number of bed diameters between the rear of a leading slug and the nose of a trailing one (N_T) has to be obtained experimentally. Kehoe and Davidson (1973 cited by Yang 2003b, p.77) report values of N_T ranging between 2 and 8.

Stewart and Davidson (1967 cited by Kunii and Levenspiel 1991, p.133) proposed that the velocity at which the slug rises (slug rise velocity) is related to the excess gas velocity ($U-U_{mf}$) by equation 2-49.

$$U_s = j(U - U_{mf}) + 0.35\sqrt{gD} \tag{2-49}$$

Nicklin (1962 cited by Dry *et al.* 1984) and later Ormiston *et al.* (1965 cited by Kunii and Levenspiel 1991, p.133) found that the excess gas velocity coefficient (j) in equation 2-49 was approximately equal to 1. However, Dry *et al.* (1984) carried out tests with fine milled iron oxide powder in a 0.05 m internal diameter column and found that their data could be better represented by equation 2-50.

$$U_s = 1.15(U - U_{mf}) + 0.63\sqrt{gD} \tag{2-50}$$

The significantly higher slug rise coefficient in equation 2-50 (0.63 compared with 0.35 in equation 2-49) was explained in terms of a low dense phase viscosity which arose from the use of a powder with a high fines content and hence a high dense phase voidage.

2.3.4.4. Factors influencing slugging

In the work of Baeyens and Geldart (1974), the column sizes ranged between 0.05 to 0.3 m in internal diameter, the particle density varied between 850 and 2800 kg/m^3, and the average particle size ranged between 55 and 3380 μm. They found that, except for the smallest column (D = 0.05 m), neither the particle size nor the particle size distribution had any effect on slugging. They claimed that the data from the 0.05 m column was abnormal. Dry *et al.* (1984) however, showed that the fines content of the powder does affect the slug velocity. There was no mention of the effect of particle shape in both the work of Dry *et al.* (1984) and Baeyens and Geldart (1974).

Choi *et al.* (2003) discusses the effect of temperature on the slug properties in a slugging bed of FCC catalyst and in general they found that U_{ms} and the slug frequency decreased slightly with an increase in the bed temperature (in the temperature range 25 to 400 °C). Based on their data they developed equation 2-51 which incorporates the effect of temperature and gas velocity on the slug rise velocity.

$$U_s = (0.01T_b + 0.97)(U - U_{mf}) + 0.35\sqrt{gD} \qquad (2\text{-}51)$$

Of the literature reviewed there was nothing reported on the effect of pressure on slugging fluidized beds. However, as will be shown in the next section, an increase in pressure normally reduces the bubble size. Hence, for slugging beds an increase in pressure is expected to delay the onset of slugging.

2.3.5. Bubbling regime

The bubbling regime occurs in columns, which are sufficiently large such that the bubble sizes are not influenced by the size of the column. As illustrated in Figure 2-6, the bubbling regime exists as long as the gas velocity is above the minimum bubbling velocity (U_{mb}) and below the velocity at which transition to the turbulent regime occurs (U_c). An increase in the gas velocity between U_{mb} and U_c generally results in an increase in the bubble activity, which promotes good mixing and solids circulation in the fluidized bed. In this regime the bed consists essentially of two phases namely the dense phase (also called the emulsion phase) and the bubble phase (also called the dilute phase) as shown in Figure 2-9.

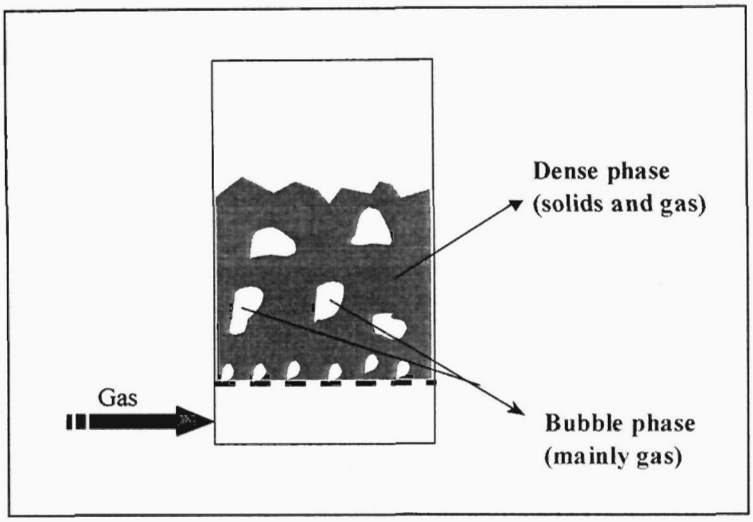

Figure 2-9: Dense and bubble phases in the bubbling fluidization regime.

The gas hold-up (voidage) in the dense phase and the bubble phase, the gas velocity in the dense phase, the bubble size and bubble velocity are important parameters that can be used to characterize the hydrodynamics of the bubbling fluidization regime. The dense phase voidage, bubble fraction and overall bed voidage are defined by equations 2-52, 2-53 and 2-54 respectively.

$$\varepsilon_d = \frac{\text{volume of gas in the dense phase}}{\text{total volume of the dense phase}} = \frac{V_{gd}}{V_d} \qquad (2\text{-}52)$$

$$\varepsilon_b = \frac{\text{Volume gas present as bubbles in the bed}}{\text{Total volume of the fluidized bed}} = \frac{V_b}{V_{bed}} \qquad (2\text{-}53)$$

$$\varepsilon = \frac{\text{Volume gas in the fluidized bed}}{\text{Total volume of the fluidized bed}} = \frac{V_g}{V_{bed}} \qquad (2\text{-}54)$$

2.3.5.1. Voidage measurement

The voidage in a fluidized bed can be conveniently measured using the bed collapse technique, which was proposed by Rietema (1967 cited by Barreto *et al.* 1983). According to this technique, the bed is fluidized at the desired superficial gas velocity and at time t = 0 the gas supply is suddenly shut off using, for example, a solenoid valve. The bed then settles as shown in Figure 2-10.

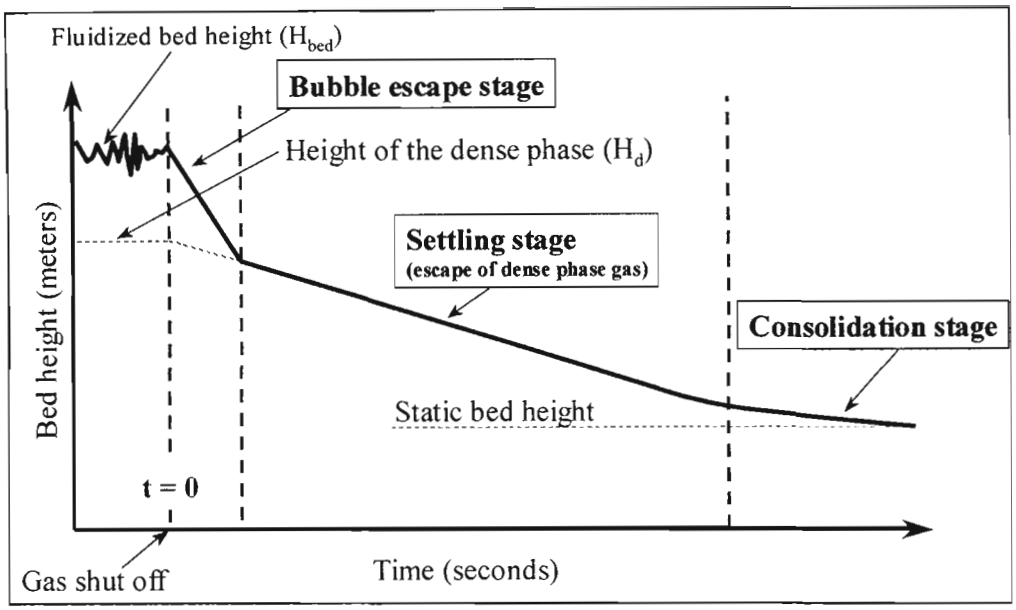

Figure 2-10: Collapsing stages during a bed collapse experiment with a group A powder.

The initial collapse of the bed is rapid and occurs as the bubbles escape from the bed. This is followed by the settling stage where the bed collapses linearly with time, as the dense phase gas escapes and this is referred to as the settling stage. During the settling stage the bed collapses at a much slower rate than during the bubble escape stage. The settling stage is followed by the consolidation stage. Only Geldart group A powders exhibit all three bed collapsing stages shown in Figure 2-10. With group B and D powders, the bed collapses so fast making this method of voidage determination impractical. By extrapolating the line representing the settling stage to time t = 0, one can obtain an estimate of the height of the dense phase (H_d) and the dense phase voidage can be calculated using equation 2-55.

$$\varepsilon_d = 1 - \frac{W}{A\rho_p H_d} \tag{2-55}$$

Once H_d is known, the bubble voidage can then calculated using equation 2-56.

$$\varepsilon_b = 1 - \frac{H_d}{H_{bed}} \tag{2-56}$$

The overall bed voidage can then be calculated using equation 2-57.

$$\varepsilon = 1 - \left[(1 - \varepsilon_d)(1 - \varepsilon_b) \right] \tag{2-57}$$

The derivation of equations 2-55 to 2-57 is given in Appendix C (section C2).

Using the bed collapse technique provides average voidages for the bed as a whole. Some researchers, for example, Oltrogge (1972 cited by Abrahamsen and Geldart 1980a) and Drinkenburg (1973 cited by Abrahamsen and Geldart 1980a) have used the slope of the line during the settling stage (settling rate) as the gas velocity in the dense phase (U_d). However, Abrahamsen and Geldart (1980a) have shown that this slope (rate of settling) is dependant on various factors such as the gas distributor pressure drop and the volume of the plenum chamber. The collapse rate decreases as the pressure drop across the gas distributor increases and as the volume of the plenum chamber increases.

Grace (1992 cited by Lorences *et al.* 2003) also showed that the location of the flow interruption device used for the bed collapse test also influences the collapse rate of the bed. He described three types of collapse tests: single drainage, double drainage and controlled-double drainage. In single drainage bed collapse tests the gas is shut-off upstream of the plenum chamber and in this case the rate at which the bed collapses is slower because the gas in the plenum and piping vents through the bed. In the double drainage bed collapse test, the gas flow is shut-off and the plenum is vented to atmosphere simultaneously. The controlled double drainage bed collapse test makes use of an additional valve attached to the plenum chamber and when the gas supply is shut-off this value is used to maintain a zero pressure drop across the gas distributor. Lorences *et al.* (2003) compared the single drainage and double drainage bed collapse rates and found that the collapse time employing the single drainage method was about two times longer than that employing the double drainage method. They further recommend that the single drainage method should be used only to compare the differences between powders but it should not be used for hydrodynamic modelling without accounting for the volume of the plenum and tubing upstream of the distributor.

Nie and Liu (1998) developed a model to describe the pressure variation at different locations in the bed during a bed collapse test to study the collapsing process of the fluidized bed. They showed that the model results were in good agreement with the experimental data and that information such as the dense phase voidage, bubble fraction, bubble velocity and the slip velocity of the particles could be estimated using their model. The benefit of this technique is that it provides more information than the conventional bed collapse test and it could be used to obtain information at different axial locations in the bed.

Rowe, *et al.* (1978) and Barreto *et al.* (1983) used an X-ray absorption technique to study the effect of particle size on the division of gas between the dense phase and bubble phase and to obtain the dense phase voidage and the gas velocity in the dense phase. However, Rowe *et al.* (1978) acknowledge that this technique is restricted to low gas velocities since the data interpretation gets too confusing at higher gas velocities. Barreto *et al.* (1983) compared the dense phase voidage results obtained using the X-ray absorption technique and the conventional bed collapse test and concluded that there was good agreement between the two techniques. However, the advantage of the X-ray technique is that it can be used to obtain information on the axial variation of voidage in the fluidized bed, which is not possible with the conventional bed collapse test.

2.3.5.2. Two-phase theory of fluidization

According to Clift (1986), the actual flow rate of gas in the bubble phase consists of the visible bubble flow rate (Q_b) and the bulk through flow of gas into and out of the bubbles. The visible bubble flow rate is defined as the volume of gas passing a given cross section of the bed as bubbles per unit time. The total gas entering the fluidized bed is distributed between the dense phase and bubble phase in relative amounts that have to be determined experimentally. However, Toomey and Johnstone (1952 cited by Clift 1986, p. 81) proposed the two-phase theory of fluidization to account for the distribution of gas between the dense and bubble phases. This theory states that all gas in excess of that required to bring the bed to minimum fluidization conditions passes through the bed in the form of bubbles. It is further assumed that the gas velocity in the dense phase and the voidage of the dense phase is equivalent to that prevailing at incipient fluidization conditions. In its original form the two-phase theory of fluidization can be expressed mathematically by equation 2-58 (Clift 1986, p. 81), however, it can also be expressed by equation 2-59 to 2-61 (Dry *et al.* 1983).

$$\frac{Q_b}{A} = U - U_{mf} \tag{2-58}$$

$$\frac{Q_b}{A} = U - U_d = U_b \varepsilon_b \tag{2-59}$$

$$U_d = U_{mf} \tag{2-60}$$

$$\varepsilon_d = \varepsilon_{mf} \tag{2-61}$$

Equations 2-60 and 2-61 are essentially the assumptions built into the two-phase theory of fluidization. King and Harrison (1980 cited by Dry *et al.* 1983) found that the two phase theory of fluidization describes the behaviour of group B powders fairly well but it has been shown not to be valid for group A materials, for example, by Rowe *et al.* (1978), Abrahamsen and Geldart (1980), Barreto *et al.* (1983) and Dry *et al.* (1983). The research of the latter authors show that the main reason for the two-phase theory being invalid for group A powders is because the actual dense phase voidage and dense phase gas velocity are considerably higher than that at incipient fluidization conditions. For example, Rowe *et al.* (1978) have shown that the dense phase velocity is strongly dependent on the amount of fines and can be as much as 25 times higher than the incipient fluidization velocity. More information on the effect of powder properties on the dense phase is provided in section 2.3.5.4.

Davidson and Harrison (1966 cited by Dry *et al.* 1983) proposed that U_{mf} in equation 2-58 be multiplied by a factor k to account for deviations from the two-phase theory, which then results in equation 2-62.

$$\frac{Q_b}{A} = U - kU_{mf} \tag{2-62}$$

Lockett *et al.* (1967 cited by Rowe *et al.* 1978) proposed that equation 2-63 could be used to predict k based on a theoretical assessment of gas through flow in and out of the bubbles.

$$k = 1 + 2\varepsilon_b \tag{2-63}$$

However, Grace and Harrison (1969 cited by Dry *et al.* 1983) showed that equation 2-63 still provided an under-prediction of observed data. Grace and Clift (1974 cited by Rowe *et al.* 1978) report values of k ranging between 0.7 and 27, which was derived from measurements of visible bubble flow rate. Abrahamsen and Geldart (1980a) measured U_d using the bed collapse experiment for 13 air-solid systems and correlated their results with equation 2-64.

$$k = \frac{U_d}{U_{mf}} = \frac{188\rho_g^{0.089}\mu^{0.371}\exp(0.508F_{45})}{d_{sv}^{0.568}g^{0.663}(\rho_p - \rho_g)^{0.663}H_{bed}^{0.244}} \tag{2-64}$$

Equation 2-64 reflects the significant influence of fines on k. Dry *et al.* (1983) also provided a correlation for k based on bed collapse experiments carried out with powders having average particle sizes ranging between 12 and 67 μm and particle densities varying between

1300 and 5190 kg/m^3. This correlation is given by equation 2-65 and is based on U_{mf} obeying the Wen and Yu (1966 cited by Dry *et al.* 1983) correlation (equation 2-28).

$$k = 0.73\exp(6.42F_{22}) \tag{2-65}$$

Corrections for the dense phase voidage have not been as forthcoming as those for the dense phase gas velocity (Dry *et al.* 1983). Abrahamsen and Geldart (1980a) correlated their dense phase voidage data using equation 2-66.

$$\frac{1-\varepsilon_{mf}}{1-\varepsilon_d} = \frac{2.54\rho_g^{0.016}\mu^{0.066}\exp(0.090F_{45})}{d_{sv}^{0.1}g^{0.118}(\rho_p-\rho_g)^{0.118}H_{mf}^{0.043}} \tag{2-66}$$

Again, the strong effect of the fines on the dense phase voidage can be clearly seen. Weimer and Quarderer (1985) report good agreement of their experimental data with equation 2-66, except for the 66 μm powder, which they used. They found that with this powder, equation 2-66 underestimated the effect of pressure. However, they found "excellent agreement" when they compared their results to the correlation of Kmiec (1982) given by equation 2-67 (note this equation was derived based on data for a solid-liquid fluidized bed). Re_p is calculated from: $Re_p = d_p\rho_g U/\mu$.

$$\varepsilon_d = \frac{(18Re_p + 2.7Re_p^{1.687})^{0.209}}{Ar^{0.209}} \tag{2-67}$$

Abrahamsen and Geldart (1980a) also proposed equation 2-68 for calculating the dense phase velocity.

$$\left(\frac{\varepsilon_d}{\varepsilon_{mf}}\right)^3\left(\frac{1-\varepsilon_{mf}}{1-\varepsilon_d}\right) = \left(\frac{U_d}{U_{mf}}\right)^{0.70} \tag{2-68}$$

Dry *et al.* (1983) provide a correlation for the dense phase voidage based on bed collapse experiments. This correlation is given by equation 2-69.

$$1-\varepsilon_d = 0.212\exp\left[1.13\exp(-2.07F_{22})\right] \tag{2-69}$$

The strong influence of fines is again demonstrated by this equation.

2.3.5.3. Bubble parameters

In the bubbling regime bubbles formed at the gas distributor rise through the bed and grow in size. In so doing they create solids movement and promote mixing in the fluidized bed. Bubble parameters that are important in the bubbling regime include the bubble size, the bubble rise velocity, the bubble frequency and the bubble fraction.

According to Kunii and Levenspiel (1991, p. 115) a bubbling fluidized bed behaves in many ways like a bubbling liquid of low viscosity. Some of the similarities include: similar bubble shape, the bubble velocity increases with bubble size, bubbles coalesce to form larger bubbles and the bubble rise velocity depends on the same factors and can be described by similar expressions. Thus, based on the early work of Davies and Taylor (1950 cited by Kunii and Levenspiel 1991, p. 116) and a summary of experimental measurements made by other workers (Kunii and Levenspiel 1991, p. 116) the rise velocity of single bubbles in a fluidized bed can be expressed by equation 2-70.

$$U_{br} = 0.711\sqrt{gd_{be}} \tag{2-70}$$

Davidson and Harrison (1963 cited by Kunii and Levenspiel 1991), on the basis of the two-phase theory of fluidization, proposed equation 2-71 for the rise velocity of bubbles in a fluidized bed.

$$U_b = U - U_{mf} + 0.711\sqrt{gd_{be}} \tag{2-71}$$

Since equation 2-71 is based on the two-phase theory it is expected not to be applicable to fine group A powders, whereas, it should provide a reasonable approximation for larger group B powders. This was confirmed to be true from the data presented by Kunii and Levenspiel (1991, p. 148-149). Dry *et al.* (1984) also found that the bubble rise coefficient (0.711) in equation 2-71 was too low to provide reasonable predictions of bubble diameter for their system and proposed that reasonable estimates of bubble sizes could be obtained if it were increased to between 1.5 and 1.6. Werther (1981 cited by Kunii and Levenspiel 1991, p. 147) proposed equation 2-72 to account for the effect of particle size and column diameter on bubble rise velocity.

$$U_b = \varphi(U - U_{mf}) + \beta U_{br} \tag{2-72}$$

The fraction of visible bubbles (φ) is defined by equation 2-73 and β is a factor that accounts for deviations from single bubble behaviour.

$$\varphi = \frac{\text{observed bubble flow}}{\text{excess flow from two-phase theory}} = \frac{Q_b}{A(U - U_{mf})} \qquad (2\text{-}73)$$

Werther (1981 cited by Kunii and Levenspiel 1991, p. 149) proposed equations 2-74 to 2-76 to describe the relationship between α and column diameter.

Group A powders (0.05 m < D < 1.0 m): $\beta = 3.2D^{1/3}$ (2-74)

Group B powders (0.1 m < D < 1.0 m): $\beta = 2.0D^{1/2}$ (2-75)

Group D powders (0.1 m < D < 1.0 m): $\beta = 0.87$ (2-76)

Based on the experimental data of Hilligardt and Werther (1986 cited by Kunii and Levenspiel 1991, p. 148), Kunii and Levenspiel (1991, p. 149) proposed equation 2-77 and 2-78 for the calculation of bubble rise velocities.

Group A powders ($D \leq 1$ m):

$$U_b = 1.55D^{0.32}\left[(U - U_{mf}) + 14.1(d_{be} + 0.005)\right] + U_{br} \qquad (2\text{-}77)$$

Group B powders ($D \leq 1$ m):

$$U_b = 1.6D^{1.35}\left[(U - U_{mf}) + 1.13d_{be}^{0.5}\right] + U_{br} \qquad (2\text{-}78)$$

Werther (1983 cited by Ellenberger and Krishna 1994) later proposed that the bubble rise velocity could be correlated using equation 2-79 and provided values for β as a function of column diameter as shown in equations 2-80 and 2-81.

$$U_b = \beta\sqrt{gd_{be}} \qquad (2\text{-}79)$$

For group A powders (eg. FCC):

$$\begin{aligned} &\beta = 1.0 && \text{for } D < 0.1 \text{ m} \\ &\beta = 2.5D^{0.4} && \text{for } 0.1 \leq D \leq 1 \text{ m} \\ &\beta = 2.5 && \text{for } D > 1 \text{ m} \end{aligned} \qquad (2\text{-}80)$$

For group B powders (eg. sand):

$$\begin{aligned} &\beta = 0.64 && \text{for } D < 0.1 \text{ m} \\ &\beta = 1.6D^{0.4} && \text{for } 0.1 \le D \le 1 \text{ m} \\ &\beta = 1.6 && \text{for } D > 1 \text{ m} \end{aligned} \qquad (2\text{-}81)$$

Ellenberger and Krishna (1994) concluded that β could be related to the column diameter by equation 2-82 and the constants (β_0 and x) in the equation could be determined experimentally.

$$\beta = \beta_0 D^x \qquad (2\text{-}82)$$

As shown above the bubble rise velocity depends on the bubble diameter. The bubble diameter has been found to depend on the physical properties of the powder (Kunii and Levenspiel 1991, p. 144-145; Weimer and Quarderer 1985). For group B and D powders the bubbles tend to increase in size as they travel up the bed and the depth of the bed therefore limits their size. For group A powders the bubbles increase in size as they travel up the bed but attain a maximum stable bubble size at some height in the bed above which there is no further increase in the bubble size. Bubble growth is primarily attributed to bubble coalescence (Yang 2003a). The existence of a maximum stable bubble size can be attributed to bubble splitting when bubble sizes become unstable.

Various correlations have been developed for predicting the bubble diameter in fluidized beds and some of these are now presented. Geldart (1972 cited by Darton *et al.* 1977) proposed equation 2-83 for predicting the frontal diameter of bubbles in a fluidized bed.

$$d_{bf} = 1.43 g^{-0.2} [A_0 (U - U_{mf})]^{0.4} + 2.05 (U - U_{mf})^{0.94} z \qquad (2\text{-}83)$$

Mori and Wen (1975 cited by Yang 2003b, p. 72) assumed that all gas in excess of U_{mf} formed a single train of bubbles in the centre of the bed. This assumption led to the development of equations 2-84 to 2-87 for bubble size predictions.

$$\frac{d_{bm} - d_{be}}{d_{bm} - d_{b0}} = \exp\left(\frac{-0.3z}{D}\right) \qquad (2\text{-}84)$$

$$d_{bm} = 0.652\left[A\left(U - U_{mf}\right)\right]^{0.4} \qquad (2\text{-}85)$$

For perforated plates:

$$d_{bo} = 0.347\left[\frac{A(U - U_{mf})}{N_o}\right]^{0.4} \quad (2\text{-}86)$$

For porous plates:

$$d_{bo} = 0.00376(U - U_{mf})^2 \quad (2\text{-}87)$$

The range of conditions at which the above correlations were obtained is as follows:

- $0.3 < D < 1.30$ m
- $60 < d_p < 450$ μm
- $0.005 < U_{mf} < 0.2$ m/s
- $U - U_{mf} < 0.48$ m/s

Rowe (1976) proposed equation 2-88 for calculating the bubble diameter.

$$d_{be} = \frac{(U - U_{mf})^{0.5}(z + z_0)^{0.75}}{g^{0.25}} \quad (2\text{-}88)$$

z_0 is zero for porous plates and was found to increase with bed height according to equation 2-89. No information for z_0 was given for other types of gas distributors.

$$z_0 = 0.772 + 0.6z \quad (2\text{-}89)$$

Darton *et al.* (1977) proposed equation 2-90 which was developed on the basis of the two-phase theory. z_0 is given by equation 2-91.

$$d_{be} = \frac{0.54(U - U_{mf})^{0.4}(z + z_0)^{0.8}}{g^{0.2}} \quad (2\text{-}90)$$

$$z_0 = 4\sqrt{A_o} \quad (2\text{-}91)$$

Ellenberger and Krishna (1994) proposed that equation 2-90 could be written in general terms by replacing the factor 0.54 with α (to be determined experimentally) and replacing U_{mf} with U_d (to account for deviations from the two-phase theory) and introducing, z*, the

height from the gas distributor at which the bubbles attain the maximum stable size, d_{be}^{*}, which remains constant above z*. In this case equations 2-92 and 2-93 can be written.

$$d_{be} = \frac{\alpha(U - U_d)^{0.4}(z + z_0)^{0.8}}{g^{0.2}} \quad \text{for } z \le z^{*} \tag{2-92}$$

$$d_{be}^{*} = \frac{\alpha(U - U_d)^{0.4}(z^{*} + z_0)^{0.8}}{g^{0.2}} \quad \text{for } z^{*} \le z \le H_{bed} \tag{2-93}$$

According to Ellenberger and Krishna (1994) the bubble fraction in the bed can be expressed by equation 2-94

$$\varepsilon_b = \frac{1}{H_{bed}} \int_0^{H_{bed}} \frac{U - U_d}{U_b} dz \tag{2-94}$$

By substituting equations 2-79, 2-82, 2-92, 2-93 into equation 2-94 and integrating, Ellenberger and Krishna (1994) found that the solution could be given by equations 2-95 and 2-96 (note z_0 is given by equation 2-91).

For $H_{bed} \le z^{*}$

$$\varepsilon_b = \frac{\left[(H_{bed} + z_0)^{0.6} - z_0^{0.6}\right](U - U_d)^{0.8}}{0.6 g^{0.4} H_{bed} \sqrt{\alpha}\beta_0 D^{x}} \tag{2-95}$$

For $H_{bed} > z^{*}$

$$\varepsilon_b = \frac{\left[(z^{*} + z_0)^{0.6} - z_0^{0.6}\right](U - U_d)^{0.8}}{0.6 g^{0.4} H_{bed} \sqrt{\alpha}\beta_0 D^{x}} + \frac{(H_{bed} - z^{*})(U - U_d)^{0.8}}{g^{0.4} H_{bed} \sqrt{\alpha}\beta_0 D^{x} (z^{*} + z_0)^{0.4}} \tag{2-96}$$

Ellenberger and Kishna (1994) also found that z* could be correlated by equation 2-97 (note b_0 and b_1 has to be determined experimentally).

$$z^{*} = b_0 + b_1(U - U_d) \tag{2-97}$$

The above equations for ε_b provide a convenient method to correlate experimental data. From the literature reviewed no empirical correlations could be found for ε_b except for that of Dry (1982) who proposed equation 2-98 for correlating the effect of superficial gas velocity on ε_b.

$$\varepsilon_b = 0.436U^{0.9} \quad (2\text{-}98)$$

2.3.5.4. Factors influencing the dense phase

The particle size distribution and in particular the fraction of fines has been found to affect the dense phase voidage and the gas velocity in the dense phase. Rowe *et al.* (1978) used an X-ray absorption technique to measure the dense phase voidage and dense phase gas velocity of commercial silica base catalyst (d_{sv} = 52 μm) having varying fines (< 45 μm) content. They found that the dense phase voidage and the dense phase gas velocity increased with an increase in the fines content. The dense phase voidage initially decreased with an increase in gas velocity (for U < 0.04 m/s) and thereafter there was a slight increase with gas velocity (for 0.04 m/s < U < 015 m/s).

Abrahamsen and Geldart (1980) used the bed collapse technique to study the effect of particle properties on ε_d and U_d. They used 13 powders varying in average size (29 μm < d_{sv} < 70.5 μm), particle density (1117 kg/m^3 < ρ_p < 3970 kg/m^3) and shape and concluded that ε_d and U_d increase with an increase in fines content (< 45 μm) in the velocity range that they employed (0 < U < 0.06). They also found that ε_d and U_d decreased with an increase in bed height and that the type of gas distributor did not have an effect on the dense phase properties above a superficial gas velocity of 0.04 m/s. Based on the correlations they developed (equations 2-64 and 2-66) they noted that the dense phase voidage increases with a decrease in the particle density, mean particle size and bed height and increases with an increase in the fines fraction, gas viscosity and gas density. They conclude that the dense phase voidage is close to ε_{mf} at the top of a deep bed and increases towards the gas distributor and that U_d does not exceed U_{mb}.

Barreto *et al.* (1983) used both the X-ray absorption and bed collapse techniques with FCC powders varying in mean particle size (39.8 μm < d_{sv} < 70.7 μm), particle density (886 kg/m^3 < ρ_p < 1264 kg/m^3), fines fraction (0.04 < F_{45} < 0.5) and found that dense phase properties (ε_d and U_d) increased with an increase in the fines fraction. The dense phase voidage was also found to decrease with increasing bed height, which is in agreement with the findings of Abrahamsen and Geldart (1980a). However, it should be noted that the bed height used by Barreto *et al.* (1983) was in the range used by Abrahamsen and Geldart (1980a).

Dry *et al.* (1983) used the bed collapse technique to measure ε_d and U_d of 11 different powders varying in average particle size (12 μm < d_v < 67 μm), particle density (1300 kg/m^3 < ρ_p < 5190 kg/m^3) and fines fraction (0.042 < F_{22} < 0.862). They also found that the dense

phase properties (ε_d and U_d) increased with an increase in the fines content and based on their data they developed correlations (equations 2-65 and 2-69) for these. Dry *et al.* (1983) however, found that the dense phase properties were not dependent on the particle density and bed height, which is contrary to the findings of Abrahamsen and Geldart (1980a). Dry *et al.* (1983) explained the apparent contradiction of the bed height effect by noting that bed heights in their experiments were roughly twice that used by Abrahamsen and Geldart (1980a) and concluded that above a bed height of about 1 m the dense phase properties are not affected by the bed height. Dry *et al.* (1983) also showed that the dense phase properties were not affected by column size (columns with hydraulic diameters of 0.05 m, 0.14 m, 0.18 m and 0.41 m were used in their study) provided the gas velocity was above 0.4 m/s. Below this velocity the dense phase voidage was found to be lower in the columns having a larger hydraulic diameter (0.18 and 0.41 m) and this was attributed to the effect of the gas distributor.

No information could be found on the effect of particle shape on the dense phase properties except for that of Goosen (1988 p.105) who contends that, for equivalent particle size and density, the gas flow through the dense phase will be roughly doubled if the particle sphericity is changed from 0.9 to 0.7. This was deduced from an analysis of the effect of particle shape on the ratio $\Phi^2\varepsilon_{mb}^3/(1-\varepsilon_{mb})$. No experimental data was provided to show the effect of particle shape on the dense phase properties.

Weimer and Quarderer (1985) and Guedes de Carvalho (1981) have reported on the effect of pressure on the dense phase properties. They found that in general an increase in pressure results in an increase in the dense phase voidage and dense phase gas velocity. Weimer and Quarderer (1985) also found that the effect of pressure on the dense phase properties appears to be more pronounced the smaller the particles average size.

2.3.5.5. Factors influencing bubble parameters

Particle properties, gas properties, column geometry and operating conditions such as pressure and temperature are expected to have an influence on the bubble parameters in the bubbling fluidization regime. Ellenberger and Krishna (1994) studied an air-FCC system and found that the bubble fraction was a strong function of the column diameter. An increase in the column diameter resulted in a decrease in the bubble fraction. However, they warn that the Werther (1983 cited by Ellenberger and Krishna 1994) correlations (equations 2-80 and 2-81), which seems to imply that the column diameter dependence vanishes above D = 1 m, has not been verified experimentally in the literature on gas-solid fluidization. The bubble

fraction was also found to increase with an increase in bed height but was found to remain fairly constant with an increase in gas density. They conclude that the latter finding is significant since experiments carried out at ambient conditions could be used to predict the bubble fraction at high pressure.

Dry (1982) found that the superficial velocity had a strong influence on the bubble fraction and found that the bubble fraction increased with an increase in superficial gas velocity (equation 2-98). An increase in bubble size with an increase in gas velocity was also reported by Weimer and Quarderer (1985), however they also showed that the pressure had a more significant effect on bubble size especially for the smaller particles. They found that the bubble size of the powder having an average particle size of 66 μm decreased significantly with an increase in pressure from 1 to 20.7 bar. For the same increase in pressure the bubble size did not decrease as much for the powder having an average particle size of 171 μm as it did for the 66 μm powder. Yates (1996) suggests that the reason for the decrease in bubble size with increasing pressure may be due the increase in the emulsion phase voidage or a decrease in the stability of the bubbles at higher pressure. Barreto *et al.* (1983b) also report the same effect of pressure on bubble size and add that the bubble frequency increases and the bubble velocity decreases with an increase in pressure. They also concluded that bubble hold-up decreases with an increase in pressure which is in contradiction to the conclusion of Ellenberger and Krishna (1994). This discrepancy could be due to the fact that Ellenberger and Krishna (1994) did not study the effect of pressure on bubble hold-up but they varied the gas density within a narrow range. On closer inspection of the work of Barreto *et al.* (1983b) it was found that they also observed a contradiction in their results when comparing the bubble hold-up obtained from the bed collapse test to that obtained from the visible bubble flow rate. The former showed an increase with an increase in pressure while the latter showed a decrease with an increase in pressure. Subzwari *et al.* (1978 cited by Barreto *et al.* 1983b) and Rowe and MacGillivray (1980 cited by Barreto *et al.* 1983b) found that the bubble hold-up decreases with an increase in pressure, which supports the results, based on the visible bubble flow rate of Barreto *et al.* (1983b).

Rowe and Yacono (1976) report that bubble size and shape is unaffected by particle size but bubble velocities increase by as much as 30 % with a decrease in particle size. Chan *et al.* (1987) report that the bubble frequency decreases with an increase in particle size. They also confirmed that the bubble size decreases, bubble velocity decreases and bubble frequency increases with an increase in system pressure. Finally, they report that the bubble size decreases slightly with increasing particle density at low pressures, but increases with increasing particle density at higher pressures.

2.3.5.6. Bed expansion

In the bubbling regime the bed expands as the gas velocity is increased. This expansion is related to the increase in the gas hold-up in the dense phase and bubble phase. If the dense phase voidage and bubble fraction is known then the overall bed voidage can be calculated using equation 2-57. The bed expansion can then be calculated using equation 2-99 (Yang 2003b, p. 67).

$$\frac{H_{bed}}{H_{mf}} = \frac{1-\varepsilon_{mf}}{1-\varepsilon} \tag{2-99}$$

Use of equation 2-99 requires experimental determination of H_{mf} and ε_{mf} or they could be calculated using a suitable correlation for estimation purposes.

Geldart (2004) provides a method for estimating the bed expansion of groups A and B powders. This method is based on the generalised relationship given in equation 2-100.

$$\frac{H_{bed}}{H_{mf}} = \frac{\overline{U_b}}{\overline{U_b} - Y(U - U_d)} \tag{2-100}$$

The average bubble velocity can be estimated using suitable correlations given in section 2.3.5.3. The factor Y accounts for deviations from the two-phase theory and according to Geldart (2004) it can be calculated using equation 2-101.

$$Y = 1.64Ar^{0.2635} \tag{2-101}$$

Xavier *et al.* (1978 cited by Yang 2003b, p. 67) presented a more empirical approach based on the Darton *et al.* (1977) bubble correlation. This correlation is given in equation 2-102.

$$\begin{aligned} H_{bed} = H_{mf} &+ \left(\frac{5b}{3}\right)\left[(H_{bed} + z_o)^{0.6} - z_0^{0.6}\right] \\ &- 5b^2\left[(H_{bed} + z_0)^{0.2} - z_0^{0.2}\right] \\ &+ 5b^{2.5}\left\{\tan^{-1}\left[\frac{(H_{bed} + z_0)^{0.2}}{b^{0.5}}\right] - \tan^{-1}\left[\frac{z_0^{0.2}}{b^{0.5}}\right]\right\} \end{aligned} \tag{2-102}$$

The factor b in equation 2-102 is calculated using equation 2-103 while z_0 is obtained from equation 2-91.

$$b = \frac{1.917(U - U_{mf})^{0.8}}{g^{0.4}} \tag{2-103}$$

A more practical method of calculating the fluidized bed height is based upon knowledge of the bed density. The bed density will also depend on the gas hold-up, which in turn depends on the particle properties and operating conditions. If the gas hold-up is known then according to Hilal and Gunn (2002) the bed density can be calculated from the relationship given in equation 2-104.

$$\rho_{bed} = \rho_p(1-\varepsilon) + \rho_g\varepsilon \tag{2-104}$$

In gas-solid fluidized bed systems the particle density is generally much larger than the gas density and equation 2-104 is normally approximated by equation 2-105.

$$\rho_{bed} = \rho_p(1-\varepsilon) \tag{2-105}$$

With the above approximation that the particle density is much greater than the gas density, equation 2-18 can be simplified resulting in equation 2-106.

$$\Delta P_{bed} = \frac{wg}{A} = \rho_p(1-\varepsilon)gH_{bed} \tag{2-106}$$

Combining equations 2-105 and 2-106 and solving for H_{bed}, results in equation 2-107 and 2-108.

$$H_{bed} = \frac{w}{A\rho_{bed}} \tag{2-107}$$

$$H_{bed} = \frac{\Delta P_{bed}}{\rho_{bed}g} \tag{2-108}$$

In practice, the fluidized bed height can be conveniently measured using two pressure drop measurements as illustrated in Figure 2-11.

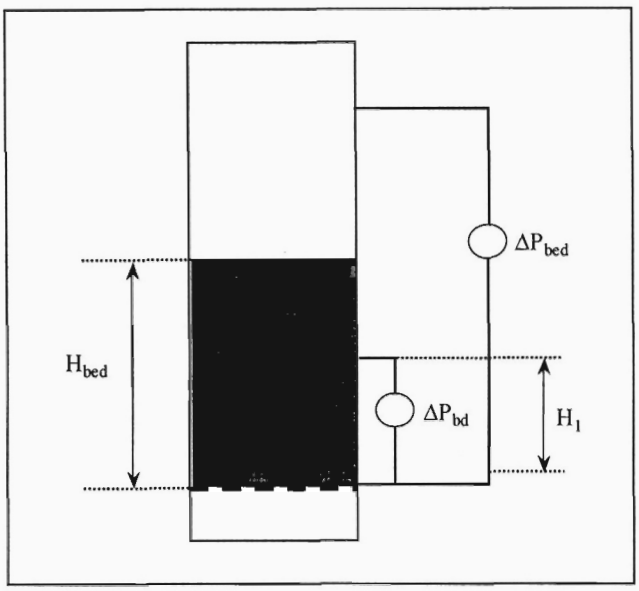

Figure 2-11: Measurement of fluidized bed height.

With reference to Figure 2-11, the bed density can be obtained using equation 2-109.

$$\rho_{bed} = \frac{\Delta P_{bd}}{gH_l} \tag{2-109}$$

Substituting equation 2-109 into equation 2-107, results in equation 2-110.

$$H_{bed} = \frac{\Delta P_{bed}}{\Delta P_{bd}} H_l \tag{2-110}$$

Hilal and Gunn (2002) have reported that the bed density is related to incipient fluidization conditions by equation 2-111, where ω is system dependant and can be calculated from equation 2-112 once k_1 has been determined experimentally.

$$\frac{\rho_{bed}}{\rho_{bed,mf}} = \exp\left[-\omega\left(\frac{U}{U_{mf}} - 1\right)\right] \tag{2-111}$$

$$\omega = k_1 U_t \left(\frac{\rho_g}{\mu g}\right)^{1/3} \tag{2-112}$$

2.3.6. Turbulent regime

The turbulent fluidization regime exists between the bubbling and fast fluidization regimes and is characterized by the disappearance of clearly defined bubbles and an increase in the entrainment rate of particles from the bed. The break down of large bubbles in this regime and the turbulent nature of the bed makes this regime desirable for commercial operations requiring high throughput and high heat and mass transfer rates and limited back-mixing. In the bubbling regime the bed consists essentially of a dense continuous phase of particles and a dispersed phase comprising gas regions (dilute phase). On the other extreme, the so-called fast fluidization (transport) regime the gas forms the continuous phases and clusters of particles form the dispersed phase. The structure of the turbulent bed therefore lies somewhere between these two extremes and is aptly defined by Bi *et al.* (2000) "as the range in which there is no clear continuous phase, but instead, either via intermittency or by interspersing voids and dense regions, a competition between dense and dilute phases in which neither gains the ascendancy".

Despite the widely used term "turbulent regime" there is considerable debate, confusion and controversy in the literature concerning the existence or non-existence of the turbulent regime. Rhodes (1996) carried out an extensive review of the literature pertaining to turbulent fluidization and found that there was a large portion of the literature, which used the term "turbulent regime" based on the gas velocity of operation without any mention of the change in the hydrodynamic structure of the bed. Controversy also surrounds the structure of the bed in the turbulent or transition regime. Rhodes and Geldart (1985, 1986 cited by Rhodes 1996) observe an increase in the entrainment rate of solids from the bed. Chehbouni *et al.* (1994) suggest that bubble break up overpowers bubble coalescence resulting in the complete disappearance of bubbles. Bi *et al.* (2000) propose that this regime is characterized by intermittent bursts of fast fluidization-like behaviour and suggest three modes of turbulent fluidization. Horio (1992 cited by Rhodes 1996) suggests that it is a transition regime in which particle clusters become fully suspended or fluidized. On the other hand, Bi *et al.* (2000) claim that the turbulent fluidization regime satisfies the three criteria proposed by Grace *et al.* (1999 cited by Bi *et al.* 2000) for any flow regime, namely, the regime must have distinctive features, it must have distinctive trends and it should be capable of being both fully developed and statistically steady. Clearly, more research is required in this fluidization regime to enable a proper and widely accepted view. Despite the lack of fundamental understanding of what goes on in the turbulent regime, it has been exploited by industry based on empirical approaches. A more fundamental understanding will clearly allow for more robust application and therefore Grace (2001) urged the fluidization community to study and provide useful models for the turbulent regime.

Based on an analysis of pressure fluctuations it has been observed, amongst others, by Chehbouni *et al.* (1994), Bai *et al.* (1996) and Yerushalmi and Cankurt (1979 cited by Bi *et al.* 2000) that a plot of the standard deviation of bed pressure fluctuations versus superficial gas velocity first increases with increasing gas velocity, then reaches a maximum and then decreases and stabilizes (in some cases) as shown in Figure 2-12. The gas velocity (U_c) at which the standard deviation of the bed pressure fluctuations reaches a maximum is conventionally taken as the transition velocity from the bubbling to the turbulent regime.

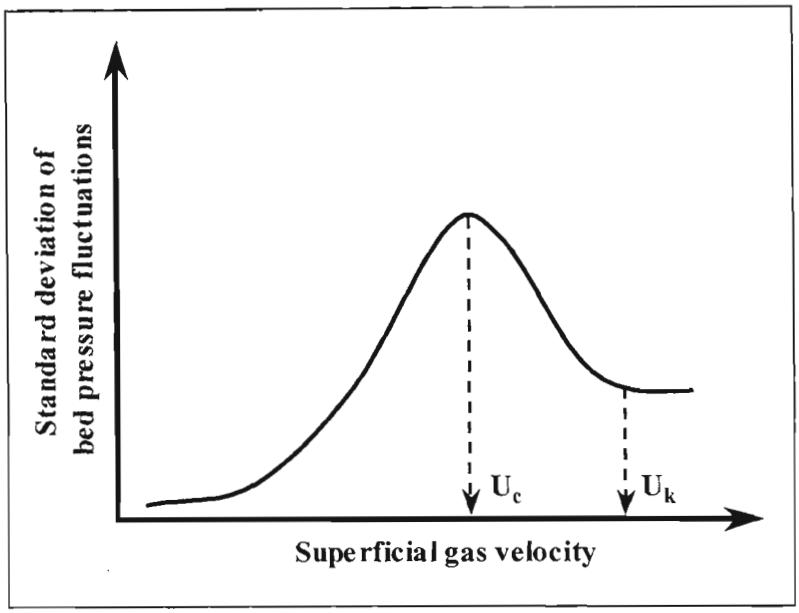

Figure 2-12: Definition of transition velocities, U_c and U_k based on standard deviation of bed pressure fluctuations.

Yerushalmi and Cankurt (1979 cited by Bi *et al.* 2000) also observed that beyond U_c, the standard deviation of differential bed pressure fluctuations seemed to stabilize and they proposed that the gas velocity at which this occurred (U_k) marked the transition to the turbulent regime. Bi *et al.* (2000) points out that this definition appears to have been the start of the confusion surrounding the existence of the turbulent regime. The confusion arose because other researchers such as Chehbouni *et al.* (1994) found that either U_k does not exist, is an artefact due to the use of differential pressure measurements, or that it actually marks the beginning of the transport regime. Bi *et al.* (2000) conclude that U_c is now widely accepted as being the superficial gas velocity at which transition from the bubbling to the turbulent regime occurs.

2.3.6.1. Transition velocity correlations

Arnaldos and Casal (1996) carried out a statistical analysis on available literature correlations for U_c and recommend that for group A powders the best correlation for predicting U_c is given by equation 2-113 (Horio 1991 cited by Bi *et al.* 2000).

$$Re_c = 0.936Ar^{0.472} \tag{2-113}$$

For group B powders, they recommend equation 2-114 (Nakajima *et al.* 1991 cited by Bi *et al.* 2000).

$$Re_c = 0.663Ar^{0.467} \tag{2-114}$$

Re_c is defined by equation 2-115.

$$Re_c = \frac{\rho_g U_c d_p}{\mu} \tag{2-115}$$

Bi *et al.* (2000) recommends the use of equations 2-116 (Bi and Grace 1995 cited by Bi *et al.* 2000) and 2-117 (Cai *et al.* 1989 cited by Bi *et al.* 2000), which are based on absolute pressure fluctuation measurements.

$$Re_c = 0.565Ar^{0.461} \tag{2-116}$$

$$\frac{U_c}{\sqrt{gd_p}} = \left(\frac{\mu_{g,20}}{\mu_g}\right)^{0.2}\left[\left(\frac{0.211}{D^{0.27}} + \frac{0.00242}{D^{1.27}}\right)^{1/0.27}\left(\frac{\rho_{g,20}}{\rho_g}\right)\left(\frac{\rho_p - \rho_g}{\rho_g}\right)\left(\frac{D}{d_p}\right)\right]^{0.27} \tag{2-117}$$

For data based on differential pressure fluctuation measurements, Bi *et al.* (2000) recommends the use of equation 2-118 (Bi and Grace 1995 cited by Bi *et al.* 2000).

$$Re_c = 1.243Ar^{0.447} \tag{2-118}$$

2.3.6.2. Factors influencing transition

The velocity at which transition from the bubbling regime to the turbulent regime occurs is dependent on the particle properties, operating conditions and column size. In general, U_c

increases with increasing particle size and density (Bi *et al.* 2000). However, Sun and Grace (1990 cited by Bi *et al.* 2000) report that U_c also depends on the particle size distribution and experimental results indicate that powders having a wide size distribution have lower values of U_c than those having a narrow particle size distribution. No report was made on the effect of particle shape on U_c.

Cai (1989 cited by Bi *et al.* 2000) found that the column diameter has an influence on U_c. It was found that U_c decreases with increasing column diameter up to about 0.2 m and remains fairly insensitive to column diameter thereafter. This effect is probably due to the effect of column diameter on bubble size, bubble hold-up and bubble rise velocity. Zhao and Yang (1991 cited by Bi *et al.* 2000) found that U_c was lower in columns having internals. This is probably due to enhanced bubble break-up, which is a feature of internals in fluidized beds.

It appears that conditions that promote smaller bubble sizes generally result in lower values for U_c. Therefore, it would be expected that U_c would decrease with an increase in pressure. Cai *et al.* (1989 cited by Bi *et al.* 2000) amongst others confirmed the effect of pressure on U_c. They found that U_c decreases with an increase in pressure. Temperature was found to have the opposite effect on U_c. Cai *et al.* (1989 cited by Bi *et al.* 2000) and Foka *et al.* (1996) found that U_c increased with an increase in temperature.

2.3.6.3. Measurement techniques

This section provides a review of some of the measurement techniques used to prove the existence of the turbulent regime and to quantify the velocity at which a regime transition occurs from the bubbling regime to the turbulent regime. For a review of measurement techniques used to study other aspects of fluidized bed behaviour the reader is referred to Werther (1999) and Horio *et al.* (2003).

Pressure fluctuations and differential pressure fluctuations have been widely used to study the fluidization behaviour of powders. It is therefore not surprising that these measurement techniques are also commonly used to measure the transition from bubbling (and slugging) to the turbulent regime. Yerushalmi and Cankurt (1979 cited by Bi *et al.* 2000) were the first to use a plot of the standard deviation of bed pressure fluctuations versus superficial gas velocity to define transition velocities as shown schematically in Figure 2-12. Although, U_c has been generally accepted as marking the transition to the turbulent regime, the existence of U_k as shown in Figure 2-12 has been questioned, since it only appears with differential pressure measurements as shown by Chehbouni *et al.* (1994). Bi and Grace (1995 cited by Bi *et al.*2000) showed that the value of U_c obtained by absolute pressure measurements is

generally higher than U_c obtained from differential pressure measurements. Chehbouni *et al.* (1994), who uses a sampling frequency of 90 Hz, also report that the U_c value obtained from differential pressure measurements increases as the distance between the measurement probes increase.

Chehbouni *et al.* (1994) indicate that in addition to the standard deviation there are many other ways to analyse the pressure fluctuation signals such as analysis of the average amplitude and the dominant frequency obtained by fast Fourier transform. Bai *et al.* (1996) used differential pressure measurements at a sampling frequency of 100 Hz to characterize fluidization regime transitions of FCC and sand.

Kehoe and Davidson (1970 cited by Bi *et al.* 2000) used visual observations to define the onset of turbulent fluidization, however, Bi *et al.* (2000) point out that this method could only be suitable for systems where there is a sharp transition such as for group A powders. For group B and D powders the transition is more gradual.

Chehbouni *et al.* (1994) used capacitance probes to measure the change in the local voidage as a function of superficial gas velocity. They took the velocity at which the voidage profile first changed to be U_c and claimed that using this technique there was no evidence of U_k. This is in contradiction to Lancia *et al.* (1988 cited by Smolders and Baeyens 2001) who also used a capacitance probe and found the existence of both U_c and U_k. Chehbouni *et al.* (1994) also found that the capacitance probe technique gave similar results for U_c when compared to values obtained using absolute differential pressure measurements. Bi *et al.* (2000) point out that it is difficult to determine a transition point based on the standard deviation of local voidage fluctuations and that alternative approaches such as the heterogeneity index as proposed by Lanneau (1960 cited by Bi *et al.* 2000) should be used. The heterogeneity index was defined as being half the average absolute deviation of the local bed density from its mean value based on capacitance signals. This value was found to increase with increasing gas velocity, reach a maximum at U_c and then decrease with a further increase in gas velocity.

Avidan and Yerushalmi (1982 cited by Bi *et al.* 2000) found that there was an abrupt change in the bed expansion when the superficial gas velocity was increased and they ascribed this change to be due to the transition from bubbling to turbulent fluidization. Others such as Lee and Kim (1990 cited by Bi *et al.* 2000) found similar results. However, Bi *et al.* (2000) warns that this method is dependent on the solids collection and return system since these abrupt changes in bed expansion tend to disappear if the entrained solids are efficiently returned to the bed.

Makkawi and Wright (2002) and Du *et al.* (2005) used electrical capacitance tomography to study the fluidization regimes in fluidized beds and found it to be a useful non-intrusive technique for characterizing fluidization regime transitions.

Foka *et al.* (1996) claim that their work demonstrated that in addition to pressure fluctuation and capacitance probe techniques, dispersion fluctuations can also be used to characterise fluidized bed hydrodynamics and the transition from bubbling to turbulent fluidization regime.

2.3.7. Entrainment

In the preceding sections it has been shown that as the superficial gas velocity is increased different regimes of fluidization are encountered. During this process bubble activity increases and the drag force on the particles increases resulting in particles being thrown out of the fluidized bed into the region above. Some of these particles immediately fall back into the bed, while others are carried out of the column with the gas. This process of particle carryover with the gas is called entrainment and is directly related to many factors such as the particle properties, the superficial gas velocity, column diameter, pressure and temperature. The entrained particles usually have to be separated from the gas stream and returned to the bed otherwise the bed inventory will decrease. In industrial processes, entrainment is often considered a nuisance since it demands the use of efficient gas-solid separation devices such as cyclones or filters to maintain the solids inventory in the reactor and prevent downstream equipment problems associated with the carryover of fine particles. Nevertheless, from a practical point of view entrainment has to be endured in exchange for a host of other benefits afforded by the use of a fluidized bed.

2.3.7.1. Particle terminal velocity

When a particle is allowed to fall freely through a fluid it will accelerate and eventually reach a maximum velocity called the terminal velocity or terminal settling velocity. During the particles movement through the fluid it experiences various forces such s its own weight, buoyancy, and drag. When these forces are in equilibrium the net force causing the acceleration of the particles is zero and the particle thereafter falls at the terminal velocity. By defining a drag coefficient (C_D) as the ratio of the drag force to the inertial forces, it can be shown (Geldart 1986b p.129; Yang 2003 p.15) that the drag force and terminal velocity of a single spherical particle can be calculated using equation 2-119 and 2-120 respectively.

$$F_d = 0.5 C_D A_p \rho_g U_r^2 \tag{2-119}$$

$$U_t = \sqrt{\frac{4 d_p (\rho_p - \rho_f) g}{3 \rho_f C_D}} \tag{2-120}$$

The particle terminal velocity is widely used in entrainment correlations and to explain the entrainment behaviour of particles. Theoretically, if the superficial gas velocity is higher than the particle terminal velocity then the particle will be entrained. The drag force depends on the projected area of the particle normal to the flow direction (A_p), which will depend on the particle shape. The drag coefficient is a function of the particle Reynolds number (Re_p) where Re_p is defined by equation 2-121.

$$Re_p = \frac{\rho_g d_p U_r}{\mu} \tag{2-121}$$

When the particle reaches the terminal velocity, $U_r = U_t$ and Re_t can be defined by equation 2-122.

$$Re_t = \frac{\rho_g d_p U_t}{\mu} \tag{2-122}$$

Clift *et al.* (1978 cited by Yang 2003a p.17) recommended preferred correlations for the drag coefficients. The correlations require Re_p and three of these are given in equations 2-123 to 2-125. For a more complete list of correlations the reader is referred to Yang (2003a p.17).

$$\text{For } Re_p < 0.01: \quad C_D = \frac{3}{16} + \frac{24}{Re_p} \tag{2-123}$$

$$\text{For } 0.01 < Re_p \le 20: \quad C_D = \frac{24}{Re_p}\left[1 + 0.1315 Re_p^{(0.82 - 0.05 \log_{10} Re_p)}\right] \tag{2-124}$$

$$\text{For } 20 < Re_p \le 260: \quad C_D = \frac{24}{Re_p}\left[1 + 0.1935 Re_p^{0.6305}\right] \tag{2-125}$$

Turton and Levenspiel (1989 cited by Yang 2003a p.16) proposed equation 2-126 for the entire range of Re_p.

$$C_D = \frac{24}{Re_p}\left[1 + 0.173 Re_p^{0.657}\right] + \frac{0.413}{1 + 16.3 Re_p^{-1.09}} \qquad (2\text{-}126)$$

For particles of arbitrary shape, there is no satisfactory method for calculating the drag coefficient (Yang 2003a p.17). For the particle terminal velocity, Clark *et al.* (1989) recommend that d_p in equation 2-120 be replace by d_v. Haider and Levenspiel (1989 cited by Yang 2003a p.17) proposed equation 2-127 for the drag coefficient calculation of non-spherical particles, which reduces to equation 2-128 for spherical particles.

$$C_D = \frac{24}{Re_p}\left\{1 + \left[8.1716\exp(-4.0655\Phi) Re_p^{0.0964 + 0.5565\Phi}\right]\right\} + \frac{73.69\exp(-5.0748\Phi) Re_p}{Re_p + 5.378\exp(6.2122\Phi)} \qquad (2\text{-}127)$$

$$C_D = \frac{24}{Re_p} + 3.3643 Re_p^{0.3471} + \frac{0.4607 Re_p}{Re_p + 2682.5} \qquad (2\text{-}128)$$

Haider and Lenvenspiel (1989 cited by Yang 2003a p.19) further recommended the use of equation 2-129 for an approximate calculation of the particle terminal velocity, where dimensionless particle size (d_p^*) and dimensionless particle velocity (U^*) are calculated using equations 2-130 and 2-131 respectively.

$$\text{For } 0.5 < \Phi < 1: \quad U_t^* = \left[\frac{18}{(d_p^*)^2} + \frac{2.335 - 1.744\Phi}{(d_p^*)^{0.5}}\right] \qquad (2\text{-}129)$$

$$d_p^* = d_p\left[\frac{\rho_g(\rho_p - \rho_g)g}{\mu^2}\right]^{1/3} = Ar^{1/3} \qquad (2\text{-}130)$$

$$U^* = U\left[\frac{\rho_g^2}{\mu(\rho_p - \rho_g)g}\right]^{1/3} = \frac{Re_p}{Ar^{1/3}} \qquad (2\text{-}131)$$

In general, the larger and denser the particles the higher will be the particle terminal velocity. Equation 2-127 predicts that the more spherical the particles the lower the drag coefficient. Therefore, based on this it appears that for equivalent particle size and density, the more spherical the particle the higher is the particle terminal velocity. For group A powders the

terminal velocity decreases with increasing temperature and pressure. For group B and D powders the terminal velocity increases with temperature and decreases with increasing pressure. Pressure has a larger influence on terminal velocity of group B and D powders than it does for group A powders.

2.3.7.2. Zones in a fluidized bed

A column containing a fluidized bed can be divided into different zones as shown in Figure 2-13. The column consists of two zones namely, the dense bed and the freeboard. The freeboard refers to that portion of the column that is between the surface of the dense bed and the gas exit point. The bottom region of the freeboard is called the splash zone and this is typically the region where particles, which are thrown out of the fluidized bed, fall back. The solid hold-up decreases rapidly from the dense bed and eventually a height is reached in the freeboard beyond which the solids hold-up remains fairly constant. The height at which this occurs is called the transport disengagement height (TDH).

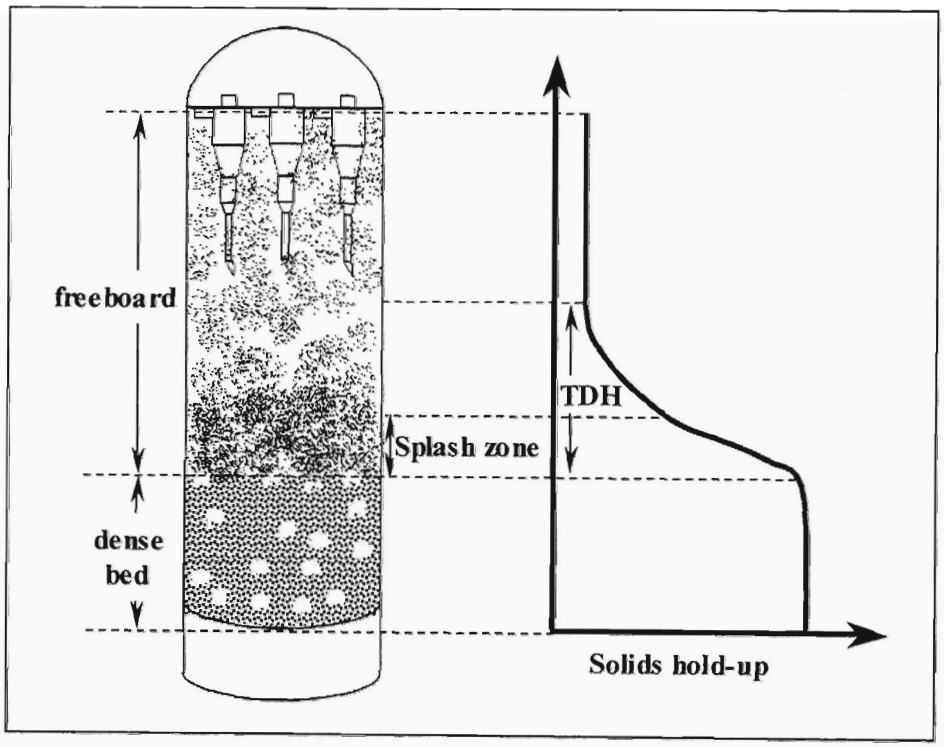

Figure 2-13: Zones in a fluidized bed.

2.3.7.3. Entrainment mechanisms

In order for particles to be entrained in the gas stream leaving the bed they have to be ejected out of the bed. Therefore, particle ejection from the bed forms the basis of all entrainment mechanisms reported in the literature. There are however, differences in opinion on the exact mechanism of particle ejection but there is general agreement that the bubbles clearly have an important role to play.

In general, according to Zenz and Weil (1958), bubbles burst at the bed surface throwing particles into the gas stream. These particles are then acted upon by inertial, gravitational and drag forces resulting in some particles being carried out with the gas stream while other particles are carried only to a certain height and then fall back to the bed.

According to Wen and Hashinger (1960), the actual local velocity in the bed is much higher than the superficial gas velocity so the bubbles carry the fines as well as the coarse particles through the fluidized bed. As the particles reach the surface of the bed a sudden eruption of gas bubbles takes place, throwing particles out of the bed. The sudden expansion of the gas reduces the gas velocity below the terminal velocity of the coarse particles resulting in the coarse particles falling back into the bed. Those particles, which have a terminal velocity lower than the gas velocity, are carried out of the column. For group A powders, it is possible to have a stable bubbling bed when all the particles have a terminal velocity lower than the superficial gas velocity. Particle collisions and the velocity profile above the bed also have an impact on particles returning to the bed.

There are two theories that have been proposed to explain particle ejection from the bed, namely the wake theory and the bubble roof theory. The wake theory assumes that particles that are carried in the wakes of bubbles are ejected out of the bed when the bubbles burst, while the roof theory claims that particles on the roof (also called bulge or dome) are ejected out of the bed. This is illustrated in Figure 2-14.

Lin *et al.* (1980) support the wake theory. They studied the entrainment of char and silica sand mixtures and found that a char layer was present at the surface of the bed. They reasoned that if the entrainment were due to particles being ejected from the roof of bubbles then it would have been much lower than what they measured. Therefore, they concluded that the entrainment mechanism in this case was due to particle ejection from the wakes of rising bubbles and this was consistent with the results of George and Grace (1976 cited by Lin *et al.* 1980). Leva and Wen (1971 cited by Wen and Chen 1982) and Yates and Rowe (1977 cited by Wen and Chen 1982) also support this. They believe that some of the solids,

which are lifted by the bubble wakes, are thrown upwards following the bursting of bubbles at the bed surface.

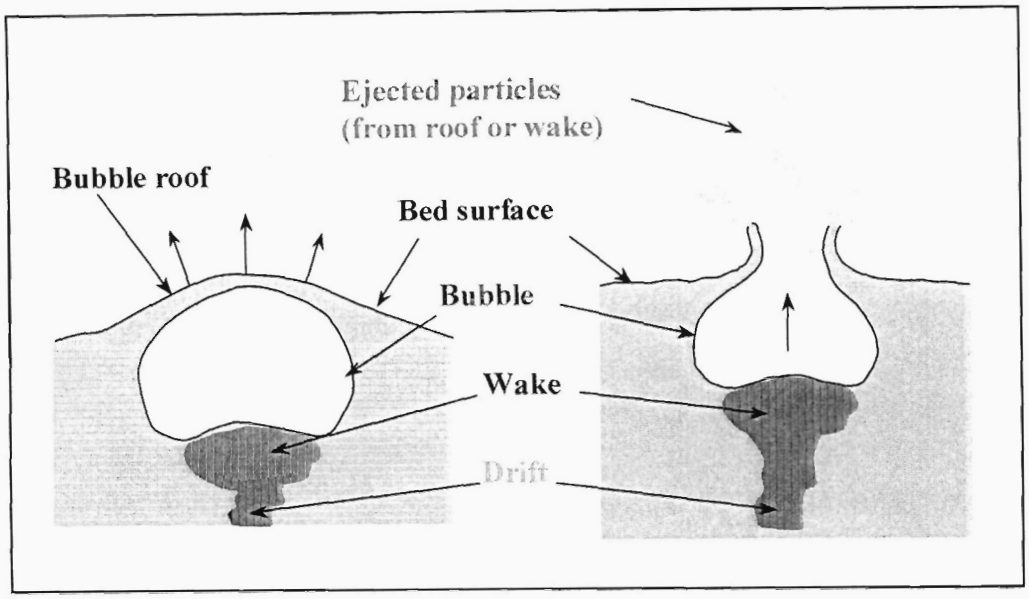

Figure 2-14: Mechanisms for particle ejection from the bed.

George and Grace (1978 cited by Wen and Chen 1982) provided further support for the bubble wake theory. They carried out experiments in which thin layers of coke particles were put on top of a bed of silica sand and ejected particles were caught 0.03 m above the bed surface. They observed that the fraction of coke particles in the entrained sample was always less than 3% by weight from which they concluded that the majority of ejected particles arose from the bubble wakes and not the roof.

Support for the bubble roof theory is also overwhelming. Rowe and Partridge (1962 cited by Wen and Chen 1982) injected a bubble into a two dimensional bed which had a layer of dyed solids above the gas distributor. The results indicated that the coloured solids in the wake of the bed were retained in the bed when the bubble burst at the bed surface. Do *et al.* (1972 cited by Wen and Chen 1982) filmed the motion of bubbles in a two-dimensional bed and found that particles ejected from the bed originated from the nose of the bursting bubbles and not their wakes. Peters *et al.* (1983) used an image carrying fibre optic probe to record the bubble eruption process of a single bubble in a bed of spherical glass particles and observed that the ejected particles primarily arose form the dome of a bursting bubble. However, the particles that made up the dome of the bubble were not necessarily from the original surface of the bed. The original particles on the surface of the bed were observed to drain laterally away from the bubble as the dome rose and particles that were ejected came from below the

original surface and were ejected radially in all directions. The particle ejection velocities were approximately equal to the bubble rise velocity at the surface.

Pemberton and Davidson (1986) reported that the particle ejection mechanism depends on U/U_{mf}. For group B powders with $U/U_{mf} < 10 - 15$, bubbles erupt one by one and particle ejection from the bed occurs primarily from the roof of each bursting bubble. For group A and B particles having $U/U^{mf} > 10 - 15$, bubble coalescence at the bed surface results in particles being ejected from the wakes of coalescing bubbles. The elutriation rate based on the theory of particle ejection from the wakes is much higher than that based on the theory that the particles are ejected from the bubble roof. George and Grace (1981) noted that only about 0.1 to 5 % of the entrainable particles ejected into the freeboard were carried over, with the proportion entrained increasing with increasing gas velocity. Pemberton and Davidson (1986) concluded that data from two-dimensional beds favour the bubble roof ejection mechanism, whereas, data from three-dimensional beds favour the wake ejection mechanism. Levy *et al.* (1983 cited by Pemberton and Davidson 1986) suggested that bubble coalescence near the bed surface favours wake ejection while bubbles bursting on their own, project particles from its roof.

Baron *et al.* (1990) reported that tracer measurements confirm that jets of particles are ejected from the bed only when two or more bubbles coalesce near the bed surface.

2.3.7.4. Flow structure in the freeboard

Zenz and Weil (1958) proposed that gas bubbles bursting at the surface are like intermittent jets imposing a highly irregular velocity profile across the vessel. The jet velocity eventually reduces to the superficial gas velocity at some equilibrium height called the TDH. The entrainment rate above this height is constant and equal to the maximum particle-carrying capacity of the gas stream at its superficial velocity. TDH is the design optimum for the location of cyclones and is a function of bed diameter and gas velocity. An increase in gas velocity increases the rate of rise and frequency of bubble eruptions at the bed surface, which would in turn require a greater distance for dissipation of the fluctuating velocity profiles. The effect of diameter may be a result of wall effects for small diameter columns and poor gas distribution in the case of large diameter columns. Based on laboratory entrainment experiments carried out at M W Kellogg it was found that the TDH is not related to the size of bubbles bursting at the bed surface.

Horio *et al.* (1980 cited by George and Grace 1981) showed that particle transport through the freeboard is controlled primarily by turbulence considerations. They observed that the

turbulence frequency in the freeboard was similar to the bubble bursting frequency, from which it was deduced that the turbulence in the freeboard was initiated by the erupting bubbles at the bed surface. They also postulated that the decay of the turbulence with height in the freeboard was similar to that of a pulsed jet.

Pemberton and Davidson (1984) used the theory of ghost bubbles to explain the turbulent flow structure in the freeboard. They assumed that the gas from an erupting bubble retains its identity when rising through similar gas in the freeboard. Measurement of the turbulent gas motion above a continuously bubbling fluidized bed showed a fluctuating gas velocity, which was closely related to the frequency and size of bursting bubbles. The decay of freeboard turbulence was predicted by assuming dissipation of ghost bubbles through viscous processes. However, Duursma *et al.* (2001) used particle image velocimetry to produce vector maps of the gas flow in the freeboard region and found no evidence to support the ghost bubble hypothesis. Yorquez-Ramirez and Duursma (2001) also used particle image velocimetry to study the flow structure in the freeboard and showed that the gas flow in this region was characterized by the presence of eddies and vortices, which were generated by bubble eruption at the bed surface and as a result the gas residence time in the freeboard was not uniform. Vortex rings originating from ghost bubbles were not found.

Grace and Tuot (1979 cited by Subbarao 1986) report that a uniform dispersion of particles in a gas is unstable and can lead to the formation of particle clusters in a continuum of gas. This view is supported by Kunii and Levenspiel (1991, p.184) who proposed that there are three distinct phases present in the freeboard: (1) gas stream with completely dispersed solids transported upward pneumatically, (2) upward-moving agglomerates or particle clusters projected by bubbles and (3) descending agglomerates returning to the bed. Geldart (1986c p.137) also included the emulsion phase moving downward at the wall as a fourth phase. These four phases are illustrated in Figure 2-15. Baron *et al.* (1988) developed a model to account for the particle clusters on entrainment rate and suggest that the TDH represents the height at which the cluster flux becomes negligible.

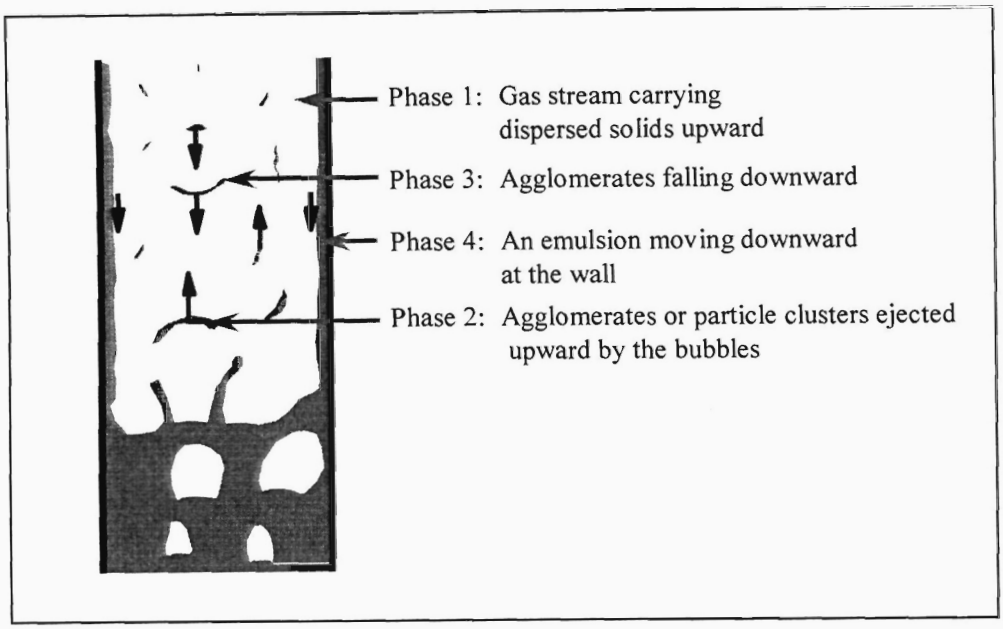

Figure 2-15: Phases present in the freeboard – adapted from Geldart (1986c, p. 137).

2.3.7.5. Effect of particle properties

Wen and Hashinger (1960) reported that elutriation rates were observed to decrease markedly with increasing particle size and this was attributed to a reduction in the entrainment driving force caused by an increase in the particle terminal velocity. Merrick and Highley (1974) found that the entrainment rate in a fluidized bed combustor was a strong function of the particle size: doubling the particle size decreased the entrainment rate by up to two orders of magnitude. Particles having a terminal velocity larger than the superficial gas velocity were entrained even with a freeboard height of between 2.7 and 3.4 m. George and Grace (1981) found a similar effect of particle size on entrainment when they compared their data for 102 μm silica sand with that of Large *et al.* (1976 cited by George and Grace 1981) who also used silica sand having average sizes of 134 and 125 μm. They observed that a relatively small variation in particle size distribution resulted in two orders of magnitude variation in the entrainment rate.

Geldart *et al.* (1979) used mixtures of coarse sand and fine alumina containing from 5 % to 75 % alumina and indicated that the entrainment of fines was not influenced by the coarse particles. The entrainment rate of the coarse particles however, increased significantly by the presence of fines. They proposed that this phenomenon could be explained in terms of momentum-interchange transfer between the fine and coarse particles but found it too

complex to model and chose rather to use an effective gas density to account for the interaction between the fine and coarse particles. Geldart and Pope (1983) reported a similar interaction between the fines and coarse particles. Based on tests carried out with three types of sand having average sizes of 200, 1000 and 2500 μm in a 0.29 m column they made the following observations: the amount of coarse particles at a given height in the freeboard increases with an increase in gas velocity irrespective of the absence or presence of fine particles; the hold-up of coarse particles increases dramatically when fine particles are present and the larger the coarse particles the smaller was the effect of the fines even at high gas velocity. This interaction between the fine and coarse particles in the freeboard was described qualitatively as being due to momentum interchange by collisions between the fast moving fine particles and the slower moving coarse particles. Choi *et al.* (2001) used a 0.1 m diameter column, 1.97 m tall with sand as bed material and found that the elutriation rate of the coarse particles increased with an increase of fine material in the bed. This effect decreased as the gas velocity increased.

Wen and Chen (1982) observed that the elutriation rate constant decreases with increasing particle size and the higher the particle density the smaller the elutriation rate constant. Pemberton and Davidson (1986) claimed that particle size, shape and density affect the bubble wake fraction and hence the quantity of particles ejected from the wakes, when this entrainment mechanism predominates. Rowe and Partridge (1965 cited by Pemberton and Davidson 1986) used X-ray photographs to show that the wake fraction increased as the particle size decreased and that for similar size particles, the wake fraction was larger for spherical particles (eg. FCC) compared to angular particles (eg. sand).

Baeyens *et al.* (1992) studied the entrainment behaviour of group A powders in the presence of superfine material (mean diameter 10 – 14 μm). It was found that the elutriation rate constant increased with decreasing particle size until a critical particle size was observed below which the elutriation rate constant either levelled off or decreased with a decrease in particle size. This observation was attributed to inter-particle forces. Smolders and Baeyens (1997) found that at low air velocities the entrainment rate decreased with decreasing particle size indicating the role of inter-particle adhesion forces. At higher air velocities it was found that the elutriation rate increased with an increase in gas velocity even for the fine particles and this was attributed to shear forces dominating over the adhesion effect. Ma and Kato (1998) reported that the elutriation rate constant of group C powders decreased with decreasing particle size indicating that inter-particle forces were playing a role in the entrainment mechanism of these powders. Shin *et al.* (2007) observed a similar effect when studying the entrainment behaviour of carbon black powder (a group C powder).

From the above it is quite clear that, in general, decreasing the particle size generally causes an increase in the entrainment rate up to a critical particle size below which the entrainment rate either levels off or decreases due to inter-particle forces. The presence of fines has also been shown to influence the entrainment of coarse particles. However, the literature reviewed did not contain any systematic studies illustrating the effect of particle shape on the entrainment rate. This is therefore seen as an area where more research is required as it could provide further insight into the entrainment behaviour of fluidized powders.

2.3.7.6. Effect of gas velocity

Leva (1951 cited by Wen and Hashinger 1960) considered the superficial gas velocity as the driving force for entrainment while Osberg and Charlesworth (1951, cited by Wen and Hashinger 1960) considered the driving force for entrainment to be the difference between the superficial gas velocity and the particle terminal velocity ($U - U_t$). In either case an increase in the superficial gas velocity will result in an increase in the entrainment rate. Lin *et al.* (1980) studied the entrainment behaviour of char and silica sand mixtures and found that the elutriation rate constant increased with an increase in superficial gas velocity. George and Grace (1981) and Choi *et al.* (1989) reported a similar effect of gas velocity on the entrainment rate.

2.3.7.7. Effect of bed hydrodynamics

According to Wen and Chen (1982) the bed hydrodynamics, which are characterized by variables such as minimum fluidization velocity, bubble size and velocity, bed internals etc. does not have any effect on the elutriation rate above the transport disengagement height. However, the entrainment rate below the transport disengagement height would be affected by bed hydrodynamics. The results of Tweddle *et al.* (1970) and Choi *et al.* (1989) would appear to support this as they found that the bed height had a negligible effect on the entrainment rate.

On the other hand, Baron *et al.* (1990) studied the effect of bed height on entrainment in a 0.61 m diameter column with silica sand having a Sauter mean diameter of 65 μm. It was found that both the flux of particles ejected from the bed surface and that entrained above TDH increased with an increase in bed height. They were able to model this by including the effects of gulf streaming which they explained as follows: bubbles rise through the bed through preferential tracks which become fewer as the bed height is increased and the bubbles become larger and less numerous. Due to fewer bubble tracks the local

concentration of bubbles increases and hence the probability of bubble coalescence and particle ejection from the bed increases.

2.3.7.8. Effect of column geometry

Wen and Hashinger (1960) believe that column diameter will only have a small effect on entrainment rate, when the diameter of the column is large enough, so that channelling and slugging can be eliminated. The results of Lewis *et al.* (1962 cited by Wen and Chen 1982) would appear to agree with this. They found that there was a sharp rise in entrainment rate for small diameter columns ranging from 0.009 to 0.02 m in diameter and the entrainment rate was independent of column diameter for columns greater than about 0.08 to 0.1 m in diameter. Tasirin and Geldart (1998) also found that the entrainment flux in the 0.076 m column was higher than that in the 0.152 m column and explained this difference in terms of the gas velocity profile being different in the two columns. Colakyan and Levenspiel (1984) used three columns to the test the entrainment of polyethylene, silica and zirconia. The smallest column was 0.1 m in diameter. The middle-sized column was a 0.3 m square column and the largest column was a 0.92 m square column. All the columns had a freeboard height of 7.5 m. The elutriation rate constant was found to be statistically insignificant to column diameter.

On the other hand, Wen and Chen (1982) based on their observation that the descending particles appear to fall down predominantly along the wall, expect that the elutriation rate would increase with increasing column size. This is related to a decrease in the surface-area-to-volume ratio with an increase in column diameter. Data from large-scale fluidized beds indicate that under similar operating conditions, the elutriation rate constant from the large-scale bed tends to be much higher than that from the small-scale beds (Merrick and Highley 1974; Fournol *et al.* 1973, Nazemi *et al.* 1974, Large *et al.* 1976, Colakyan *et al.* 1979 cited by Wen and Chen 1982).

Shin *et al.* (2007) reports that the entrainment of carbon black powder (a group C powder) was 5 to 12 times higher in a cylindrical column compared to a conical column.

2.3.7.9. Effect of column internals

There are differences in opinion on the effect of column internals on the entrainment rate and it appears that the hydrodynamics of the bed and the design of the internals also determine whether the column internals have an effect on the entrainment rate or not. Wen and Hashinger (1960) found that the entrainment rate increased when baffles were used with a

slugging fluidized bed. The baffles had no effect on the entrainment rate when the bed was freely bubbling. Lewis *et al.* (1962 cited by Tweddle *et al.* 1970) and Overcashier *et al.* (1959 cited by Tweddle *et al.* 1970) reported that the effect of column internals on entrainment rate was inconclusive since the use of baffles may increase, decrease or have no effect on the entrainment rate. George and Grace (1981) showed that the presence of a tube bundle in the splash zone of the freeboard did not affect the entrainment rate of 102 μm silica sand. Colakyan *et al.* (1979 cited by Wen and Chen 1982) measured the elutriation of sand particles in a 0.9 m square column by putting immersed tubes in different positions and reported that the presence or the position of the immersed tubes did not influence the elutriation rates.

Tweddle *et al.* (1970) claims that screen packing in the dense bed reduces the rate at which particles are projected from the bed surface but the rate of particle disengagement from the gas is reduced in the disengagement space above the bed. To minimize particle carryover in screen-packed beds the packing needs to terminate at the bed surface and not extend into the freeboard. Williams (1971 cited by Harrison *et al.* 1974) studied the use of horizontal tube arrays in the freeboard and found that a suitable tube array can reduce the entrainment by about 20 to 30% from that observed without the tube array. Harrison *et al.* (1974) claim that a plane baffle array in the freeboard above a gas fluidized bed reduces the rate of particle entrainment by up to 80% of that found without the baffle array. Duursma *et al.* (2001) also showed that internals could reduce the entrainment rate.

It therefore appears that the use of internals above the dense bed can reduce the entrainment rate both below and above TDH because of the additional particle disengagement facilitated by direct impingement on the obstructions presented by the internals and the particle flux drops below the saturation carrying capacity of the gas. George and Grace (1980 cited by Wen and Chen 1982) warn however, that the elutriation rate will not be affected if the internals in the lower part of the freeboard cannot reduce the flux down below the saturation carrying capacity of the gas.

2.3.7.10. Effect of freeboard geometry

Most researches have focused on the effect of freeboard height on the entrainment rate although Smolders and Baeyens (1997) also tested the effect of freeboard diameter on the entrainment rate. They found that an increase in the diameter of the freeboard results in a decrease in the entrainment of solids from the system. Wen and Hashinger (1960) used three different freeboard heights (0.30, 0.59 and 0.91 m). The entrainment rate was found to be higher when the freeboard height was 0.30 m but did not change for the other two heights,

therefore, indicating the existence of a critical height above which the entrainment does not change. The authors claim that this critical height is required to fully develop the gas flow profile in the freeboard. Lin *et al.* (1980) studied the entrainment behaviour of char and silica sand mixtures at gas velocities ranging between 0.1 and 0.3 m/s in a 0.61 m square column. The freeboard height was varied between 0.63 and 0.327 m and the results appeared to indicate an increasing TDH with decreasing gas velocity. In particular particles that were larger than 74 μm seemed to have a larger TDH.

On the other hand, Geldart and Pope (1983) reported that they found no evidence to support the idea of a TDH except when the gas velocity was below the terminal velocities of all the particles in the bed.

2.3.7.11. Effect of pressure and temperature

A review on the effect of pressure and temperature on the entrainment rate can be found in Yates (1996). In general, the pressure has a significant effect on the entrainment rate. The entrainment rate has been found to increase with increasing pressure. This is due to the fact that an increase in pressure causes an increase in the gas density. This increase in the gas density results in an increase in the drag force on the particles and an increase in the saturation carrying capacity of the gas. Chan and Knowlton (1984) showed that the TDH increases with an increase in system pressure.

The effect of temperature is not as clear-cut since an increase in temperature affects both the gas density and viscosity. George and Grace (1981) found that the bed temperature in the range 27 to 162 °C did not influence the entrainment rate of 102 μm silica sand. Choi *et al.* (1989) report that the effect of gas velocity on the entrainment rate decreases with an increase in temperature and that the total entrainment rate decreases with an increase in temperature due to a decrease in the gas density. Choi *et al.* (1997) increased the temperature in the range 20 – 600°C and found that the entrainment rate decreased initially and above a certain temperature the entrainment rate increased for gas velocities between 0.8 and 1.4 m/s. Findlay and Knowlton (1985 cited by Yates 1996), who increased temperature while maintaining system pressure constant, found that the entrainment rate increased with an increase in the gas viscosity. This was expected since the terminal velocity of the particles is expected to decrease with an increase in gas viscosity.

2.3.7.12. Correlations and models

There have been various attempts made to correlate the TDH with system properties. The simplest is that of Zenz and Othmer (1960 cited by Werther and Hartge 2003 p.125) shown in Figure 2-16. This graphical correlation was developed for FCC type particles.

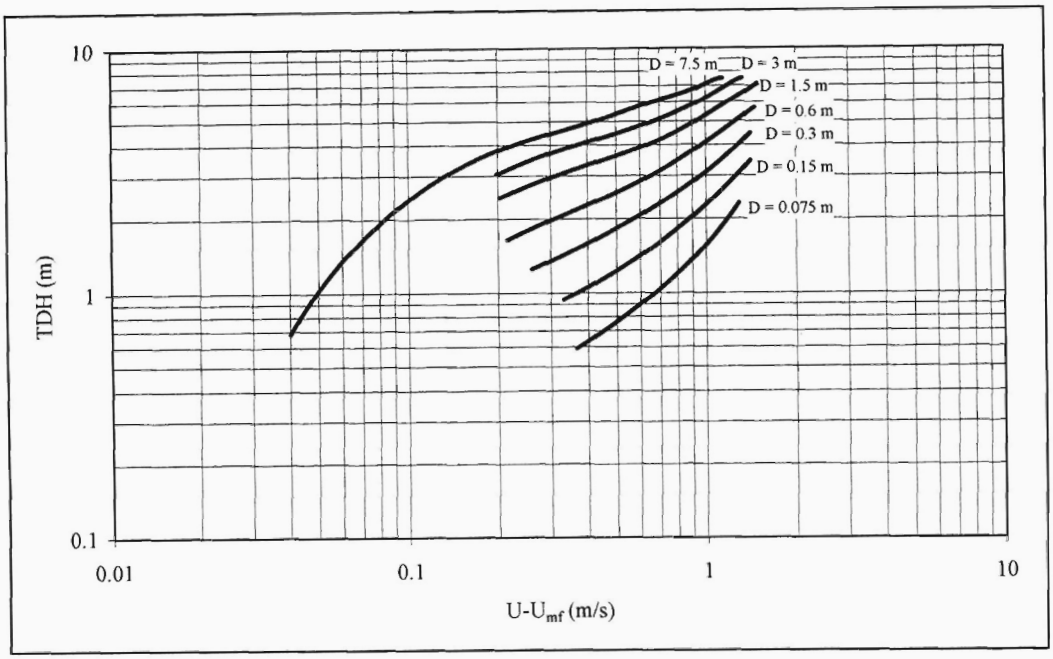

Figure 2-16: Transport disengagement height versus excess gas velocity (Zenz and Othmer 1960 cited by Werther and Hartge 2003).

Amitin (1968 cited by Geldart 1986c p.128) proposed equation 2-132 for the calculation of the TDH.

$$TDH = 0.58U^{1.2}(7.33 - 1.2\log_{10} U) \qquad (2\text{-}132)$$

Other correlations for TDH can be found in Werther and Hartge (2003 p.124).

There are various models and empirical correlations available in the literature for predicting the entrainment rate of powders at the bed surface (E_0) and above TDH (E_∞). The reader is referred to Werther and Hartger (2003) and Choi *et al.* (1989) for correlations that can be used to predict the entrainment rate at the bed surface. The reader is also referred to Milioli and Foster (1995a, b) who provide an excellent review of entrainment research and they

proposed a phenomenological model for predicting the entrainment rate and the particle size distribution of the bed and entrained material. In general, models that have been developed for predicting entrainment rates are usually based on either the bubble wake theory or the bubble roof theory to account for the ejection of particles from the bed to the freeboard (Pemberton and Davidson 1986, Smolders and Baeyens 1997).

Briens *et al.* (1988) combined the approach of particle ejection from bubble wakes with the probability of bubble coalescence and developed two physical models: one to predict the flux of particles ejected from the bed surface and the other to predict the flux of entrained particles above the TDH. The first model is based on the assumption that particles are ejected from the bed through the wakes of bubbles that coalesce near the bed surface and this bubble coalescence is predicted by a probability model. The second model is based on the assumptions that the flux of each particle size is limited by both the choking load and the flux ejected at the bed surface and that the gas preferentially entrains the smallest particles. A combination of these two models is used to predict the elutriation flux above the TDH. A disadvantage of this model is that it requires knowledge of the bubble diameter and velocity near the bed surface which is difficult to obtain and hence forces the use of empirical correlations which are system dependent. Baron *et al.* (1990) also showed that the second part of this model predicted wrong trends for the effect of bed height on entrainment rate and it could be improved through incorporation of gulf streaming effects.

According to Tasirin and Geldart (1998), it is generally accepted that the entrainment rate of size fraction d_{pi} from a fluidized bed of solids is proportional to its concentration in the bed and the bed cross-sectional area and is given by equation 2-133.

$$F_i = \frac{d(X_{bi} w)}{dt} = K^*_{i\infty} A X_{bi} \qquad (2\text{-}133)$$

$K^*_{i\infty}$ is termed the elutriation rate constant and is a function of the gas velocity, particle properties and gas properties. The total entrainment rate is obtained by summing the entrainment rate of each size fraction as shown in equation 2-134.

$$F_T = \sum F_i = A \sum K^*_{i\infty} X_{bi} \qquad (2\text{-}134)$$

The total entrainment flux above TDH can then be expressed by equation 2-135.

$$E_\infty = \sum K^*_{i\infty} X_{bi} \qquad (2\text{-}135)$$

According to Wen and Chen (1982) the entrainment flux at any height in the freeboard can be expressed by equation 2-136.

$$E_h = E_\infty + (E_0 - E_\infty)\exp(-\eta h) \tag{2-136}$$

The factor η has been found to vary between 3.5 and 6.4 m^{-1} and since the estimation of the entrainment rate is not so sensitive to this value, it is recommended that a value of η = 4 m^{-1} be used for a system in which no information on entrainment rate is available (Wen and Chen 1982).

The entrainment correlations given in the literature are expressed in terms of the elutriation rate constant $K_{i\infty}^*$. Equations 2-137 to 2-151 provides some of the entrainment correlations that have been developed based on data from various systems.

- **Yagi and Aochi (1955 cited by Werther and Hartge 2003, p. 122):**

$$\frac{K_{i\infty}^* g d_{pi}^2}{\mu (U - U_{ti})^2} = 0.0015 Re_t^{0.6} + 0.01 Re_t^{1.2} \tag{2-137}$$

- **Zenz and Weil (1958 cited by Tasirin and Geldart 1998):**

$$K_{i\infty}^* = \begin{cases} 1.26\times10^7 (\rho_g U)\left(\dfrac{U^2}{g d_{pi}\rho_p^2}\right)^{1.88} & \text{when} \quad \dfrac{U^2}{g d_{pi}\rho_p^2} < 3\times10^{-4} \\ 4.31\times10^4 (\rho_g U)\left(\dfrac{U^2}{g d_{pi}\rho_p^2}\right)^{1.18} & \text{when} \quad \dfrac{U^2}{g d_{pi}\rho_p^2} > 3\times10^{-4} \end{cases} \tag{2-138}$$

- **Wen and Hashinger (1960):**

$$K_{i\infty}^* = 1.52\times10^{-5}\rho_g (U - U_{ti})\left[\frac{(U - U_{ti})^2}{g d_{pi}}\right]^{0.5} Re_t^{0.725}\left(\frac{\rho_p - \rho_g}{\rho_g}\right)^{1.15} \tag{2-139}$$

- **Tanaka *et al.* (1972):**

$$K_{ic}^{*} = 4.6\times10^{-2}\rho_g\left(U-U_{ti}\right)\left[\frac{\left(U-U_{ti}\right)^2}{gd_{pi}}\right]^{0.5} Re_t^{0.3}\left(\frac{\rho_p-\rho_g}{\rho_g}\right)^{0.15} \qquad (2\text{-}140)$$

- **Merrick and Highley (1974):**

$$K_{ic}^{*} = \rho_g U\left\{B+130\exp\left[-10.4\left(\frac{U_t}{U}\right)^{0.5}\left(\frac{U_{mf}}{U-U_{mf}}\right)^{0.25}\right]\right\} \qquad (2\text{-}141)$$

where $B = 10^{-3}$ to 10^{-4}

- **Geldart *et al.* (1979):**

$$K_{ic}^{*} = 23.7\rho_e U\exp\left(\frac{-5.4U_{ti}}{U}\right) \qquad (2\text{-}142)$$

$$\rho_e = \rho_g + \sum\rho_i \qquad (2\text{-}142a)$$

- **Lin *et al.* (1980):**

$$K_{ic}^{*} = 9.43\times10^{-4}\rho_g U\left(\frac{U^2}{gd_{pi}}\right)^{1.65} \qquad (2\text{-}143)$$

- **Wen and Chen (1982):**

$$K_{ic}^{*} = \rho_p\left(1-\varepsilon_i\right)\left(U-U_{ti}\right) \qquad (2\text{-}144)$$

$$\varepsilon_i = \left[1+\frac{\lambda\left(U-U_{ti}\right)^2}{2gD}\right]^{-1/4.7} \qquad (2\text{-}144a)$$

when $\frac{\rho_g (U - U_{ti}) d_{pi}}{\mu} \leq \frac{2.38}{D}$

$$\frac{\lambda \rho_p}{d_{pi}^2}\left(\frac{\mu}{\rho_g}\right)^{2.5} = 5.17 D^2 \left[\frac{\rho_g (U - U_{ti}) d_{pi}}{\mu}\right]^{-1.5}$$

when $\frac{\rho_g (U - U_{ti}) d_{pi}}{\mu} \geq \frac{2.38}{D}$

$$\frac{\lambda \rho_p}{d_{pi}^2}\left(\frac{\mu}{\rho_g}\right)^{2.5} = 12.3 D \left[\frac{\rho_g (U - U_{ti}) d_{pi}}{\mu}\right]^{-2.5} \qquad (2\text{-}144b)$$

- **Colakyan and Levenspiel (1984):**

$$K_{i\infty}^{*} = 0.011 \rho_p \left(1 - \frac{U_{ti}}{U}\right)^2 \qquad (2\text{-}145)$$

- **Kato *et al.* (1985, cited by Tasirin and Geldart 1998):**

$$K_{i\infty}^{*} = 2.8 \times 10^{-2} (D_h)^{-0.65} \left(\frac{U - U_{ti}}{U_{ti}}\right)^{1.6} \left(\frac{\rho_p - \rho_g}{\rho_g}\right)^{0.54 U_h^{2.1}} \qquad (2\text{-}146)$$

note D_h =D for a bed without internals

- **Sciazko *et al.* (1991):**

$$K_{i\infty}^{*} = 1.6 (\rho_g U)\left(\frac{U}{U_{ti}}\right)\left(1 - \frac{U_{ti}}{U}\right) \qquad (2\text{-}147)$$

- **Baeyens *et al.* (1992):**

$$K_{i\infty}^{*} = 5.4 \times 10^{-5} (\rho_p)\left(\frac{U}{0.2}\right)^{3.4}\left(1 - \frac{U_{ti}}{U}\right)^2 \quad \text{for } d_{pi} \leq \frac{10325}{\rho_p^{0.725}} \qquad (2\text{-}148)$$

- **Nakagawa *et al.* (1994):**

$$K_{i\infty}^{*} = 0.35(\rho_p U)(1-\varepsilon)_H$$

with:

$$(1-\varepsilon)_H = 7.41\times10^{-3} R^{1.87} A^{0.55} H_{fbd}^{-0.64} \qquad (2\text{-}149)$$

and:

$$R = \sum_{i=1}^{n} X_{bi}\left(\frac{U-U_{ti}}{U_{ti}}\right) \text{ for } U_{ti} < U$$

- **Tasirin and Geldart (1998):**

$$K_{i\infty}^{*} = \begin{cases} 23.7(\rho_g)(U)^{2.5}\exp\left(\dfrac{-5.4U_{ti}}{U}\right) \text{for Re} < 3000 \\ 14.5(\rho_g)(U)^{2.5}\exp\left(\dfrac{-5.4U_{ti}}{U}\right) \text{for Re} > 3000 \end{cases} \qquad (2\text{-}150)$$

$$Re = \frac{\rho_g U D}{\mu}$$

- **Choi *et al.* (1999):**

$$K_{i\infty}^{*} = \left(\frac{\mu}{d_{pi}}\right)(Ar)^{0.5}\exp\left(6.92 - 2.11F_g^{0.303} - \frac{13.1}{F_{da}^{0.902}}\right)$$

$$F_g = g d_{pi}(\rho_p - \rho_g) \text{ gravity force per projection area} \qquad (2\text{-}151)$$

$$F_{da} = \frac{C_D \rho_g U^2}{2} \text{ drag force per projection area}$$

The reason for the numerous entrainment correlations is no doubt due to the lack of a fundamental and mechanistic understanding of the entrainment process (Peters *et al.* 1983). The correlations are therefore highly system dependent and the errors between experimental and predicted entrainment rates are unlikely to be better than ± 100 % (Geldart 1986c). For example, Geldart *et al.* (1979) using sand, alumina, and metal shot found that the Merrick and Highley correlation over-predicted $K_{i\infty}^{*}$ by a factor of 10 to 100, while the Zenz and Weil correlation showed a much stronger dependence on particle density than found experimentally. George and Grace (1981) reported that the correlations of Merrick and

Highley (1974) and Colakyan *et al.* (1979 cited by George and Grace 1981) consistently over estimated their experimental results while the correlations of Geldart *et al.* 1979, Wen and Hashinger (1960) and Tanaka *et al.* (1972) underestimated the data especially at high gas velocity. The Zenz and Weil correlation was found to provide the best fit to their experimental data.

Wen and Chen (1982) add that of the large number of entrainment rate correlations available in the literature, many are unreliable or unsatisfactory for predicting entrainment rates for design and freeboard modelling purposes. The lack of good correlations stems mainly from the difficulty in obtaining accurate entrainment rate data. Data obtained using similar equipment and experimental conditions could differ considerably. Many of the experiments are obtained using relatively small diameter columns while the effect of column diameter and column internals could be considerable and has not been clearly established. Bulau and Hallstrom (1998) noted that experimental and calculated entrainment rates differ widely especially for small particle sizes.

Another reason for the large errors that result when correlations are used to predict the entrainment rate for systems other than for which they were developed stems from the lack of a systematic study on the effect of particle shape on the entrainment process. The effect of particle shape is currently being accounted for in the entrainment correlations through the calculation of the single particle terminal velocity, which are based on equations developed for spherical particles only. Corrections for the drag coefficient of non-spherical particles have been suggested as was presented in section 2.3.7.1, but these are often based on sphericity, which has been shown in section 2.1.3 not to be a universally accepted particle shape descriptor. It is envisaged that the current study will shed some light on the effect of particle shape on the entrainment behaviour of powders.

3. POWDER PROPERTIES

3.1. Physical Properties

In order to study the effect of particle properties on the fluidized bed hydrodynamics and entrainment rate, powders having a wide variety of particle shapes, particle size distribution and particle densities were used for the tests.

The particle size, density and shape descriptors of the powders used for the fluidization tests are summarised in Table 3-1 (refer to Appendix A for more detail on the particle size distribution of the powders used). Images of the particles where obtained using a Scanning Electron microscope (SEM), which was manufactured by LEO, model number 1430.

Table 3-1: Summary of powder properties.

Powder	d_{sv} (μm)	d_m (μm)	ρ_p (kg/m^3)	F_{22} (%)	Particle shape description
P1	56	61	2300	1	Spherical
P2	48	54	1900	3.1	Spherical
P3	28	42	4600	26.3	Spherical + Rounded
P4	60	91	4600	5.9	Spherical + Rounded
P5	28	49	3200	24.4	Rounded
P6	23	40	4600	28.7	Angular/Irregular
P7	42	66	1300	9.6	Spherical
P8	16	37	4600	29.5	Angular/irregular
P9	49	80	4600	9	Spherical + Rounded
P10	16	21	4600	55.1	Spherical + Rounded

The SEM images of the particles were used to visually characterise the particle shapes and the particles were described as being spherical, rounded or angular/irregular. In some cases a single descriptor for particle shape could not be used and in this case multiple descriptors are used to describe the particle shape (eg. P3, P4, P9, P10). The SEM images of some of the powders are shown in Figure 4-1 to illustrate the differences between spherical, rounded and angular.

An attempt was made to quantify the particle shapes using image analysis provided by the Malvern ParticleScan software. This software was developed by Integrated X-ray Flourescence (IXRF) Systems to be used in conjunction with the LEO SEM. Powders P1, P3

and P6 were used in this study. The ParticleScan software provided information on the following shape factors (Note: These shape factors/descriptors should not be confused with those given by equations 2-9 and 2-10):

Shape factor: This is defined as the ratio between the maximum Feret diameter and the minimum Feret diameter.

Roughness: Is the ratio between the external perimeter and the convex perimeter.

Compactness: Defined as $(\text{perimeter})^2/4\pi(\text{area})$. This ratio should be 1 for a perfect circle.

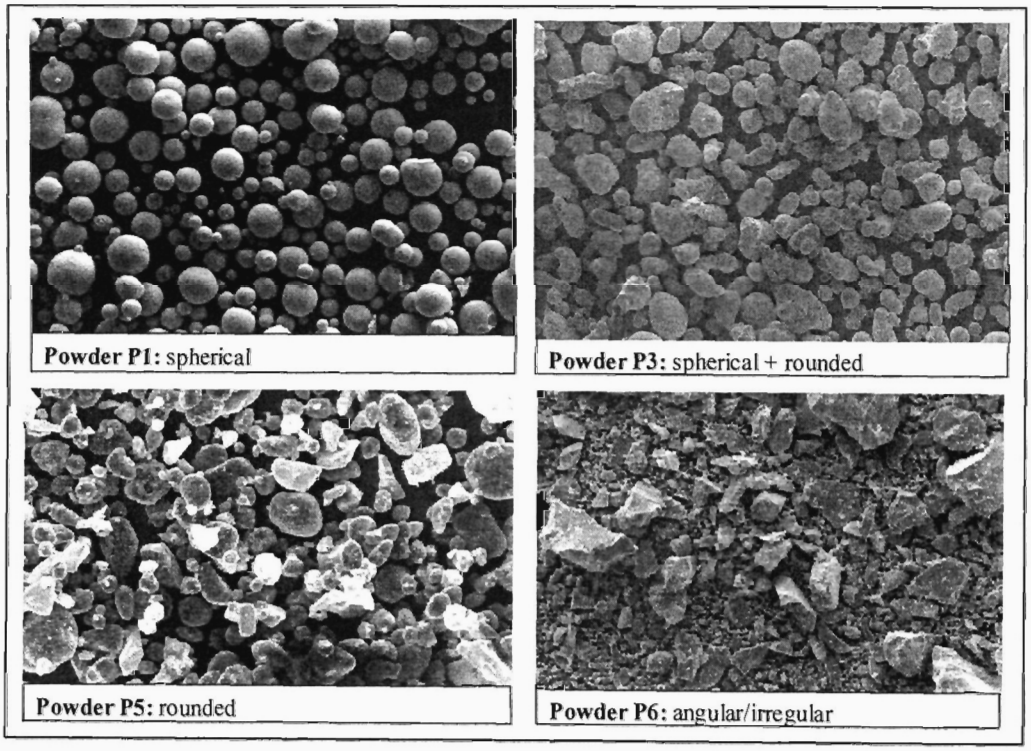

Figure 3-1: SEM images of some of the powders illustrating the different particle shapes.

The results of the particle shape analysis obtained from the ParticleScan Software for powders P1, P3 and P6 are illustrated graphically in Figures 3-2 to 3-4.

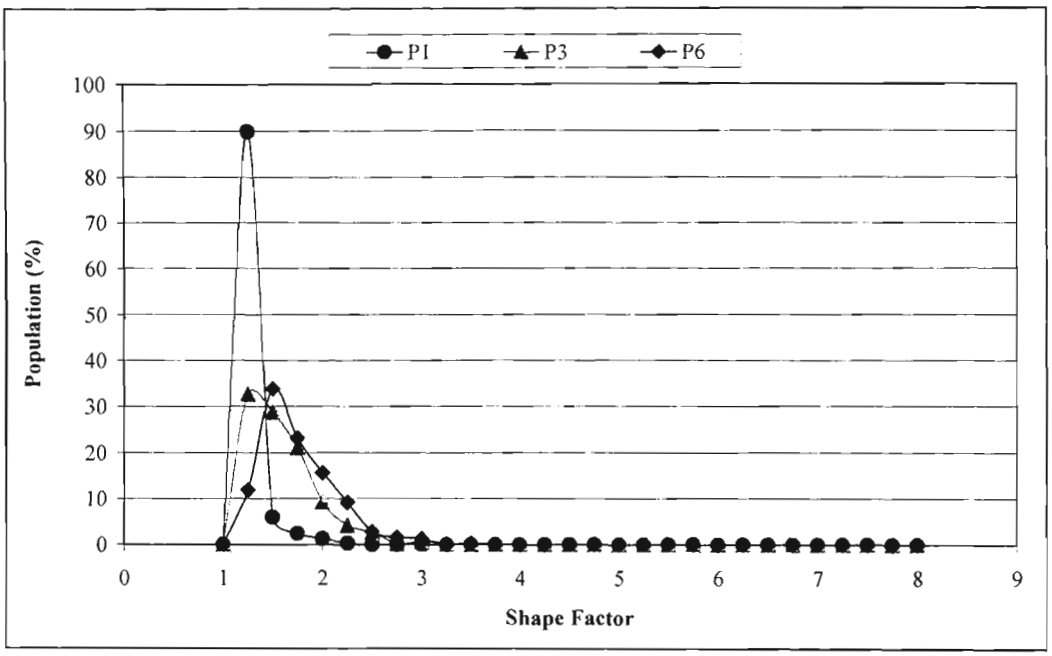

Figure 3-2: Comparison of Shape factor.

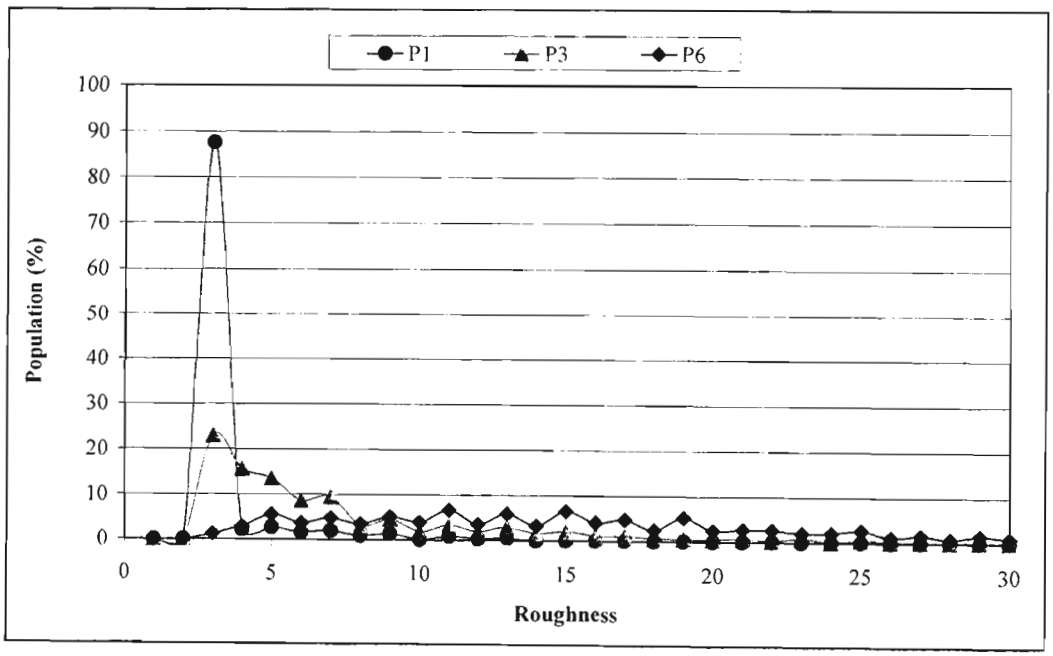

Figure 3-3: Comparison of Roughness.

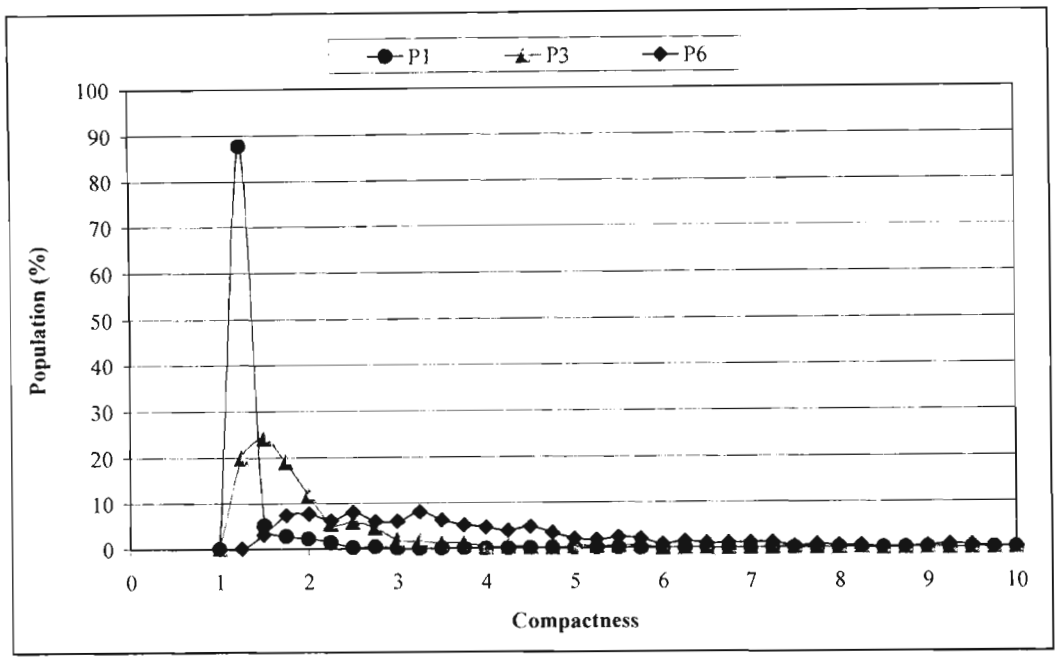

Figure 3-4: Comparison of Compactness.

From Figure 3-2 to Figure 3-4 it can be seen that particles of powder P1 are the most spherical while the particles of powder P6 are the least spherical. The shapes of the particles of powder P3 are in between that of powders P1 and P6. These quantitative results are in agreement with visual observations (SEM images) of the particles. Although all the shape factors presented above provide a clear distinction between the particle shapes of the different powders it is clear that some are more sensitive than others. For example, the Roughness factor is more sensitive than the Shape factor.

It is also clear from the above figures that particles that make up a certain powder have different shapes which results in a powder having a shape distribution. It is therefore envisaged that relating the particle shape to its fluidization behaviour will not be a trivial matter. However, as will be shown later the differences observed in the overall fluidization behaviour of different powders can to some extent be attributed to differences in particle shapes.

Based on the data presented in Figures 3-2 to 3-4, the cumulative distribution could be calculated and plotted for each of the shape factors presented above and an average shape factor was defined as that shape factor corresponding to the 50% point on the cumulative distribution plot (this is analogous to the d_m obtained from a cumulative particle size

distribution plot). This is illustrated in Figure 3-5 where the cumulative Compactness distribution is plotted and the average Compactness factor for powder P6 is shown.

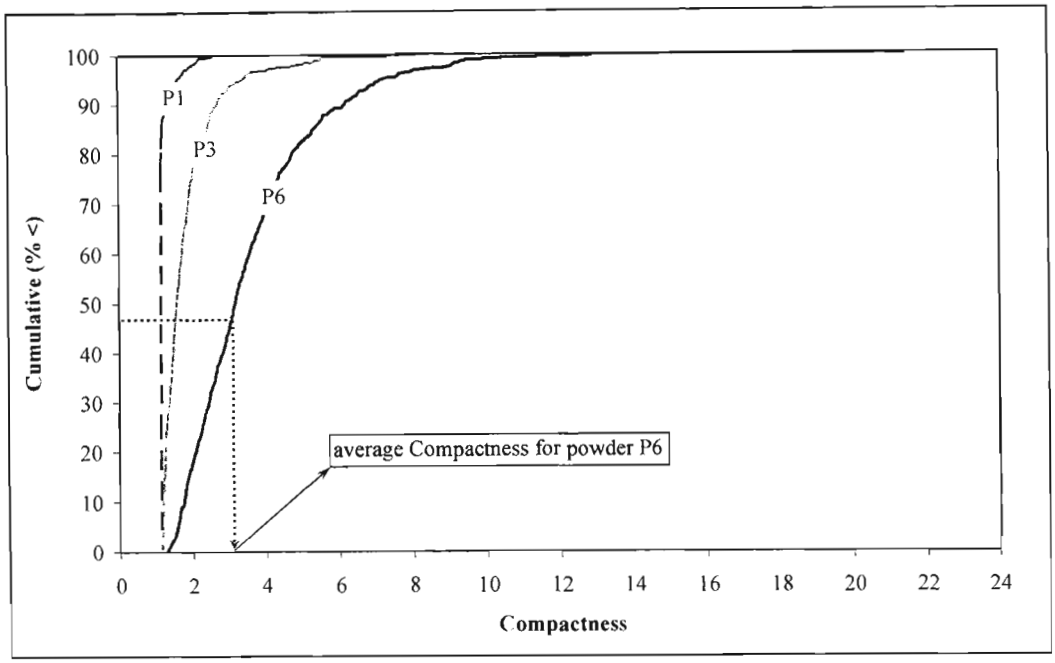

Figure 3-5: Cumulative Compactness distribution.

The procedure used to calculate the average shape factor as illustrated in Figure 3-5 was repeated for the other shape factors (Shape factor, Roughness) and the results are summarised in Table 3-2.

Table 3-2: Average shape factors.

Powder	P1	P3	P6
Shape factor	1.06	1.40	1.55
Roughness	1.04	1.09	1.33
Compactness	1.14	1.58	3.18

The conclusion that can be drawn from the above information is that powder P3 is more spherical (or less angular) than powder P6 and since they have the same particle density and a similar particle size distribution, the differences in their fluidization behaviour can be attributed to some extent to the difference in the shape of the particles. This will become clearer during the discussion of the fluidization test results in chapter 6.

3.2. Geldart's Powder Classification

The Geldart (1973) group classification of powders P1 to P10 is shown in Table 3-3.

Table 3-3: Powder classification according to Geldart groups.

Powder	d_{sv} (μm)	d_m (μm)	ρ_p (kg/m^3)	F_{22} (%)	Geldart group classification
P1	56	61	2300	1	Group A
P2	48	54	1900	3.1	Group A
P3	28	42	4600	26.3	Group A
P4	60	91	4600	5.9	Group B
P5	28	49	3200	24.4	Group A
P6	23	40	4600	28.7	Group A
P7	42	66	1300	9.6	Group A
P8	16	37	4600	29.5	Group A
P9	49	80	4600	9	Group B
P10	16	21	4600	55.1	Group A/C

All the powders used for this work can be classified as Geldart group A powders except for powders P4 and P9 which are Geldart group B powders and P10 which is a group A/C powder (since it lies more in the boundary region between group C and group A).

A large number of the powders used for the fluidization tests lie in Group A, hence they should display the fluidization properties associated with Group A powders. However, these powders differ in particle size distribution, shape and density, which is expected to result in fluidization differences (eg. entrainment rate, bubble voidages and fluidization regime) that cannot be explained merely by the powders Geldart group classification.

However, the overall fluidization properties of the bed were in agreement with some of their group properties, for example, the bed collapse tests could be easily carried out on Group A powders due to their aeratable nature. In contrast it was not possible to record any data from the bed collapse test of Group B powders since their de-aeration time was so fast and high-speed video equipment would be required to capture the de-aeration time of the bed or an alternative technique to measure the bed voidages would be required. In addition the group B powders displayed a higher standard deviation of the bed pressure drop fluctuations, which was indicative of higher bubble activity and/or bubble size.

4. EXPERIMENTAL EQUIPMENT

The fluidization tests were carried out using two sets of Plexiglas equipment having an internal diameter of 0.05 m and 0.14 m respectively. These two sets of equipment were used firstly; to study the effect of particle properties on the fluidization regime in small diameter columns where slugging is expected to occur. In addition the 0.05 m column is representative of some industrial pilot scale fluidized bed reactors and hence it was desired to gain some insight into the effect of particle properties on the operation of these types of units. Secondly, by using two columns of different diameter, the effect of column diameter on the fluidization regime and entrainment rate could be investigated.

The larger 0.14 m internal diameter column was also used to compare the fluidization properties of the powders and to study the effect of powder properties on the fluidization behaviour of the bed as a function of superficial gas velocity. Sookai *et al.* (2001) have shown that the overall bed voidage obtained from a 0.14 m internal diameter column operating at ambient conditions were in line with that obtained from a high pressure commercial scale fluidized bed reactor (the approximately 10% difference in bed voidages observed between the commercial unit and cold model was explained in terms of operating pressure). In addition a 0.14 m internal diameter column provides a good compromise between the amount of powder required for the tests and the relevance of the tests to commercial scale units.

4.1. Set-up of the 0.05 m plexiglas column

The set-up of the 0.05 m plexiglas column is shown schematically in Figure 4-1. The fluidization column is about 6 m tall from the gas distributor. The test powder was loaded from the top of the column by opening the top flange.

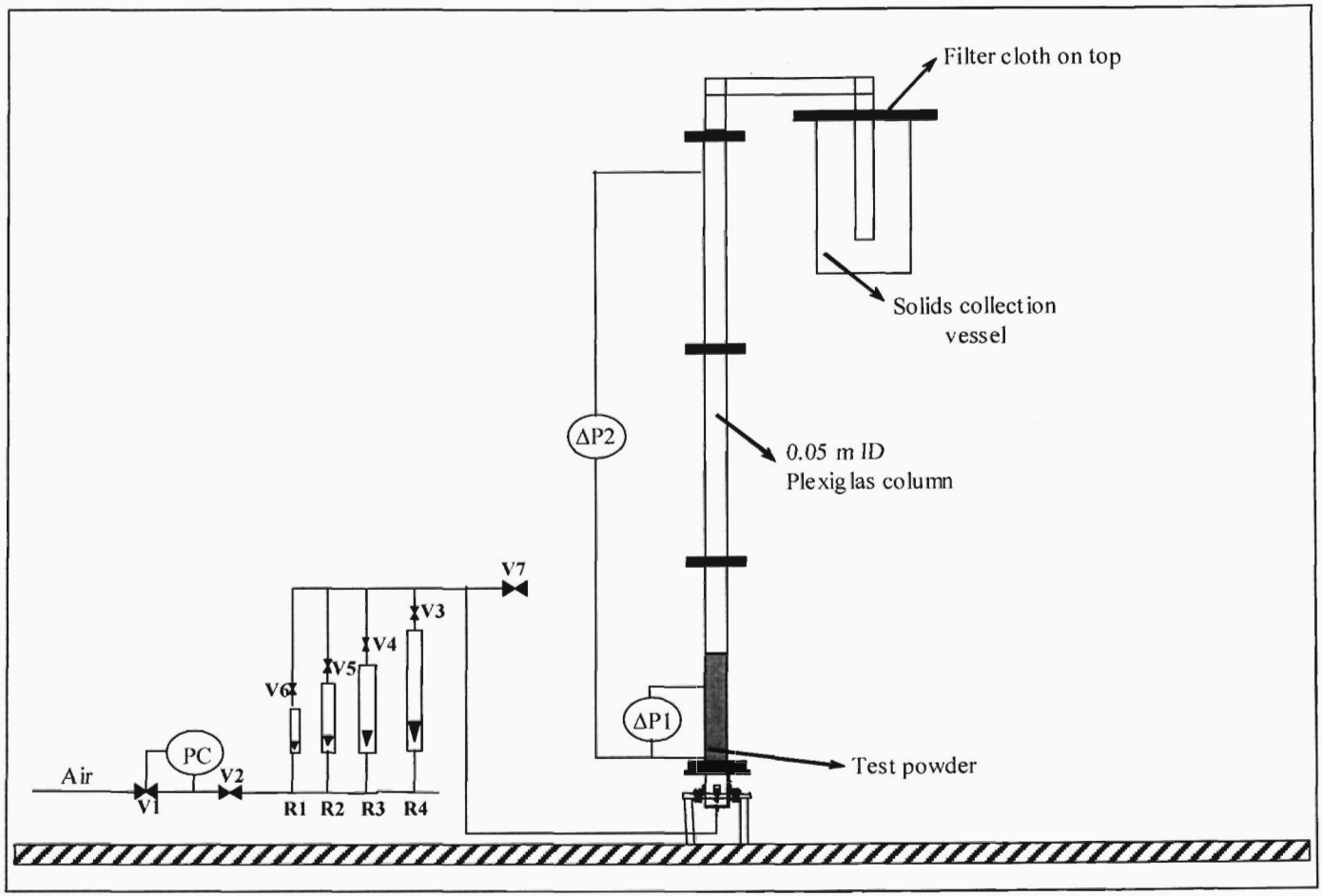

Figure 4-1: Set-up of the 0.05 m internal diameter fluidization test column.

Compressed air (available at 8 bar gauge) was used as the fluidizing gas and the pressure at the inlet of the flow meters was controlled at 4-bar gauge with a pressure control valve. The reason for this was to ensure that the flow meters operated at a pressure at which they were calibrated. The air flow rate to the column could be controlled with the rotameters R1 to R4 in order to obtain a desired superficial gas velocity in the column. At the top of the column a solids collection vessel that has a filter was used to capture the entrained solids. The differential pressures ΔP1 and ΔP2 were measured using mercury manometers and Rosemount differential pressure transmitters. The latter differential pressures were recorded using a Honeywell TrendViewer recorder. The maximum frequency at which data could be recorded was 5 Hz due to limitations of the differential pressure transmitter.

4.2. Set-up of the 0.14 m plexiglas column

The set-up of the 0.14 m plexiglas column is shown schematically in Figure 4-2. The fluidization column is about 6 m tall from the gas distributor. The test powder was loaded from the top of the column through valve V12. The test powder was added into the column until the settled bed height of the powder was around 1 meter. Compressed air (available at 8 bar gauge) was used as the fluidizing gas and the pressure at the inlet of the flow meters was automatically controlled at 4-bar gauge. This pressure was used to ensure that the flow meters operated at the pressure at which they were calibrated. The flow meters R1 to R4 were used to set the gas velocity in the column at a desired value (between 0 and 0.8 m/s). The flow meter R5 was used to measure the air flow rate to the cyclone in addition to that flowing through the column. In this way, the air flow rate through R5 could be varied to ensure that the cyclone inlet velocity remained constant at about 20 m/s. Maintaining a relatively high and consistent inlet velocity to the cyclone ensured that the cyclone operated at maximum particle collection efficiency irrespective of the superficial velocity in the column. During normal operation the solid laden gas leaving the fluidization column was passed through the cyclone; thereafter the solids were collected in the dipleg and periodically returned to the bed. The gas leaving the cyclone passed through one of the bag filters before being discharged to atmosphere. During the test where entrainment was measured, the cyclone was by-passed so that all the entrained solids could be collected in the filter. Rosemount differential pressure transmitters were used to measure the pressure drops ΔP3, ΔP4. The signals from the transmitters were recorded using a Honeywell TrendViewer recorder. The pressure in the column relative to atmosphere was monitored using a U-tube mercury manometer.

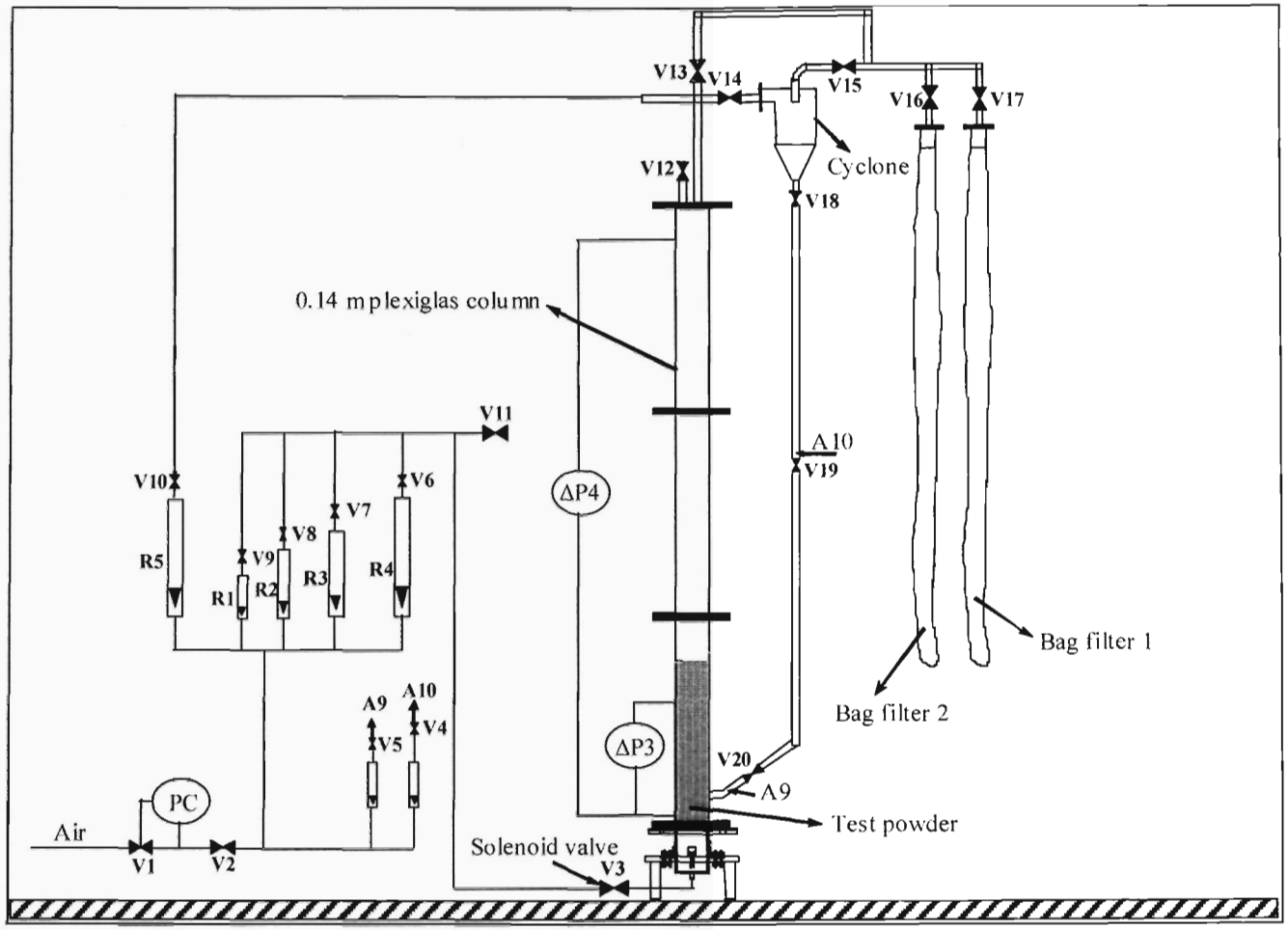

Figure 4-2: Set-up of the 0.14 m internal diameter fluidization test column.

5. EXPERIMENTAL PROCEDURE

In addition to visual observations, measurements were made to determine the fluidized bed expansion ratio, the dense phase voidage, bubble fraction, overall bed voidage, bed pressure drop, bed density and the catalyst entrainment or carryover rate. These tests were carried out in either the 0.05 m or 0.14 m Plexiglas columns described in the previous section. The procedures used for these measurements are discussed next.

5.1. Measurement of entrainment rate in the 0.05 m column

The entrainment rate measurement procedure used for the 0.05 m column differed from that utilized for the 0.14 m column in that only a single gas velocity was used and elutriated material was not returned to the bed after each test. The following procedure was used (with reference to Figure 4-1):

- The solids collection vessel was weighed and installed.
- 2 kg of powder was added to the column. The static bed height varied between 0.3 and 0.4 m depending on the particle density.
- The bed was fluidized at a superficial gas velocity of 0.38 m/s (this velocity was chosen arbitrarily since the focus was on comparing the fluidization behaviour of the powders).
- On an hourly basis, the system was shut down and the solids collection vessel was removed, weighed and the difference in weight was recorded.
- The average entrainment rate was then obtained by dividing the weight difference of the solids collection vessel by the time interval of 1 hour.
- This was repeated until successive average entrainment rates did not change significantly.

5.2. Measurement of bed expansion

At each velocity setting the minimum and maximum fluidized bed height was marked on masking tape stuck to the plexiglas column and then measured relative to the gas distributor. From these heights, the average fluidized bed height was calculated. The bed expansion was then obtained by dividing the average fluidized bed height by the average settled bed height or un-fluidized bed height. The average settled bed height was taken to be the settled bed height that resulted two minutes after the gas supply to the column was shut off. The

masking tape was then replaced and the procedure was repeated for the next superficial gas velocity.

5.3. Measurement of bed voidages

The single drainage bed collapse experiment was used to measure the dense phase and bubble fraction as discussed in section 2.3.5.1. The single drainage method was used because of equipment limitations. However, the single drainage bed collapse test can still be used to make hydrodynamic comparisons between powders as recommended by Lorences *et al.* (2003). The bed collapse experiment was carried out as follows (with reference to Figure 4-2):

- All valves were closed except for V14, V15, V16, V18 and V19.
- Valve V12 was opened and the powder was weighed and loaded into the column to give a settled bed height of approximately 1 m. V12 was then closed.
- V11 was opened to discharge any air trapped in the lines. V11 was then closed.
- The bed was then fluidized by opening valve V7.
- Once the bed was fluidized, V6 was opened and V7 was closed. The air flow rate was then set by adjusting V7 until the reading on rotameter R4 gave the desired superficial gas velocity.
- The maximum and minimum fluidized bed height was then measured as described in section 5.2.
- V3 was then closed and simultaneously a stopwatch was started.
- As the bed settled, its height was recorded at regular time intervals.
- For each gas velocity the above was repeated three times.
- The above procedure was repeated for each powder.

5.4. Measurement of entrainment rate in the 0.14 m column

For each powder the entrainment rate was measured as a function of superficial gas velocity as follows (with reference to Figure 4.2):

- Bag filter number 2 was weighed and installed.
- Closing V13 and V17 and opening V14, V15 and V16 isolated bag filter number 2.
- Flow meters R4 and R5 were set to give the desired gas velocity in the column and cyclone respectively.

- The bed was kept fluidized for about 10 minutes. At higher velocities this time was cut to a minimum because of the higher entrainment rates.
- For the entrainment rate measurement. the cyclone was by-passed by opening V13 and closing V14 and V15.
- V17 was then opened and V16 was closed and a stopwatch was started simultaneously.
- After a fixed time interval, V16 was opened, V17 was closed, V14 and V15 were opened and V13 was closed. At low gas velocities a time interval of 10 minutes was used and at higher gas velocities a time interval of 1 minute was used.
- Bag filter number 2 was then removed and weighed. The difference in mass was recorded. The entrainment rate was obtained by dividing this mass by the time interval. Prior to the next test, the solids collected in the filter and dipleg was returned to the bed.

For each velocity used, the above was repeated three times and an average value was reported.

6. RESULTS AND DISCUSSION

Fluidization tests were carried out in both the 0.05 m internal diameter column and the 0.14 m internal diameter column. However, all the tests were not carried out on all the powders. The 0.05 m internal diameter column was mainly used to study the effect that particle properties have on the operating fluidization regime and entrainment rate as a function of time at a fixed superficial gas velocity of 0.38 m/s. The 0.14 m internal diameter column was used to study the bed hydrodynamics, fluidization regime and entrainment rate as a function of superficial gas velocity. Table 6-1 summarises the tests carried out and the powders used for each test.

Table 6-1: Summary of tests carried out and the powders used.

0.05 m internal diameter column			
Tests carried out	Fluidization regime	Entrainment rate	
Powders used	P3, P5, P6, P8, P9, P10	P3, P5, P6, P8, P9, P10	
Superficial gas velocity	0.38 m/s		
0.14 m internal diameter column			
Tests carried out	Fluidization regime	Bed collapse/ hydrodynamics	Entrainment rate
Powders used	P1, P3, P4, P5, P6	P2, P3, P5, P6, P7	P1, P3, P4, P5, P6
Superficial gas velocity	Varied from 0 to 0.78 m/s		

The results obtained will be presented and discussed in the following sections.

6.1. Results from the 0.05 m internal diameter column

The 0.05 m column was operated at a superficial gas velocity of about 0.38 m/s for all the powders tested. The entrainment rate of each powder was monitored as a function of time. The results of these tests were then analysed to determine the effect of particle shape, particle size, particle density and the use of baffles on the operating fluidization regime and resulting entrainment rate. These results will now be discussed individually. The reader is referred to Appendix B for the detailed experimental results.

6.1.1. Fluidization regime

For each powder the fluidization regime was observed visually and where possible, the standard deviation of the bed pressure drop fluctuations was also analysed to compare the operating fluidization regimes of the powders. The standard deviation of the bed pressure drop fluctuations for some of the powders is shown in Figure 6-1 (the data for the other powders could not be included because there was a problem with the pressure transmitter).

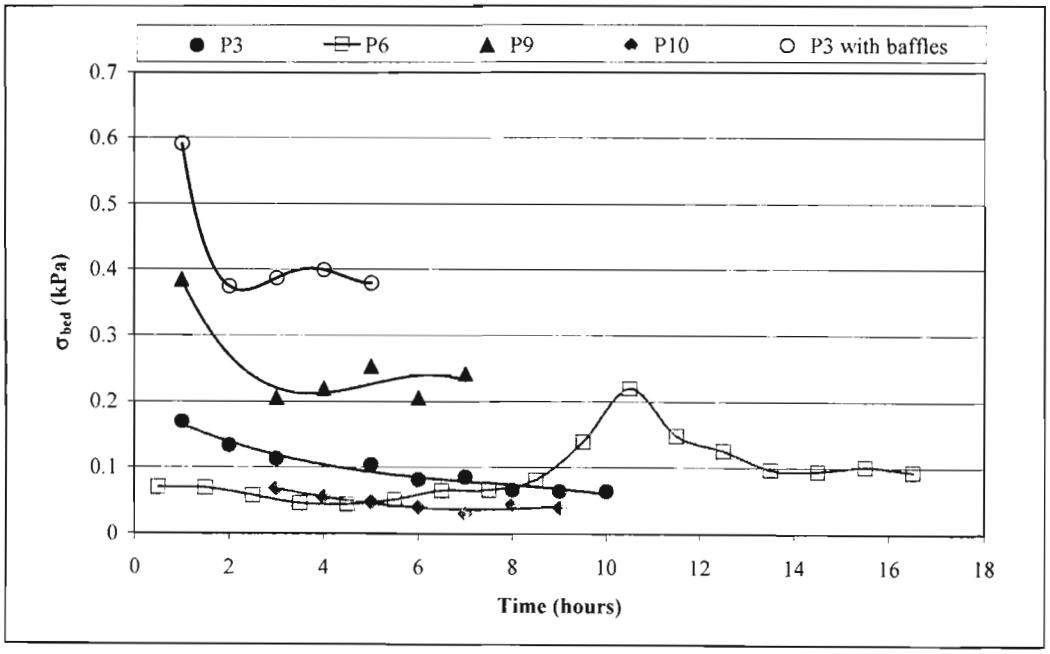

Figure 6-1: Standard deviation of the bed pressure drop fluctuations at U = 0.38 m/s.

In general it was found that only the irregular/angular shaped particles (P6 and P8) operated in the bubbling regime initially and gradually began to slug with time after the fines were lost (Note: no data was recorded for P8). The other powders (P3 with and without baffles, P9 and P10) started to slug from the beginning and had higher initial standard deviation of the bed pressure drop fluctuations. It was also found that the standard deviation of the bed pressure drop fluctuations decreased with a decrease in bed height for some of the powders even though slugging was still observed.

The Stewart and Davidson (1967 cited by Yang 2003b] criterion for slugging (equation 2-43) was used as a comparison to the observed fluidization regime. U_{mf} was calculated using equation 2-27. The results of the comparison are presented in Table 6-2.

Table 6-2: Comparison of observed fluidization regimes with the Stewart and Davidson criterion for slugging.

Powder	Stewart and Davidson criterion: $\frac{U - U_{mf}}{0.07\sqrt{gD}} > 1$	Visual observations on operating fluidization regime
P3	7.70	Slugging throughout
P5	7.70	Slugging throughout
P6	7.70	Initially bubbling but turned to slugging after about 6 hours
P8	7.71	Initially bubbling but turned to slugging after about 7/8 hours
P9	7.56	Slugging throughout
P10	7.74	Slugging throughout

According to the Stewart and Davidson criterion for slugging, all the powders should have been slugging at the operating conditions used for the tests, which is contrary to the observations made in this work. Slugging was only observed with the more spherically shaped particles. It is clear from these results that the Stewart and Davidson criterion for slugging is not applicable to angular shaped particles or it does not incorporate the effect of fines on slugging.

6.1.2. The effect of particle shape

The major difference between powders P3 and P6 is the shape of the particles. The particles of powder P3 are more spherical in shape than those of powder P6. Therefore the differences observed in the fluidization behaviour of these two powders at similar operating conditions could be attributed to the differences in particle shape. It was found that powder P3 operated in the flat-nose slugging regime from the beginning whereas powder P6 operated in the bubbling regime. As time progressed, powder P3 continued to operate in the slugging regime while with powder P3 the fluidization regime started to change to the slugging regime, as the fines were lost through entrainment. This was also clearly observed from an analysis of the standard deviation of the bed pressure drop fluctuations, which is shown in Figure 6-2.

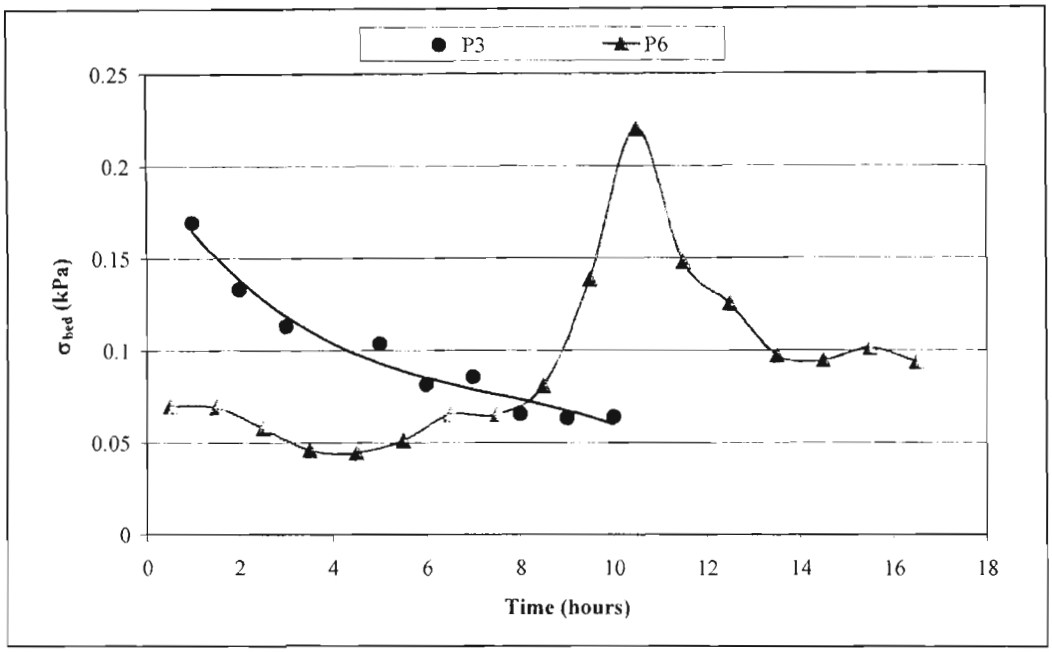

Figure 6-2: Standard deviation of the bed pressure drop fluctuations for powders P3 and P6.

The change in the bed pressure drop with time (which is a measure of the mass of powder in the column) is shown in Figure 6-3.

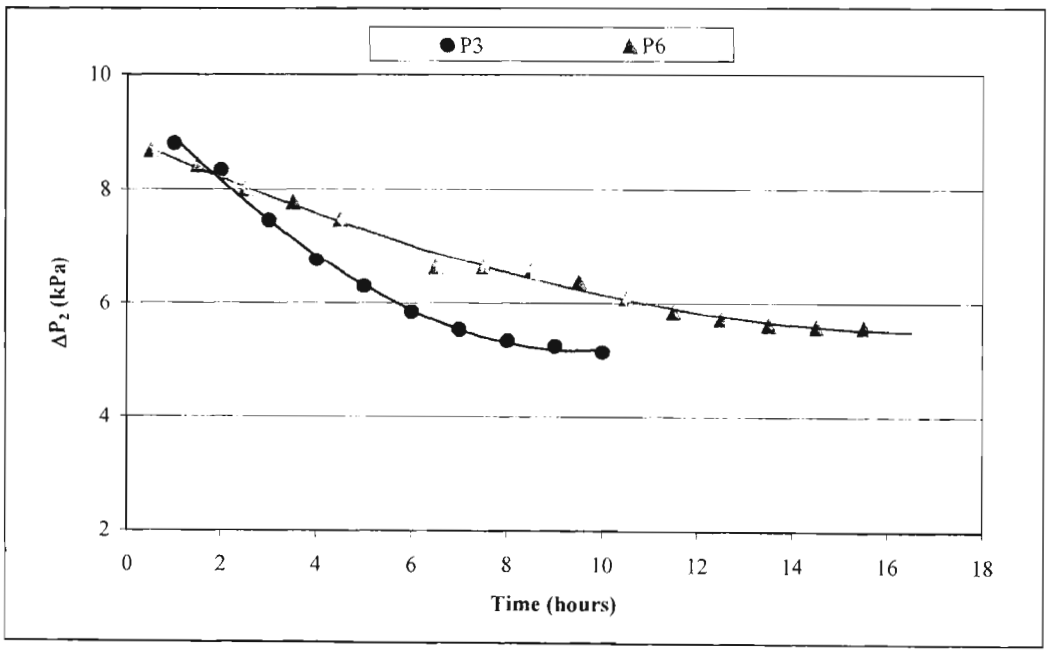

Figure 6-3: Change in the bed pressure drop of powders P3 and P6.

According to Figure 6-2, powder P3 started off with a higher standard deviation of the bed pressure drop fluctuations, which from visual observations corresponded to the slugging fluidization regime. Thereafter, the standard deviation of the bed pressure drop fluctuations started to decrease due to the decrease in the bed height as a result of the loss of material due to entrainment (the entrained material that was collected was not returned to the bed – also refer to Figure 6-3). With powder P6 the standard deviation of the bed pressure drop fluctuations started to increase after about six hours on-line and this was also around the time that the fluidization regime started to change from bubbling to slugging. The standard deviation of the bed pressure drop fluctuations reached a maximum after about 10 hours of operation after which it decreased with time corresponding to the decrease in bed level. An analysis of the average entrainment rates for these two powders indicated that the entrainment rate for powder P3 was higher than that of powder P6. This is illustrated in Figure 6-4.

According to Figure 6-4, the initial entrainment rate of powder P3 was over six times higher than that of powder P6.

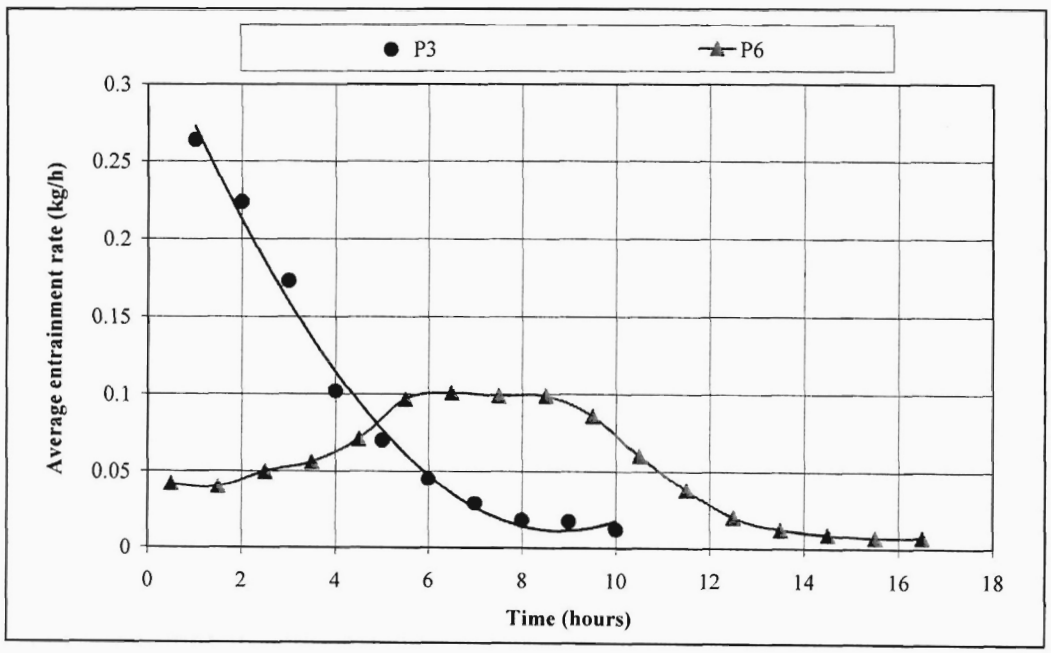

Figure 6-4: Comparison of the average entrainment rate of powders P3 and P6.

This result is attributed to the difference in fluidization regimes, which was caused by the difference in the particle shapes. The slugging bed of powder P3 produced a higher entrainment rate than the bubbling bed of powder P6. The entrainment rate of powder P3 started to decrease with time and this is probably due to the decrease in the amount of

entrainable material in the bed at 0.38 m/s. In contrast the entrainment rate of powder P6 started of low while the bed operated in the bubbling fluidization regime. Thereafter, the entrainment rate started to increase and reach a maximum when the bed was fully slugging, after which it started to decrease for the same reasons as for powder P3. Once powder P6 had lost a certain amount of fines, its entrainment rate was very similar to that of powder P3. This can be clearly seen from Figure 6-3 by comparing the entrainment rates of powder P6 after 9.5 hours to that of powder P3 after 5 hours.

Since the only major difference between powder P3 and P6 is the particle shape, the results presented above indicate that the more spherical the particle shape, the higher the entrainment rate. Additionally, it also shows that fines play a significant role in controlling the fluidization behaviour of angular shaped particles because once a critical amount of fines was lost from the bed of powder P6, the fluidization regime and entrainment rate was similar to that of powder P3. It is therefore hypothesised that the presence of fines in angular shaped particles causes bubble splitting, which decreases the maximum stable bubble size and prevents slug formation in small diameter columns. Since the bubbles have an important role to play in controlling the entrainment rate (Geldart 1986c), it is proposed that the smaller the maximum stable bubble sizes the lower the entrainment rate. In powders having spherically shaped particles the fines do not have the same effect on the bubble size, hence they are lost quite easily from the bed through entrainment.

The effect of the bubbles on the entrainment rate probably only applies in the region just above the bed surface. Once the particles are ejected from the bed into the freeboard, they have a higher probability of being entrained. However, some researchers (Yerushalmi *et al.* 1978 cited by Geldart 1986 p.135; Hatano and Ishida 1983; Yorquez-Ramirez and Duursma 2001) have found that particles form clusters or agglomerates in the freeboard, which make it possible for fines to remain in the system even at high gas velocities. If it is assumed that angular shaped particles have a higher tendency towards particle cluster formation, then this could be another reason why a lower initial entrainment rate was observed with angular shaped particles. However, based on the experimental data of this work no conclusion can be made on whether particle cluster formation in the freeboard is more pronounced with angular shaped particles or spherical particles. The conclusion that can be made is that the bed behaviour clearly controls the rate at which the particles or particle clusters are entrained from the bed.

In order to test the effect of particle shape on fluidized bed behaviour and entrainment rate further, a coarse fraction of powder P3 was crushed and sieved to yield different size fractions. These size fractions were then blended in proportions so as to yield powder P8

having a particle size distribution similar to powder P6 and P3. The cumulative size distribution of powder P8 relative to powder P3 and P6 is shown in Figure 6-5.

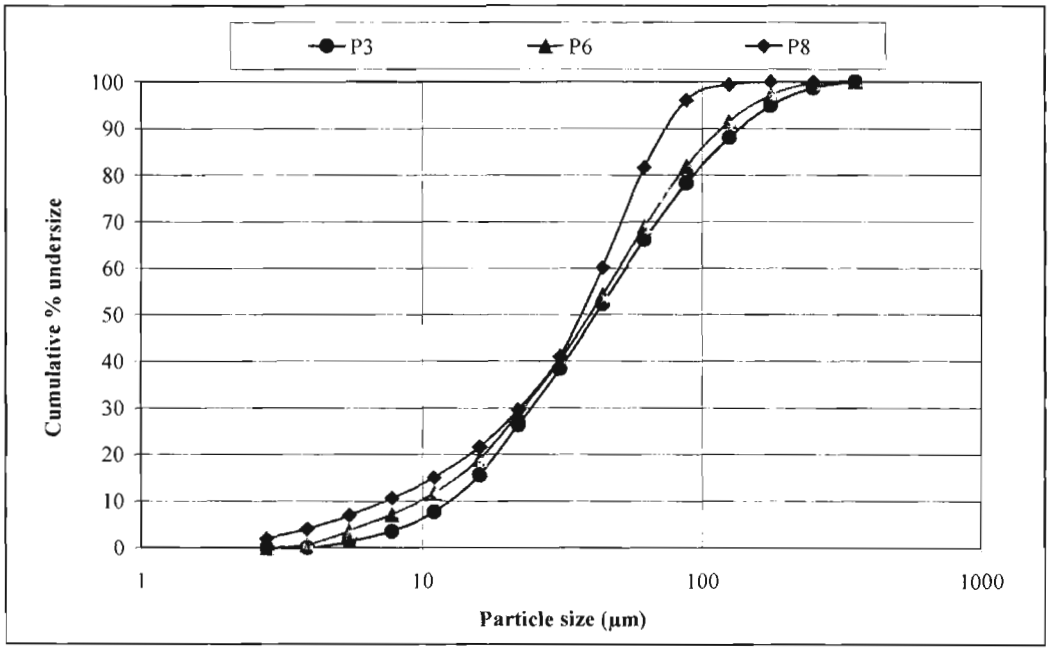

Figure 6-5: Comparison of the particle size distribution of powders P3, P6 and P8.

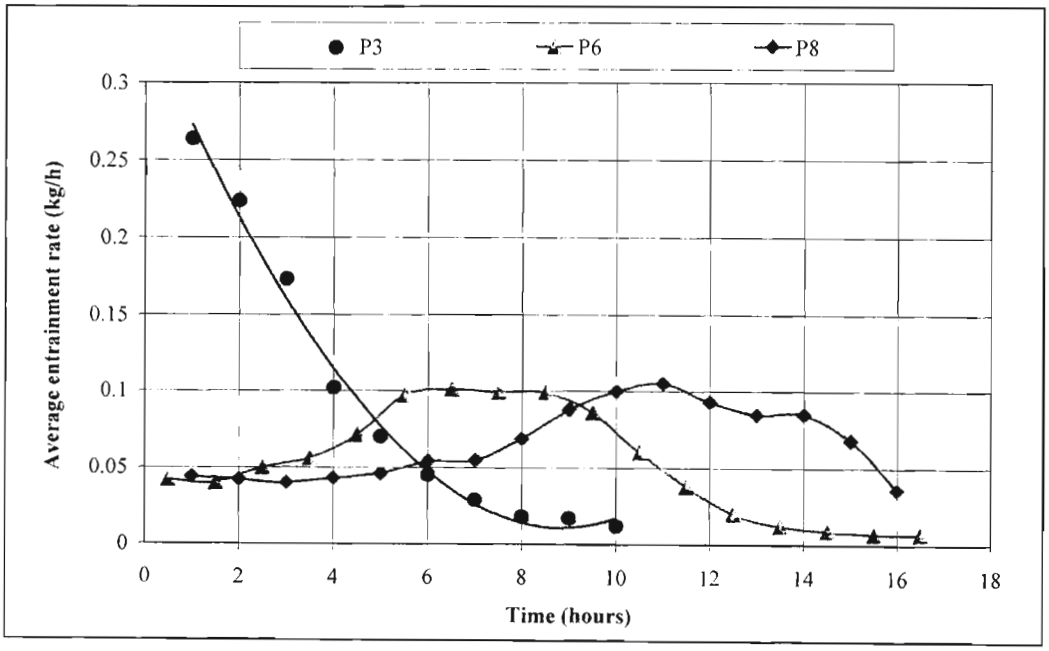

Figure 6-6: Comparison of the entrainment rate of powders P3, P6 and P8.

Unfortunately, the particle size distribution of powder P8 did not match that of powder P3 or P6 exactly. Since powder P8 was finer than powder P3 and P6, it was expected to have a higher entrainment rate when compared to P3 and P6. However, as shown in Figure 6-6, this was found not to be the case. Comparing the entrainment rate of powders P3 and P8, it is clear that particle shape plays a significant role in controlling the fluidization behaviour of the bed. This is deduced from the fact that powder P3 and P8 are the same material except that powder P3 is more spherical and has less fines when compared to powder P8. In fact the fluidized bed of powder P8 showed very similar characteristics to that of powder P6 although there was some difference in the entrainment rate, which could be explained in terms of the higher fines content of powder P8.

Powder P8 initially operated in the bubbling regime and started to move into the slugging regime, as the fines were lost through entrainment. However, due to the higher fines content, the bed operated in the bubbling regime longer than that of powder P6; hence the entrainment rate remained low for a longer period. Thereafter, as was found with powder P6, the entrainment rate reached a maximum once the bed was fully slugging and began to decrease as the concentration of entrainable material in the bed decreased. The result obtained from this test provides further evidence of the important influence which fine particles have on the fluidized bed behaviour of angular-shaped particles. The bed behaviour in turn controls the entrainment rate of particles or particle clusters from the bed.

6.1.3. The effect of PSD for angular particles

The results so far have indicated conclusively that the particle shape plays a significant role in determining the resulting fluidization regime and entrainment rate of a powder. In addition, the above results also showed that the presence of fines in angular shaped powders enhances the fluidization properties of the bed and prevents slug formation in small diameter columns. The result is that angular-shaped particles tend to entrain at a slower rate than spherically-shaped particles. This finding has a significant application to the operation of small diameter pilot scale fluidised bed reactors where the slugging fluidization regime is not desired. By operating such reactors with angular-shaped particles and with a recycle of entrained material to the bed, bubbling fluidization conditions can be maintained even in small diameter columns.

6.1.4. The effect of PSD for spherical particles

In the preceding section it was shown that for angular shaped particles the presence of fines reduces the maximum stable bubble size and allows operation in the bubbling fluidization

regime even in small diameter columns, which in turn reduces the entrainment rate. It was therefore decided to test whether a similar behaviour would be observed for the more spherical particles of powder P3. To test this, two additional powders were prepared. Powders P9 and P10 were prepared such that they had a coarser and finer particle size distribution than powder P3 respectively. The particle size distribution of these powders is shown in Figure 6-7.

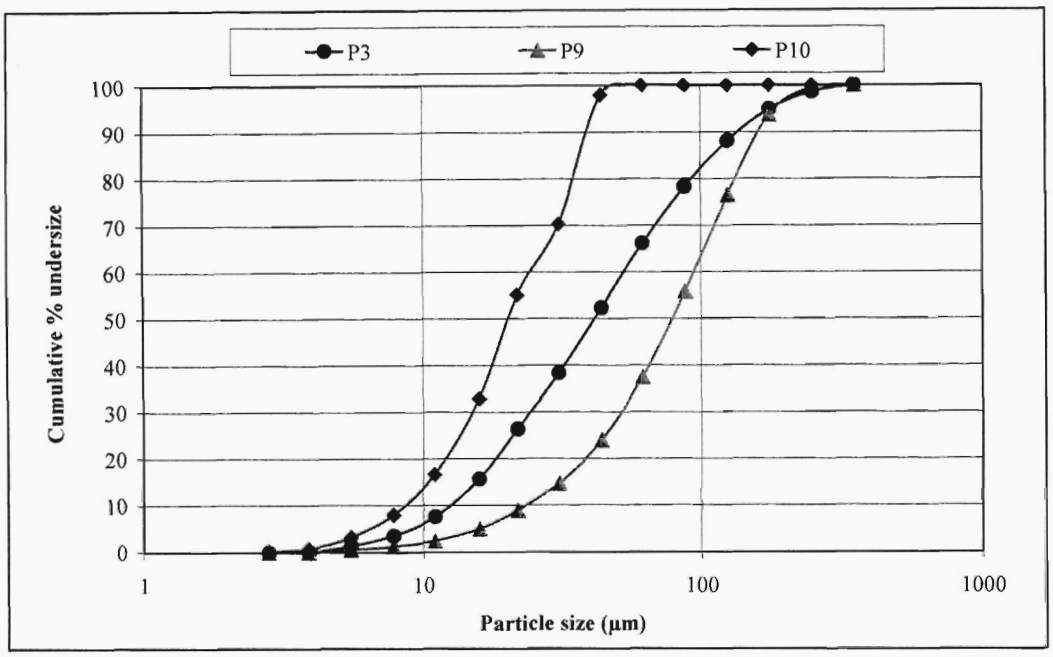

Figure 6-7: Comparison of the particle size distribution of powders P3, P9 and P10.

From Figure 6-7 (and Table 3-1) it can be seen that the average particle size (d_m) of powder P9 is approximately twice that of powder P3 while the average particle size of powder P10 is approximately half that of powder P3. The standard deviation of the bed pressure drop fluctuations for powder P3 and P9 are compared in Figure 6-8. These results indicate that the coarser the particle size distribution of the powder the higher the standard deviation of the bed pressure drop fluctuations. Combined with visual observations it was found that the fluidized bed of powder P9 operated with larger slugs than that of powder P3. Despite the more violent slug formations observed with powder P9 the average entrainment rate was lower than that of powder P3 as shown in Figure 6-9. This was expected due to the coarser particle size distribution of powder P9.

A comparison of the entrainment rate of powder P3 and P10 showed that powder P10 had a higher average entrainment rate than powder P3. Hence, the expectation that the presence of fines would reduce the maximum stable bubble size, which in turn would reduce the

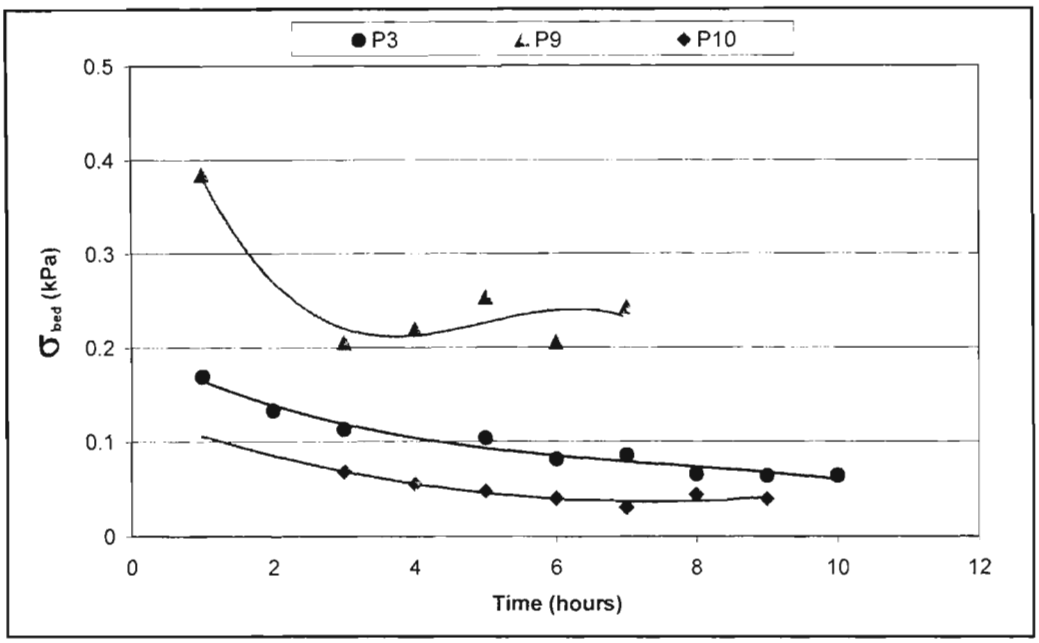

Figure 6-8: Comparison of the standard deviation of the bed pressure drop fluctuations of powders P3, P9 and P10.

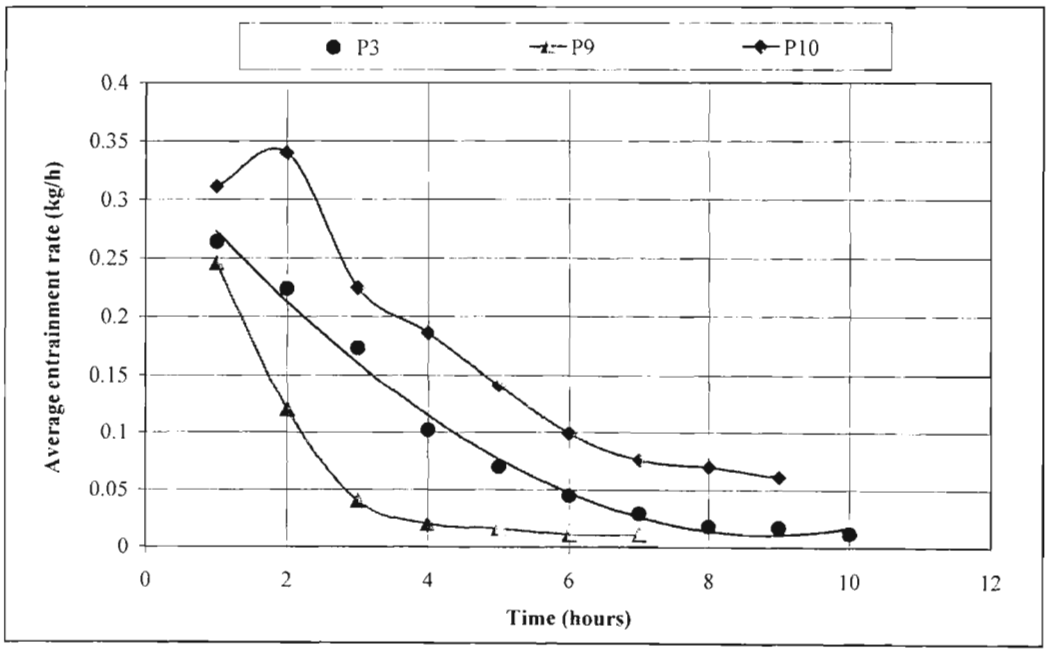

Figure 6-9: Comparison of the entrainment rate of powders P3, P9 and P10.

entrainment rate, did not occur as was observed with the angular shaped particles. It was therefore concluded that for spherical particles, the fines do not affect the maximum stable bubble size, fluidization regime and entrainment rate in the same way as was found for angular shaped particles.

6.1.5. The effect of particle density

In order to draw a conclusion on the effect of particle density on the entrainment rate it is important to ensure that all other particle properties and operating conditions are the same. From the available test results the best comparison to see the effect of particle density could be obtained by comparing the results for powders P3 and P5. These two powders have a similar particle size distribution as shown in Figure 6-10 and powder P5 has a lower particle density than powder P3. However, the similarity of the particle shapes is questionable (refer to Figure 3-1). Powder P3 appears to be more spherical in shape than powder P5.

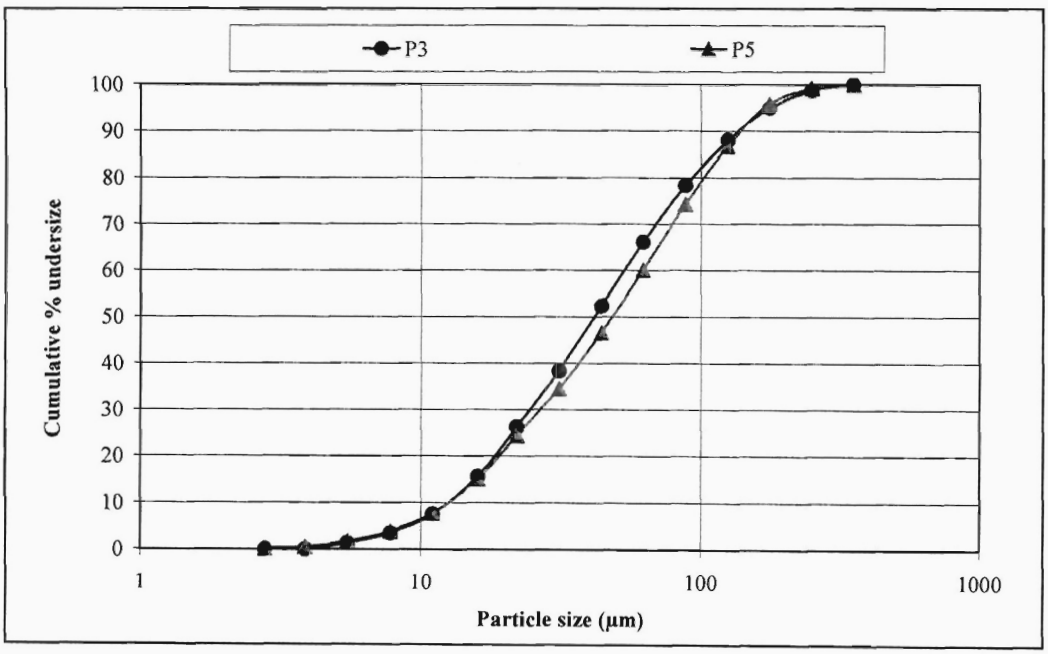

Figure 6-10: Comparison of the particle size distribution of powders P3 and P5.

Intuitively one would expect that the lower the particle density the higher would be the entrainment rate. However, as can be seen from Figure 6-11 the initial entrainment rate of powder P5 was lower than powder P3, which is counter-intuitive. The entrainment rate of powder P5 was slightly higher than that of powder P3 only after about 3 hours of operation. The initial unexpected difference in the entrainment rate between powders P3 and P5 could be explained in terms of particle shape effects and/or particle cluster formation. It appears

that powder P5 is more angular in shape compared to powder P3 resulting in bubbling fluidization and hence a lower initial entrainment rate of powder P5. However, an alternative explanation would be that the entrainment rate was initially lower due to particle cluster formation, in other words, powder P5 formed larger particle clusters in the freeboard than powder P3. These particle clusters gradually became smaller in size as the fines were lost and the fluidized bed became more slugging in nature.

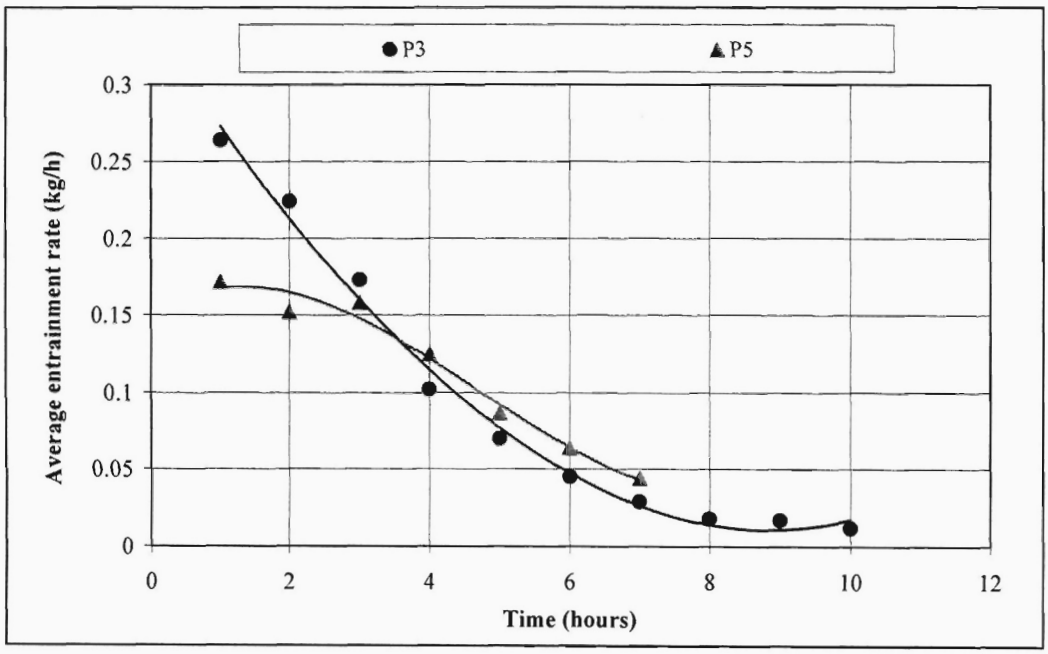

Figure 6-11: Comparison of the entrainment rate of powders P3 and P5.

Assuming that the particle shape cannot be changed, the particle size distribution is an important variable that can be manipulated, within reasonable limits, to control the entrainment rate of a powder. However, it must be remembered that a possible consequence of making the particle size distribution coarser to decrease the entrainment rate for spherical or rounded particles is a change in the Geldart group classification of the powder and a corresponding change in the fluidization regime (shift to group B and more slugging behaviour).

6.1.6. The effect of in-bed baffles

Another method of decreasing the solids entrainment rate is by the use of in-bed baffles (Jin *et al.* 2003). The effect of an in-bed baffle on the entrainment rate of powder P3 was investigated. The photograph of the baffle used is shown in Figure 6-12. The entrainment

rate of powder P3 with and without the baffles was compared along with the bed pressure drop and the standard deviation of the bed pressure drop fluctuations. These results are shown in Figures 6-13, 6-14 and 6-15 respectively.

It was found that the use of in-bed baffles reduced the entrainment rate of powder P3 but not to the extent that changing the particle shape did (compare Figures 6-6 and 6-13. The bed pressure drop however increased with the use of in-bed baffles (Note: the same mass of powder P3 was used for these tests), which is expected due the baffle causing an extra resistance to gas and solid flow.

The standard deviation of the bed pressure drop fluctuations also increased by the use of baffles. This indicates that the baffles did not stop the slug formation as expected. The slug frequency and length changed resulting in the higher standard deviation of the bed pressure drop fluctuations. The reduced entrainment observed with the in-bed baffles was therefore not a consequence of a change in the fluidization regime but rather it could have been a result of the change in slug properties brought about by the presence of the in-bed baffles.

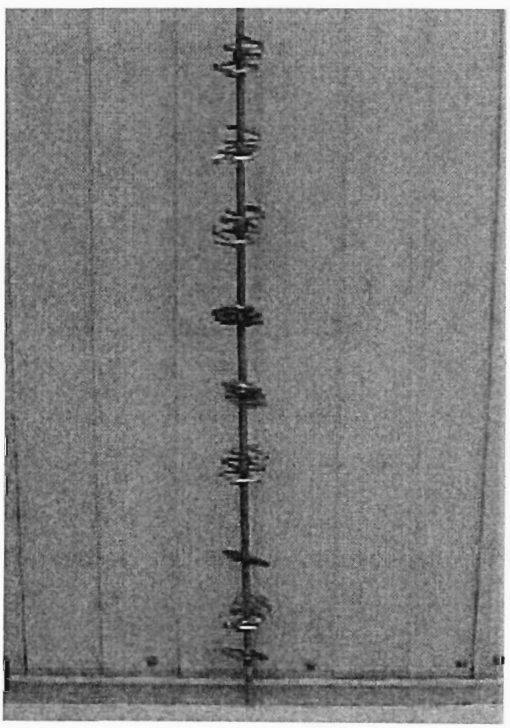

Figure 6-12: Photograph of the in-bed baffles used in the 0.05 m Plexiglas column.

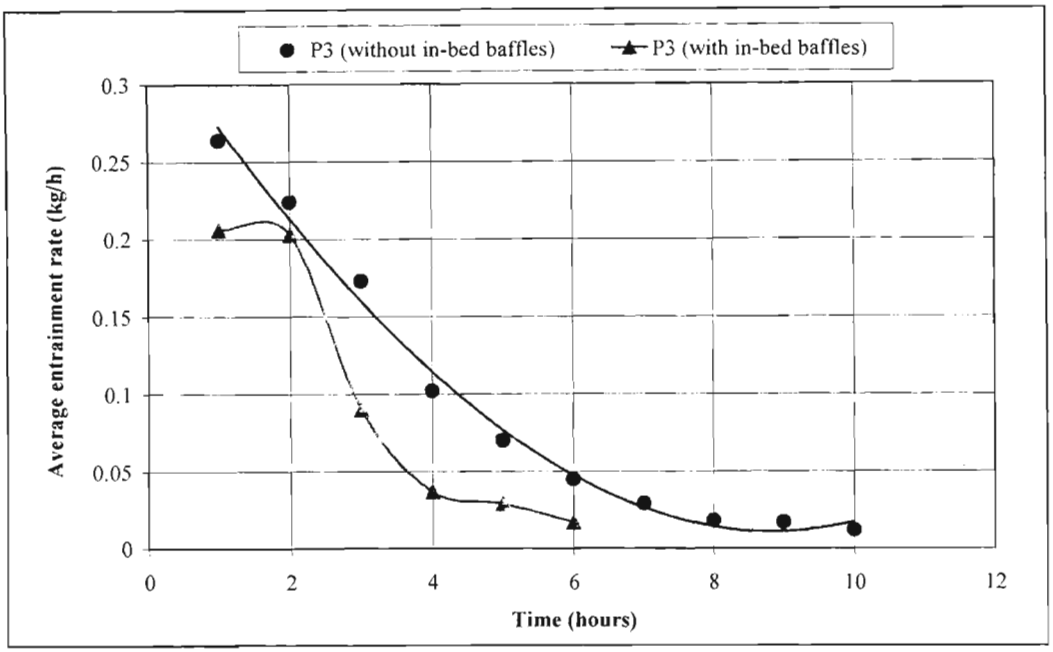

Figure 6-13: Comparison of the entrainment rate obtained with powder P3 with and without the use of in-bed baffles.

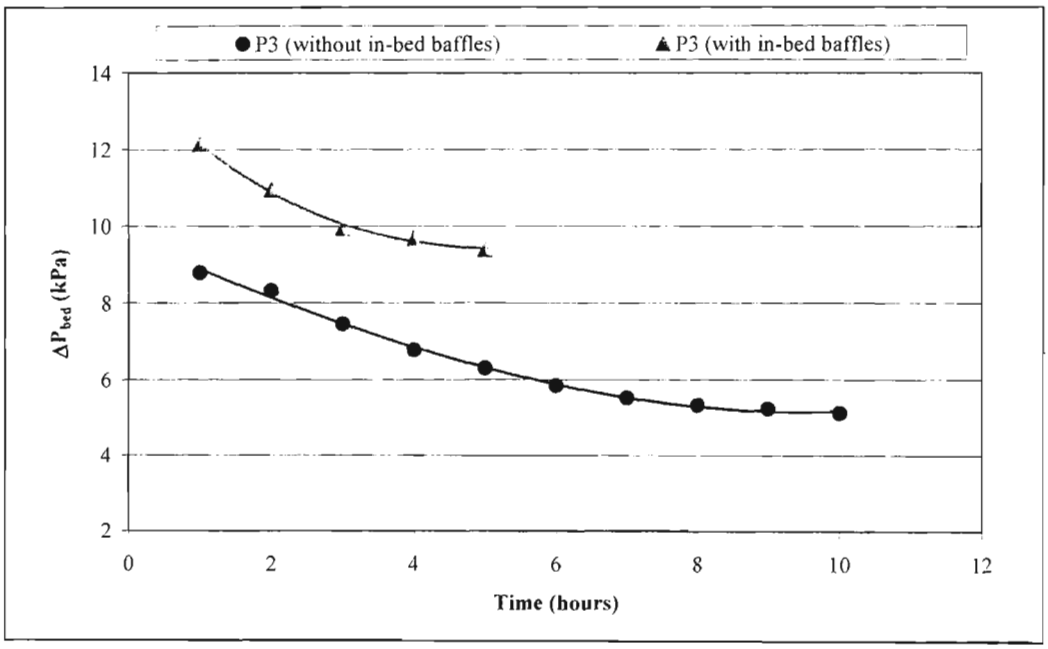

Figure 6-14: Comparison of the bed pressure drop of powder P3 with and without the use of in-bed baffles.

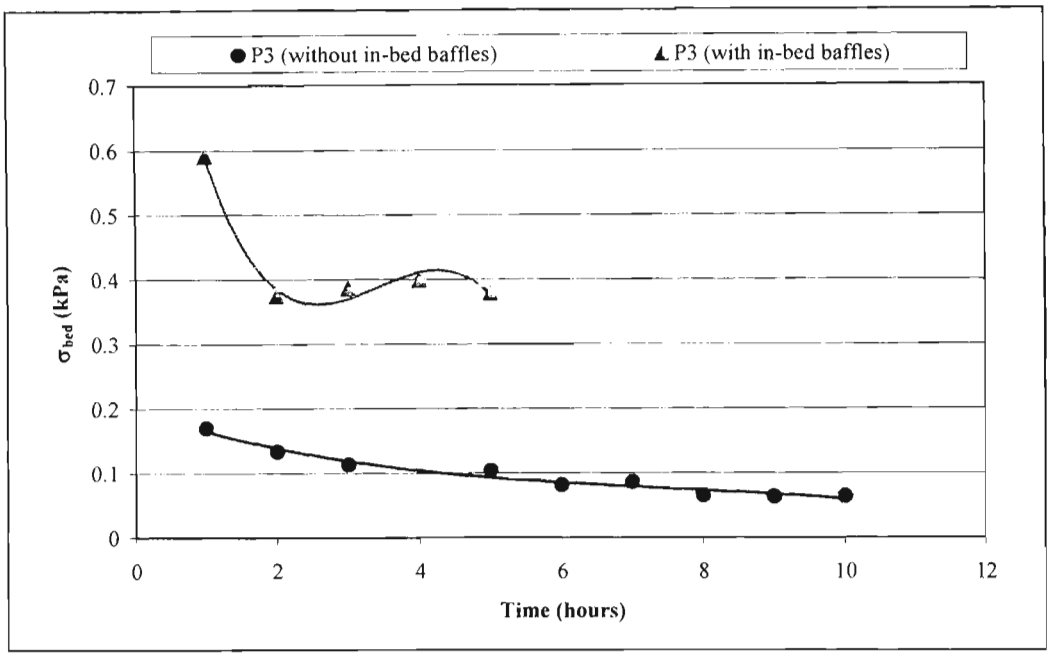

Figure 6-15: Comparison of the standard deviation of the bed pressure drop of powder P3 with and without the use of in-bed baffles.

6.1.7. Summary of test results

The following is a summary of the test results obtained from the 0.05 m column:

- The fluidization behaviour of powders in small diameter columns is strongly affected by the physical properties of the powder (particle density, size and shape).
- For powders having the same particle density and particle size distribution the particle shape determines the fluidization regime: bubbling regime for angular-shaped particles and slugging regime for spherically-shaped particles.
- The presence of fines improves the fluidization behaviour of angular shaped particles. Due to bubble splitting and a decrease in the maximum stable bubble size, the entrainment rate also decreases as the fines content is increased. This is not the case with spherical particles.
- The entrainment rate of spherical particles was found to be higher than that of angular shaped particles.
- The entrainment rate for spherical or rounded particles can be decreased by the use of in-bed baffles but the bed pressure drop and the standard deviation of the bed pressure drop fluctuations increase.

- The decrease in entrainment rate obtained by using in-bed baffles is not as significant as the decrease in entrainment rate obtained by changing the particle shape from spherical to angular. Angular shaped particles with fines present are therefore preferred for pilot scale operations where slugging is undesirable.

6.2. Results from the 0.14 m internal diameter column

6.2.1. Fluidization regime

The operating fluidization regime was observed visually and quantified through the standard deviation of the bed pressure drop fluctuations. These results are presented in Figure 6-16.

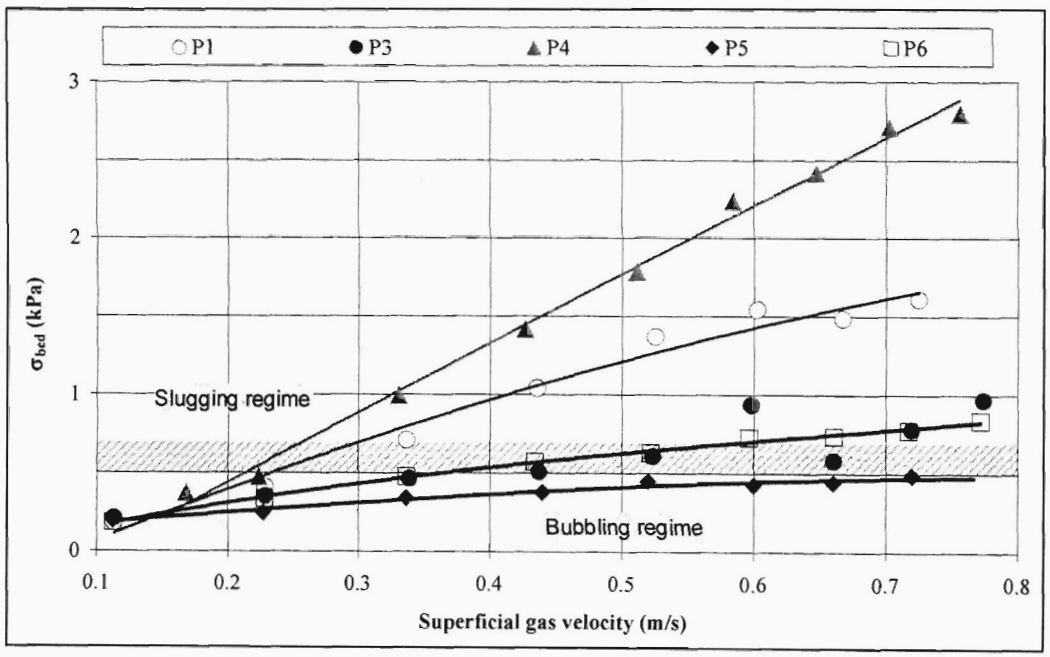

Figure 6-16: Standard deviation of bed pressure drop fluctuations for powders P1, P3, P4, P5 and P6.

The standard deviations of the bed pressure drop fluctuations presented above are based on a sampling frequency of 5 Hz for a period of two minutes. This was the maximum frequency at which the differential pressure transmitter could operate. In the literature it is reported that sampling frequencies much higher than 5 Hz have been used for capturing the bed differential pressure signals. For example, Chehbouni *et al.* (1994) used a sampling frequency of 90 Hz. In the current work it was found that a sampling frequency of 5 Hz was sufficient to compare between the fluidization regimes of the different powders tested. Based

on visual observations, it was found that when the standard deviation of the bed pressure drop fluctuations in the 0.14 m column exceeded about 0.5 to 0.7 kPa the bed operated in the slugging regime. Hence, two fluidization regimes, namely the bubbling and slugging regimes could be observed and these are shown in Figure 6-16. From this figure it can also be seen that at low superficial gas velocities (less than about 0.25 m/s) all the powders operated more or less in the bubbling fluidization regime. Thereafter, an increase in the superficial gas velocity causes a change in the fluidization regime, which is dependant on the powder properties. For example powder P3, P5 and P6 have relatively higher fines content than powders P1 and P4. Therefore, powders P1 and P4 started to enter the slugging regime much sooner than powders P3, P5 and P6. This is due to the fact that powders having low fines content tend to form larger bubbles as the superficial gas velocity is increased. It will be shown later how the bed voidage measurement also supports this observation. Based on the results presented in Figure 6-16 it can also be concluded that the coarser the average particle size distribution of the powder, the sooner the bed will start to slug (in small diameter columns) as the superficial gas velocity is increased.

In addition it will be noticed from Figure 6-16 that that the standard deviation of the bed pressure drop fluctuations did not reach a turning point for any of the powders over the superficial gas velocity range used in this work. Hence it was concluded that transition to the turbulent fluidization regime did not take place and that the fluidization regime remained in the bubbling regime (or slugging regime for some powders) for the velocity range investigated here.

These observations were compared with the criterion for slugging given by equation 2-43 by calculating the superficial velocity at which slugging occurs in a 0.14 m internal diameter column. Equation 2-27 was used for the calculation of U_{mf} and equations 2-45 and 2-46 were used to calculate the minimum bed height required for stable slugging and the maximum bed height below which the bed will be freely bubbling respectively. The velocity at which the fluidization regime changes from the bubbling to the turbulent regime (U_c) was calculated using the correlation given by equations 2-118.

The results of these calculations are summarised in Table 6-3. The results show that according to the Stewart and Davison criterion for slugging, the minimum velocity required for slugging in the 0.14 m internal diameter column varies between 0.084 to 0.094 m/s. This does not agree with the observations from this work since it was shown earlier that slugging only occurred with powders P1 and P4 above 0.25 m/s and with powders P3 and P6 above 0.6 m/s (refer to Figure 6-16).

Table 6-3: Results of literature correlations for slugging and transition from bubbling to turbulent regime

Powder	U_{ms} (m/s)	H_{ms} (m)	H_{fb} (m)	U_c eq. 2-118 (m/s)
P1	0.085	0.95	0.22	1.26
P2	0.084	0.95	0.22	1.11
P3	0.085	0.95	0.22	1.52
P4	0.094	0.95	0.22	1.98
P5	0.085	0.95	0.22	1.36
P6	0.084	0.95	0.22	1.49
P7	0.084	0.95	0.22	1.01

According to equations 2-45 and 2-46, the minimum bed height required for stable slugging and the maximum bed height below which the bed will be freely bubbling are independent of the powder properties. In the present work this was not found to be case since the powder properties did influence the fluidization regime (slugging or bubbling). Slugging was only observed for the coarse powders (eg. P1 and P4 above 0.25 m/s). Before these beds started to display slugging properties, bubbling fluidization was observed even with the fluidized bed height exceeding 0.22 m. With other powders (eg, P3 and P6) bubbling fluidization was observed at velocities below 0.6 m/s even though the fluidized bed height exceeded H_{ms} (0.95m) and H_{fb} (0.22 m) and with powder P5 no slugging was observed although the fluidized bed height exceeded H_{ms}. These results show that the criteria for slugging given by equations 2-43, 2-45 and 2-46 are not valid for the powders used in these tests.

As mentioned earlier, in this work the standard deviation of the bed pressure drop fluctuations did not reach a turning point in the gas velocity range investigated, which is indicative that transition from the bubbling to the turbulent regime did not take place. Further support of this is provided in Table 6-3, where it can be seen that for all powders equation 2-118 predicts that U_c (which varies between 1.01 and 1.98 m/s depending on the powder) is higher than the maximum velocity used in the current work (0.78 m/s). It was therefore concluded that the fluidization regime for all the powders tested in the 0.14 m column did not enter into the turbulent regime.

6.2.2. Bed collapse test results

The bed collapse test was used to measure the average dense phase voidage, bubble fraction and overall bed voidage as a function of superficial gas velocity. Powders P2, P3, P5, P6 and P7 were used for these tests. The detail experimental data and a sample calculation of the dense phase voidage, bubble fraction, overall bed voidage, bed density, bed height and bed expansion ratio are presented in Appendix C.

6.2.3. Dense phase voidage

The measured dense phase voidage as a function of superficial gas velocity for powders P2, P3, P5, P6 and P7 is shown in Figure 6-17.

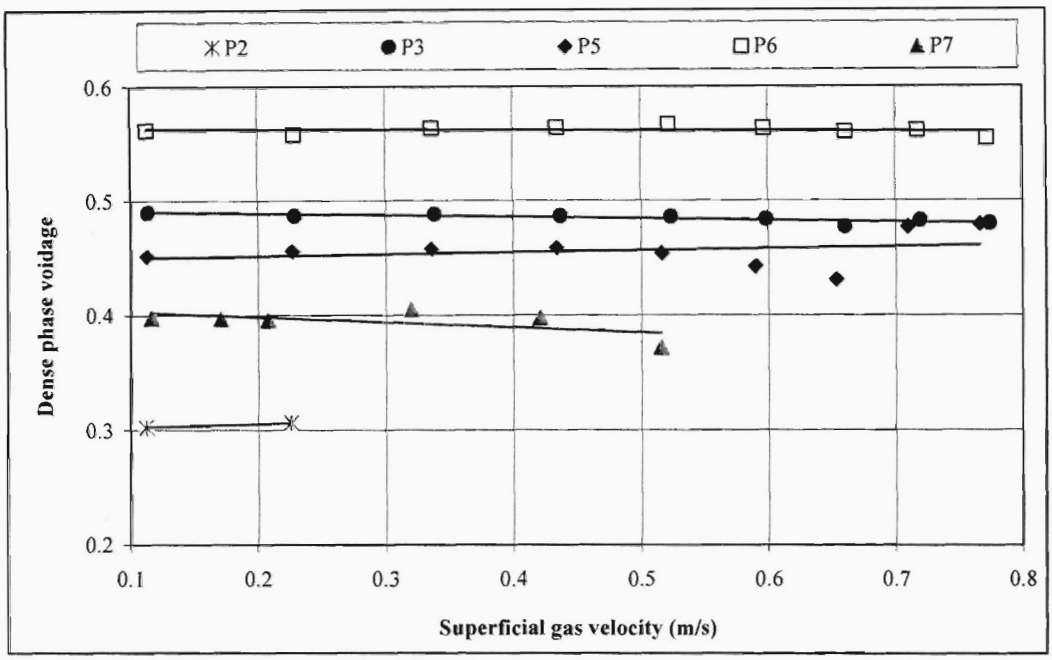

Figure 6-17: Dense phase voidage versus superficial gas velocity.

The above results indicate that the dense phase voidage is not a strong function of the superficial gas velocity. The data however suggests that the dense phase voidage is more dependent on the particle properties namely, density, size and shape. The effect of the concentration of fines (< 22 μm) is illustrated in Figure 6-18 and these results are in agreement with the findings of Dry (1982) and Rowe *et al.* (1978). The slight decrease in the dense phase voidage at higher gas velocities for some of the powders could therefore be the result of the loss of fines due to entrainment.

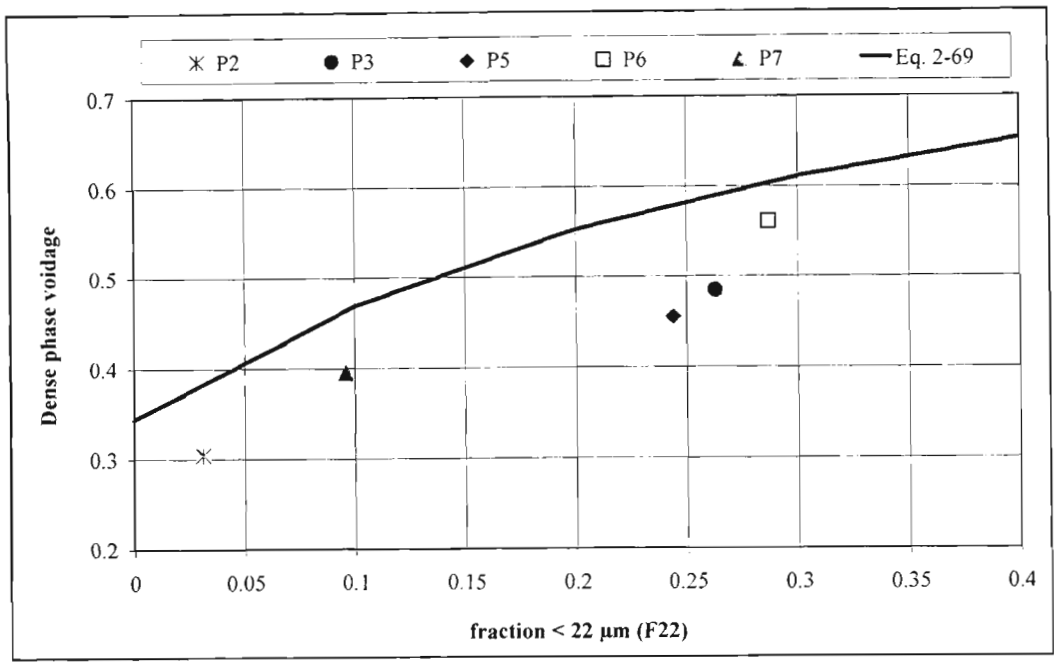

Figure 6-18: Dense phase voidage as a function of fines (< 22 µm) fraction.

It is clear from Figure 6-18 that the dense phase voidage is a strong function of the fines content (in this case the fraction less than 22 µm).

Also illustrated in Figure 6-18 is the fact that equation 2-69 tends to over-predict the results of this work. An attempt was made to correlate the dense phase voidage with fines fraction and the result was equation 6-1.

$$\varepsilon_d = 0.675\left(F_{22}\right)^{0.786} + 0.268 \qquad (6\text{-}1)$$

Equation 6-1 appears to fit the data slightly better than equation 2-69 as shown in Figure 6-19 and the error is within 10 % for all powders, as illustrated in Figure 6-20. In Figure 6-19 it can be seen that the measured dense phase voidage of powder P6 is significantly higher than the other powders and that this difference cannot be explained in terms of the difference in fines concentration. This is particularly noticeable if the dense phase voidage of powders P3 and P6 are compared since these powders differ mainly in particle shape. It is therefore proposed that the irregular or angular shape particles have a higher dense phase voidage when compared to more spherical particles having the same particle density and similar fines concentration. This observation is in agreement with Goosen (1988) who postulated that the more irregular the particle shape the higher the dense phase voidage.

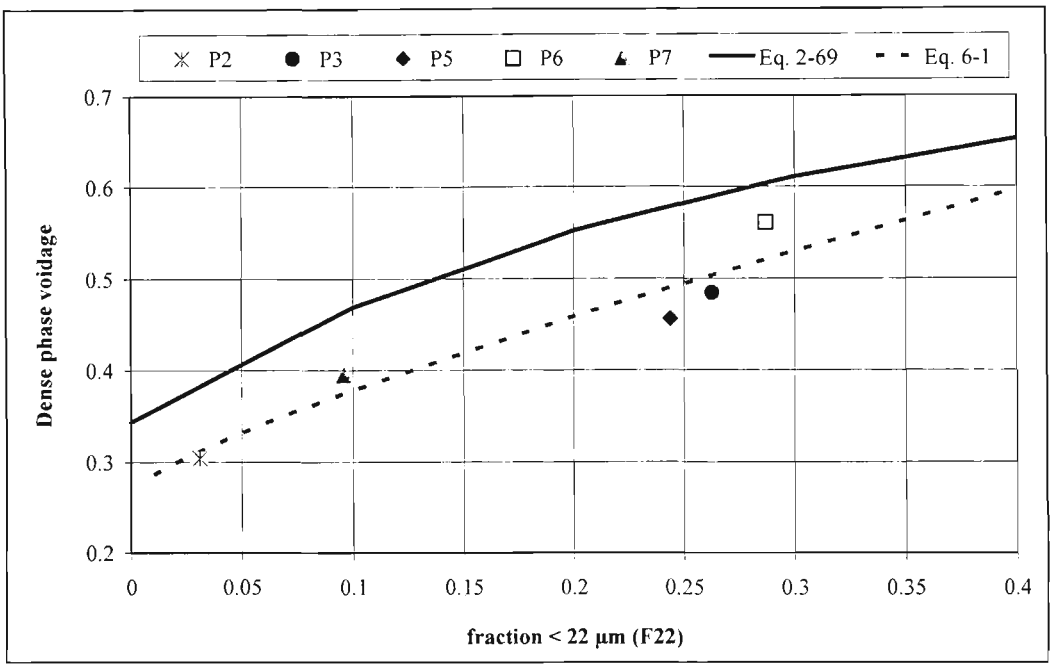

Figure 6-19: Dense phase voidage versus the fines fraction compared to equations 2-69 and 6-1.

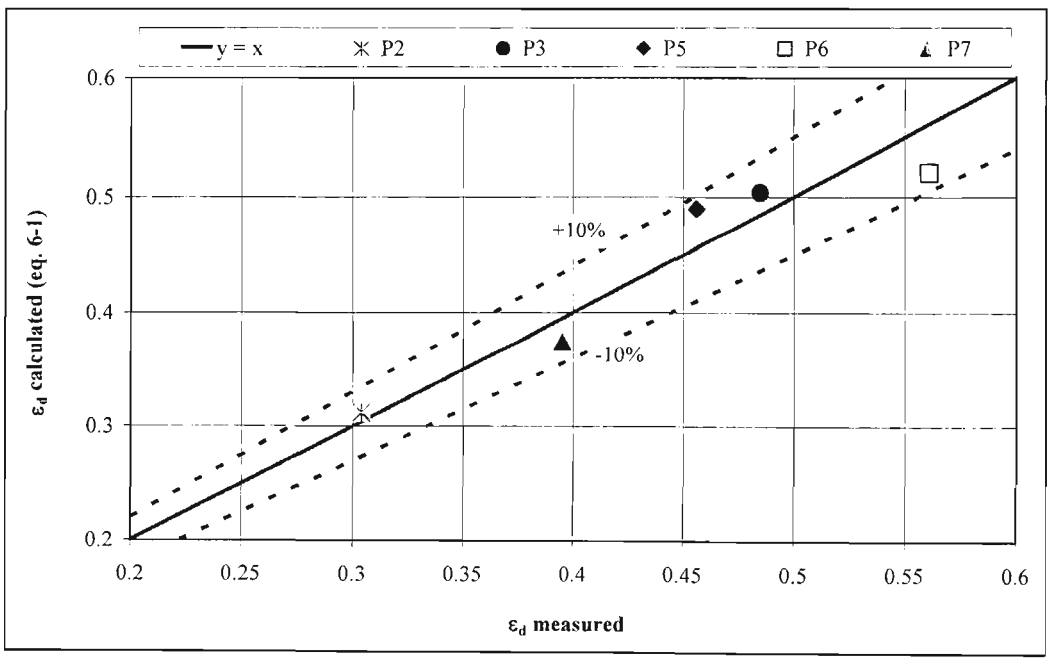

Figure 6-20: Calculated versus measured dense phase voidage using equation 6-1.

In summary it has been shown that the dense phase voidage increases with an increase in the fines fraction (< 22 μm) and remains fairly constant with an increase in the superficial gas velocity. In addition, the particle shape also affects the dense phase voidage in that the more spherical or rounded the particle shape, the lower the dense phase voidage.

6.2.4. Bubble fraction

The measured bubble fraction as a function of superficial gas velocity is shown in Figure 6-21. The bubble fraction was found to increase with an increase in superficial gas velocity. The bubble fraction was also found to increase with an increase in the average particle size. This finding is in agreement with both visual observations and the fluidization regime data presented earlier. In addition, a comparison of the bubble fraction data for powders P3 and P6 shows that the bubble fraction is higher the more spherical the particle shape.

When compared to the bubble fraction correlation of Dry (1982) (equation 2-98) there is generally a large scatter in the data, although it does provide a fairly good prediction for powder P3.

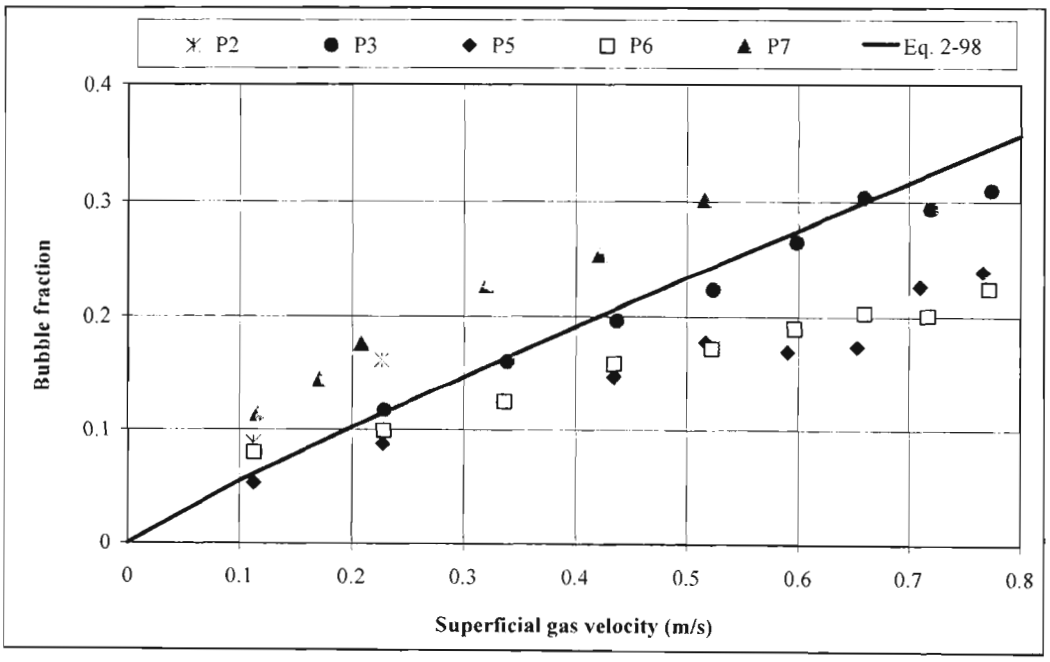

Figure 6-21: Bubble fraction versus superficial gas velocity in comparison to equation 2-98.

The Dry bubble fraction correlation tends to only predict the bubble fraction for powder P3 quite well. This indicates that other powder properties also influence the bubble fraction. An attempt was therefore made to correlate the experimental bubble fraction data with the particle density, average particle size (d_{sv}) and superficial gas velocity. The result is Equation 6-2 and the calculated versus measured bubble fraction is shown in Figure 6-22. The error on most of the data is within ± 30 %.

$$\varepsilon_b = 65295\left(\rho_p\right)^{0.20}\left(d_{sv}\right)^{1.31}\left(U\right)^{0.75} \qquad (6\text{-}2)$$

The scatter in the data and relatively large errors of the correlation can be attributed to the differences in particle shape (which is not a parameter in equation 6-2) and to some extent experimental error. The bed collapse technique for measuring bed voidages is not very accurate at high gas velocities due to high entrainment rates (and resulting loss of fines) and difficulties associated with determining the fluidized bed level.

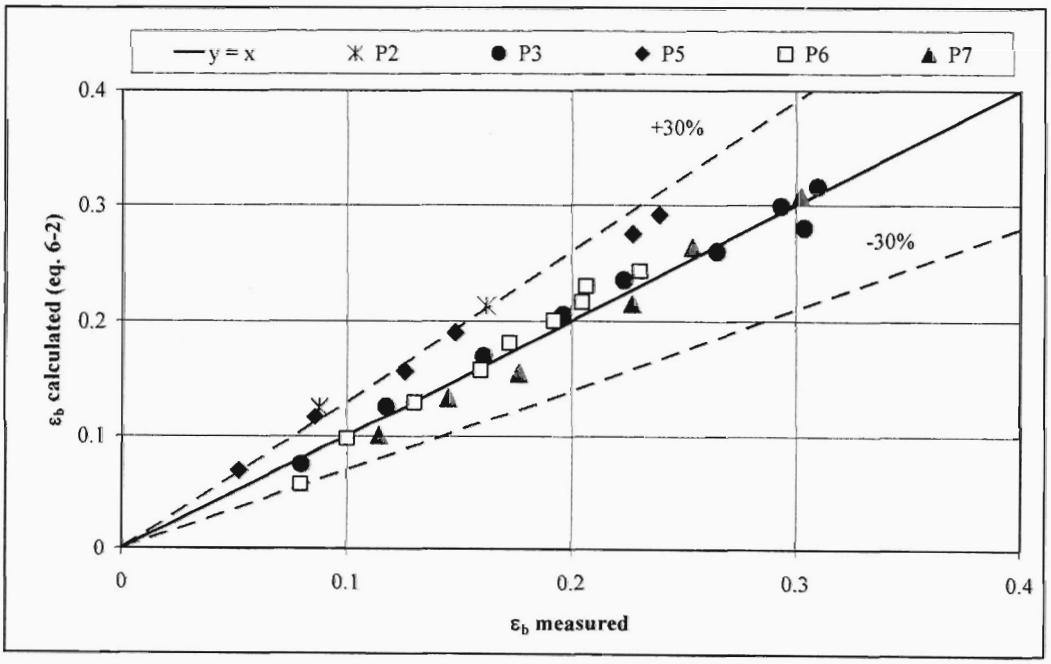

Figure 6-22: Calculated versus measured bubble fraction using equation 6-2.

In summary it the following parameters causes an increase in the bubble fraction:

- An increase in the superficial gas velocity (from Figure 6-21 and equation 6-2)
- An increase in the average particle size (inferred from equation 6-2)
- An increase in the particle density (inferred from equation 6-2)
- An increase in the particle sphericity (from Figure 6-21, comparing P3 and P6)

6.2.5. Overall bed voidage, bed density and bed expansion

The overall bed voidage was calculated from the dense phase voidage and bubble fraction. These results are presented in Figure 6-23. As expected the overall bed voidage increases with an increase in the superficial gas velocity. The overall bed voidage increases due to an increase the bubble fraction as described in the previous section.

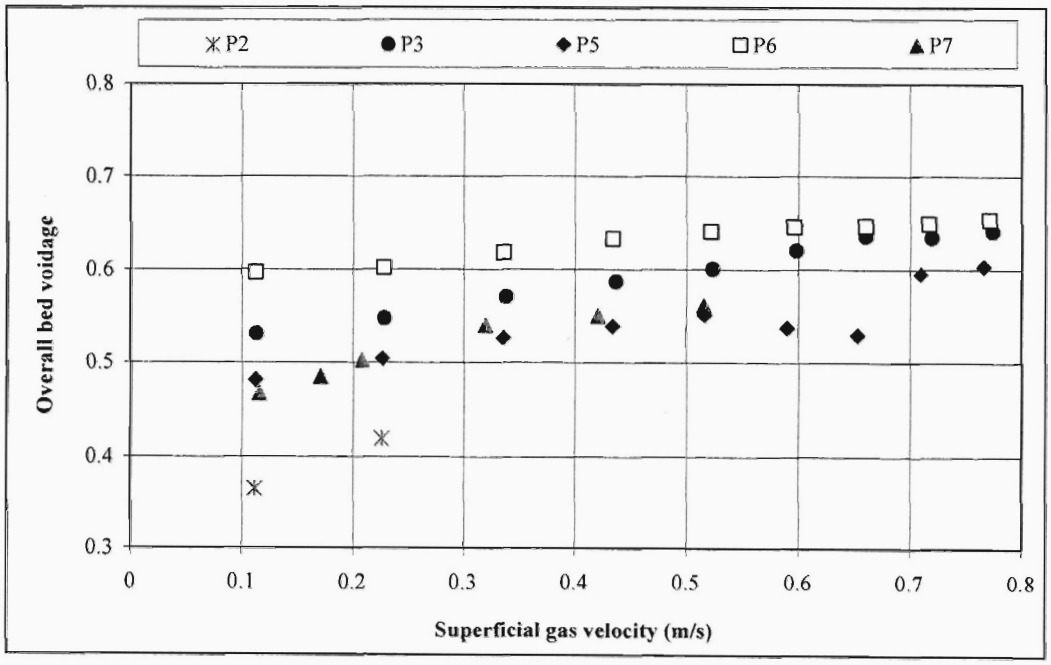

Figure 6-23: Overall bed voidage as a function of superficial gas velocity.

Figure 6-24 shows a graph of the average bed density versus superficial gas velocity. The average bed density was calculated using the particle density and the measured overall bed voidage. The bed density was unfortunately not measured due to malfunctioning of the differential pressure transmitter (ΔP_3 in Figure 4-2). Figure 6-25 provides a graph of the bed expansion ratio versus the superficial gas velocity.

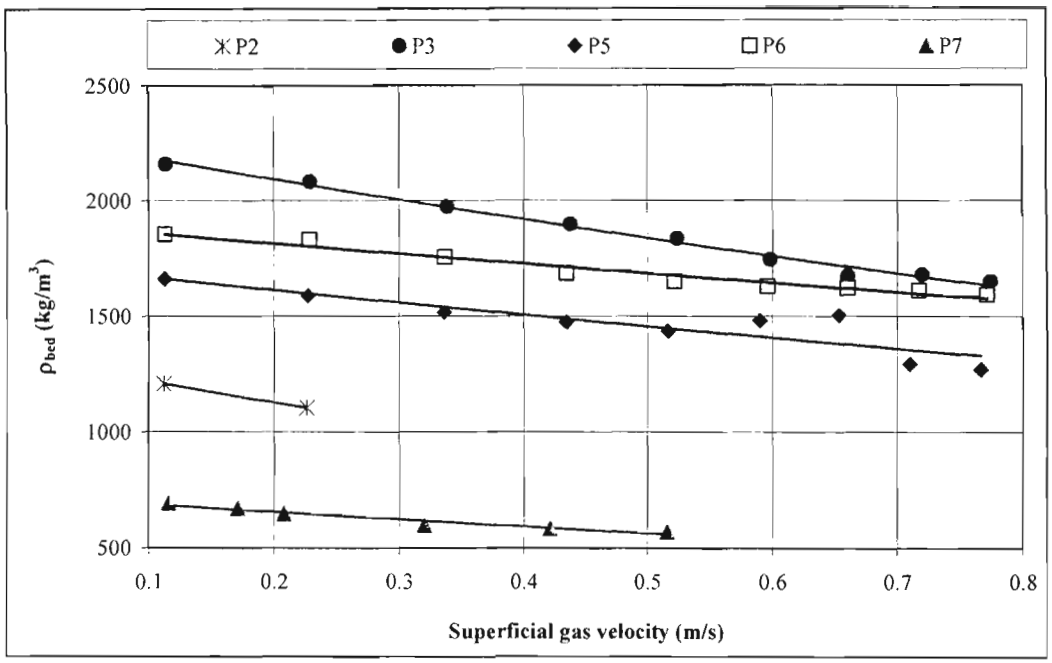

Figure 6-24: Average bed density as a function of superficial gas velocity.

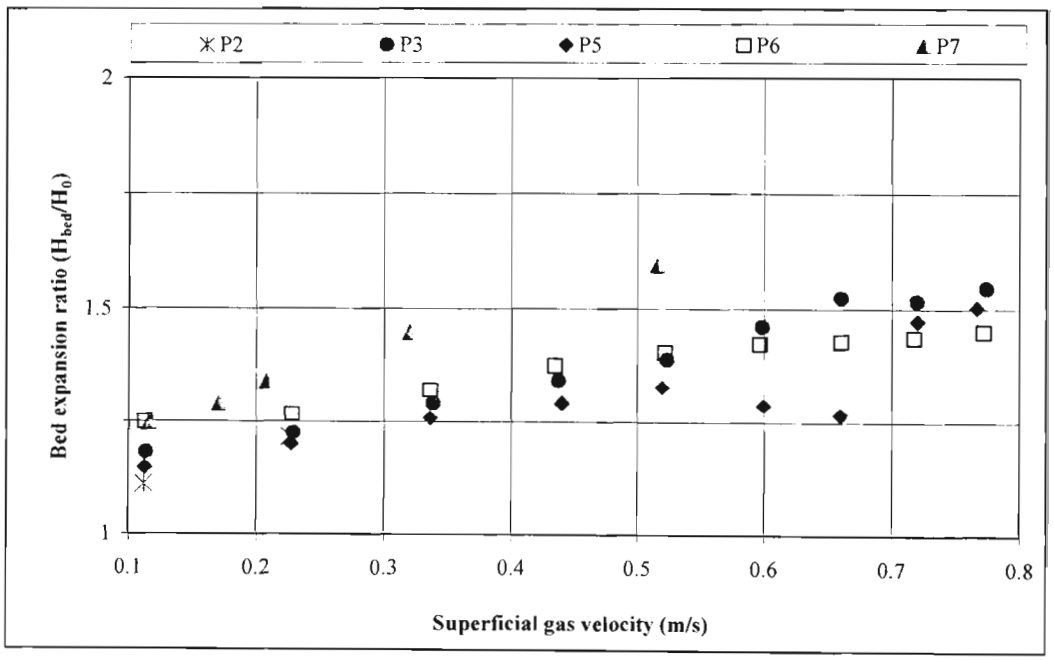

Figure 6-25: Average bed expansion ratio as a function of superficial gas velocity.

From Figure 6-25 it can be seen that the bed expansion ratio increases as the superficial gas velocity increases. This is expected due to the increase in the overall bed voidage and corresponding decrease in the average bed density. This information is very important when retrofitting an existing reactor with a new catalyst powder. If for example, the new powder has a lower particle density than the old powder, for the same bed expansion, less catalyst mass will be in the reactor and this could impact on the reactor conversion. These simple cold model hydrodynamic tests are therefore very useful especially for comparing the fluidization properties of different powders.

6.2.6. Entrainment

The entrainment rate of powders P1, P3, P4, P5 and P6 was measured as a function of the superficial gas velocity. The results are shown in Figure 6-26 and the reader is referred to Appendix D for tabulated entrainment values. The entrainment results reported in Figure 6-26 is believed to be above the Transport Disengagement Height (TDH). Figure 6-27 supports this, where it is shown that the available freeboard height (distance between the average fluidized bed height and the gas exit) for the different powders is above the TDH calculated using equation 2-132 and Figure 2-16. In Figure 2-16, the TDH is presented as a function of the excess gas velocity ($U - U_{mf}$). Since the calculated U_{mf} values for the powders tested here are so small, $U - U_{mf} \cong U$ and therefore the superficial gas velocity is used instead of the excess gas velocity.

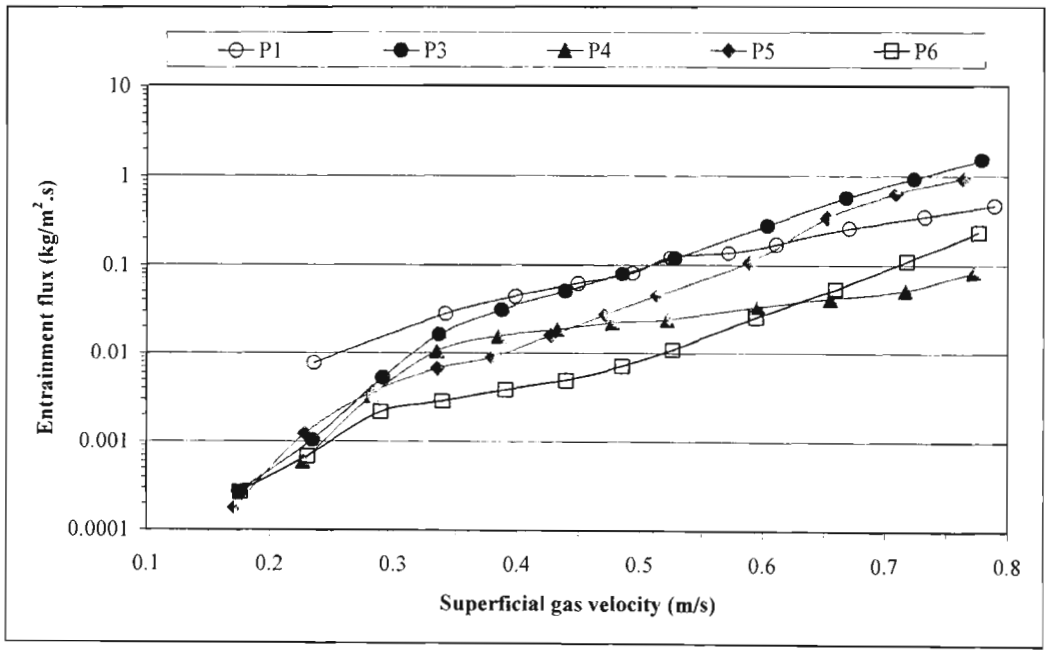

Figure 6-26: Measured entrainment flux as a function of superficial gas velocity.

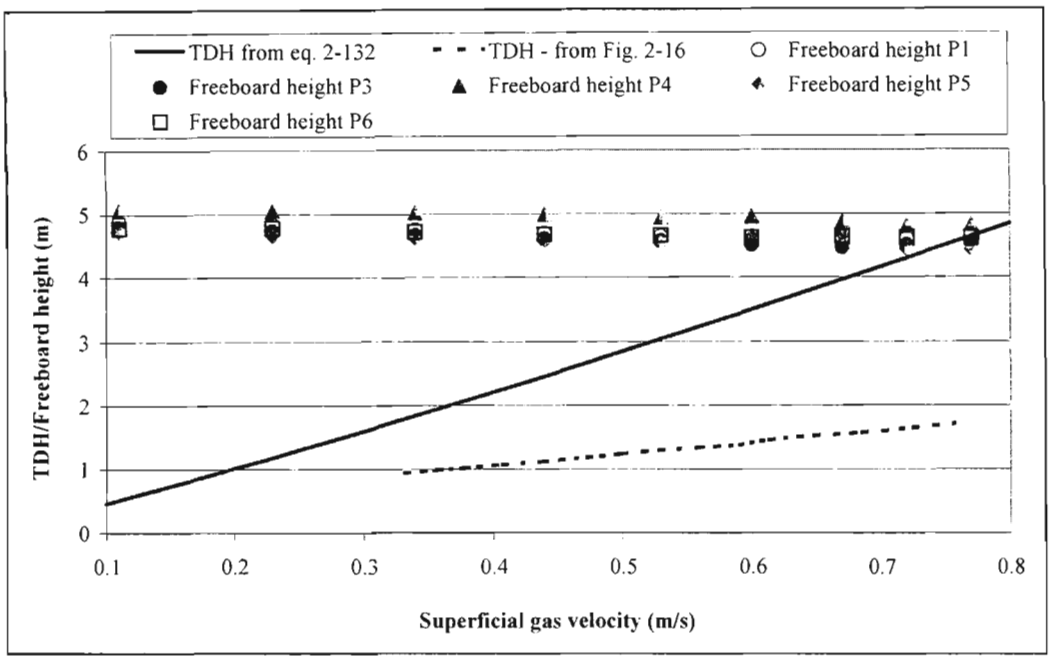

Figure 6-27: Comparison of available freeboard height with literature correlations for TDH.

It was found that at superficial gas velocities less than about 0.3 m/s, all the powders had a similar entrainment flux, except for powder P1, which had a higher entrainment rate than the other powders. At superficial gas velocities higher than 0.3 m/s, the entrainment flux of the powders was different. The differences could be related to differences in the powder physical properties as well as differences in the fluidized bed hydrodynamics or operating regime, which can be seen from a plot of the standard deviation of the bed pressure drop fluctuations, which is shown in Figure 6-16. The higher the standard deviation of the bed pressure drop fluctuations, the more the bed operated in the slugging regime and slugging was observed to occur when the standard deviation of the bed pressure drop fluctuations exceeded about 0.5 to 0.7 kPa. This boundary between the bubbling and slugging regime is indicated as the hatched region in Figure 6-16.

6.2.6.1. Effect of particle shape

In order to determine the effect of the powder physical properties on the entrainment rate it is important to ensure that the operating fluidization regimes are similar. From the above results only powder P3 and P6 have similar fluidization regimes over the velocity range tested and these powders have similar particle size distribution and particle density. The only significant difference between these two powders is their shape. As was shown in section 3.1, powder P6 is more angular in shape than powder P3. The measured entrainment flux of

these powders is shown in Figure 6-28 for better clarity. It can be clearly seen that the entrainment flux of powder P6 is lower than that of powder P3. Since it has been shown that the only significant difference between these two powders is the particle shape it can be concluded that the more spherical the particle shape, the higher the entrainment rate. This conclusion is in agreement with the conclusion made from the tests carried out in the 0.05 m internal diameter column. However, in the 0.05 m diameter column there was clearly also a difference in the fluidization regime between these two powders. In the 0.14 m column it was shown above that the fluidization regime is quite similar, hence the difference observed in the entrainment rate is purely due to differences in particle shape.

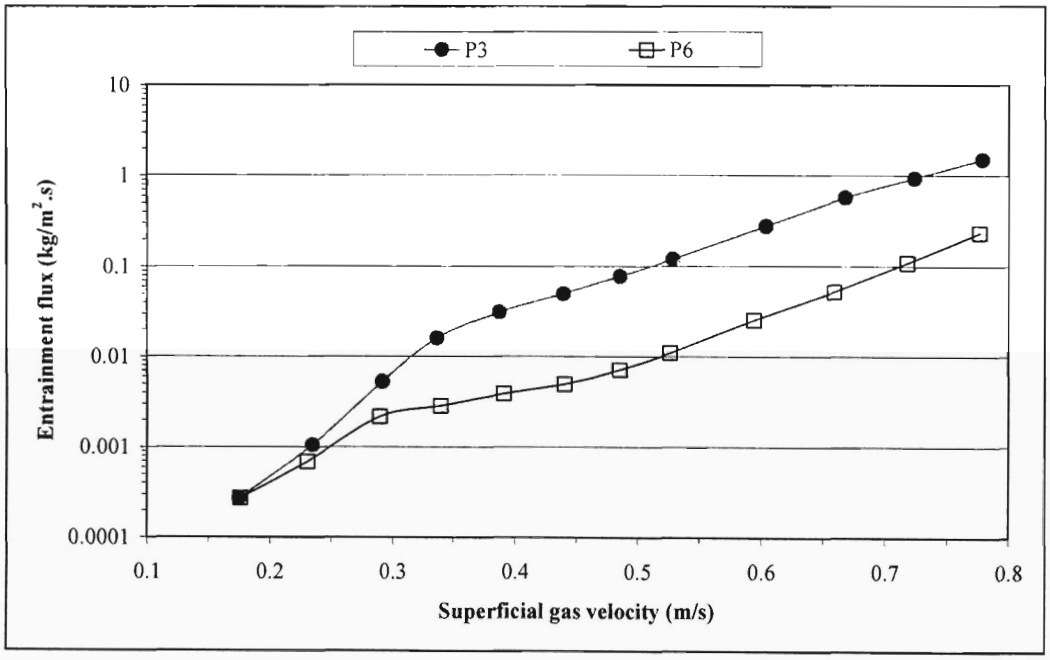

Figure 6-28: Comparison of the measured entrainment flux of powders P3 (spherical) and P6 (angular).

The literature does not provide any direct information on the effect of particle shape on the entrainment rate, however, from this study, it is clear that the particle shape has a significant effect on the entrainment rate; the more spherical the particle shape the higher the entrainment rate. One possible explanation is in terms of particle-cluster formation or particle clumping which is a result of inter-particle forces. It is proposed that angular shaped particles experience higher inter-particle forces and can interlock and form particle clusters much easier than spherically shaped particles. Particle cluster formation with angular shaped particles therefore results in larger and stronger particle clusters that have a higher terminal settling velocity than those of equivalent spherically shaped particles. This could then explain why angular shaped particles have a lower entrainment rate than more spherically shaped particles. The reason provided here to explain the observed differences in

entrainment rate between spherical and angular shaped particles is merely a hypothesis since no experimental work was carried out to prove that particle cluster formation is more pronounced for angular shaped particles. To prove the hypotheses proposed above more detailed and sophisticated experimental work needs to be carried out to, for example, measure the size of particle clusters or clumps that are formed in the freeboard and to determine how the size of these clumps changes with particle shape. This is envisaged not to be a trivial exercise and is therefore proposed as a future research area.

Another possible (more likely) explanation for the difference in entrainment rate between angular and spherical/rounded particles was given in section 6.1.2. It is possible that both explanations play a role but most of the evidence from the 0.05m column results suggests that the bed behaviour rather than a freeboard phenomenon is controlling the entrainment rate.

6.2.6.2. Effect of particle size

The effect of particle size on the entrainment rate is largely as expected in that the larger the average particle size the lower the entrainment rate. This is expected since the particle terminal velocity increases as the particle size increases. The effect of particle size on the entrainment rate was obtained by comparing the entrainment rate of powders P3 and P4 since these two powders differ mainly in the particle size distribution. A comparison of the entrainment rate of these two powders is shown in Figure 6-29.

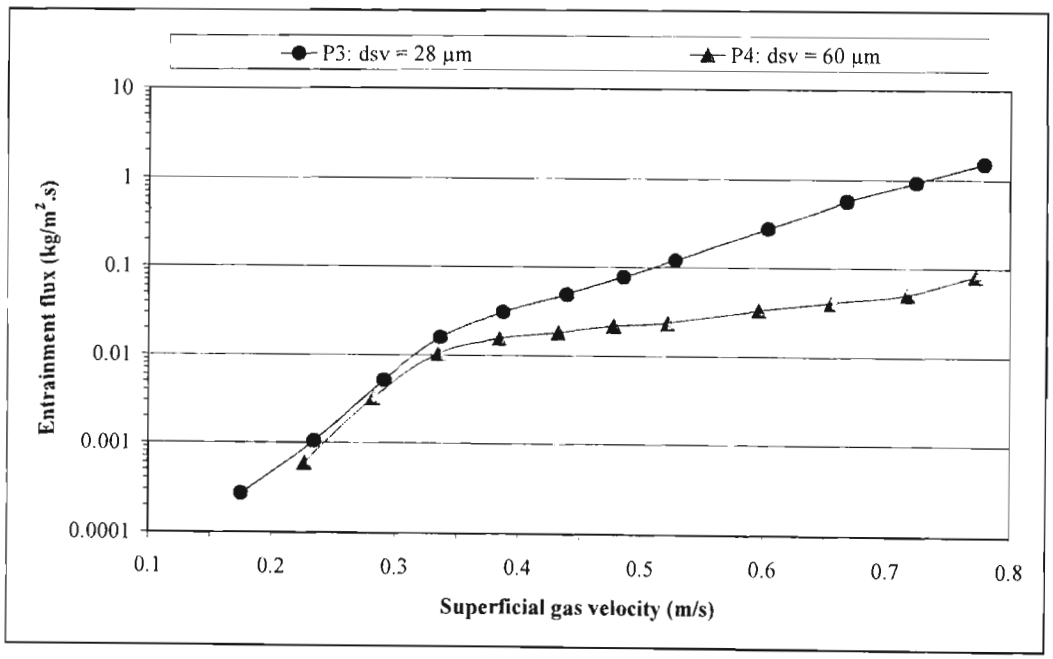

Figure 6-29: The effect of particle size on the entrainment flux.

6.2.6.3. Effect of superficial gas velocity

The dependence of the entrainment flux on the superficial gas velocity was found to vary depending on the powder properties. In general, it was found that the entrainment flux could be correlated using equations 6-3 and 6-4 depending on whether the gas flow profile in the freeboard was laminar (Re < 3000) or turbulent (Re > 3000). The values of the coefficients and exponent in equations 6-3 and 6-4 as obtained from the results of this work are summarised in Table 6-4. These results are in general agreement with the work of Tasirin and Geldart (1998) who also found that the gas flow regime in the freeboard influenced the relationship between the entrainment flux and the superficial gas velocity for FCC catalyst. However, their results could be correlated by equation 6-3 in both the laminar and turbulent gas-flow regimes, with the value of r being lower in the turbulent regime.

$$\text{For Re} < 3000: E_\infty = K_1 U^r \qquad (6\text{-}3)$$

$$\text{For Re} > 3000: E_\infty = K_2 \exp(mU) \qquad (6\text{-}4)$$

Table 6-4: Values obtained for the parameters in equations 6-3 and 6-4.

Powder	*Re < 3000*		*Re > 3000*	
	K_1	r	K_2	m
P1	No data		4.19×10^{-3}	6.07
P3	12.46	6.26	5.79×10^{-4}	10.20
P4	34.79	7.38	3.15×10^{-3}	4.02
P5	3.00	5.43	7.11×10^{-5}	12.65
P6	0.19	3.78	3.94×10^{-5}	11.01

6.2.6.4. Effect of column diameter

By comparing the initial entrainment rate obtained from the 0.05 m column to the entrainment rate obtained from the 0.14 m column at a superficial gas velocity of 0.38 m/s the effect of column diameter on the entrainment rate can be seen. Since only powders P3, P5 and P6 were used for the tests in both columns, only the results of these powders can be used to see the effect of column internal diameter on the entrainment rate. These results are shown in Table 6-5.

Table 6-5: Comparison of entrainment data obtained from the 0.05 m and 0.14 m columns for powders P3, P5, P6 at U = 0.38 m/s.

Powder	Entrainment flux (kg/m^2.s)		Entrainment rate (kg/h)	
	D = 0.05 m	D = 0.14 m	D = 0.05 m	D = 0.14 m
P3	0.0373	0.0309	0.264	1.710
P5	0.0243	0.0089	0.172	0.494
P6	0.0059	0.0039	0.042	0.214

Since data for only two column diameters are presented, no definite conclusions can be drawn from the above data. However, it appears that the entrainment flux decreased and the entrainment rate increased when the column diameter was increased from 0.05 m to 0.14 m. This is in agreement with the results of Tasarin and Geldart (1998) who found that for FCC catalyst, the entrainment flux decreased and the entrainment rate increased when the column diameter was changed from 0.076 m to 0.152 m. The reason given for this was that the gas flow profile was different in the two columns.

6.2.6.5. Comparison with correlations

In order to determine the predictive capabilities of published entrainment correlations the measured entrainment flux of powders P1. P3, P4, P5 and P6 were compared to the calculated entrainment flux using literature correlations. The literature correlations used for this exercise were presented earlier in section 2.3.7.12 (equations 2-137 to 2-151) and sample calculations are provided in Appendix E. The results of this comparison are shown in Figures 6-30 to 6-34. For these calculations the terminal velocity was calculated using equation 2-120 and drag coefficients were calculated using equations 2-123 to 2-125. However these equations were developed based on spherical particles. To analyse the sensitivity of the results to particle shape effects, the entrainment calculations were also carried out using equation 2-127 for the calculation of the drag coefficient. Table 6-6 shows a representative set of results, which was calculated for powder P6, using equation 2-150.

The results indicate that the calculated entrainment flux is quite sensitive to the drag coefficient used for the calculation of the particle terminal velocity. However, the higher the sphericity the worse off is the calculated entrainment rate when compared to the measured data. It is also interesting to note that the entrainment correlation when combined with equation 2-127 predicts that the lower the sphericity the higher the entrainment rate, which is contrary to the results, obtained in this study (compare Table 6-6 with Figure 6-28).

Table 6-6: The effect of particle sphericity on the calculated entrainment flux of powder P6.

U (m/s)	Experimentally measured entrainment flux of powder P6 ($kg/m^2.s$)	Calculated entrainment flux of powder P6 based on C_D being calculated using equations 2-123 to 2-125 ($kg/m^2.s$)	Calculated entrainment flux of powder P6 based on C_D being calculated using equation 2-127 with $\Phi = 1$ ($kg/m^2.s$)	Calculated entrainment flux of powder P6 based on C_D being calculated using equation 2-127 with $\Phi = 0.7$ ($kg/m^2.s$)	Calculated entrainment flux of powder P6 based on C_D being calculated using equation 2-127 with $\Phi = 0.5$ ($kg/m^2.s$)
0.18	0.000271	0.0189	0.0191	0.0208	0.0248
0.23	0.000686	0.0449	0.0453	0.050	0.0597
0.29	0.00217	0.0932	0.0942	0.105	0.125
0.34	0.00285	0.156	0.158	0.176	0.211
0.39	0.00386	0.149	0.150	0.169	0.202
0.44	0.00491	0.216	0.218	0.246	0.295
0.49	0.00708	0.295	0.297	0.336	0.403
0.53	0.0110	0.380	0.383	0.435	0.521
0.59	0.0253	0.560	0.563	0.642	0.769
0.66	0.0526	0.772	0.776	0.888	1.061
0.72	0.110	1.007	1.011	1.159	1.383
0.78	0.235	1.279	1.283	1.473	1.756

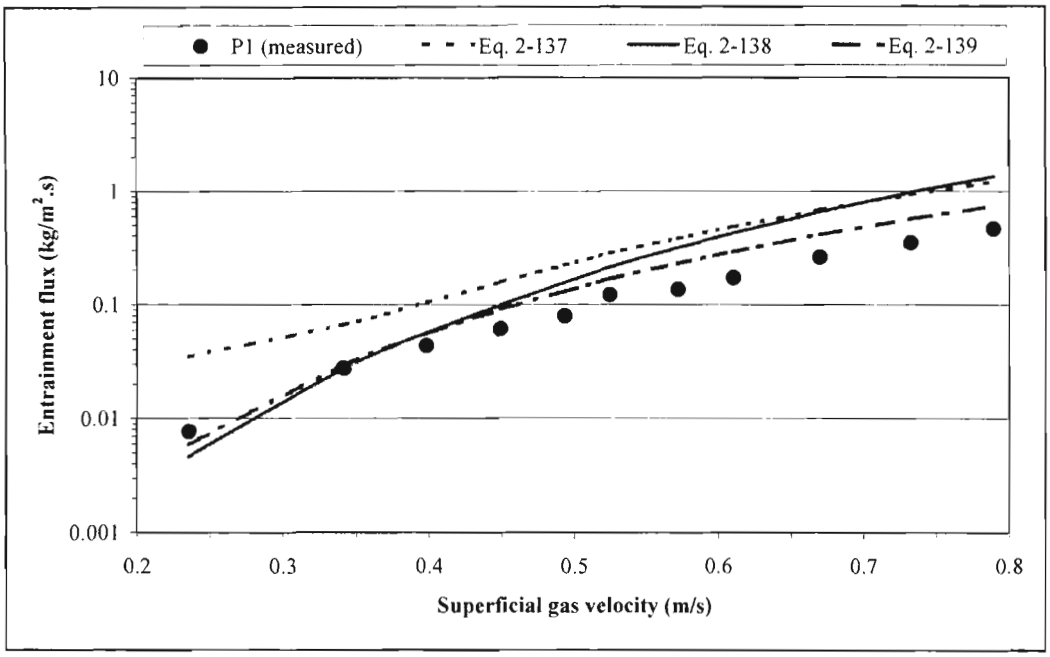

Figure 6-30(a): Comparison of measured and calculated entrainment flux for powder P1 using equations 2-137 to 2-139.

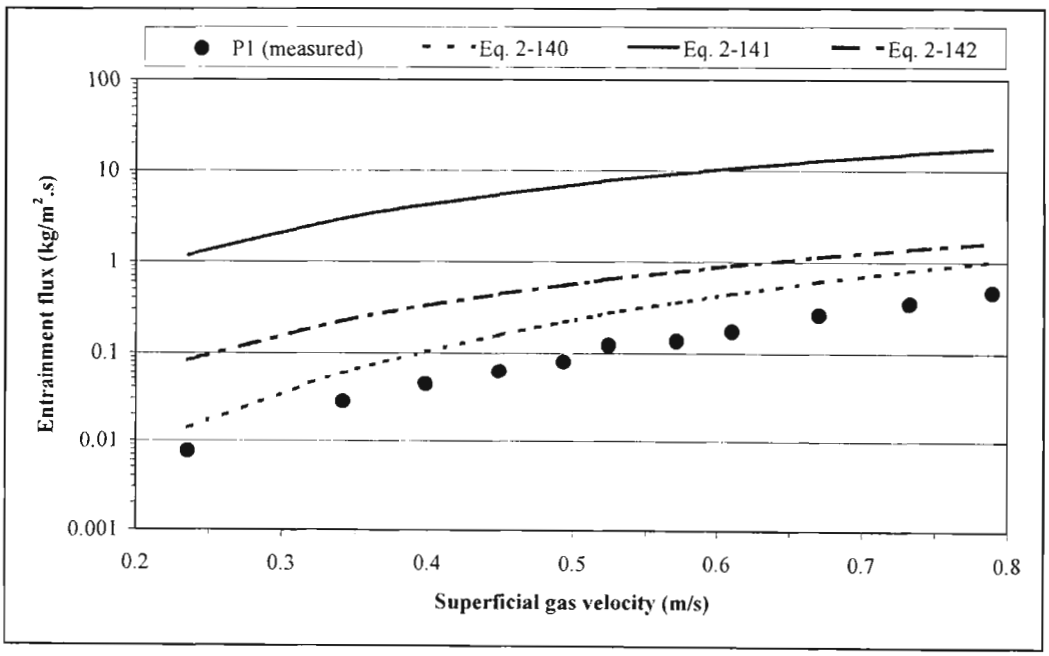

Figure 6-30(b): Comparison of measured and calculated entrainment flux for powder P1 using equations 2-140 to 2-142.

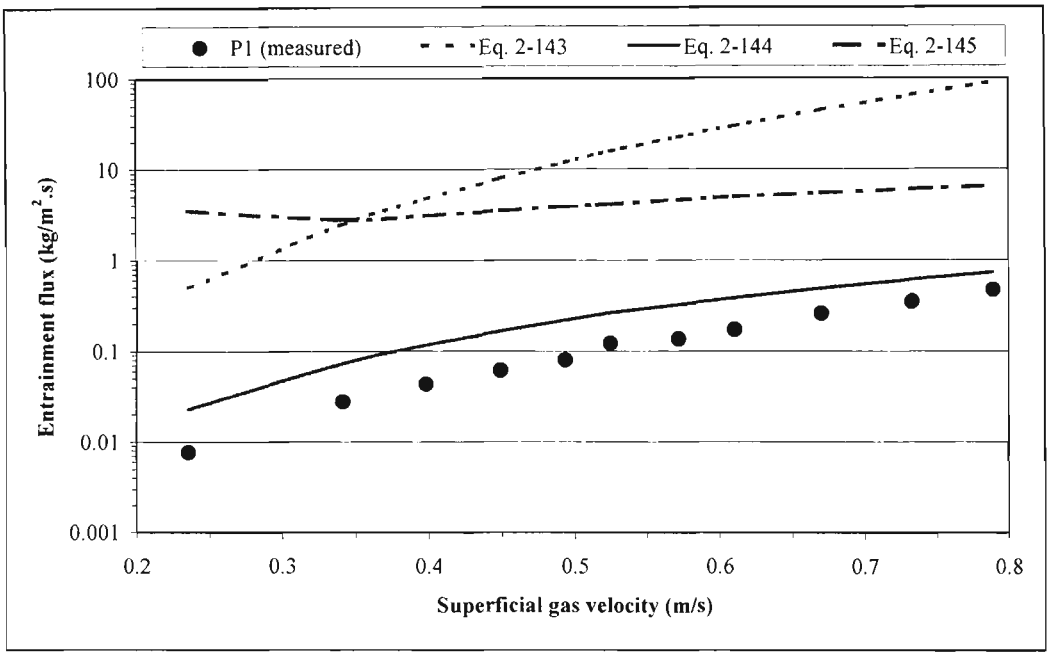

Figure 6-30(c): Comparison of measured and calculated entrainment flux for powder P1 using equations 2-143 to 2-145.

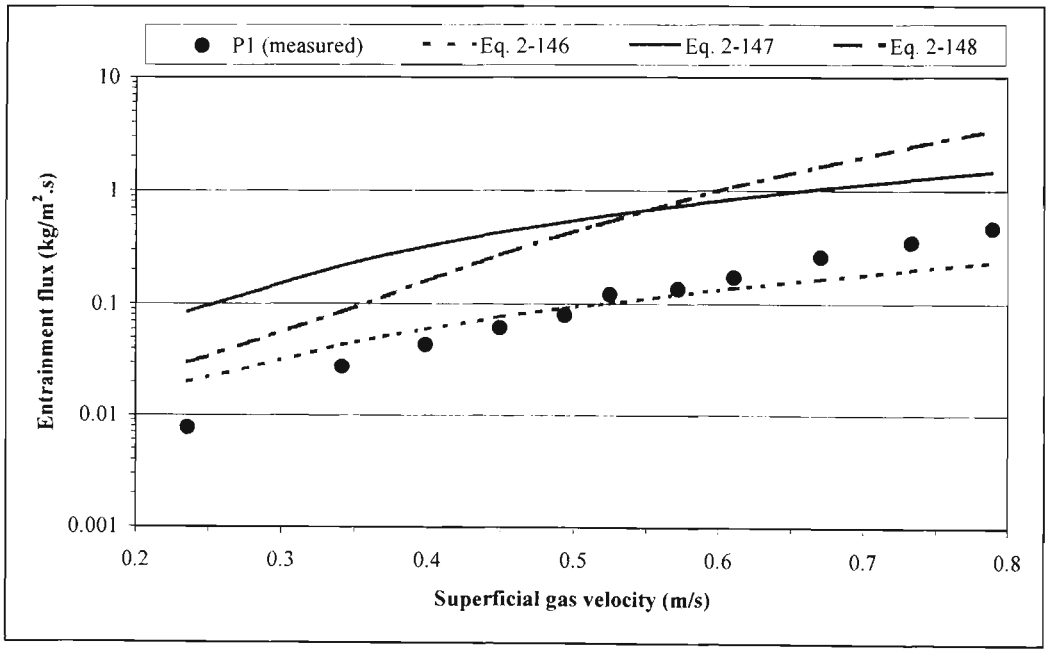

Figure 6-30(d): Comparison of measured and calculated entrainment flux for powder P1 using equations 2-146 to 2-148.

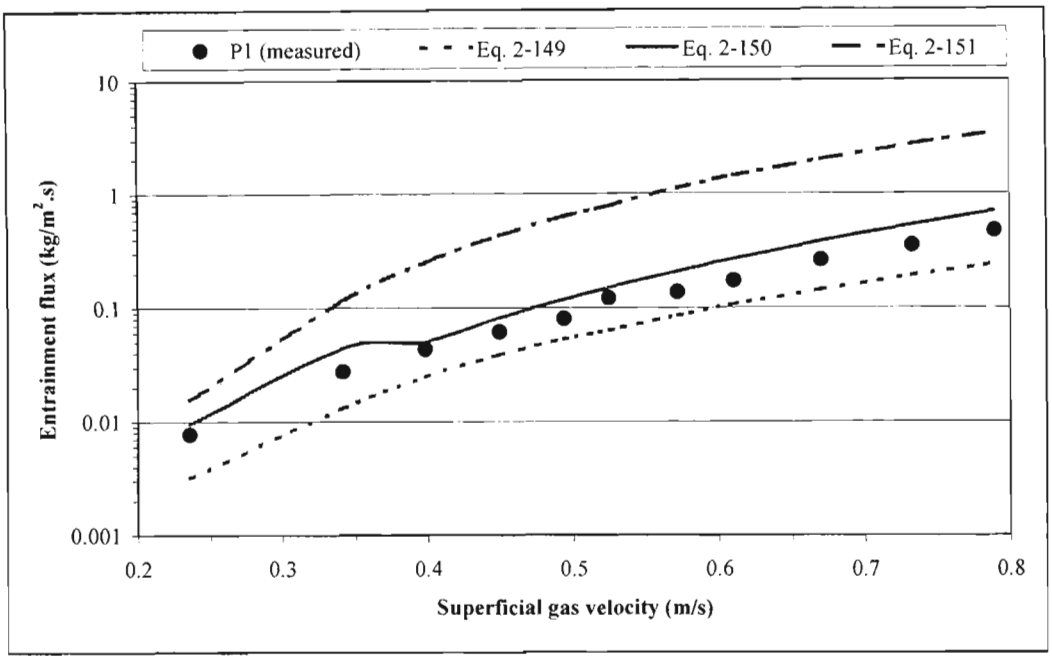

Figure 6-30(e): Comparison of measured and calculated entrainment flux for powder P1 using equations 2-149 to 2-151.

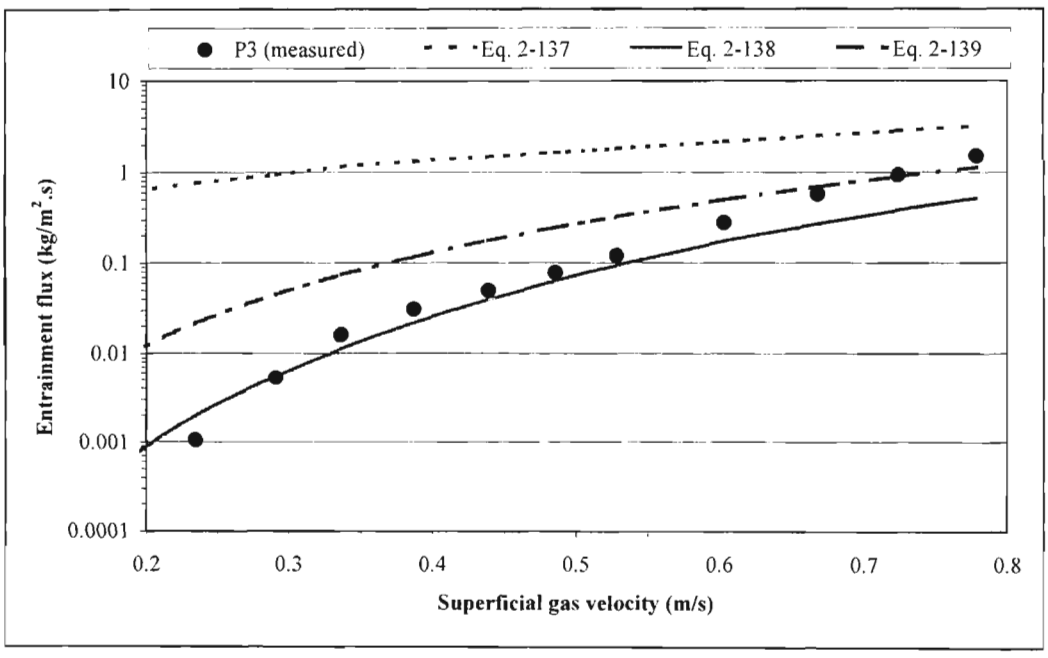

Figure 6-31(a): Comparison of measured and calculated entrainment flux for powder P3 using equations 2-137 to 2-139.

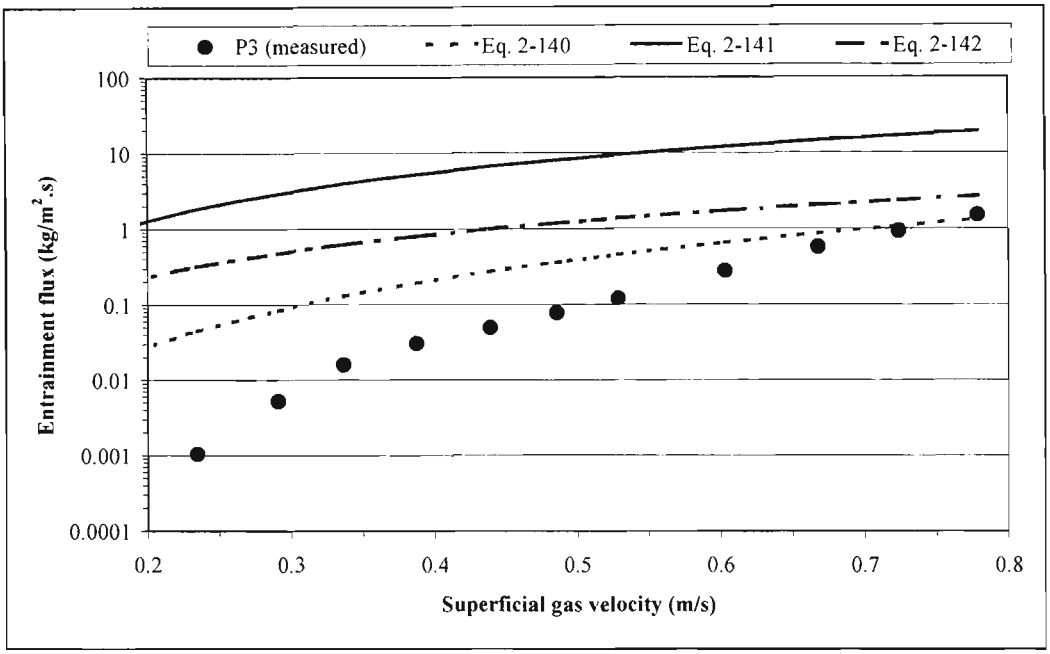

Figure 6-31(b): Comparison of measured and calculated entrainment flux for powder P3 using equations 2-140 to 2-142.

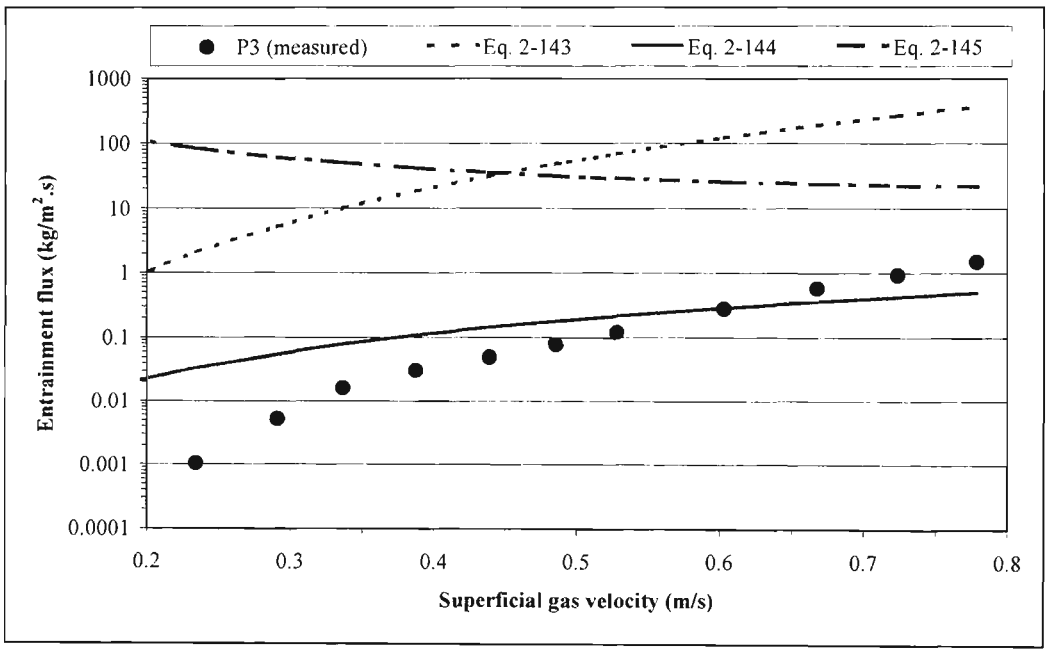

Figure 6-31(c): Comparison of measured and calculated entrainment flux for powder P3 using equations 2-143 to 2-145.

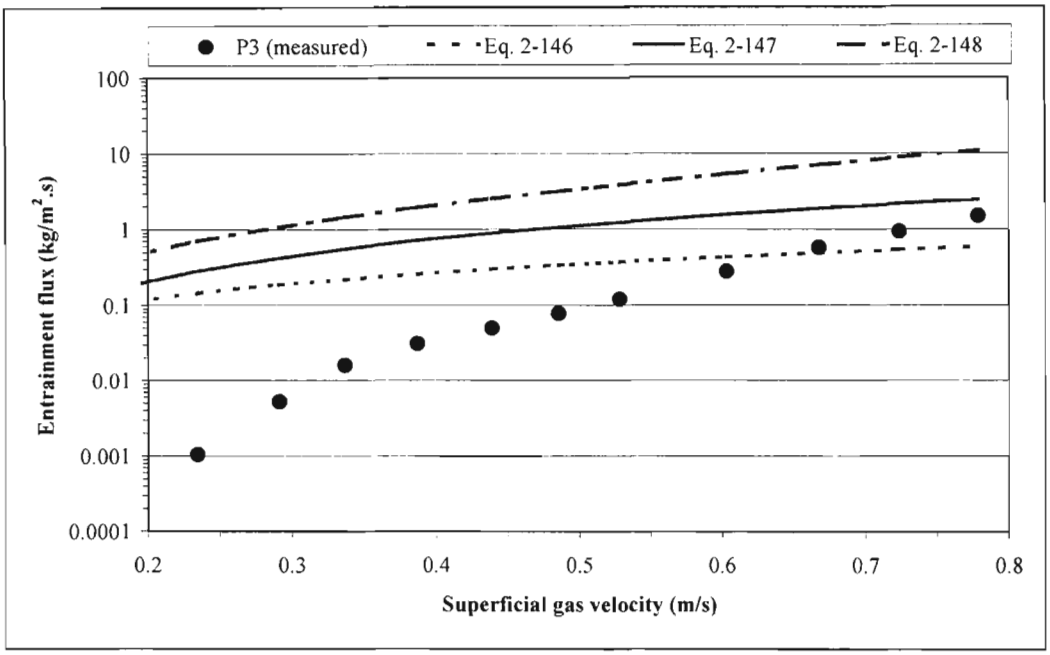

Figure 6-31(d): Comparison of measured and calculated entrainment flux for powder P3 using equations 2-146 to 2-148.

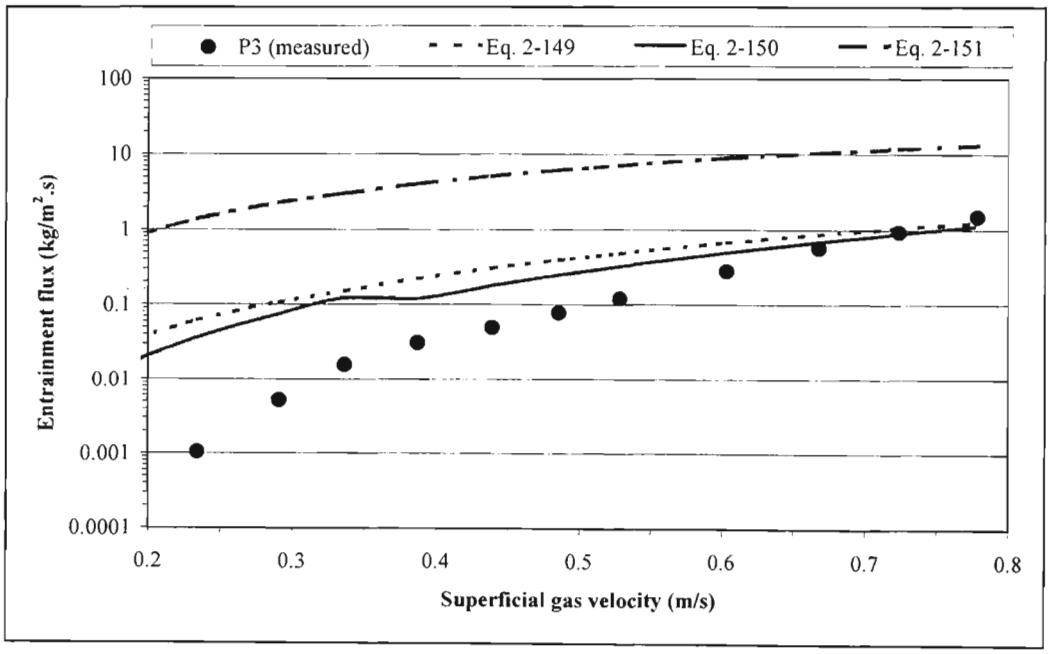

Figure 6-31(e): Comparison of measured and calculated entrainment flux for powder P3 using equations 2-149 to 2-151.

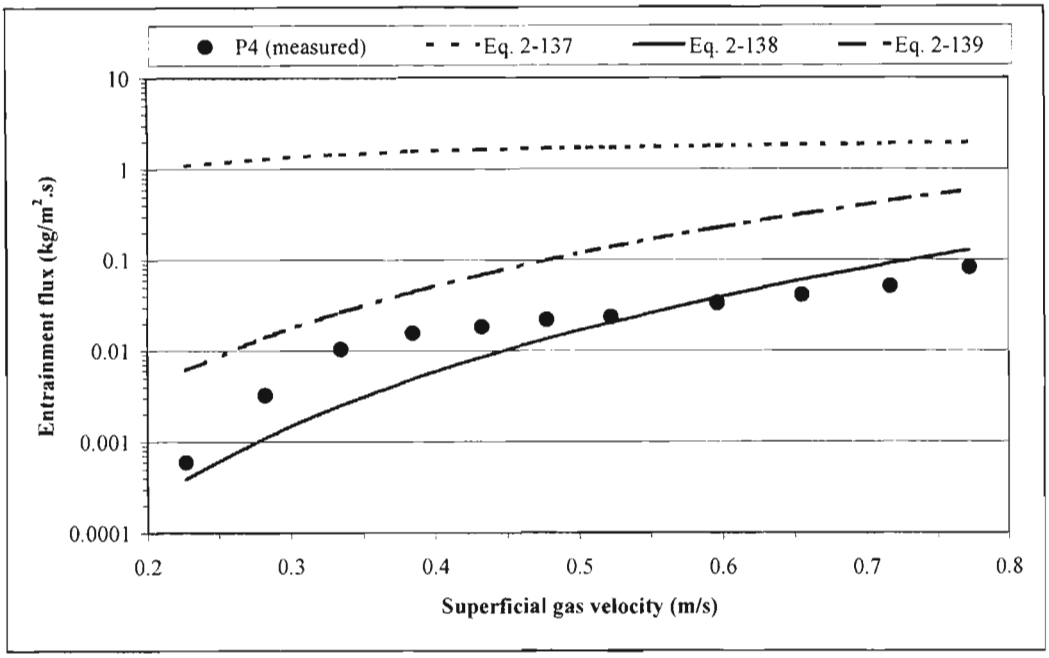

Figure 6-32(a): Comparison of measured and calculated entrainment flux for powder P4 using equations 2-137 to 2-139.

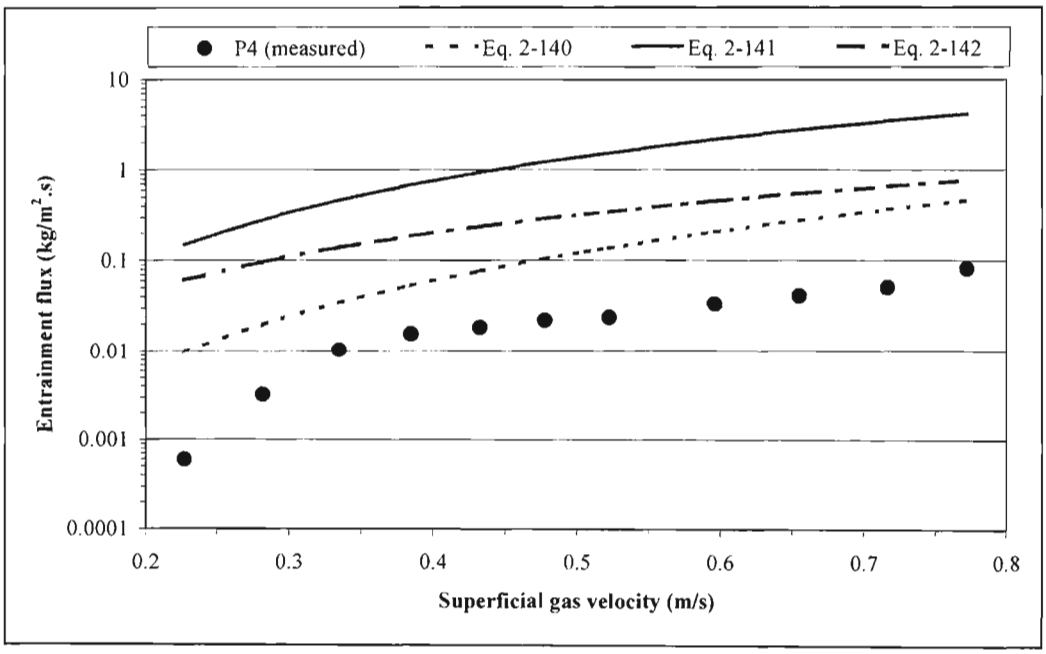

Figure 6-32(b): Comparison of measured and calculated entrainment flux for powder P4 using equations 2-140 to 2-142.

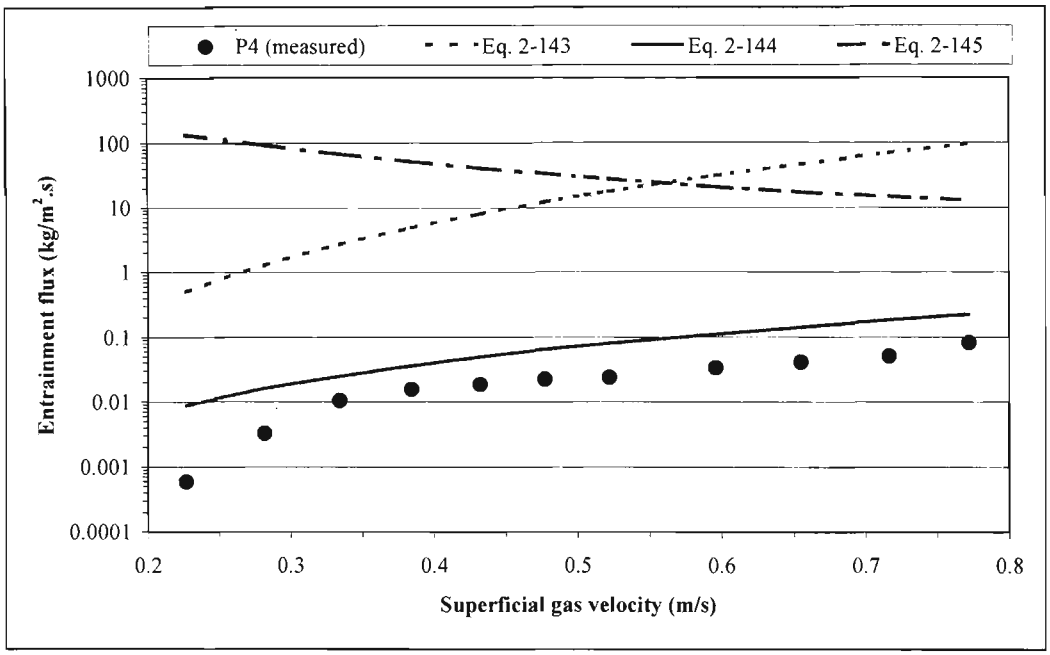

Figure 6-32(c): Comparison of measured and calculated entrainment flux for powder P4 using equations 2-143 to 2-145.

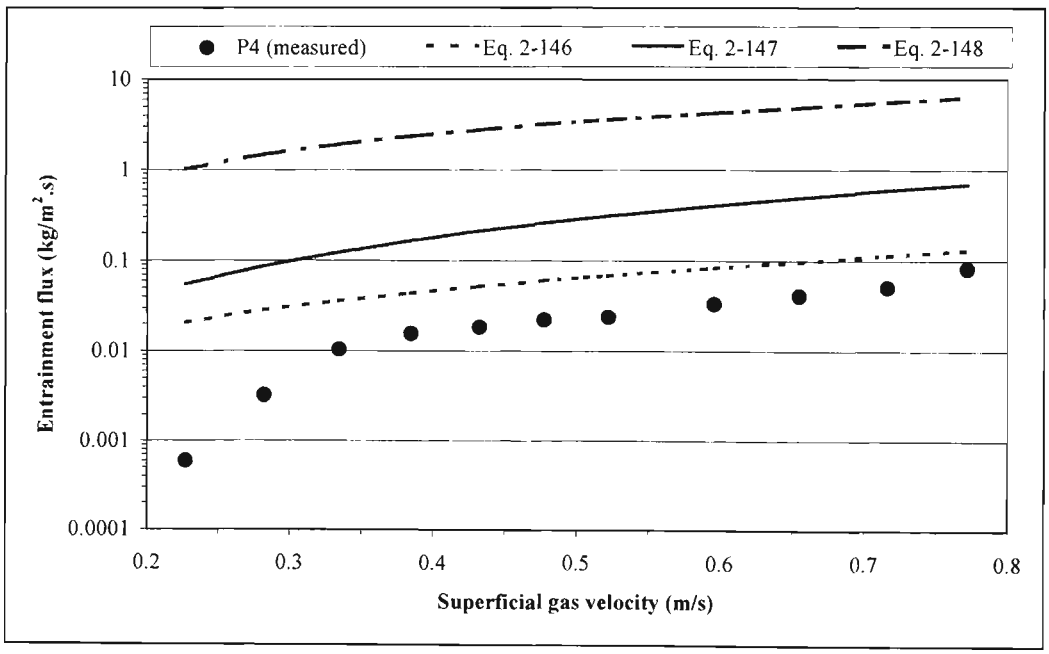

Figure 6-32(d): Comparison of measured and calculated entrainment flux for powder P4 using equations 2-146 to 2-148.

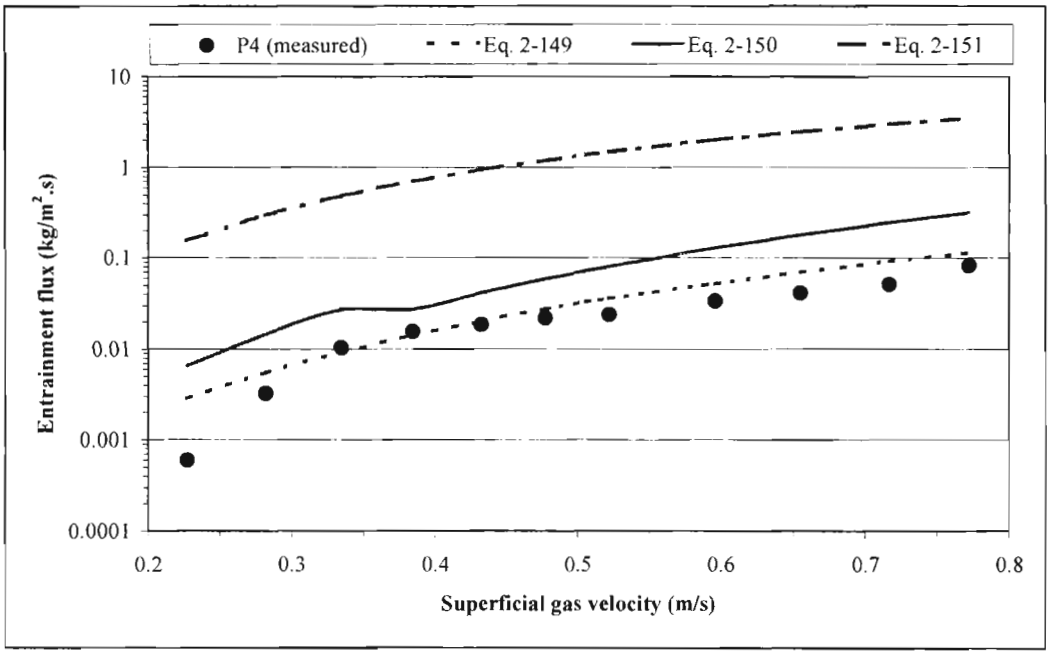

Figure 6-32(e): Comparison of measured and calculated entrainment flux for powder P4 using equations 2-149 to 2-151.

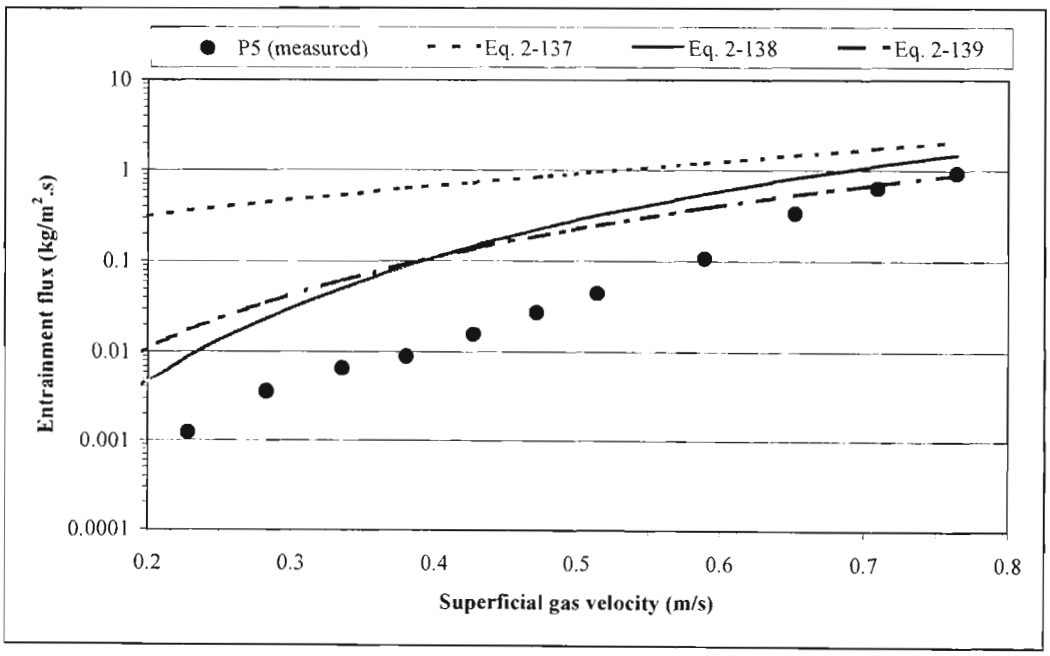

Figure 6-33(a): Comparison of measured and calculated entrainment flux for powder P5 using equations 2-137 to 2-139.

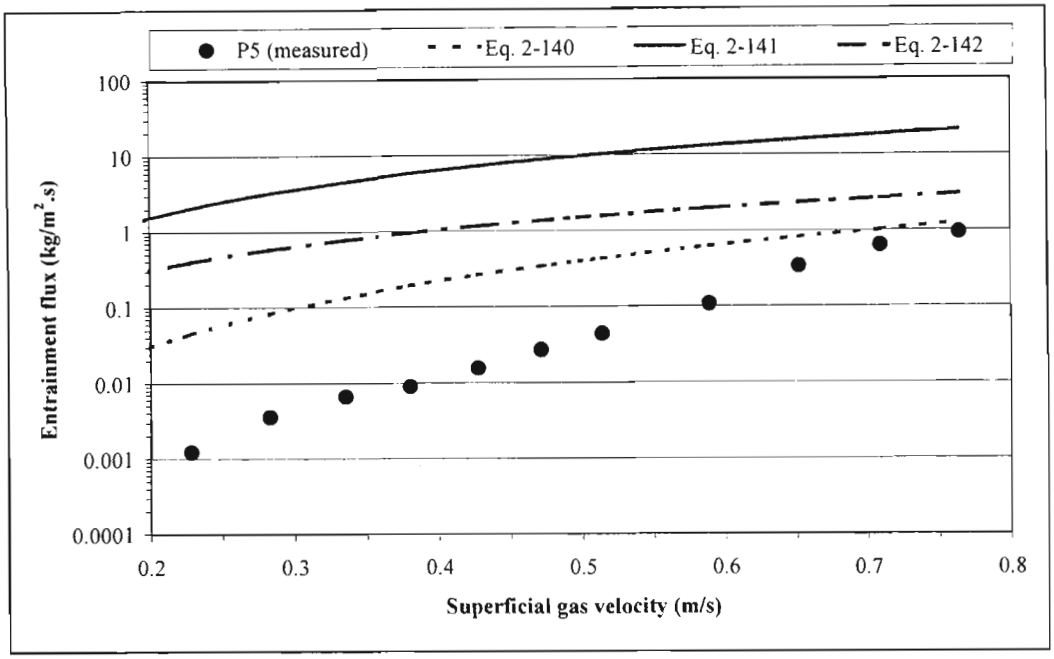

Figure 6-33(b): Comparison of measured and calculated entrainment flux for powder P5 using equations 2-140 to 2-142.

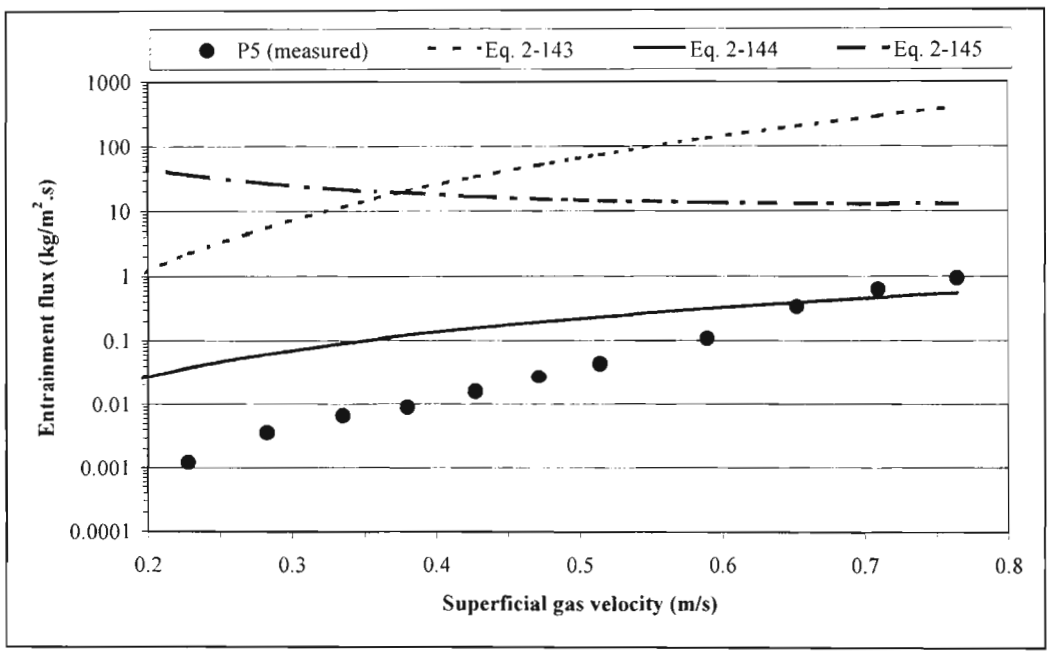

Figure 6-33(c): Comparison of measured and calculated entrainment flux for powder P5 using equations 2-143 to 2-145.

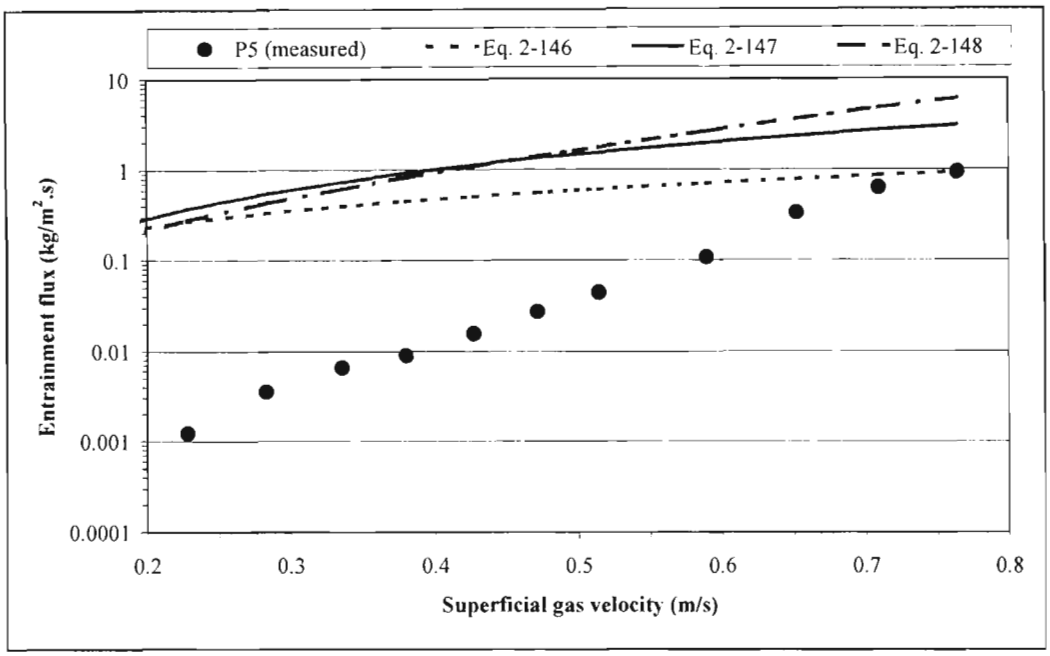

Figure 6-33(d): Comparison of measured and calculated entrainment flux for powder P5 using equations 2-146 to 2-148.

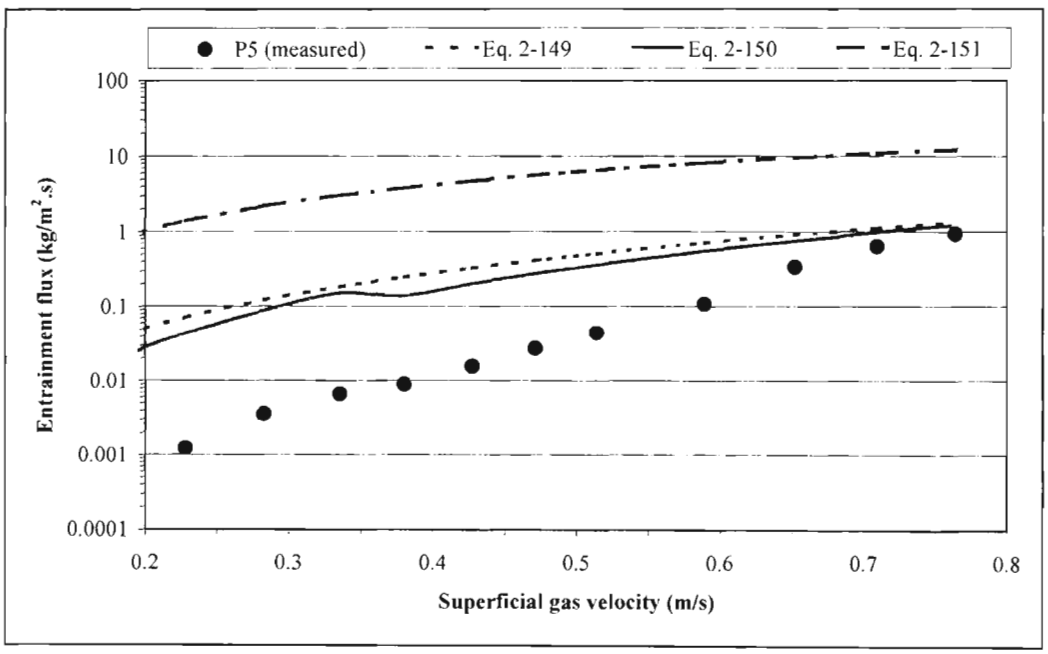

Figure 6-33(e): Comparison of measured and calculated entrainment flux for powder P5 using equations 2-149 to 2-151.

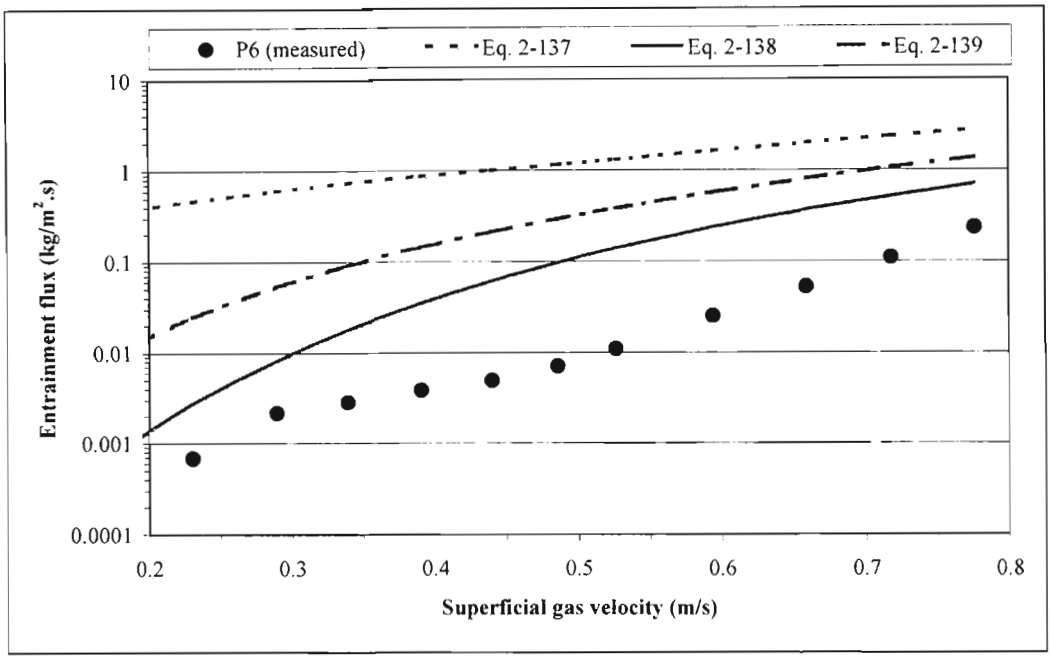

Figure 6-34(a): Comparison of measured and calculated entrainment flux for powder P6 using equations 2-137 to 2-139.

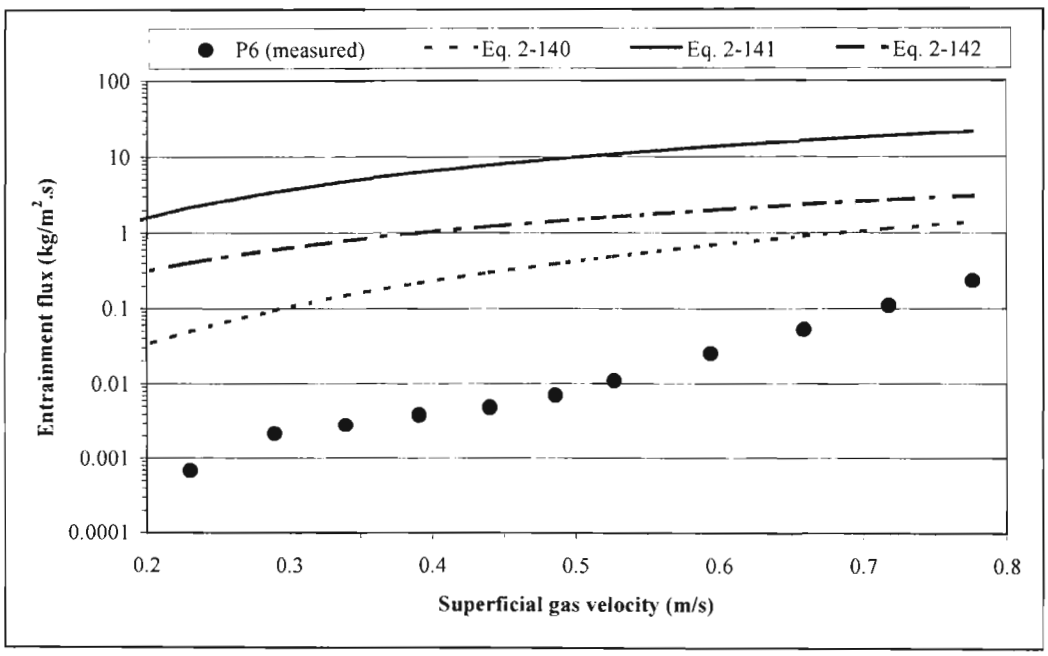

Figure 6-34(b): Comparison of measured and calculated entrainment flux for powder P6 using equations 2-140 to 2-142.

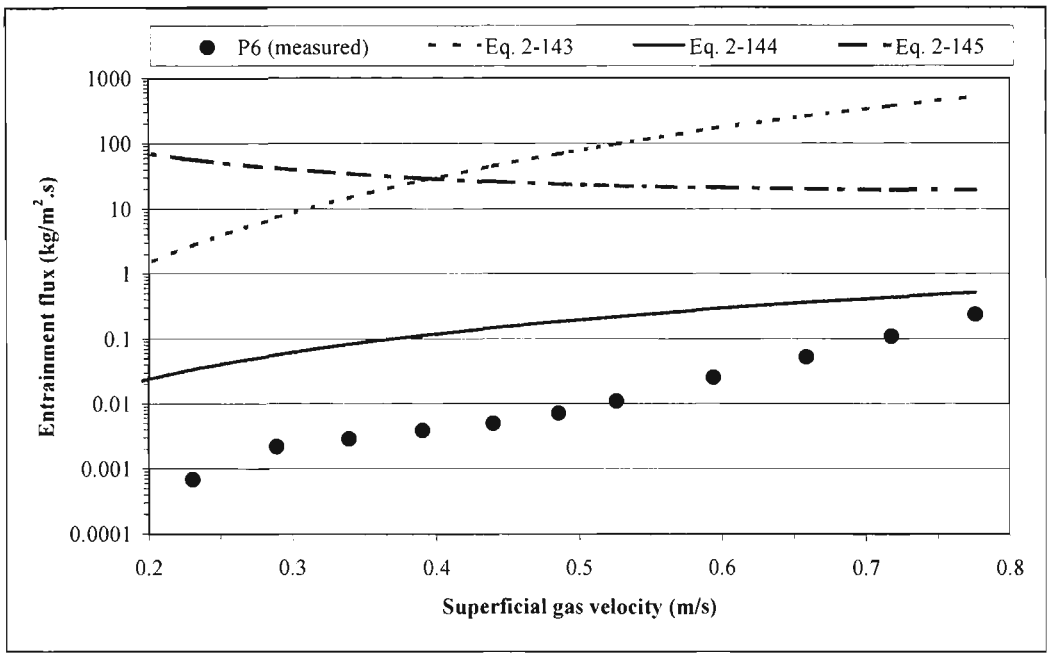

Figure 6-34(c): Comparison of measured and calculated entrainment flux for powder P6 using equations 2-143 to 2-145.

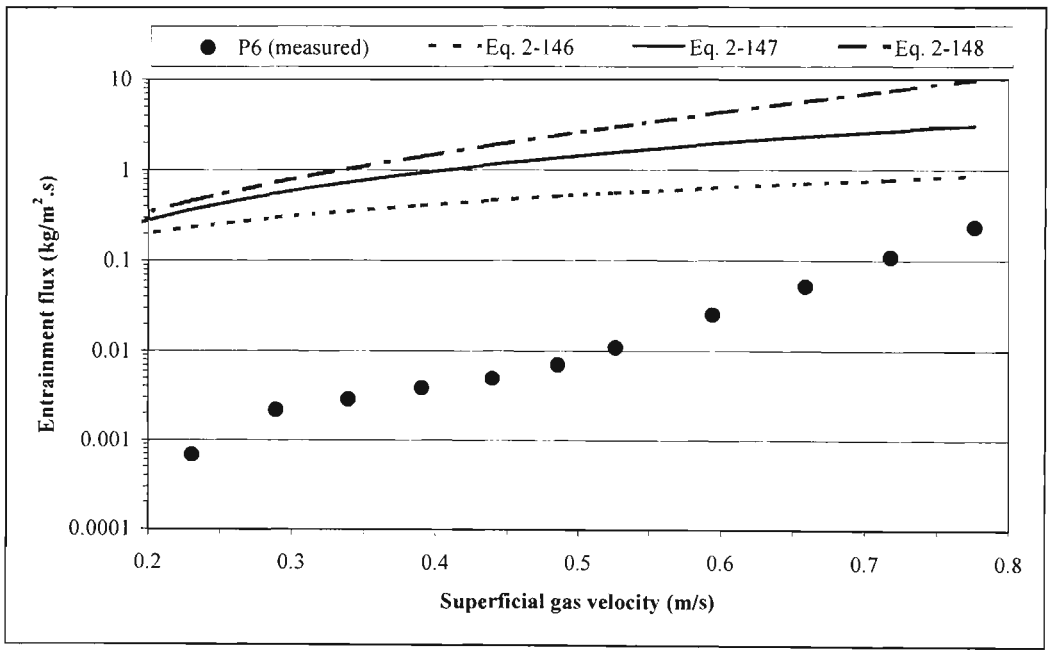

Figure 6-34(d): Comparison of measured and calculated entrainment flux for powder P6 using equations 2-146 to 2-148.

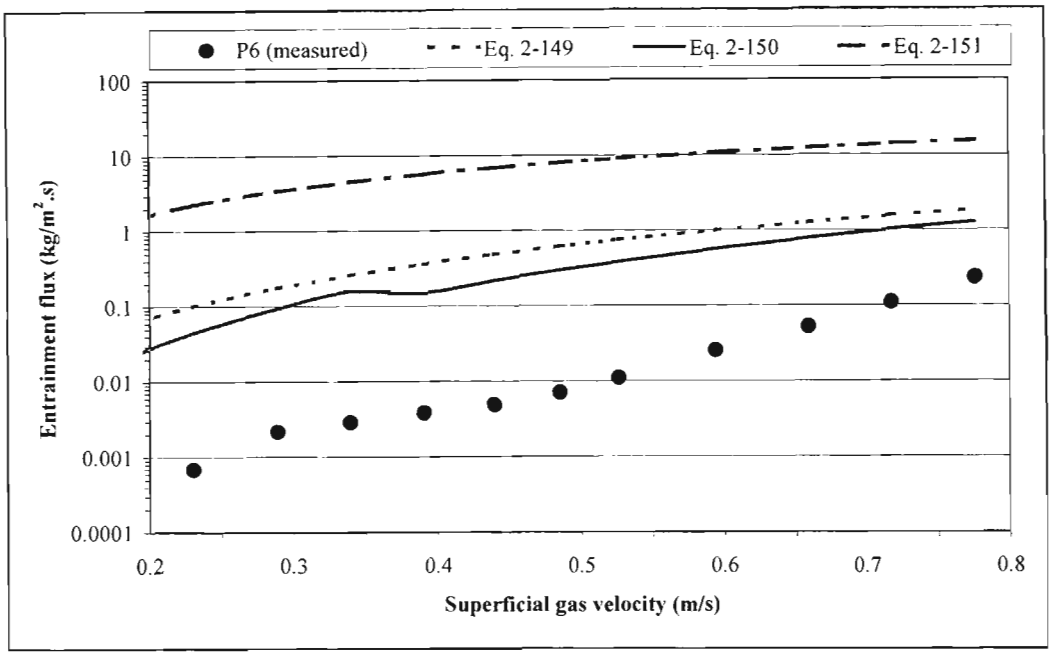

Figure 6-34(e): Comparison of measured and calculated entrainment flux for powder P6 using equations 2-149 to 2-151.

From the above results it is clear that no single entrainment correlation could be used to predict the experimental entrainment data for all the powders. In most cases the correlations tend to over-predict the entrainment rate while in some cases the relationship between the entrainment flux and superficial gas velocity is contrary to the experimental data (for example refer to the predictions of equation 2-145) Some of the correlations provide fairly good predictions for some of the powders, for example, equation 2-150 (Tasirin and Geldart 1998) provides a fairly good approximation for powder P1, while equation 2-138 (Zenz and Weil 1958) provides the best predictions for powder P3. Hence, it would be dangerous to use an entrainment correlation to model a particular system without having any experimental data for that system. It would be safer rather to measure the entrainment rate of the particular system of interest in a cold model.

From this work it has been shown that the particle properties have a significant effect on the entrainment rate and this could explain why different entrainment correlations predict widely different entrainment rates when they are applied to systems other than those for which they were developed. In particular the particle shape is not often reported in the literature and it is not often included in the entrainment correlations. Recommended ways of improving entrainment correlations are incorporation of the particle shape factor in the correlation and ensuring that measured entrainment rates are in fact above the TDH. Other system properties

such as column diameter, freeboard height and gas properties can also influence the measurement of the entrainment rate.

6.2.6.6. Summary of test results

The following summary was made based on the results obtained from the 0.14 m column:

- The dense phase voidage is a strong function of the fines content (% < 22 μm) of the powder. The higher the fines content, the higher the dense phase voidage.
- For the same particle density and particle size distribution, the more spherical the particle shape the lower the dense phase voidage.
- The dense phase voidage is not a strong function of the superficial gas velocity.
- For the same particle density, particle size distribution and superficial gas velocity, the more spherical the particle shape the higher the bubble fraction and the lower the overall bed voidage.
- The fluidized bed density decreases and the bed expansion increases with an increase in the superficial gas velocity.
- The more spherical the particle shape the higher the entrainment rate. The evidence presented strongly suggests that this is due to differences in bed behaviour rather than a freeboard phenomenon.
- The larger the particles the lower is the entrainment rate for spherical/rounded particles.
- The higher the superficial gas velocity the higher the entrainment rate.
- The rate of increase of the entrainment rate with an increase in gas velocity is dependent on whether the gas flow profile in the freeboard is laminar or turbulent.
- The predictions of dense phase voidage, bubble fraction and entrainment rate using literature correlations did not provide good agreement with the experimental data of this study. The discrepancies were more marked for angular particles.
- Literature correlations predict that the entrainment rate decreases as the particle sphericity increases which is contrary to the experimental results of this study.

7. CONCLUSIONS

The following conclusions can be drawn based on the experimental results:

1) The use of cold models has been shown to be invaluable for comparing the fluidization properties and behaviour of different powders.
2) The particle size distribution and shape play a significant role in controlling the maximum stable bubble size, and gas distribution between the dense and bubble phases. For angular or irregular-shaped particles the presence of fines promotes bubble splitting and hence the maximum stable bubble size is smaller. This translates to a delay in the onset of slugging and a lower entrainment rate when compared to spherical particles having the same particle density and size distribution.
3) The dense phase voidage is higher and the bubble fraction is lower for angular shape particles. Thus, a fluidized bed of angular particles could potentially have a higher gas conversion when compared to a fluidized bed of equivalent spherically-shaped particles.
4) The more spherical the particle's shape the higher the entrainment rate. The implication is that a fluidized bed of spherical particles could potentially enter the transport regime at a lower superficial gas velocity when compared to a fluidized bed of equivalent angular particles.
5) The entrainment rate of spherical particles from a slugging column can be reduced by the use of in-bed baffles. However, the bed pressure drop and the standard deviation of the bed pressure drop fluctuations increase; the latter is an indication of unstable fluidization.
6) The decrease in entrainment rate obtained by using in-bed baffles is not as significant as the decrease in entrainment rate obtained by changing the particle shape from spherical to angular. Angular shaped particles are therefore preferred for pilot scale operations where slugging is undesirable.
7) Angular-shaped particles are recommended for fluidized bed reactors because when compared to equivalent spherically-shaped particles they have the following potential benefits: the gas conversion would potentially be higher due to the higher dense phase voidage and lower bubble fraction and the gas throughput could be potentially higher due to the lower entrainment rate.
8) Empirical and semi-empirical correlations available in the literature are highly system dependent and the predictions have differed significantly from the experimental data obtained in this study. These correlations should therefore be used with caution. Fluidization tests should rather be carried out when in doubt.

8. RECOMMENDATIONS

In view of the important role that particle shape plays in controlling the fluidization properties and behaviour of fluidized beds, it is recommended that future work should be carried out under reaction conditions to prove the hypothesis made here that angular particles have the potential for higher gas conversion and higher gas throughput. If these benefits are demonstrated it could have significant impact on industrial applications of fluidized beds.

It is also recommended that future fluidization research should focus on a standard way of characterizing particle shape and that the option of using the particle's shape as a design variable for optimisation and process intensification of fluidized bed reactors should be considered.

The use of empirical correlations for predicting fluidization properties should be used with caution in the absence of experimental data. Particle shape effects should be accounted for when developing empirical correlations for fluidized beds. This can only be achieved once a standardized or universally accepted method of particle shape characterization has been developed.

Finally, the results from this work point to the need for further studies on the effect of particle shape on the mechanisms controlling entrainment and the preferential loss of fines from a fluidized bed. It is therefore recommended that a mechanistic model be used to investigate entrainment in future studies.

REFERENCES

Abdullah, E.C., Geldart, D., 1999. The use of bulk density measurements as flowability indicators. *Powder Technology*, 102, 151-165.

Abou-Chakra, H., Baxter, J., Tuzun, U., 2004. Three-dimensional particle shape descriptors for computer simulation of non-spherical particulate assemblies. *Advanced Powder Technology*, 15 (1), 63-77.

Abrahamsen, A.R., Geldart, D., 1980a. Behaviour of gas-fluidized beds of fine powders – Part 1: Homogenous expansion. *Powder Technology*, 26, 35-46.

Abrahamsen, A.R., Geldart, D., 1980b. Behaviour of gas-fluidized beds of fine powders – Part 2: Voidage of the dense phase in bubbling beds. *Powder Technology*, 26, 47-55.

ASTM D5757 – 95, 1995. Standard test method for determination of attrition and abrasion of powdered catalysts by air jets. ASTM, Philadelphia, PA, 158–-1585.

Baeyens, J., Geldart, D., 1974. An investigation into slugging fluidized beds. *Chemical Engineering Science*, 29, 255-265.

Baeyens, J., Geldart, D., Wu, S.Y., 1992. Elutriation of fines from gas fluidized beds of Geldart A-type powders – effect of adding superfines. *Powder Technology*, 71, 71-80.

Bai, D., Shibuya, E., Nakagawa, N., Kato, K., 1996. Characterization of gas fluidization regimes using pressure fluctuations. *Powder Technology*, 87, 105-111.

Baron, T., Briens, C.L., Bergougnou, M.A., 1988. Measurement of the flux of clusters ejected from a fluidized bed. *Powder Technology*, 55, 115-125.

Baron, T., Briens, C.L., Galtier, P., Bergougnou, M.A., 1990. Effect of bed height on particle entrainment from gas-fluidized beds. *Powder Technology*, 63, 149-156.

Barreto, G.F., Yates, J.G., Rowe, P.N., 1983a. The measurement of emulsion phase voidage in gas fluidized beds of fine powders. *Chemical Engineering Science*, 38 (3), 345-350.

Barreto, G.F., Yates, J.G., Rowe, P.N., 1983b. The effect of pressure on the flow of gas in fluidized beds of fine particles. *Chemical Engineering Science*, 38 (12), 1935-1945.

Bi, H.T., Ellis, N., Abba, I.A., Grace, J.R., 2000. A state-of-the-art review of gas-solid turbulent fluidization. *Chemical Engineering Science*, 55, 4789-4825.

Bouwman, A.M., Bosma, J.C., Vonk, P., Wesselingh, J.H.A., Frijlink, H.W., 2004. Which shape factor(s) best describe granules? *Powder Technology*, 146, 66-72.

Briens, C.L., Bergougnou, C.L., Baron, T., 1988. Prediction of entrainment from gas-solid fluidized beds. *Powder Technology*, 54, 183-196.

Bulau, H.C., Hallstrom, A., 1998. Carry-over from shallow fluidized beds. *Powder Technology*, 97, 45-50.

Chan, I.H., Knowlton, T.M., 1984. The effect of system pressure on the transport disengaging height (TDH) above bubbling fluidized beds. *AIChE Symposium Series*, 80 (241), 24-33.

Chan, I.H., Sishtla, C., Knowlton, T.M., 1987. The effect of pressure on bubble parameters in gas-fluidized beds. *Powder Technology*, 53, 217-235.

Chehbouni, A., Chaouki, J., Guy, C., Klvana, D., 1994. Characterization of the flow transition between bubbling and turbulent fluidization. *Ind. Eng. Chem. Res.*, 33, 1889-1896.

Choi, J.H., Son, J.E., Kim, S.D., 1989. Solid entrainment in fluidized bed combustors. *Journal of Chemical Engineering of Japan*, 22 (6), 597-606.

Choi, J.H., Choi, K.B., Kim, P., Shun, D.W., Kim, S.D., 1997. The effect of temperature on particle entrainment rate in a gas fluidized bed. *Powder Technology*, 92, 127-133.

Choi, J.H., Chang, I.Y., Shun, D.W., Yi, C.K., Son, J.E., Kim, S.D., 1999. Correlation on the particle entrainment rate in gas fluidized beds. *Ind. Eng. Chem. Res.*, 38, 2491-2496.

Choi, J.H., Suh, J.M., Chang, I.Y., Shun, D.W., Yi, C.K., Son, J.E., Kim, S.D., 2001. The effect of fine particles on elutriation of coarse particles in a gas fluidized bed. *Powder Technology*, 121, 190-194.

Choi, J.H., Kim, T.W., Moon, Y.S., Kim, S.D., Son, J.E., 2003. Effect of temperature on slug properties in a gas fluidized bed. *Powder Technology*, 131, 15-22.

Clark, N.N., 1986. Three techniques for implementing digital fractal analysis of particle shape. *Powder Technology*, 46, 45-52.

Clark, N.N., 1987. A new scheme for particle shape characterization based on fractal harmonics and fractal dimensions. *Powder Technology*, 51, 243-249.

Clark, N.N., Gabriele, P., Shuker, S., 1989. Drag coefficient of irregular particles in Newton's settling regime. *Powder Technology*, 59, 69-72.

Clift, R., 1986. Hydrodynamics of bubbling fluidized beds. *In:* Geldart, D., ed. *Gas fluidization technology*. New York: John Wiley & Sons, 53-95.

Colakyan, M., Levenspiel, O., 1984. Elutriation from fluidized beds. *Powder Technology*, 38, 223-232.

Darton, R.C., LaNauze, R.D., Davidson, J.F., Harrison, D., 1977. Bubble growth due to coalescence in fluidized beds. *Trans. IChemE*, 55, 274-280.

Drolon, H., Druaux, F., Faure, A., 2000. Particle shape analysis and classification using the wavelet transform. *Pattern Recognition Letters*, 21, 473-482.

Dry, R.J., 1982. *Gas distribution in fluidized beds of fine powders*. Thesis, (MSc). University of Natal, South Africa.

Dry, R.J., Judd, M.R., Shingles, T., 1983. Two-phase theory and fine powders. *Powder Technology*, 34, 213-223.

Dry, R.J., Judd, M.R., Shingles, T., 1984. Bubble velocities in fluidized beds of fine, dense powders. *Powder Technology*, 39, 69-75.

Du, B., Warsito, W., Fan, L.S., 2005. ECT studies of gas-solid fluidized beds of different diameters. *Ind. Eng. Chem. Res.*, 44, 5020-5030.

Duursma, G.R., Glass, D.H., Rix, S.J.L., Yorquez-Ramirez, M.I., 2001. PIV investigations of flow structures in the fluidized bed freeboard region. *Powder Technology*, 120, 2-11.

Ellenberger, J., Krishna, R., 1994. A unified approach to the scale-up of gas-solid fluidized bed and gas-liquid bubble column reactors. *Chemical Engineering Science*, 49 (24B), 5391-5411.

Felipe, C.A.S., Rocha, S.C.S., 2007. Prediction of minimum fluidization velocity of gas-solid fluidized beds by pressure fluctuation measurements – Analysis of the standard deviation methodology. *Powder Technology*, 174, 104-113.

Flemmer, R.L.C., Pickett, J., Clark, N.N., 1993. An experimental study in the effect of particle shape on fluidization behavior. *Powder Technology*, 77, 123-133.

Foka, M. Chaouki, J., Guy, C., Klvana, D., 1996. Gas phase hydrodynamics of a gas-solid turbulent fluidized bed reactor. *Chemical Engineering Science*, 51 (5), 713-723.

Fong, S.T., Beddow, J.K., Vetter, A.F., 1979. A refined method of particle shape representation. *Powder Technology*, 22, 17-21.

Geldart, D., 1973. Types of gas fluidization. *Powder Technology*, 7, 285-292.

Geldart, D., Cullinan, J., Georghiades, S., Gilvray, D., Pope, D.J., 1979. The effect of fines on entrainment from gas fluidized beds. *Trans. IChemE*, 57, 269-275.

Geldart, D., Pope, D.J., 1983. Interaction of fine and coarse particles in the freeboard of a fluidized bed. *Powder Technology*, 34, 95-97.

Geldart, D., 1986a. Single particles, fixed and quiescent beds. *In:* Geldart, D., ed. *Gas fluidization technology*. New York: John Wiley & Sons, 11-32.

Geldart, D., 1986b. Characterization of fluidized powders. *In:* Geldart, D., ed. *Gas fluidization technology*. New York: John Wiley & Sons, 33-51.

Geldart, D., 1986c. Particle entrainment and carryover. *In:* Geldart, D., ed. *Gas fluidization technology*. New York: John Wiley & Sons, 123-153.

Geldart, D., 2004. Expansion of gas fluidized beds. *Ind. Eng. Chem. Res.*, 43, 5802-5809.

George, S.E., Grace, J.R., 1981. Entrainment of particles from a pilot scale fluidized bed. *The Canadian Journal of Chemical Engineering*, 59, 279-284.

Goosen, R., 1988. *Particle shape effects on the captive fluidization characteristics of fine dense powders*. Thesis, (MSc.). University of Natal, South Africa.

Goossens, W.R.A., 1998. Classification of fluidized particles by Archimedes number. *Powder Technology*, 98, 48-53.

Grace, J.R., 2000. Reflections on turbulent fluidization and dense suspension upflow. *Powder Technology*, 113, 242-248.

Guedes de Carvalho, J.R.F., 1981. Dense phase expansion in fluidized beds of fine particles – the effect of pressure ob bubble stability. *Chemical Engineering Science*, 36, 413-416.

Harrison, D., Aspinall, P.N., Elder, J., 1974. Suppression of particle elutriation from a fluidized bed. *Trans. IChemE*, 52, 213-216.

Hatano, H., Ishida, M., 1983. Study of the entrainment of FCC particles from a fluidized bed. *Powder Technology*, 35, 201-209.

Hayakawa, O., Nakahira, K., Naito, M., Tsubaki, J., 1998. Experimental analysis of sample preparation conditions for particle size measurement. *Powder Technology*, 100, 61-68.

Hilal, N., Gunn, D.J., 2002. Solid hold-up in gas fluidized beds. *Chemical Engineering and Processing*, 41, 373-379.

Horio, M., Kobylecki, R.P., Tsukada, M., 2003a. Instrumentation and measurements; *In:* Yang, W.C., ed. *Handbook of fluidization and fluid-particle systems.* New York: Marcel Decker Inc., 643-704.

Hundal, H.S., Rohani, S., Wood, H.C., Pons, M.N., 1997. Particle shape characterization using image analysis and neural networks. *Powder Technology*, 91, 217-227.

Hurter, P., Clark, N.N., 1987. Persistence of polygonal harmonics as shape descriptors. *Particle and Particle Systems Characterization*, 4, 101-105.

Jin, Y., Wei, F., Wang, Y., 2003. Effect of internal tubes and baffles, *In:* Yang, W.C., ed. *Handbook of fluidization and fluid-particle systems*, New York: Mercel Decker Inc., 171-199.

Kmiec, A., 1982. Equilibrium of forces in a fluidized bed – experimental verification. *The Chemical Engineering Journal*, 23, 133-136.

Kunii, D., Levenspiel, O., 1991. Fluidization Engineering. 2nd ed. Boston: Butterworth-Heinemann.

Lin, L., Sears, J.T., Wen, C.Y., 1980. Elutriation and attrition of Char from a large fluidized bed. *Powder Technology*, 27, 105-115.

Lorences, M.J., Patience, G.S., Diez, F.V., Coca, J., 2003. Fines effects on collapsing fluidized beds. *Powder Technology*, 131, 234-240.

Luckos, A., den Hoed, P., 2004. Fluidization and flow regimes of titaniferous solids. *Ind. Eng. Chem. Res.*, 43, 5645-5652.

Ma, X., Kato, K., 1998. Effect of interparticle adhesion forces on elutriation of fine powders from a fluidized bed of a binary particle mixture. *Powder Technology*, 95, 93-101.

Ma, Z., Merkus, H.G., de Smet, J.G.A.E., Heffels, C., Scarlett, B., 2000. New developments in particle characterization by laser diffraction: size and shape. *Powder Technology*, 111, 66-78.

Makkawi, Y.T., Wright, P.C., 2002. Fluidization regimes in a conventional fluidized bed characterized by means of electrical capacitance tomography. *Chemical Engineering Science*, 57, 2411-2437.

Merrick, D., Highley, J., 1974. Particle size reduction and elutriation in a fluidized bed process. *AIChE Symposium Series*, 70 (137), 366-378.

Milioli, F.E., Foster, P.J., 1995a. Entrainment and elutriation modelling in bubbling fluidized beds. *Powder Technology*, 83, 233-243.

Milioli, F.E., Foster, P.J., 1995b. A model for particle size distribution and elutriation in fluidized beds. *Powder Technology*, 83, 265-280.

Mohammadi, M.S., Harnby, N., 1997. Bulk density modelling as a means of typifying the microstructure and flow characteristics of cohesive powders. *Powder Technology*, 92, 1-8.

Naito, M., Hayakawa, O., Nakahira, K., Mori, H., Tsubaki, J., 1998. Effect of particle shape on the particle size distribution measured with commercial equipment. *Powder Technology*, 100, 52-60.

Nakagawa, N., Arita, S., Uchida, H., Takamura, N., Takarada, T., Kato, K., 1994. Particle hold-up and elutriation rate in the freeboard of fluid beds. *Journal of Chemical Engineering of Japan*, 27 (1), 79-84.

Nie, Y., Liu, D., 1998. Dynamics of collapsing fluidized beds and its application in the simulation of pulsed fluidized beds. *Powder Technology*, 99, 132-139.

Pemberton, S.T., Davidson, J.F., 1984. Turbulence in the freeboard of a gas-fluidized bed – the significance of ghost bubbles. *Chemical Engineering Science*, 39 (5), 829-840.

Pemberton, S.T., Davidson, J.F., 1986. Elutriation from fluidized beds – 1. Particle ejection from the dense phase into the freeboard. *Chemical Engineering Science*, 41 (2), 243-251.

Peters, M.H., Fan, L.S., Sweeney, T.L., 1983. Study of particle ejections in the freeboard region of a fluidized bed with an image carrying probe. *Chemical Engineering Science*, 38 (3), 481-485.

Pickett, J., Clark, N., Shuker, S., 1991. A re-examination of Piper's shape analysis technique. *Particle and Particle Systems Characterization*, 8, 110-115.

Piepers, H.W., Cottaar, E.J.E., Verkooijen, A.H.M., Rietema, K., 1984. Effects of pressure and type of gas on particle-particle interaction and the consequences for gas-solid fluidization behaviour. *Powder Technology*, 37, 55-70.

Rhodes, M., 1996. What is turbulent fluidization? *Powder Technology*, 88, 3-14.

Rowe, P.N., 1976. Prediction of bubble size in a gas fluidized bed. *Chemical Engineering Science*, 31, 285-288.

Rowe, P.N., Yacono, C.X.R., 1976. The bubbling behaviour of fine powders when fluidized. *Chemical Engineering Science*, 31, 1179-1192.

Rowe, P.N., Santoro, L., Yates, J.G., 1978. The division of gas between bubble and interstitial phases in fluidized beds of fine powders. *Chemical Engineering Science*, 33, 133-140.

Sciazko, M., Bandrowski, J., Raczek, J., 1991. On the entrainment of solid particles from a fluidized bed. *Powder Technology*, 66, 33-39.

Shin, M. K., Kim, E.M., Koo, B.S., Han, G.Y., Yoon, K.J., Lee, D.H., Kim, S.D., 2007. Entrainment characteristics of fine particles in cylindrical and conical inert-medium fluidized beds. *Ind. Eng. Chem. Res.*, 46, 1408-1414.

Sidorenko, I., Rhodes, M.J., 2004. Influence of pressure on fluidization properties. *Powder Technology*, 141, 137-154.

Silva, M.A., Miranda, M.N.N., 2003. Estimation of properties of ternary mixtures of solids using the mixing rule. *Powder Technology*, 134, 16-23.

Smolders K., Baeyens, J., 1997. Elutriation of fines from gas fluidized beds: mechanisms of elutriation and effect of freeboard geometry. *Powder Technology*, 92, 35-46.

Smolders, K., Baeyens, J., 2001. Gas fluidized beds operating at high velocities: a critical review of occurring regimes. *Powder Technology*, 119, 269-291.

Sookai, S., Langenhoven, P.L., Shingles, T., 2001. Scale-up and commercial reactor fluidization related experience with Synthol, gas to liquid fuel, dense phase fluidized bed reactors. *In:* Kuauk, M., Li, J., Yang, W.C., eds. *Fluidization X: Proceedings of the 10th United Engineering Foundation Conference*. New York, 621-628.

Squires, A.M., 2005. Perspectives in fluid-bed arts: looking back and ahead. *Powder Technology*, 151, 15-18.

Subbarao, D., 1986. Clusters and lean-phase behaviour. *Powder Technology*, 46, 101-107.

Tanaka, I., Shinohara, H., Hirose, H., Tanaka, Y., 1972. Elutriation of fines from fluidized bed – study of transport disengaging height. *Journal of Chemical Engineering of Japan*, 5, 51-56.

Tasirin, S.M., Geldart, D., 1998. Entrainment of FCC from fluidized beds – a new correlation for the elutriation rate constant $K_{i,r}^{*}$. *Powder Technology*, 95, 240-247.

Taylor, M.A., Garboczi, E.J., Erdogan, S.T., Fowler, D.W., 2006. Some properties of irregular 3-D particles. *Powder Technology*, 162, 1-15.

Tweddle, T.A., Capes, C.E., Osberg, G.L., 1970. Effect of screen packing on entrainment from fluidized beds. *Ind. Eng. Chem. Proc. Des. Develop.* 9 (1), 85-88.

Vigneau, E., Loisel, C., Devaux, M.F., Cantoni, P., 2000. Number of particles for the determination of size distribution from microscopic images. *Powder Technology*, 107, 243-250.

Wang, Z., Li, H., 1995. A new criterion for prejudging the fluidization behaviour of powders. *Powder Technology*, 84, 191-195.

Weimer, A.W., Quarderer, G.J., 1985. On dense phase voidage and bubble size in high pressure fluidized beds of fine powders. *AIChE Journal*, 31 (6), 1019-1028.

Wen, C.Y., Chen, L.H., 1982. Fluidized bed freeboard phenomena: entrainment and elutriation. *AIChE Journal*, 28 (1), 117-128.

Wen, C.Y., Hashinger, R.F., 1960. Elutriation of solid particles from a dense-phase fluidized bed. *AIChE Journal*, 6 (2), 220-226.

Werther, J., 1999. Measurement techniques in fluidized beds. *Powder Technology*, 102, 15-36.

Werther, J., Hartge, E.U., 2003. Elutriation and Entrainment. *In:* Yang, W.C., ed. *Handbook of fluidization and fluid-particle systems*, New York: Marcel Decker Inc., 113-128.

Xie, H.Y., Geldart, D., 1995. Fluidization of FCC powders in the bubble-free regime: effect of types of gases and temperature. *Powder Technology*, 82, 269-277.

Xie, H.Y., Zhang, D.W., 2001. Stokes shape factor and its application in the measurement of sphericity of non-spherical particles. *Powder Technology*, 114, 102-105.

Yang W.C., 2003a. Particle Characterization and Dynamics. *In:* Yang, W.C., ed. *Handbook of fluidization and fluid-particle systems*, New York: Marcel Decker, Inc, 1-27.

Yang W.C., 2003b. Bubbling fluidized beds. *In:* Yang, W.C. ed. *Handbook of fluidization and fluid-particle systems*, New York: Marcel Decker Inc, 53-111.

Yang, W.C., 2007. Modification and re-interpretation of Geldart's classification of powders. *Powder Technology*, 171, 69-74.

Yates, J.G., 1996. Effects of temperature and pressure on gas-solid fluidization. *Chemical Engineering Science*, 51 (2), 167-205.

Yorquez-Ramirez, M.J., Duursma, G.R., 2001. Insights into the instantaneous freeboard flow above a bubbling fluidized bed. *Powder Technology*, 116, 76-84.

Zeidan, M., Jia, X., Williams, R.A., 2007. Errors implicit in digital particle characterization. *Chemical Engineering Science*, 62, 1905-1914.

Zenz, F.A., Weil, N.A., 1958. A theoretical-empirical approach to the mechanism of particle entrainment from fluidized beds. *AIChE Journal*, 4 (4), 472-479.

Zhang, S.J., Yu, A.B., 2002. Computational investigation of slugging behaviour in gas-fluidized beds. *Powder Technology*, 123, 147-165.

APPENDIX A: PARTICLE SIZE DISTRIBUTION OF POWDERS

Table A1: Particle size distribution of powders.

Powder	P1	P2	P3	P4	P5	P6	P7	P8	P9	P10
% < 352 μm	100	100	100	100	100	100	100	100	100	100
% < 249 μm	100	100	98.7	100	99.1	99.7	100	100	99.5	100
% < 176 μm	100	100	94.9	100	95.9	97.1	98.6	100	93.8	100
% < 125 μm	100	99.8	88.1	59.9	86.9	91.5	89.8	99.4	76.5	100
% < 88 μm	83	92.9	78.3	47.6	74.3	82.0	70.4	96.1	55.9	100
% < 62 μm	52	66.5	66.1	30.4	60.1	69.0	46.8	81.6	37.5	100
% < 44 μm	22	31.0	52.3	18.8	46.6	54.3	28.1	60.1	23.9	98.0
% < 31 μm	5	9.3	38.3	10.9	34.5	40.1	16.1	41.0	14.7	70.3
% < 22 μm	1	3.1	26.3	5.9	24.4	28.7	9.6	29.5	9.0	55.1
% < 16 μm	0	1.0	15.6	2.7	15.1	19.0	5.7	21.6	5.0	32.8
% < 11 μm	0	0	7.6	0.9	7.8	11.7	3.2	15.0	2.4	16.6
% < 7.8 μm	0	0	3.5	0.3	3.9	7.1	2.0	10.6	1.2	8.0
% < 5.5 μm	0	0	1.3	0	1.7	3.6	1.1	6.9	0.5	3.2
% < 3.9 μm	0	0	0	0	0.5	0.6	0	4.0	0	0.7
% < 2.8 μm	0	0	0	0	0.2	0	0	2.0	0	0.2

APPENDIX B: ENTRAINMENT RESULTS FROM THE 0.05 M INTERNAL DIAMETER COLUMN

Table B1: Entrainment rate data from the 0.05 m internal diameter column for powders P3 (with and without baffles), P5 and P6.

P3		P5		P6	
Time (h)	Entrainment rate (kg/h)	Time (h)	Entrainment rate (kg/h)	Time (h)	Entrainment rate (kg/h)
1	0.264	1	0.172	0.5	0.042
2	0.224	2	0.152	1.5	0.040
3	0.173	3	0.158	2.5	0.050
4	0.102	4	0.125	3.5	0.056
5	0.070	5	0.087	4.5	0.071
6	0.045	6	0.064	5.5	0.097
7	0.029	7	0.044	6.5	0.101
8	0.018			7.5	0.099
9	0.017			8.5	0.099
10	0.012			9.5	0.086
				10.5	0.060
P3 with in-bed baffles				11.5	0.038
Time (h)	Entrainment rate (kg/h)			12.5	0.020
				13.5	0.012
1	0.206			14.5	0.009
2	0.203			15.5	0.007
3	0.090			16.5	0.007
4	0.037				
5	0.029				
6	0.017				

Table B2: Entrainment rate data from the 0.05 m internal diameter column for powders P8, P9 and P10.

P8		P9		P10	
Time (h)	Entrainment rate (kg/h)	Time (h)	Entrainment rate (kg/h)	Time (h)	Entrainment rate (kg/h)
1	0.044	1	0.246	1	0.311
2	0.042	2	0.120	2	0.340
3	0.040	3	0.040	3	0.225
4	0.043	4	0.020	4	0.186
5	0.046	5	0.016	5	0.141
6	0.054	6	0.011	6	0.099
7	0.055	7	0.011	7	0.076
8	0.069			8	0.07
9	0.088			9	0.061
10	0.100				
11	0.105				
12	0.093				
13	0.085				
14	0.085				
15	0.068				
16	0.036				

APPENDIX C: DATA FROM BED COLLAPSE TESTS AND SAMPLE CALCULATIONS OF BED VOIDAGES

C1 Data from bed collapse tests

C1.1 Powder P2

Table C1: Data from the 0.14 m internal diameter column for powder P2 at superficial gas velocities of 0.11, and 0.23 m/s.

Time (s)	U = 0.11 m/s			U = 0.23 m/s		
	Run 1	Run 2	Run 3	Run 1	Run 2	Run 3
	Bed height (m)			*Bed height (m)*		
5	1.132	1.127	1.128	1.130	1.129	-
10	1.127	1.122	1.123	1.126	1.124	-
15	1.120	1.118	1.119	1.122	1.120	-
20	1.119	1.116	1.116	1.115	1.116	-
25	1.118	1.114	1.115	1.115	1.110	-
30	1.117	1.113	1.114	1.115	1.110	-
40	1.116	1.112	1.113	1.115	1.110	-
50	1.113	1.111	1.111	1.115	1.110	-
60	1.114	1.111	1.111	1.115	1.110	-
80	1.114	1.111	1.111	1.115	1.110	-
100	1.114	1.111	1.111	1.115	1.110	-
120	1.114	1.111	1.111	1.115	1.110	-
H_{bed} (m)	1.244	1.229	1.236	1.349	1.357	-
H_d (m)	1.136	1.130	1.114	1.134	1.133	-
w (kg)	23.03	22.96	22.96	23.05	22.94	-
ε_d	0.307	0.305	0.295	0.305	0.308	-
ε_b	0.086	0.080	0.099	0.159	0.165	-
ε	0.367	0.361	0.365	0.416	0.422	-
	Averages			*Averages*		
ε_d	0.302			0.306		
ε_b	0.088			0.162		
ε	0.364			0.419		
H_{bed} (m)	1.236			1.353		
H_0 (m)	1.112			1.113		
ΔP_{bed} (kPa)	-			-		
ρ_{bed} (kg/m^3)	1208			1104		
δ_{bed} (kPa)	-			-		

Average bulk density (kg/m^3)	1343
Particle density (kg/m^3)	1900
Column cross-sectional area (m^2)	0.01539

C1.2 Powder P3

Table C2: Data from the 0.14 m internal diameter column for powder P3 at superficial gas velocities of 0.11, 0.23 and 0.34 m/s.

Time (s)	U = 0.11 m/s			U = 0.23 m/s			U = 0.34 m/s		
	Run 1	Run 2	Run 3	Run 1	Run 2	Run 3	Run 1	Run 2	Run 3
	Bed height (m)			*Bed height (m)*			*Bed height (m)*		
5	1.091	1.095	1.103	1.101	1.098	1.099	1.118	1.101	1.105
10	1.078	1.082	1.089	1.089	1.087	1.088	1.104	1.090	1.092
15	1.066	1.069	1.077	1.078	1.075	1.077	1.090	1.079	1.081
20	1.054	1.054	1.067	1.066	1.064	1.067	1.077	1.068	1.072
25	1.043	1.046	1.057	1.058	1.055	1.057	1.067	1.059	1.062
30	1.036	1.038	1.046	1.052	1.048	1.049	1.059	1.053	1.056
40	1.027	1.029	1.034	1.042	1.038	1.039	1.047	1.044	1.042
50	1.023	1.025	1.026	1.037	1.032	1.032	1.042	1.038	1.040
60	1.018	1.021	1.024	1.035	1.030	1.028	1.036	1.033	1.036
80	1.018	1.021	1.020	1.031	1.026	1.028	1.032	1.033	1.036
100	1.018	1.021	1.020	1.031	1.026	1.028	1.032	1.033	1.036
120	1.018	1.021	1.020	1.031	1.026	1.028	1.032	1.033	1.036
H_{bed} (m)	1.207	1.209	1.199	1.265	1.269	1.245	1.328	1.328	1.350
H_d (m)	1.102	1.109	1.114	1.113	1.110	1.110	1.132	1.112	1.115
w (kg)	39.96	40.08	40.04	40.47	40.27	40.35	40.51	40.55	40.67
ε_d	0.488	0.490	0.492	0.486	0.488	0.487	0.495	0.485	0.485
ε_b	0.087	0.083	0.071	0.120	0.125	0.108	0.147	0.162	0.174
ε	0.532	0.532	0.528	0.548	0.552	0.542	0.569	0.569	0.574
	Averages			*Averages*			*Averages*		
ε_d	0.490			0.487			0.488		
ε_b	0.080			0.118			0.161		
ε	0.531			0.547			0.571		
H_{bed} (m)	1.205			1.260			1.335		
H_0 (m)	1.020			1.028			1.034		
ΔP_{bed} (kPa)	22.95			23.35			23.62		
ρ_{bed} (kg/m^3)	2158			2082			1975		
δ_{bed} (kPa)	0.21			0.35			0.46		

Table C3: Data from the 0.14 m internal diameter column for powder P3 at superficial gas velocities of 0.44, 0.52 and 0.60 m/s.

Time (s)	U = 0.44 m/s			U = 0.52 m/s			U = 0.60 m/s		
	Run 1	Run 2	Run 3	Run 1	Run 2	Run 3	Run 1	Run 2	Run 3
	Bed height (m)			*Bed height (m)*			*Bed height (m)*		
5	1.110	1.101	1.105	1.104	1.095	1.095	1.095	1.093	1.074
10	1.096	1.090	1.092	1.091	1.085	1.083	1.085	1.080	1.063
15	1.084	1.081	1.079	1.079	1.075	1.072	1.075	1.069	1.051
20	1.075	1.071	1.068	1.066	1.065	1.060	1.065	1.059	1.040
25	1.066	1.067	1.058	1.059	1.058	1.051	1.058	1.051	1.033
30	1.059	1.056	1.052	1.05	1.050	1.043	1.053	1.042	1.028
40	1.048	1.045	1.045	1.042	1.041	1.033	1.044	1.034	1.020
50	1.041	1.039	1.037	1.034	1.034	1.028	1.037	1.029	1.017
60	1.038	1.036	1.032	1.031	1.031	1.025	1.035	1.024	1.015
80	1.036	1.034	1.032	1.031	1.031	1.025	1.035	1.024	1.010
100	1.036	1.034	1.032	1.031	1.031	1.025	1.035	1.024	1.010
120	1.036	1.034	1.032	1.031	1.031	1.025	1.035	1.024	1.010
H_{bed} (m)	1.393	1.375	1.400	1.453	1.435	1.400	1.513	1.493	1.480
H_d (m)	1.121	1.111	1.117	1.117	1.105	1.107	1.105	1.104	1.086
w (kg)	40.67	40.59	40.51	40.47	40.47	40.24	40.63	40.20	39.65
ε_d	0.488	0.484	0.488	0.488	0.483	0.487	0.481	0.486	0.484
ε_b	0.195	0.192	0.202	0.231	0.230	0.209	0.269	0.260	0.266
ε	0.588	0.583	0.591	0.607	0.602	0.594	0.621	0.620	0.622
	Averages			*Averages*			*Averages*		
ε_d	0.487			0.486			0.484		
ε_b	0.196			0.223			0.265		
ε	0.587			0.601			0.621		
H_{bed} (m)	1.389			1.429			1.495		
H_0 (m)	1.034			1.029			1.023		
ΔP_{bed} (kPa)	23.83			23.80			23.49		
ρ_{bed} (kg/m^3)	1898			1836			1745		
δ_{bed} (kPa)	0.51			0.61			0.94		

Table C4: Data from the 0.14 m internal diameter column for powder P3 at superficial gas velocities of 0.66, 0.72 and 0.77 m/s.

Time (s)	U = 0.66 m/s			U = 0.72 m/s			U = 0.77 m/s		
	Run 1	Run 2	Run 3	Run 1	Run 2	Run 3	Run 1	Run 2	Run 3
	Bed height (m)			*Bed height (m)*			*Bed height (m)*		
5	1.075	1.059	1.038	1.044	1.054	1.031	1.008	0.990	1.014
10	1.067	1.049	1.032	1.034	1.042	1.021	1.000	0.980	1.003
15	1.057	1.039	1.027	1.023	1.031	1.011	0.990	0.969	0.992
20	1.048	1.029	1.020	1.010	1.022	1.000	0.980	0.958	0.981
25	1.041	1.021	1.014	1.002	1.014	0.990	0.972	0.952	0.973
30	1.034	1.015	1.010	0.996	1.006	0.982	0.968	0.945	0.966
40	1.023	1.006	1.003	0.989	0.996	0.977	0.965	0.939	0.959
50	1.022	1.006	1.000	0.986	0.993	0.973	0.962	0.937	0.955
60	1.017	1.000	1.000	0.986	0.993	0.973	0.962	0.937	0.953
80	1.016	1.000	0.999	0.986	0.992	0.973	0.962	0.937	0.953
100	1.016	1.000	0.999	0.986	0.992	0.973	0.962	0.937	0.953
120	1.016	1.000	0.999	0.986	0.992	0.973	0.962	0.937	0.953
H_{bed} (m)	1.565	1.5485	1.483	1.483	1.525	1.470	1.498	1.450	1.460
H_d (m)	1.085	1.069	1.044	1.056	1.064	1.042	1.018	0.999	1.024
w (kg)	39.88	39.25	39.21	38.70	38.94	38.19	37.76	36.78	37.41
ε_d	0.481	0.481	0.470	0.482	0.483	0.482	0.476	0.480	0.484
ε_b	0.307	0.310	0.296	0.288	0.302	0.291	0.320	0.311	0.299
ε	0640	0.642	0.626	0.631	0.639	0.633	0.644	0.642	0.638
	Averages			*Averages*			*Averages*		
ε_d	0.477			0.483			0.480		
ε_b	0.304			0.294			0.310		
ε	0.636			0.635			0.641		
H_{bed} (m)	1.532			1.493			1.469		
H_0 (m)	1.005			0.984			0.951		
ΔP_{bed} (kPa)	23.17			22.93			22.57		
ρ_{bed} (kg/m^3)	1674			1681			1650		
δ_{bed} (kPa)	0.58			0.78			0.97		
Average bulk density (kg/m^3)	2550								
Particle density (kg/m^3)	4600								
Column cross-sectional area (m^2)	0.01539								

C1.3 Powder P5

Table C5: Data from the 0.14 m internal diameter column for powder P5 at superficial gas velocities of 0.11, 0.23 and 0.34 m/s.

Time (s)	U = 0.11 m/s			U = 0.23 m/s			U = 0.34 m/s		
	Run 1	Run 2	Run 3	Run 1	Run 2	Run 3	Run 1	Run 2	Run 3
	Bed height (m)			*Bed height (m)*			*Bed height (m)*		
5	1.196	1.188	1.193	1.200	1.207	1.201	1.198	1.179	1.186
10	1.186	1.180	1.184	1.193	1.198	1.193	1.183	1.171	1.178
15	1.177	1.171	1.177	1.184	1.192	1.184	1.169	1.161	1.166
20	1.163	1.163	1.167	1.173	1.183	1.173	1.160	1.151	1.153
25	1.155	1.153	1.156	1.159	1.171	1.162	1.149	1.139	1.142
30	1.145	1.146	1.147	1.146	1.163	1.150	1.135	1.129	1.132
40	1.132	1.134	1.125	1.128	1.149	1.131	1.118	1.110	1.112
50	1.122	1.115	1.114	1.118	1.131	1.118	1.106	1.096	1.100
60	1.117	1.109	1.109	1.112	1.124	1.109	1.099	1.090	1.095
80	1.114	1.104	1.105	1.108	1.118	1.104	1.095	1.088	1.092
100	1.113	1.103	1.103	1.107	1.116	1.102	1.095	1.088	1.092
120	1.113	1.103	1.103	1.107	1.115	1.102	1.095	1.088	1.092
H_{bed} (m)	1.280	1.270	1.260	1.330	1.340	1.320	1.390	1.370	1.360
H_d (m)	1.207	1.197	1.203	1.21	1.22	1.210	1.21	1.190	1.200
w (kg)	32.67	32.37	32.37	32.49	32.72	32.34	32.14	31.93	32.05
ε_d	0.451	0.451	0.454	0.455	0.455	0.457	0.461	0.455	0.458
ε_b	0.057	0.058	0.045	0.090	0.090	0.083	0.130	0.131	0.118
ε	0.482	0.483	0.478	0.504	0.504	0.503	0.531	0.527	0.522
	Averages			*Averages*			*Averages*		
ε_d	0.452			0.457			0.458		
ε_b	0.053			0.083			0.126		
ε	0.481			0.503			0.526		
H_{bed} (m)	1.270			1.330			1.373		
H_0 (m)	1.106			1.108			1.092		
ΔP_{bed} (kPa)	18.95			18.90			18.65		
ρ_{bed} (kg/m^3)	1661			1589			1516		
δ_{bed} (kPa)	0.20			0.25			0.34		

Table C6: Data from the 0.14 m internal diameter column for powder P5 at superficial gas velocities of 0.44, 0.52 and 0.60 m/s.

Time (s)	U = 0.44 m/s			U = 0.52 m/s			U = 0.60 m/s		
	Run 1	Run 2	Run 3	Run 1	Run 2	Run 3	Run 1	Run 2	Run 3
	Bed height (m)			*Bed height (m)*			*Bed height (m)*		
5	1.191	1.195	1.187	1.166	1.182	1.172	1.143	1.134	1.121
10	1.180	1.184	1.175	1.152	1.170	1.161	1.139	1.128	1.114
15	1.169	1.171	1.163	1.143	1.158	1.149	1.127	1.116	1.104
20	1.155	1.159	1.152	1.136	1.145	1.137	1.119	1.108	1.095
25	1.142	1.148	1.138	1.126	1.132	1.128	1.109	1.100	1.087
30	1.129	1.137	1.128	1.116	1.121	1.118	1.099	1.092	1.078
40	1.110	1.117	1.112	1.100	1.105	1.100	1.085	1.080	1.068
50	1.098	1.106	1.101	1.091	1.094	1.089	1.077	1.073	1.066
60	1.093	1.099	1.095	1.085	1.089	1.086	1.072	1.071	1.065
80	1.091	1.097	1.093	1.082	1.087	1.084	1.071	1.071	1.065
100	1.091	1.097	1.093	1.082	1.087	1.084	1.071	1.071	1.065
120	1.091	1.097	1.093	1.082	1.087	1.084	1.071	1.071	1.065
H_{bed} (m)	1.420	1.410	1.410	1.440	1.450	1.430	1.400	1.350	1.380
H_d (m)	1.205	1.207	1.199	1.173	1.195	1.182	1.155	1.143	1.130
w (kg)	32.02	32.20	32.08	31.76	31.90	31.81	31.43	31.43	31.26
ε_d	0.461	0.459	0.457	0.450	0.458	0.454	0.448	0.442	0.438
ε_b	0.151	0.144	0.150	0.185	0.176	0.173	0.175	0.153	0.181
ε	0.542	0.536	0.538	0.552	0.553	0.548	0.544	0.527	0.540
	Averages			*Averages*			*Averages*		
ε_d	0.459			0.454			0.443		
ε_b	0.148			0.178			0.170		
ε	0.539			0.551			0.537		
H_{bed} (m)	1.413			1.440			1.377		
H_0 (m)	1.094			1.084			1.069		
ΔP_{bed} (kPa)	18.64			17.69			18.29		
ρ_{bed} (kg/m^3)	1475			1436			1481		
δ_{bed} (kPa)	0.38			0.45			0.43		

Table C7: Data from the 0.14 m internal diameter column for powder P5 at superficial gas velocities of 0.66, 0.72 and 0.77 m/s.

Time (s)	U = 0.66 m/s			U = 0.72 m/s			U = 0.77 m/s		
	Run 1	Run 2	Run 3	Run 1	Run 2	Run 3	Run 1	Run 2	Run 3
	Bed height (m)			*Bed height (m)*			*Bed height (m)*		
5	1.100	1.093	1.087	1.207	1.186	-	-	-	-
10	1.094	1.089	1.082	1.194	1.174	-	-	-	-
15	1.088	1.086	1.073	1.174	1.144	1.134	1.157	1.145	1.144
20	1.081	1.078	1.064	1.167	1.137	1.121	1.141	1.131	1.120
25	1.074	1.071	1.055	1.137	1.120	1.108	1.126	1.113	1.105
30	1.068	1.063	1.049	1.117	1.104	1.094	1.107	1.098	1.092
40	1.058	1.057	1.045	1.091	1.081	1.071	1.083	1.074	1.068
50	1.058	1.054	1.045	1.076	1.069	1.057	1.069	1.060	1.052
60	1.058	1.054	1.045	1.069	1.061	1.052	1.059	1.053	1.046
80	1.058	1.054	1.045	1.063	1.055	1.049	1.054	1.049	1.043
100	1.058	1.054	1.045	1.061	1.055	1.048	1.052	1.048	1.041
120	1.058	1.054	1.045	1.060	1.055	1.048	1.052	1.048	1.041
H_{bed} (m)	1.350	1.340	1.310	1.570	1.550	1.540	1.600	1.570	1.550
H_d (m)	1.107	1.101	1.096	1.229	1.202	1.174	1.207	1.193	1.192
w (kg)	31.05	30.93	30.67	31.11	30.96	30.76	30.87	30.76	30.55
ε_d	0.431	0.430	0.432	0.486	0.477	0.468	0.481	0.477	0.480
ε_b	0.180	0.178	0.163	0.217	0.225	0.238	0.246	0.240	0.231
ε	0.533	0.531	0.525	0.598	0.594	0.595	0.608	0.602	0.600
	Averages			*Averages*			*Averages*		
ε_d	0.431			0.477			0.479		
ε_b	0.174			0.227			0.239		
ε	0.530			0.596			0.604		
H_{bed} (m)	1.333			1.553			1.573		
H_0 (m)	1.052			1.054			1.047		
ΔP_{bed} (kPa)	17.24			17.09			14.52		
ρ_{bed} (kg/m^3)	1505			1294			1269		
δ_{bed} (kPa)	0.44			0.49			-		
Average bulk density (kg/m^3)	1907								
Particle density (kg/m^3)	3200								
Column cross-sectional area (m^2)	0.01539								

C1.4 Powder P6

Table C8: Data from the 0.14 m internal diameter column for powder P6 at superficial gas velocities of 0.11, 0.23 and 0.34 m/s.

Time (s)	U = 0.11 m/s			U = 0.23 m/s			U = 0.34 m/s		
	Run 1	Run 2	Run 3	Run 1	Run 2	Run 3	Run 1	Run 2	Run 3
	Bed height (m)			*Bed height (m)*			*Bed height (m)*		
5	1.104	1.108	1.100	1.085	1.078	1.088	1.110	1.080	1.115
10	1.089	1.089	1.081	1.067	1.059	1.074	1.094	1.064	1.095
15	1.072	1.072	1.067	1.054	1.046	1.059	1.078	1.048	1.072
20	1.058	1.058	1.054	1.042	1.031	1.045	1.064	1.037	1.053
25	1.044	1.045	1.043	1.030	1.020	1.035	1.048	1.027	1.035
30	1.035	1.034	1.033	1.020	1.009	1.025	1.038	1.020	1.021
40	1.017	1.018	1.016	1.007	0.993	1.009	1.012	1.005	1.000
50	1.007	1.005	1.006	0.993	0.981	0.996	1.000	0.995	0.998
60	0.996	0.995	0.995	0.985	0.975	0.989	0.992	0.984	0.982
80	0.987	0.986	0.985	0.975	0.963	0.981	0.977	0.975	0.978
100	0.980	0.980	0.978	0.966	0.957	0.975	0.977	0.970	0.970
120	0.975	0.973	0.971	0.963	0.954	0.970	0.972	0.968	0.963
H_{bed} (m)	1.222	1.214	1.215	1.231	1.206	1.221	1.286	1.261	1.290
H_d (m)	1.120	1.124	1.114	1.098	1.092	1.103	1.125	1.094	1.136
w (kg)	34.82	34.75	34.68	34.39	34.07	34.64	34.71	34.57	34.39
ε_d	0.561	0.563	0.560	0.558	0.559	0.556	0.564	0.554	0.572
ε_b	0.084	0.074	0.083	0.108	0.095	0.097	0.125	0.132	0.119
ε	0.598	0.596	0.597	0.605	0.601	0.599	0.619	0.613	0.623
	Averages			*Averages*			*Averages*		
ε_d	0.562			0.558			0.563		
ε_b	0.080			0.100			0.126		
ε	0.597			0.602			0.618		
H_{bed} (m)	1.217			1.219			1.279		
H_0 (m)	0.973			0.962			0.968		
ΔP_{bed} (kPa)	21.65			21.29			21.73		
ρ_{bed} (kg/m^3)	1855			1831			1755		
δ_{bed} (kPa)	0.18			0.34			0.48		

Table C9: Data from the 0.14 m internal diameter column for powder P6 at superficial gas velocities of 0.44, 0.52 and 0.60 m/s.

Time (s)	U = 0.44 m/s			U = 0.52 m/s			U = 0.60 m/s		
	Run 1	Run 2	Run 3	Run 1	Run 2	Run 3	Run 1	Run 2	Run 3
	Bed height (m)			*Bed height (m)*			*Bed height (m)*		
5	1.097	1.079	1.098	1.094	1.097	1.080	1.093	-	1.090
10	1.080	1.062	1.078	1.079	1.076	1.060	1.079	1.085	1.078
15	1.064	1.047	1.059	1.059	1.054	1.040	1.060	1.065	1.059
20	1.046	1.034	1.043	1.042	1.038	1.026	1.043	1.044	1.039
25	1.035	1.022	1.026	1.029	1.024	1.013	1.029	1.031	1.025
30	1.022	1.010	1.014	1.016	1.013	1.004	1.019	1.018	1.014
40	1.006	0.993	0.996	0.998	0.994	0.986	1.008	1.004	0.996
50	0.991	0.984	0.979	0.984	0.982	0.979	0.997	0.993	0.984
60	0.982	0.975	0.973	0.977	0.974	0.966	0.989	0.986	0.975
80	0.970	0.970	0.966	0.970	0.963	0.958	0.982	0.979	0.970
100	0.967	0.963	0.958	0.964	0.958	0.952	0.977	0.970	0.965
120	0.964	0.957	0.953	0.959	0.952	0.950	0.969	0.970	0.963
H_{bed} (m)	1.320	1.311	1.322	1.343	1.342	1.334	1.370	1.375	1.387
H_d (m)	1.114	1.093	1.116	1.113	1.116	1.097	1.111	1.126	1.110
w (kg)	34.43	34.18	34.04	34.25	34.00	33.93	34.61	34.64	34.39
ε_d	0.564	0.558	0.569	0.565	0.570	0.563	0.560	0.566	0.562
ε_b	0.156	0.166	0.156	0.171	0.168	0.178	0.189	0.181	0.200
ε	0.632	0.632	0.636	0.640	0.642	0.641	0.643	0.644	0.650
	Averages			*Averages*			*Averages*		
ε_d	0.564			0.566			0.563		
ε_b	0.159			0.172			0.190		
ε	0.633			0.641			0.646		
H_{bed} (m)	1.318			1.340			1.377		
H_0 (m)	0.958			0.954			0.967		
ΔP_{bed} (kPa)	21.79			21.83			22.06		
ρ_{bed} (kg/m^3)	1687			1652			1629		
δ_{bed} (kPa)	0.57			0.63			0.73		

Table C10: Data from the 0.14 m internal diameter column for powder P6 at superficial gas velocities of 0.66, 0.72 and 0.77 m/s.

Time (s)	U = 0.66 m/s			U = 0.72 m/s			U = 0.77 m/s		
	Run 1	Run 2	Run 3	Run 1	Run 2	Run 3	Run 1	Run 2	Run 3
	Bed height (m)			*Bed height (m)*			*Bed height (m)*		
5	1.074	1.075	1.078	-	1.098	1.078	1.048	-	1.061
10	1.064	1.066	1.067	1.046	1.086	1.069	1.038	-	1.051
15	1.045	1.050	1.047	1.031	1.068	1.052	1.030	1.038	1.041
20	1.030	1.030	1.026	1.012	1.055	1.034	1.012	1.024	1.024
25	1.019	1.013	1.009	0.997	1.039	1.018	0.997	1.009	1.005
30	1.006	1.000	1.000	0.984	1.025	1.010	0.985	0.998	0.993
40	0.994	0.982	0.989	0.970	1.006	0.990	0.970	0.982	0.979
50	0.982	0.974	0.972	0.959	0.994	0.980	0.960	0.972	0.971
60	0.976	0.966	0.967	0.955	0.985	0.975	0.955	0.969	0.966
80	0.969	0.960	0.960	0.950	0.975	0.966	0.945	0.962	0.957
100	0.965	0.952	0.955	0.943	0.967	0.961	0.945	0.956	0.953
120	0.963	0.950	0.952	0.941	0.964	0.958	0.942	0.954	0.953
H_{bed} (m)	1.367	1.374	1.380	1.369	1.397	1.389	1.386	1.373	1.374
H_d (m)	1.091	1.093	1.099	1.081	1.114	1.096	1.063	1.082	1.078
w (kg)	34.39	33.93	34.00	33.61	34.43	34.21	33.64	34.07	34.04
ε_d	0.555	0.562	0.563	0.561	0.564	0.559	0.553	0.555	0.554
ε_b	0.202	0.205	0.204	0.210	0.203	0.211	0.233	0.212	0.215
ε	0.645	0.651	0.652	0.653	0.652	0.652	0.657	0.650	0.650
	Averages			*Averages*			*Averages*		
ε_d	0.560			0.561			0.554		
ε_b	0.203			0.208			0.220		
ε	0.649			0.652			0.652		
H_{bed} (m)	1.365			1.372			1.378		
H_0 (m)	0.955			0.954			0.950		
ΔP_{bed} (kPa)	21.78			21.71			21.57		
ρ_{bed} (kg/m^3)	1613			1599			1599		
δ_{bed} (kPa)	0.74			0.77			0.84		
Average bulk density (kg/m^3)	2320								
Particle density (kg/m^3)	4600								
Column cross-sectional area (m^2)	0.01539								

Table C11: Data from the 0.14 m internal diameter column for powder P7.

Time (s)	0.09 m/s	0.12 m/s	0.17 m/s	0.21 m/s	0.32 m/s	0.42 m/s	0.52 m/s
	Bed height (m)						
5	1.152	1.148	1.145	1.141	1.159	-	1.095
10	1.142	1.138	1.134	1.131	1.148	-	1.084
15	1.131	1.126	1.122	1.121	1.137	-	1.076
20	1.119	1.116	1.112	1.111	1.125	-	1.063
30	1.100	1.095	1.092	1.087	1.105	-	1.037
40	1.081	1.078	1.073	1.071	1.082	-	1.016
50	1.065	1.068	1.059	1.055	1.063	-	1.007
60	1.057	1.057	1.052	1.050	1.052	-	0.999
80	1.050	1.050	1.047	1.045	1.045	-	0.994
100	1.046	1.046	1.044	1.043	1.044	-	0.994
120	1.045	1.045	1.045	1.043	1.044	-	0.994
H_{bed} (m)	1.262	1.303	1.348	1.397	1.511	1.546	1.585
H_d (m)	1.160	1.154	1.152	1.150	1.168	1.156	1.106
w (kg)	13.90	13.90	13.90	13.90	13.90	13.90	13.90
ε_d	0.401	0.398	0.397	0.396	0.405	0.397	0.372
ε_b	0.081	0.114	0.145	0.177	0.227	0.254	0.302
ε	0.449	0.467	0.485	0.503	0.540	0.551	0.562
H_0 (m)	1.045	1.045	1.045	1.043	1.044	-	0.994
ΔP_{bed} (kPa)	7.89	7.89	7.89	7.89	7.76	7.63	6.97
ρ_{bed} (kg/m^3)	716	693	670	647	598	584	570
Average bulk density (kg/m^3)				870			
Particle density (kg/m^3)				1300			
Column cross-sectional area (m^2)				0.01539			

C2 Sample calculation of bed voidages

In this section the procedure used to calculate the dense phase voidage, bubble fraction and overall bed voidage from the experimental results will be illustrated through a sample calculation. For this sample calculation the experimental data for powder P5 will be used as given in Table C5, for U = 0.11 m/s, Run 1.

The first step is to plot the bed height as a function of time during the settling process. This is shown in Figure C1.

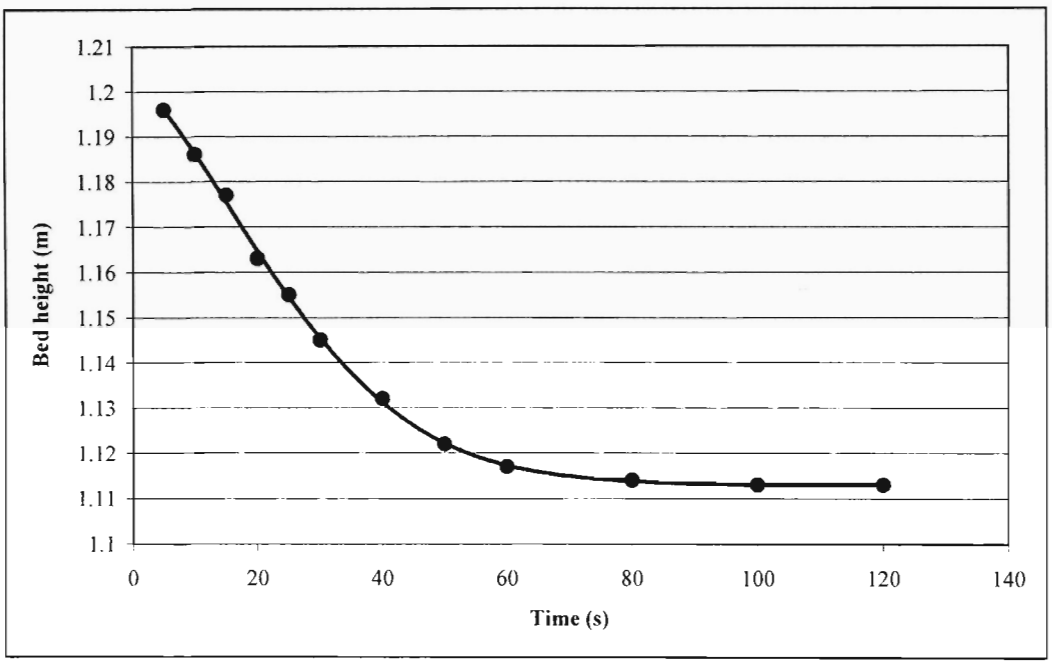

Figure C1: Bed height obtained from the bed collapse test for powder P5 at U = 0.11 m/s, Run 1.

By plotting only the linear portion during the first 30 seconds and fitting a linear equation to these data points, one can obtain the y-intercept which will be the height of the dense phase at time zero. This is illustrated in Figure C2. In this case the height of the dense phase or H_d = 1.207 m.

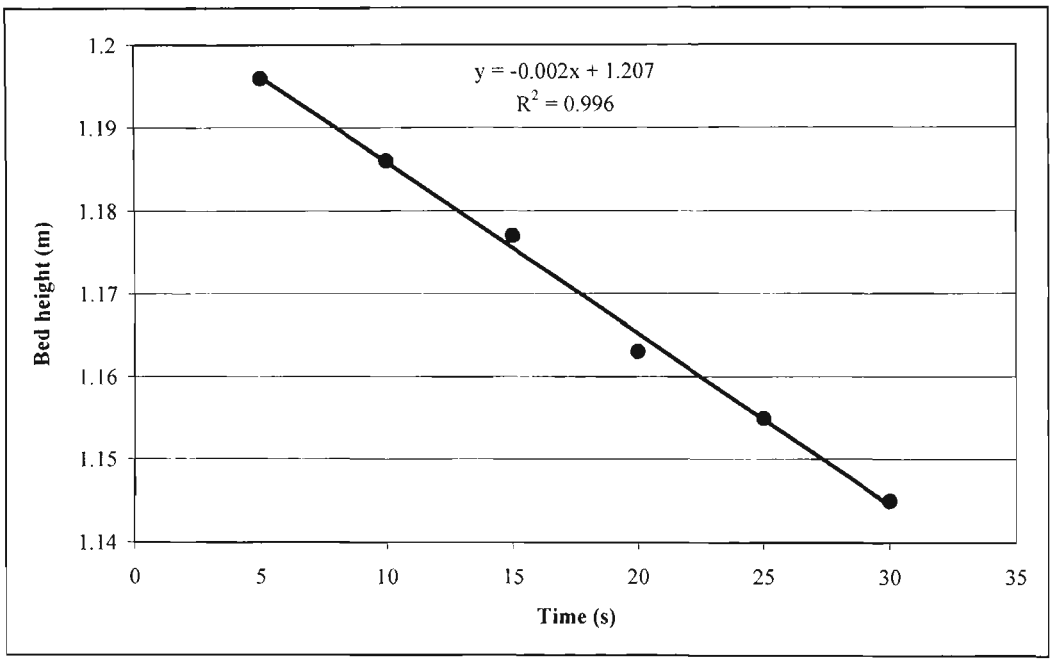

Figure C2: Linear portion of the bed collapse test data.

The following relationship can now be derived for the dense phase voidage:

$$\rho_d = \frac{w}{V_{bed}} \tag{C1}$$

$$\rho_d = \rho_p (1 - \varepsilon_d) \tag{C2}$$

$$V_{bed} = AH_d \tag{C3}$$

Substituting equations C2 and C3 into equation C1 and solving for ε_d the following expression for the dense phase voidage can be obtained:

$$\varepsilon_d = 1 - \frac{w}{A\rho_p H_d} \tag{2-55}$$

As shown above, H_d = 1.207 m. From Table C5 and C7, the following can be obtained: w = 32.67 kg, ρ_p = 3200 kg/m^3 and A = 0.01539 m^2. Substituting these values into equation 2-55, results in the following for the dense phase voidage:

$$\varepsilon_d = 1 - \frac{w}{A\rho_p H_d} = 1 - \frac{32.67}{(0.01539)(3200)(1.207)} = 1 - 0.550 = \underline{0.450}$$

According to the definition of the bubble fraction:

$$\varepsilon_b = \frac{V_b}{V_{bed}} \tag{C4}$$

And V_b is related to the volume of the bed and the volume of the dense phase as follows:

$$V_b = V_{bed} - V_d \tag{C5}$$

Hence, the equation for the bubble fraction can be simplified as follows:

$$\varepsilon_b = \frac{V_{bed} - V_d}{V_{bed}} = \frac{AH_{bed} - AH_d}{AH_{bed}} = 1 - \frac{H_d}{H_{bed}} \tag{2-56}$$

From Table C5 it can be seen that for Run 1, the average fluidized bed height is, H_{bed} = 1.280 m and from above H_d = 1.207 m. Therefore, substitution of these values into equation 2-56 results in:

$$\varepsilon_b = 1 - \frac{H_d}{H_{bed}} = 1 - \frac{1.207}{1.280} = 1 - 0.943 = \underline{0.057}\,.$$

In order to calculate the overall bed voidage (ε) from the dense phase voidage and bubble fraction an equation is required which relates the overall bed voidage to the dense phase voidage and bubble fraction. This can be obtained as follows:

$$\varepsilon = \frac{V_{gas}}{V_{bed}} = \frac{\varepsilon_b V_{bed} + \varepsilon_d V_d}{V_{bed}}$$

$$\varepsilon V_{bed} = \varepsilon_b V_{bed} + \varepsilon_d V_d \quad \text{but } V_d = V_{bed} - V_b = V_{bed} - \varepsilon_b V_{bed} = V_{bed}(1-\varepsilon_b)$$

Therefore, $\varepsilon V_{bed} = \varepsilon_b V_{bed} + \varepsilon_d \left[V_{bed}(1-\varepsilon_b) \right]$

$$\varepsilon = \varepsilon_b + \varepsilon_d (1-\varepsilon_b)$$

$$1-\varepsilon = 1-\left[\varepsilon_b + \varepsilon_d (1-\varepsilon_b) \right]$$

$$1-\varepsilon = 1-\varepsilon_b - \varepsilon_d (1-\varepsilon_b)$$

$$1-\varepsilon = (1-\varepsilon_b) - \varepsilon_d (1-\varepsilon_b)$$

$$1-\varepsilon = (1-\varepsilon_b)(1-\varepsilon_d)$$

$$\varepsilon = 1-(1-\varepsilon_b)(1-\varepsilon_d) \qquad (2\text{-}57)$$

Substituting the values obtained above for ε_b and ε_d the following is obtained:

$$\varepsilon = 1-(1-\varepsilon_b)(1-\varepsilon_d) = 1-(1-0.057)(1-0.450)$$

$$\varepsilon = 1-(0.943)(0.550)$$

$$\varepsilon = 1-0.519$$

$$\varepsilon = \underline{0.481}$$

In summary, for powder P5 at U = 0.11 m/s and Run 1: $\varepsilon_d = 0.450$, $\varepsilon_b = 0.057$ and $\varepsilon = 0.481$. Slight differences in these values and those presented in the tables above are due to rounding.

APPENDIX D: SUMMARY OF MEASURED ENTRAINMENT FLUX

Table D1: Entrainment flux data from the 0.14 m internal diameter column for powders P1, P3, P4, P5 and P6.

U (m/s)	P1 (kg/m^2.s)	U (m/s)	P3 (kg/m^2.s)	U (m/s)	P4 (kg/m^2.s)
0.24	0.00771	0.18	0.000271	0.23	0.000596
0.34	0.0277	0.23	0.00105	0.28	0.00325
0.40	0.0437	0.29	0.00525	0.33	0.0104
0.45	0.0614	0.34	0.0160	0.38	0.0155
0.49	0.0800	0.39	0.0309	0.43	0.0184
0.52	0.121	0.44	0.0495	0.48	0.0220
0.57	0.136	0.49	0.0782	0.52	0.0238
0.61	0.172	0.53	0.120	0.60	0.0336
0.67	0.260	0.60	0.278	0.65	0.0411
0.73	0.349	0.67	0.572	0.72	0.0509
0.79	0.468	0.72	0.931	0.77	0.0823
		0.78	1.503		
U (m/s)	**P5 (kg/m^2.s)**	**U (m/s)**	**P6 (kg/m^2.s)**		
0.17	0.000180	0.18	0.000271		
0.23	0.00123	0.23	0.000686		
0.28	0.00357	0.29	0.00217		
0.34	0.00664	0.34	0.00285		
0.38	0.00891	0.39	0.00386		
0.43	0.0157	0.44	0.00491		
0.47	0.0273	0.49	0.00708		
0.51	0.0444	0.53	0.0110		
0.59	0.108	0.59	0.0253		
0.65	0.338	0.66	0.0526		
0.71	0.637	0.72	0.110		
0.76	0.937	0.78	0.235		

APPENDIX E: SAMPLE CALCULATIONS AND SUMMARY OF ENTRAINMENT FLUX USING LITERATURE CORRELATIONS

In this section powder P3 will be used as an example to illustrate how the entrainment flux correlations from the literature was used to calculate the entrainment flux for powder P3 for the operating conditions used for the test work. Since all the correlations calculate the elutriation rate constant for the particle cut size i, the sample calculation will be based on only one cut size and only the final results will presented for all the other particle cut sizes. The particle properties and operating conditions that will be used for the sample calculations are summarised in Table E1.

Table E1: Properties of P3 and operating conditions used in sample calculations.

Property	Value
Particle density (kg/m^3)	4600
Mean particle size – d_m (μm)	42
Fraction less than 31 μm	0.383
Fraction less than 22 μm	0.263
Bed temperature (°C)	23.5
Freeboard pressure (kPa, absolute)	86
Gas molecular weight (kg/kmol)	28.84
Gas viscosity (kg/m.s)	1.8217×10^{-5}
Column internal diameter (m)	0.14
Freeboard height (m)	4.571
Superficial gas velocity (m/s)	0.5283

Most of the entrainment correlations make use of the particle terminal velocity and some require the minimum fluidization velocity of the powder. These will be calculated first.

E1 Calculation of minimum fluidization velocity

Since U_{mf} was not measured, it was calculated using the Wen and Yu (1966 cited by Yang 2003) correlation, which is given in equation 2-27.

$$Re_{mf} = \sqrt{33.7^2 + 0.0408Ar} - 33.7 \qquad (2\text{-}27)$$

The equations for Re_{mf} and Ar are given in equations 2-20 and 2-16 respectively.

$$Re_{mf} = \frac{d_{sv} U_{mf} \rho_g}{\mu} \tag{2-20}$$

$$Ar = \frac{d_p^3 \rho_g (\rho_p - \rho_g) g}{\mu^2} \tag{2-16}$$

The gas density was calculated using the ideal gas law (equation E1)

$$\rho_g = \frac{PM}{R_g T} \tag{E1}$$

Substituting the relevant values from Table E1, the gas density is calculated to be:

$$\rho_g = \frac{PM}{R_g T} = \frac{(86)(28.84)}{(8.314)(296.65)} = \underline{1.006 \text{ kg/m}^3}$$

The Archimedes number (Ar) is then calculated to be:

$$Ar = \frac{\rho_g d_p^3 (\rho_p - \rho_g) g}{\mu^2} = \frac{(1.006)(42 \times 10^{-6})^3 (4600 - 1.006)(9.81)}{(1.8217 \times 10^{-5})^2} = \underline{10.13}$$

From Equation 2-27, Re_{mf} is calculated to be:

$$Re_{mf} = \sqrt{33.7^2 + 0.0408(10.13)} - 33.7 = \underline{0.00613}$$

U_{mf} can then be calculated from equation 2-20 as follows:

$$U_{mf} = \frac{Re_{mf} \mu}{\rho_g d_p} = \frac{(0.00613)(1.8217 \times 10^{-5})}{(1.006)(42 \times 10^{-6})}$$

$$\underline{U_{mf} = 0.00264 \text{ m/s}}$$

E2 Calculation of the terminal velocity (U_t)

The terminal velocity of a single spherical particle can be calculated using equation 2-120:

$$U_t = \sqrt{\frac{4d_p(\rho_p - \rho_f)g}{3\rho_f C_D}} \qquad (2\text{-}120)$$

The drag coefficient was calculated using equations 2-123 and 2-124.

$$\text{For } Re_p < 0.01: \quad C_D = \frac{3}{16} + \frac{24}{Re_p} \qquad (2\text{-}123)$$

$$\text{For } 0.01 < Re_p \leq 20: \quad C_D = \frac{24}{Re_p}\left[1 + 0.1315 Re_p^{(0.82 - 0.05\log_{10} Re_p)}\right] \qquad (2\text{-}124)$$

In this example d_{pi} and X_{bi} can be calculated as follows:

fraction < 31μm = 0.383
fraction < 22μm = 0.263

$$d_{pi} = \frac{31+22}{2} = \underline{26.5\mu m}$$

$$X_{bi} = 0.383 - 0.263 = \underline{0.120}$$

Re_p for d_{pi} = 26.5 μm and U = 0.5283 m/s can then be calculated as follows:

$$Re_{pi} = \frac{\rho_g d_{pi} U}{\mu} = \frac{(1.006)(26.5\times10^{-6})(0.5283)}{1.8217\times10^{-5}}$$

$$\underline{Re_{pi} = 0.7731}$$

Since $Re_{pi} > 0.01$, equation 2-124 is used to calculate the drag coefficient:

$$C_D = \frac{24}{Re_p}\left[1 + 0.1315(Re_p)^{(0.82 - 0.05\log_{10} Re_p)}\right]$$

$$C_D = \frac{24}{0.7731}\left[1 + 0.1315(0.7731)^{(0.82 - 0.05\log_{10} 0.7731)}\right]$$

$$\underline{C_D = 34.36}$$

The terminal velocity can then be calculated using equation 2-120:

$$U_{ti} = \sqrt{\frac{4d_{pi}(\rho_p - \rho_g)g}{3\rho_g C_D}} = \sqrt{\frac{4(26.5\times10^{-6})(4600-1.006)9.81}{3(1.006)(34.34)}}$$

$$\underline{U_{ti} = 0.2148 \text{ m/s}}$$

The above terminal velocity will be used in the entrainment flux calculations even though the particles under consideration are not perfectly spherical. Since the particle sphericity was not measured, the drag coefficient could not be corrected to account for particle shape effects. An example of the effect of particle sphericity on the calculated entrainment rate is given in Table 6-6.

E3 Yagi and Aochi correlation

The correlation of Yagi and Aochi (1955 cited by Werther and Hartge 2003) is given by equation 2-137.

$$\frac{K^*_{i\infty} g d_{pi}^2}{\mu(U-U_{ti})^2} = 0.0015 Re_t^{0.6} + 0.01 Re_t^{1.2} \qquad (2\text{-}137)$$

Re_t is first calculated as follows:

$$Re_t = \frac{\rho_g d_{pi} U_{ti}}{\mu} = \frac{(1.006)(26.5\times10^{-6})(0.2148)}{1.8217\times10^{-5}}$$

$$\underline{Re_t = 0.3143}$$

The entrainment flux ($E_{i\infty}$) of d_{pi} is then calculated as follows:

$$\frac{K^*_{i\infty} g d_{pi}^2}{\mu(U-U_{ti})^2} = 0.0015 Re_t^{0.6} + 0.01 Re_t^{1.2} = 0.0015(0.3143)^{0.6} + 0.01(0.3143)^{1.2}$$

$$\frac{K^*_{i\infty}(9.81)(26.5\times10^{-6})^2}{(1.8217\times10^{-5})(0.5283-0.2148)^2} = 0.002868$$

$$K^*_{i\infty} = \frac{0.003242(1.8217\times10^{-5})(0.5283-0.2148)^2}{(9.81)(26.5\times10^{-6})^2} = \underline{0.843\ kg/m^2.s}$$

$$E_{i\infty} = K^*_{i\infty} X_{bi} = (0.843)(0.12) = \underline{0.101\ kg/m^2.s}$$

By repeating the above calculations for each d_{pi} in the particle size distribution, the elutriation rate constant and entrainment flux for each d_{pi} was calculated. The total entrainment flux (E_∞) was then calculated by summing the individual particle entrainment flux ($E_{i\infty}$). The results of these calculations are summarised in Table E2.

Table E2: Calculated entrainment flux for powder P3 at U = 0.5283 m/s using equation 2-137.

Size (μm)	% <	d_{pi} (μm)	X_{bi}	C_D	U_{ti} (m/s)	$K^*_{i\infty}$ (kg/m².s)	$E_{i\infty}$ (kg/m₂.s)
498	100	425	0.003	3.68	2.6267	64.417	0.193
352	99.7	300.5	0.010	4.67	1.9627	28.161	0.282
249	98.7	212.5	0.038	5.99	1.4571	10.991	0.418
176	94.9	150.5	0.068	7.77	1.0761	3.546	0.241
125	88.1	106.5	0.098	10.23	0.7891	0.744	0.073
88	78.3	75	0.122	13.68	0.5727	0.020	0.002
62	66.1	53	0.138	18.43	0.4147	0.122	0.017
44	52.3	37.5	0.140	25.05	0.2992	0.468	0.066
31	38.3	26.5	0.120	34.36	0.2148	0.843	0.101
22	26.3	19	0.107	46.80	0.1558	1.173	0.126
16	15.6	13.5	0.080	64.62	0.1118	1.493	0.119
11	7.6	9.4	0.041	91.39	0.0784	1.847	0.076
7.8	3.5	6.65	0.022	127.75	0.0558	2.248	0.049
5.5	1.3	4.7	0.013	179.24	0.0396	2.757	0.036
3.9	0	3.35	0	249.92	0.0283	3.413	0
2.8	0	1.4	0	592.31	0.0119	6.283	0
						$E_\infty = \sum E_{i\infty}$	**1.799**

E4 Zenz and Weil correlation

The correlation of Zenz and Weil (1958 cited by Tasirin and Geldart 1998) is given by equation 2-138.

$$K_{i\infty}^{*} = \begin{cases} 1.26\times10^{7}\left(\rho_g U\right)\left(\dfrac{U^2}{g d_{pi}\rho_p^2}\right)^{1.88} & \text{when} \quad \dfrac{U^2}{g d_{pi}\rho_p^2} < 3\times10^{-4} \\ 4.31\times10^{4}\left(\rho_g U\right)\left(\dfrac{U^2}{g d_{pi}\rho_p^2}\right)^{1.18} & \text{when} \quad \dfrac{U^2}{g d_{pi}\rho_p^2} > 3\times10^{-4} \end{cases} \qquad (2\text{-}138)$$

The entrainment flux ($E_{i\infty}$) of d_{pi} is calculated as follows:

$$\frac{U^2}{g d_{pi}\rho_p^2} = \frac{(0.5283)^2}{(9.81)\left(26.5\times10^{-6}\right)(4600)^2} = 5.0737\times10^{-5} \quad (\text{which is} < 3\times10^{-4})$$

$$K_{i\infty}^{*} = 1.26\times10^{7}\,(1.006)(0.5283)\left(\frac{0.5283^2}{(9.81)\left(26.5\times10^{-6}\right)(4600)^2}\right)^{1.88}$$

$$\underline{K_{i\infty}^{*} = 0.056 \text{ kg/m}^2\text{.s}}$$

$$E_{i\infty} = K_{i\infty}^{*} X_{bi} = (0.056)(0.12)$$

$$\underline{E_{i\infty} = 0.00677 \text{ kg/m}^2\text{.s}}$$

By repeating the above calculations for each d_{pi} in the particle size distribution, the elutriation rate constant and entrainment flux for each d_{pi} was calculated. The total entrainment flux (E_∞) was then calculated by summing the individual particle entrainment flux ($E_{i\infty}$). The results of these calculations are summarised in Table E3.

Table E3: Calculated entrainment flux for powder P3 at U = 0.5283 m/s using equation 2-138.

Size (μm)	% <	d_{pi} (μm)	X_{bi}	C_D	U_{ti} (m/s)	$K^*_{i\infty}$ (kg/m^2.s)	$E_{i\infty}$ (kg/m^2.s)
498	100	425	0.003	3.68	2.6267	0	0
352	99.7	300.5	0.010	4.67	1.9627	0.000588	0
249	98.7	212.5	0.038	5.99	1.4571	0.00113	0
176	94.9	150.5	0.068	7.77	1.0761	0.00216	0.000147
125	88.1	106.5	0.098	10.23	0.7891	0.00413	0.000405
88	78.3	75	0.122	13.68	0.5727	0.00799	0.000974
62	66.1	53	0.138	18.43	0.4147	0.0153	0.00212
44	52.3	37.5	0.140	25.05	0.2992	0.0294	0.00411
31	38.3	26.5	0.120	34.36	0.2148	0.0565	0.00677
22	26.3	19	0.107	46.80	0.1558	0.106	0.0113
16	15.6	13.5	0.080	64.62	0.1118	0.201	0.0161
11	7.6	9.4	0.041	91.39	0.0784	0.396	0.0162
7.8	3.5	6.65	0.022	127.75	0.0558	0.759	0.0167
5.5	1.3	4.7	0.013	179.24	0.0396	1.458	0.0190
3.9	0	3.35	0	249.92	0.0283	2.249	0
2.8	0	1.4	0	592.31	0.0119	6.296	0
						$E_\infty = \sum E_{i\infty}$	**0.0938**

E5 Wen and Hashinger correlation

The correlation of Wen and Hashinger (1960) is given in equation 2-139.

$$K^*_{i\infty} = 1.52\times10^{-5}\rho_g\left(U-U_{ti}\right)\left[\frac{\left(U-U_{ti}\right)^2}{gd_{pi}}\right]^{0.5} Re_t^{0.725}\left(\frac{\rho_p-\rho_g}{\rho_g}\right)^{1.15} \qquad (2\text{-}139)$$

The entrainment flux ($E_{i\infty}$) of d_{pi} is calculated as follows:

$$K^*_{i\infty} = 1.52\times10^{-5}(1.006)(0.5283-0.2148)\left[\frac{(0.5283-0.2148)^2}{(9.81)(26.5\times10^{-6})}\right]^{0.5}(0.3143)^{0.725}\left(\frac{4600-1.006}{1.006}\right)^{1.15}$$

$$\underline{K^*_{i\infty} = 0.652\ \text{kg/m}^2\text{.s}}$$

$$E_{i\infty} = K^*_{i\infty}X_{bi} = (0.652)(0.12)$$

$$\underline{E_{i\infty} = 0.078\ \text{kg/m}^2\text{.s}}$$

By repeating the above calculations for each d_{pi} in the particle size distribution, the elutriation rate constant and entrainment flux for each d_{pi} was calculated. The total entrainment flux (E_∞) was then calculated by summing the individual particle entrainment flux ($E_{i\infty}$). The results of these calculations are summarised in Table E4.

Table E4: Calculated entrainment flux for powder P3 at U = 0.5283 m/s using equation 2-139.

Size (μm)	% <	d_{pi} (μm)	X_{bi}	C_D	U_{ti} (m/s)	$K^*_{i\infty}$ (kg/m².s)	$E_{i\infty}$ (kg/m².s)
498	100	425	0.003	3.68	2.6267	0	0
352	99.7	300.5	0.010	4.67	1.9627	0	0
249	98.7	212.5	0.038	5.99	1.4571	0	0
176	94.9	150.5	0.068	7.77	1.0761	0	0
125	88.1	106.5	0.098	10.23	0.7891	0	0
88	78.3	75	0.122	13.68	0.5727	0	0
62	66.1	53	0.138	18.43	0.4147	0.161	0.022
44	52.3	37.5	0.140	25.05	0.2992	0.478	0.067
31	38.3	26.5	0.120	34.36	0.2148	0.652	0.078
22	26.3	19	0.107	46.80	0.1558	0.676	0.072
16	15.6	13.5	0.080	64.62	0.1118	0.616	0.049
11	7.6	9.4	0.041	91.39	0.0784	0.512	0.021
7.8	3.5	6.65	0.022	127.75	0.0558	0.408	0.009
5.5	1.3	4.7	0.013	179.24	0.0396	0.315	0.004
3.9	0	3.35	0	249.92	0.0283	0.240	0
2.8	0	1.4	0	592.31	0.0119	0.112	0
						$E_\infty = \sum E_{i\infty}$	**0.323**

E6 Tanaka *et al.* correlation

The correlation of Tanaka *et al.* (1972) is given in equation 2-140.

$$K_{i\infty}^{*} = 4.6\times10^{-2}\rho_g\left(U-U_{ti}\right)\left[\frac{\left(U-U_{ti}\right)^2}{gd_{pi}}\right]^{0.5} Re_t^{0.3}\left(\frac{p_p-\rho_g}{\rho_g}\right)^{0.15} \qquad (2\text{-}140)$$

The entrainment flux ($E_{i\infty}$) of d_{pi} is calculated as follows:

$$K_{i\infty}^{*} = 4.6\times10^{-2}\rho_g\left(U-U_{ti}\right)\left[\frac{\left(U-U_{ti}\right)^2}{gd_{pi}}\right]^{0.5} Re_t^{0.3}\left(\frac{p_p-\rho_g}{\rho_g}\right)^{0.15}$$

$$K_{i\infty}^{*} = 4.6\times10^{-2}(1.006)(0.5283-0.2148)\left[\frac{(0.5283-0.2148)^2}{(9.81)(26.5\times10^{-6})}\right]^{0.5}(0.3143)^{0.3}$$

$$\left(\frac{4600-1.006}{1.006}\right)^{0.15}$$

$$\underline{K_{i\infty}^{*} = 0.705\ \text{kg/m}^2\text{.s}}$$

$$E_{i\infty} = K_{i\infty}^{*}X_{bi} = (0.705)(0.12)$$

$$\underline{E_{i\infty} = 0.0846\ \text{kg/m}^2\text{.s}}$$

By repeating the above calculations for each d_{pi} in the particle size distribution, the elutriation rate constant and entrainment flux for each d_{pi} was calculated. The total entrainment flux (E_∞) was then calculated by summing the individual particle entrainment flux ($E_{i\infty}$). The results of these calculations are summarised in Table E5.

Table E5: Calculated entrainment flux for powder P3 at U = 0.5283 m/s using equation 2-140.

Size (μm)	% <	d_{pi} (μm)	X_{bi}	C_D	U_{ti} (m/s)	$K^*_{i\infty}$ (kg/m².s)	$E_{i\infty}$ (kg/m².s)
498	100	425	0.003	3.68	2.6267	0	0
352	99.7	300.5	0.010	4.67	1.9627	0	0
249	98.7	212.5	0.038	5.99	1.4571	0	0
176	94.9	150.5	0.068	7.77	1.0761	0	0
125	88.1	106.5	0.098	10.23	0.7891	0	0
88	78.3	75	0.122	13.68	0.5727	0	0
62	66.1	53	0.138	18.43	0.4147	0.0982	0.0136
44	52.3	37.5	0.140	25.05	0.2992	0.388	0.0543
31	38.3	26.5	0.120	34.36	0.2148	0.705	0.0846
22	26.3	19	0.107	46.80	0.1558	0.966	0.103
16	15.6	13.5	0.080	64.62	0.1118	1.171	0.0937
11	7.6	9.4	0.041	91.39	0.0784	1.321	0.0542
7.8	3.5	6.65	0.022	127.75	0.0558	1.410	0.0310
5.5	1.3	4.7	0.013	179.24	0.0396	1.459	0.0190
3.9	0	3.35	0	249.92	0.0283	1.477	0
2.8	0	1.4	0	592.31	0.0119	1.446	0
						$E_\infty = \sum E_{i\infty}$	**0.454**

E7 Merrick and Highley correlation

The correlation of Merrick and Highley (1974) is given in equation 2-141.

$$K^*_{i\infty} = \rho_g U\left\{B + 130\exp\left[-10.4\left(\frac{U_t}{U}\right)^{0.5}\left(\frac{U_{mf}}{U-U_{mf}}\right)^{0.25}\right]\right\} \qquad (2\text{-}141)$$

where $B = 10^{-3}$ to 10^{-4}

The entrainment flux ($E_{i\infty}$) of d_{pi} is calculated as follows (using an average value for B of 0.0055):

$$K^*_{i\infty} = (1.006)(0.5283)\left\{0.0055 + 130\exp\left[-10.4\left(\frac{0.2148}{0.5283}\right)^{0.5}\left(\frac{0.00264}{0.5283-0.00264}\right)^{0.25}\right]\right\}$$

$$K^{*}_{i\infty} = 11.811 \text{ kg/m}^2\text{.s}$$

$$E_{i\infty} = K^{*}_{i\infty} X_{bi} = (11.811)(0.12)$$

$$E_{i\infty} = 1.417 \text{ kg/m}^2\text{.s}$$

By repeating the above calculations for each d_{pi} in the particle size distribution, the elutriation rate constant and entrainment flux for each d_{pi} was calculated. The total entrainment flux (E_∞) was then calculated by summing the individual particle entrainment flux ($E_{i\infty}$). The results of these calculations are summarised in Table E6.

Table E6: Calculated entrainment flux for powder P3 at U = 0.5283 m/s using equation 2-141.

Size (μm)	% <	d_{pi} (μm)	X_{bi}	C_D	U_{ti} (m/s)	$K^{*}_{i\infty}$ (kg/m².s)	$E_{i\infty}$ (kg/m².s)
498	100	425	0.003	3.68	2.6267	0.144	0.000432
352	99.7	300.5	0.010	4.67	1.9627	0.332	0.00332
249	98.7	212.5	0.038	5.99	1.4571	0.695	0.0264
176	94.9	150.5	0.068	7.77	1.0761	1.326	0.0902
125	88.1	106.5	0.098	10.23	0.7891	2.340	0.229
88	78.3	75	0.122	13.68	0.5727	3.863	0.471
62	66.1	53	0.138	18.43	0.4147	5.937	0.819
44	52.3	37.5	0.140	25.05	0.2992	8.590	1.203
31	38.3	26.5	0.120	34.36	0.2148	11.811	1.417
22	26.3	19	0.107	46.80	0.1558	15.345	1.642
16	15.6	13.5	0.080	64.62	0.1118	19.318	1.545
11	7.6	9.4	0.041	91.39	0.0784	23.756	0.974
7.8	3.5	6.65	0.022	127.75	0.0558	28.076	0.618
5.5	1.3	4.7	0.013	179.24	0.0396	32.353	0.421
3.9	0	3.35	0	249.92	0.0283	36.373	0
2.8	0	1.4	0	592.31	0.0119	45.583	0
						$E_\infty = \sum E_{i\infty}$	**9.459**

E8 Geldart *et al.* correlation

The correlation of Geldart *et al.* (1979) is given in equations 2-142 and 2-142a.

$$K_{i\infty}^{*} = 23.7\rho_e U \exp\left(\frac{-5.4U_{ti}}{U}\right) \qquad (2\text{-}142)$$

$$\rho_e = \rho_g + \sum \rho_i \qquad (2\text{-}142a)$$

Note: To simplify the calculations, ρ_e was replaced by ρ_g. Use of equation 2-142a would have resulted in a higher entrainment rate.

The entrainment flux ($E_{i\infty}$) of d_{pi} is calculated as follows:

$$K_{i\infty}^{*} = 23.7\rho_g U \exp\left(\frac{-5.4U_{ti}}{U}\right)$$

$$K_{i\infty}^{*} = 23.7(1.006)(0.5283)\exp\left(\frac{-5.4\times 0.2148}{0.5283}\right)$$

$$\underline{K_{i\infty}^{*} = 1.401\ \text{kg/m}^2\text{.s}}$$

$$E_{i\infty} = K_{i\infty}^{*} X_{bi} = (1.401)(0.12)$$

$$\underline{E_{i\infty} = 0.168\ \text{kg/m}^2\text{.s}}$$

By repeating the above calculations for each d_{pi} in the particle size distribution, the elutriation rate constant and entrainment flux for each d_{pi} was calculated. The total entrainment flux (E_∞) was then calculated by summing the individual particle entrainment flux ($E_{i\infty}$). The results of these calculations are summarised in Table E7.

Table E7: Calculated entrainment flux for powder P3 at U = 0.5283 m/s using equation 2-142.

Size (μm)	% <	d_{pi} (μm)	X_{bi}	C_D	U_{ti} (m/s)	$K^*_{i\infty}$ (kg/m^2.s)	$E_{i\infty}$ (kg/m^2.s)
498	100	425	0.003	3.68	2.6267	0	0
352	99.7	300.5	0.010	4.67	1.9627	0	0
249	98.7	212.5	0.038	5.99	1.4571	0	0
176	94.9	150.5	0.068	7.77	1.0761	0	0
125	88.1	106.5	0.098	10.23	0.7891	0.00395	0.000387
88	78.3	75	0.122	13.68	0.5727	0.0361	0.00441
62	66.1	53	0.138	18.43	0.4147	0.182	0.0251
44	52.3	37.5	0.140	25.05	0.2992	0.591	0.0828
31	38.3	26.5	0.120	34.36	0.2148	1.401	0.168
22	26.3	19	0.107	46.80	0.1558	2.560	0.274
16	15.6	13.5	0.080	64.62	0.1118	4.016	0.321
11	7.6	9.4	0.041	91.39	0.0784	5.648	0.232
7.8	3.5	6.65	0.022	127.75	0.0558	7.118	0.157
5.5	1.3	4.7	0.013	179.24	0.0396	8.400	0.109
3.9	0	3.35	0	249.92	0.0283	9.427	0
2.8	0	1.4	0	592.31	0.0119	11.150	0
						$E_\infty = \sum E_{i\infty}$	**1.373**

E9 Lin *et al.* correlation

The correlation of Lin *et al.* (1980) is given in equation 2-143.

$$K^*_{i\infty} = 9.43\times10^{-4}\rho_g U\left(\frac{U^2}{gd_{pi}}\right)^{1.65} \qquad (2\text{-}143)$$

The entrainment flux ($E_{i\infty}$) of d_{pi} is calculated as follows:

$$K^*_{i\infty} = 9.43\times10^{-4}\rho_g U\left(\frac{U^2}{gd_{pi}}\right)^{1.65}$$

$$K^*_{i\infty} = 9.43\times10^{-4}(1.006)(0.5283)\left(\frac{0.5283^2}{9.81\times26.5\times10^{-6}}\right)^{1.65}$$

$$\underline{K^*_{i\infty} = 50.203\ \text{kg/m}^2\text{.s}}$$

$$E_{i\infty} = K^*_{i\infty}X_{bi} = (50.203)(0.12)$$

$$\underline{E_{i\infty} = 6.024\ \text{kg/m}^2\text{.s}}$$

By repeating the above calculations for each d_{pi} in the particle size distribution, the elutriation rate constant and entrainment flux for each d_{pi} was calculated. The total entrainment flux (E_∞) was then calculated by summing the individual particle entrainment flux ($E_{i\infty}$). The results of these calculations are summarised in Table E8.

Table E8: Summary of entrainment flux calculations for powder P3 at U = 0.5283 m/s using equation 2-143.

Size (μm)	% <	d_{pi} (μm)	X_{bi}	C_D	U_{ti} (m/s)	$K^*_{i\infty}$ (kg/m².s)	$E_{i\infty}$ (kg/m².s)
498	100	425	0.003	3.68	2.6267	0.516	0.00155
352	99.7	300.5	0.010	4.67	1.9627	0.913	0.00913
249	98.7	212.5	0.038	5.99	1.4571	1.618	0.0615
176	94.9	150.5	0.068	7.77	1.0761	2.859	0.194
125	88.1	106.5	0.098	10.23	0.7891	5.058	0.496
88	78.3	75	0.122	13.68	0.5727	9.021	1.101
62	66.1	53	0.138	18.43	0.4147	15.997	2.208
44	52.3	37.5	0.140	25.05	0.2992	28.310	3.963
31	38.3	26.5	0.120	34.36	0.2148	50.203	6.024
22	26.3	19	0.107	46.80	0.1558	86.924	9.301
16	15.6	13.5	0.080	64.62	0.1118	152.768	12.221
11	7.6	9.4	0.041	91.39	0.0784	277.602	11.382
7.8	3.5	6.65	0.022	127.75	0.0558	491.392	10.811
5.5	1.3	4.7	0.013	179.24	0.0396	871.209	11.326
3.9	0	3.35	0	249.92	0.0283	1523.210	0
2.8	0	1.4	0	592.31	0.0119	6426.471	0
						$E_\infty = \sum E_{i\infty}$	**69.098**

E10 Wen and Chen correlation

The correlation of Wen and Chen (1982) is given in equations 2-144 to 2-144b.

$$K_{i\infty}^{*} = \rho_p (1-\varepsilon_i)(U - U_{ti}) \tag{2-144}$$

$$\varepsilon_i = \left[1 + \frac{\lambda (U - U_{ti})^2}{2gD}\right]^{-1/4.7} \tag{2-144a}$$

$$\text{when} \quad \frac{\rho_g (U - U_{ti}) d_{pi}}{\mu} \le \frac{2.38}{D}$$

$$\frac{\lambda \rho_p}{d_{pi}^2}\left(\frac{\mu}{\rho_g}\right)^{2.5} = 5.17 D^2 \left[\frac{\rho_g (U - U_{ti}) d_{pi}}{\mu}\right]^{-1.5}$$

(2-144b)

$$\text{when} \quad \frac{\rho_g (U - U_{ti}) d_{pi}}{\mu} \ge \frac{2.38}{D}$$

$$\frac{\lambda \rho_p}{d_{pi}^2}\left(\frac{\mu}{\rho_g}\right)^{2.5} = 12.3 D \left[\frac{\rho_g (U - U_{ti}) d_{pi}}{\mu}\right]^{-2.5}$$

The entrainment flux ($E_{i\infty}$) of d_{pi} is calculated as follows:

$$\frac{2.38}{D} = \frac{2.38}{0.14} = 17$$

$$\frac{\rho_g (U - U_{ti}) d_{pi}}{\mu} = \frac{(1.006)(0.5283 - 0.2148)26.5 \times 10^{-6}}{1.8217 \times 10^{-5}} = 0.4588$$

Therefore:

$$\frac{\lambda \rho_p}{d_{pi}^2}\left(\frac{\mu}{\rho_g}\right)^{2.5} = 5.17 D^2 \left[\frac{\rho_g (U - U_{ti}) d_{pi}}{\mu}\right]^{-1.5}$$

$$\frac{\lambda (4600)}{(26.5 \times 10^{-6})^2}\left(\frac{1.8217 \times 10^{-5}}{1.006}\right)^{2.5} = 5.17 (0.14)^2 (0.4588)^{-1.5}$$

$$\lambda = 0.03567$$

$$\varepsilon_t = \left[1 + \frac{\lambda(U - U_{ti})^2}{2gD}\right]^{-1/4.7} = \left[1 + \frac{0.03567(0.5283 - 0.2148)^2}{2(9.81)(0.14)}\right]^{-1/4.7}$$

$$\varepsilon_t = 0.99973$$

$$K^*_{i\infty} = \rho_p(1 - \varepsilon_t)(U - U_{ti}) = 4600(1 - 0.99973)(0.5283 - 0.2148)$$

$$\underline{K^*_{i\infty} = 0.391 \text{ kg/m}^2.\text{s}}$$

$$E_{i\infty} = K^*_{i\infty} X_{bi} = (0.391)(0.12)$$

$$\underline{E_{i\infty} = 0.0470 \text{ kg/m}^2.\text{s}}$$

By repeating the above calculations for each d_{pi} in the particle size distribution, the elutriation rate constant and entrainment flux for each d_{pi} was calculated. The total entrainment flux (E_∞) was then calculated by summing the individual particle entrainment flux ($E_{i\infty}$). The results of these calculations are summarised in Table E9.

Table E9: Calculated entrainment flux for powder P3 at U = 0.5283 m/s using equation 2-144.

Size (μm)	% <	d_{pi} (μm)	X_{bi}	C_D	U_{ti} (m/s)	$K^*_{i\infty}$ (kg/m^2.s)	$E_{i\infty}$ (kg/m^2.s)
498	100	425	0.003	3.68	2.6267	0	0
352	99.7	300.5	0.010	4.67	1.9627	0	0
249	98.7	212.5	0.038	5.99	1.4571	0	0
176	94.9	150.5	0.068	7.77	1.0761	0	0
125	88.1	106.5	0.098	10.23	0.7891	0	0
88	78.3	75	0.122	13.68	0.5727	0	0
62	66.1	53	0.138	18.43	0.4147	0.121	0.0167
44	52.3	37.5	0.140	25.05	0.2992	0.291	0.0407
31	38.3	26.5	0.120	34.36	0.2148	0.391	0.0470
22	26.3	19	0.107	46.80	0.1558	0.429	0.0459
16	15.6	13.5	0.080	64.62	0.1118	0.428	0.0342
11	7.6	9.4	0.041	91.39	0.0784	0.401	0.0164
7.8	3.5	6.65	0.022	127.75	0.0558	0.363	0.00798
5.5	1.3	4.7	0.013	179.24	0.0396	0.321	0.00417
3.9	0	3.35	0	249.92	0.0283	0.280	0
2.8	0	1.4	0	592.31	0.0119	0.190	0
						$E_\infty = \sum E_{i\infty}$	**0.213**

E11 Colakyan and Levenspiel correlation

The correlation of Colakyan and Levenspiel (1984) is given in equation 2-145.

$$K_{i\infty}^{*} = 0.011\rho_p\left(1-\frac{U_{ti}}{U}\right)^2 \qquad (2\text{-}145)$$

The entrainment flux ($E_{i\infty}$) of d_{pi} is calculated as follows:

$$K_{i\infty}^{*} = 0.011\rho_p\left(1-\frac{U_{ti}}{U}\right)^2 = 0.011(4600)\left(1-\frac{0.2148}{0.5283}\right)^2$$

$$\underline{K_{i\infty}^{*} = 17.818 \text{ kg/m}^2\text{.s}}$$

$$E_{i\infty} = K_{i\infty}^{*} X_{bi} = (17.818)(0.12)$$

$$\underline{E_{i\infty} = 2.138 \text{ kg/m}^2\text{.s}}$$

By repeating the above calculations for each d_{pi} in the particle size distribution, the elutriation rate constant and entrainment flux for each d_{pi} was calculated. The total entrainment flux (E_∞) was then calculated by summing the individual particle entrainment flux ($E_{i\infty}$). The results of these calculations are summarised in Table E10.

Table E10: Calculated entrainment flux for powder P3 at U = 0.5283 m/s using equation 2-145.

Size (μm)	% <	d_{pi} (μm)	X_{bi}	C_D	U_{ti} (m/s)	$K^*_{i\infty}$ (kg/m².s)	$E_{i\infty}$ (kg/m².s)
498	100	425	0.003	3.68	2.6267	798.326	2.395
352	99.7	300.5	0.010	4.67	1.9627	373.022	3.730
249	98.7	212.5	0.038	5.99	1.4571	156.401	5.943
176	94.9	150.5	0.068	7.77	1.0761	54.406	3.700
125	88.1	106.5	0.098	10.23	0.7891	12.335	1.209
88	78.3	75	0.122	13.68	0.5727	0.358	0.0436
62	66.1	53	0.138	18.43	0.4147	2.339	0.323
44	52.3	37.5	0.140	25.05	0.2992	9.512	1.332
31	38.3	26.5	0.120	34.36	0.2148	17.818	2.138
22	26.3	19	0.107	46.80	0.1558	25.150	2.691
16	15.6	13.5	0.080	64.62	0.1118	31.452	2.516
11	7.6	9.4	0.041	91.39	0.0784	36.690	1.504
7.8	3.5	6.65	0.022	127.75	0.0558	40.475	0.890
5.5	1.3	4.7	0.013	179.24	0.0396	43.298	0.563
3.9	0	3.35	0	249.92	0.0283	45.321	0
2.8	0	1.4	0	592.31	0.0119	48.348	0
						$E_\infty = \sum E_{i\infty}$	**28.978**

E12 Kato *et al.* correlation

The correlation of Kato *et al.* (1985 cited by Tasirin and Geldart 1998) is given in equation 2-146.

$$K^*_{i\infty} = 2.8\times10^{-2}\left(D_h\right)^{-0.65}\left(\frac{U-U_{ti}}{U_{ti}}\right)^{1.6}\left(\frac{\rho_p-\rho_g}{\rho_g}\right)^{0.54U_{ti}^{2.1}} \qquad (2\text{-}146)$$

note D_h=D for a bed without internals

The entrainment flux ($E_{i\infty}$) of d_{pi} is calculated as follows:

$$K^*_{i\infty} = 2.8\times10^{-2}\left(D_h\right)^{-0.65}\left(\frac{U-U_{ti}}{U_{ti}}\right)^{1.6}\left(\frac{\rho_p-\rho_g}{\rho_g}\right)^{0.54U_{ti}^{2.1}}$$

$$K^*_{i\infty} = 2.8\times10^{-2}\left(0.14\right)^{-0.65}\left(\frac{0.5283-0.2148}{0.2148}\right)^{1.6}\left(\frac{4600-1.006}{1.006}\right)^{0.54(0.2148)^{2.1}}$$

$$K^*_{i\infty} = 0.220 \text{ kg/m}^2\text{.s}$$

$$E_{i\infty} = K^*_{i\infty} X_{bi} = (0.220)(0.12)$$

$$E_{i\infty} = 0.0264 \text{ kg/m}^2\text{.s}$$

By repeating the above calculations for each d_{pi} in the particle size distribution, the elutriation rate constant and entrainment flux for each d_{pi} was calculated. The total entrainment flux (E_∞) was then calculated by summing the individual particle entrainment flux ($E_{i\infty}$). The results of these calculations are summarised in Table E11.

Table E11: Summary of entrainment flux calculations for powder P3 at U = 0.5283 m/s using equation 2-146.

Size (μm)	% <	d_{pi} (μm)	X_{bi}	C_D	U_{ti} (m/s)	$K^*_{i\infty}$ (kg/m^2.s)	$E_{i\infty}$ (kg/m^2.s)
498	100	425	0.003	3.68	2.6267	0	0
352	99.7	300.5	0.010	4.67	1.9627	0	0
249	98.7	212.5	0.038	5.99	1.4571	0	0
176	94.9	150.5	0.068	7.77	1.0761	0	0
125	88.1	106.5	0.098	10.23	0.7891	0	0
88	78.3	75	0.122	13.68	0.5727	0	0
62	66.1	53	0.138	18.43	0.4147	0.0259	0.00358
44	52.3	37.5	0.140	25.05	0.2992	0.0940	0.0132
31	38.3	26.5	0.120	34.36	0.2148	0.220	0.0264
22	26.3	19	0.107	46.80	0.1558	0.444	0.0475
16	15.6	13.5	0.080	64.62	0.1118	0.863	0.0690
11	7.6	9.4	0.041	91.39	0.0784	1.680	0.0689
7.8	3.5	6.65	0.022	127.75	0.0558	3.099	0.0682
5.5	1.3	4.7	0.013	179.24	0.0396	5.630	0.0732
3.9	0	3.35	0	249.92	0.0283	9.962	0
2.8	0	1.4	0	592.31	0.0119	41.959	0
						$E_\infty = \sum E_{i\infty}$	**0.370**

E13 Sciazko *et al.* correlation

The correlation of Sciazko *et al.* (1991) is given in equation 2-147.

$$K_{i\infty}^{*} = 1.6\left(\rho_g U\right)\left(\frac{U}{U_{ti}}\right)\left(1-\frac{U_{ti}}{U}\right) \qquad (2\text{-}147)$$

The entrainment flux ($E_{i\infty}$) of d_{pi} is calculated as follows:

$$K_{i\infty}^{*} = 1.6\left(\rho_g U\right)\left(\frac{U}{U_{ti}}\right)\left(1-\frac{U_{ti}}{U}\right)$$

$$K_{i\infty}^{*} = 1.6\left(1.006\right)\left(0.5283\right)\left(\frac{0.5283}{0.2148}\right)\left(1-\frac{0.2148}{0.5283}\right)$$

$$\underline{K_{i\infty}^{*} = 1.241 \text{ kg/m}^2\text{.s}}$$

$$E_{i\infty} = K_{i\infty}^{*} X_{bi} = \left(1.241\right)\left(0.12\right)$$

$$\underline{E_{i\infty} = 0.149 \text{ kg/m}^2\text{.s}}$$

By repeating the above calculations for each d_{pi} in the particle size distribution, the elutriation rate constant and entrainment flux for each d_{pi} was calculated. The total entrainment flux (E_∞) was then calculated by summing the individual particle entrainment flux ($E_{i\infty}$). The results of these calculations are summarised in Table E12.

Table E12: Calculated entrainment flux for powder P3 at U = 0.5283 m/s using equation 2-147.

Size (μm)	% <	d_{pi} (μm)	X_{bi}	C_D	U_{ti} (m/s)	$K^*_{i\infty}$ (kg/m².s)	$E_{i\infty}$ (kg/m².s)
498	100	425	0.003	3.68	2.6267	0	0
352	99.7	300.5	0.010	4.67	1.9627	0	0
249	98.7	212.5	0.038	5.99	1.4571	0	0
176	94.9	150.5	0.068	7.77	1.0761	0	0
125	88.1	106.5	0.098	10.23	0.7891	0	0
88	78.3	75	0.122	13.68	0.5727	0	0
62	66.1	53	0.138	18.43	0.4147	0.233	0.0321
44	52.3	37.5	0.140	25.05	0.2992	0.651	0.0911
31	38.3	26.5	0.120	34.36	0.2148	1.241	0.149
22	26.3	19	0.107	46.80	0.1558	2.032	0.217
16	15.6	13.5	0.080	64.62	0.1118	3.167	0.253
11	7.6	9.4	0.041	91.39	0.0784	4.875	0.200
7.8	3.5	6.65	0.022	127.75	0.0558	7.198	0.158
5.5	1.3	4.7	0.013	179.24	0.0396	10.489	0.136
3.9	0	3.35	0	249.92	0.0283	15.009	0
2.8	0	1.4	0	592.31	0.0119	36.917	0
						$E_\infty = \sum E_{i\infty}$	**1.237**

E14 Baeyens *et al.* correlation

The correlation of Baeyens *et al.* (1992) is given in equation 2-148.

$$K^*_{i\infty} = 5.4\times10^{-5}\left(\rho_p\right)\left(\frac{U}{0.2}\right)^{3.4}\left(1-\frac{U_{ti}}{U}\right)^{2} \quad \text{for } d_{pi} \le \frac{10325}{\rho_p^{0.725}} \qquad (2\text{-}148)$$

The entrainment flux ($E_{i\infty}$) of d_{pi} is calculated as follows:

$$\frac{10325}{\rho_p^{0.725}} = \frac{10325}{(4600)^{0.725}} = 22.82 > d_{pi}\left(26.5\times10^{-6}\right)$$

$$K^{*}_{i\infty} = 5.4\times10^{-5}\left(\rho_p\right)\left(\frac{U}{0.2}\right)^{3.4}\left(1-\frac{U_{ti}}{U}\right)^{2}$$

$$K^{*}_{i\infty} = 5.4\times10^{-5}\left(4600\right)\left(\frac{0.5283}{0.2}\right)^{3.4}\left(1-\frac{0.2148}{0.5283}\right)^{2}$$

$$\underline{K^{*}_{i\infty} = 2.378\ \text{kg/m}^2\text{.s}}$$

$$E_{i\infty} = K^{*}_{i\infty} X_{bi} = \left(2.378\right)\left(0.12\right)$$

$$\underline{E_{i\infty} = 0.285\ \text{kg/m}^2\text{.s}}$$

By repeating the above calculations for each d_{pi} in the particle size distribution, the elutriation rate constant and entrainment flux for each d_{pi} was calculated. The total entrainment flux (E_∞) was then calculated by summing the individual particle entrainment flux ($E_{i\infty}$). The results of these calculations are summarised in Table E13.

Table E13: Calculated entrainment flux for powder P3 at U = 0.5283 m/s using equation 2-148.

Size (μm)	**% <**	**d_{pi} (μm)**	**X_{bi}**	**C_D**	**U_{ti} (m/s)**	**$K^{*}_{i\infty}$ (kg/m².s)**	**$E_{i\infty}$ (kg/m².s)**
498	100	425	0.003	3.68	2.6267	106.530	0.320
352	99.7	300.5	0.010	4.67	1.9627	49.777	0.498
249	98.7	212.5	0.038	5.99	1.4571	20.871	0.793
176	94.9	150.5	0.068	7.77	1.0761	7.260	0.494
125	88.1	106.5	0.098	10.23	0.7891	1.646	0.161
88	78.3	75	0.122	13.68	0.5727	0.0477	0.00582
62	66.1	53	0.138	18.43	0.4147	0.312	0.0431
44	52.3	37.5	0.140	25.05	0.2992	1.269	0.178
31	38.3	26.5	0.120	34.36	0.2148	2.378	0.285
22	26.3	19	0.107	46.80	0.1558	3.356	0.359
16	15.6	13.5	0.080	64.62	0.1118	4.197	0.336
11	7.6	9.4	0.041	91.39	0.0784	4.896	0.201
7.8	3.5	6.65	0.022	127.75	0.0558	5.401	0.119
5.5	1.3	4.7	0.013	179.24	0.0396	5.778	0.0751
3.9	0	3.35	0	249.92	0.0283	6.048	0
2.8	0	1.4	0	592.31	0.0119	6.452	0
						$E_\infty = \sum E_{i\infty}$	**3.867**

E15 Nakagawa *et al.* correlation

The correlation of Nakagawa *et al.* (1994) is given in equation 2-149.

$$K_{i\infty}^{*} = 0.35(\rho_p U)(1-\varepsilon)_H$$

with:

$$(1-\varepsilon)_H = 7.41\times10^{-3} R^{1.87} A^{0.55} H_{fbd}^{-0.64} \qquad (2\text{-}149)$$

and:

$$R = \sum_{i=1}^{n} X_{bi}\left(\frac{U-U_{ti}}{U_{ti}}\right) \text{ for } U_{ti} < U$$

The entrainment flux ($E_{i\infty}$) of d_{pi} is calculated as follows: Firstly R needs to be calculated for all $U_{ti} < 0.5283$ m/s. This is summarised in Table E14.

Table E14: Calculation of R for powder P3 at U = 0.5283 m/s.

d_{pi} (μm)	X_{bi}	U_{ti} (m/s)	$R_i = X_{bi}\left(\frac{U-U_{ti}}{U_{ti}}\right)$
53	0.138	0.4147	0.0378
37.5	0.140	0.2992	0.1072
26.5	0.120	0.2148	0.1751
19	0.107	0.1558	0.2558
13.5	0.08	0.1118	0.2980
9.4	0.041	0.0784	0.2353
6.65	0.022	0.0558	0.1863
4.7	0.013	0.0396	0.1604
		$R = \sum R_i$	**1.4559**

$$(1-\varepsilon)_H = 7.41\times10^{-3} R^{1.87} A^{0.55} h_{fbd}^{-0.64}$$

$$(1-\varepsilon)_H = 7.41\times10^{-3} (1.4559)^{1.87} (0.01539)^{0.55} (4.571)^{-0.64}$$

$$(1-\varepsilon)_H = 5.6944\times10^{-4}$$

$$K_{i\infty}^{*} = 0.35(4600)(0.5283)\left(5.6944\times10^{-4}\right)$$

$$\underline{K_{i\infty}^{*} = 0.485 \text{ kg/m}^2\text{.s}}$$

$$E_{i\infty} = K^*_{i\infty} X_{bi} = (0.485)(0.12)$$

$$\underline{E_{i\infty} = 0.0582 \text{ kg/m}^2.\text{s}}$$

By repeating the above calculations for each d_{pi} in the particle size distribution, the elutriation rate constant and entrainment flux for each d_{pi} was calculated. The total entrainment flux (E_∞) was then calculated by summing the individual particle entrainment flux ($E_{i\infty}$). The results of these calculations are summarised in Table E15.

Table E15: Calculated entrainment flux for powder P3 at U = 0.5283 m/s using equation 2-149.

Size (μm)	% <	d_{pi} (μm)	X_{bi}	C_D	U_{ti} (m/s)	$K^*_{i\infty}$ (kg/m^2.s)	$E_{i\infty}$ (kg/m^2.s)
498	100	425	0.003	3.68	2.6267	0.485	0.00146
352	99.7	300.5	0.010	4.67	1.9627	0.485	0.00485
249	98.7	212.5	0.038	5.99	1.4571	0.485	0.0184
176	94.9	150.5	0.068	7.77	1.0761	0.485	0.0330
125	88.1	106.5	0.098	10.23	0.7891	0.485	0.0476
88	78.3	75	0.122	13.68	0.5727	0.485	0.0592
62	66.1	53	0.138	18.43	0.4147	0.485	0.0670
44	52.3	37.5	0.140	25.05	0.2992	0.485	0.0680
31	38.3	26.5	0.120	34.36	0.2148	0.485	0.0582
22	26.3	19	0.107	46.80	0.1558	0.485	0.0519
16	15.6	13.5	0.080	64.62	0.1118	0.485	0.0388
11	7.6	9.4	0.041	91.39	0.0784	0.485	0.0200
7.8	3.5	6.65	0.022	127.75	0.0558	0.485	0.0107
5.5	1.3	4.7	0.013	179.24	0.0396	0.485	0.00631
3.9	0	3.35	0	249.92	0.0283	0.485	0
2.8	0	1.4	0	592.31	0.0119	0.485	0
						$E_\infty = \sum E_{i\infty}$	**0.485**

E15 Tasirin and Geldart correlation

The correlation of Tasirin and Geldart (1998) is given in equation 2-150.

$$K_{i\infty}^{*} = \begin{cases} 23.7(\rho_g)(U)^{2.5}\exp\left(\dfrac{-5.4U_{ti}}{U}\right) & \text{for } Re < 3000 \\ 14.5(\rho_g)(U)^{2.5}\exp\left(\dfrac{-5.4U_{ti}}{U}\right) & \text{for } Re > 3000 \end{cases} \qquad (2\text{-}150)$$

$$Re = \frac{\rho_g UD}{\mu}$$

The entrainment flux ($E_{i\infty}$) of d_{pi} is calculated as follows:

$$Re = \frac{\rho_g UD}{\mu} = \frac{(1.006)(0.5283)(0.14)}{(1.8217\times10^{-5})} = 4084 > 3000$$

Therefore :

$$K_{i\infty}^{*} = 14.5(\rho_g)(U)^{2.5}\exp\left(\frac{-5.4U_{ti}}{U}\right)$$

$$K_{i\infty}^{*} = 14.5(1.006)(0.5283)^{2.5}\exp\left[\frac{(-5.4)(0.2148)}{(0.5283)}\right]$$

$$\underline{K_{i\infty}^{*} = 0.329 \text{ kg/m}^2\text{.s}}$$

$$E_{i\infty} = K_{i\infty}^{*} X_{bi} = (0.329)(0.12)$$

$$\underline{E_{i\infty} = 0.039 \text{ kg/m}^2\text{.s}}$$

By repeating the above calculations for each d_{pi} in the particle size distribution, the elutriation rate constant and entrainment flux for each d_{pi} was calculated. The total entrainment flux (E_∞) was then calculated by summing the individual particle entrainment flux ($E_{i\infty}$). The results of these calculations are summarised in Table E16.

Table E16: Calculated entrainment flux for powder P3 at U = 0.5283 m/s using equation 2-150.

Size (μm)	% <	d_{pi} (μm)	X_{bi}	C_D	U_{ti} (m/s)	$K^*_{i\infty}$ (kg/m².s)	$E_{i\infty}$ (kg/m².s)
498	100	425	0.003	3.68	2.6267	0	0
352	99.7	300.5	0.010	4.67	1.9627	0	0
249	98.7	212.5	0.038	5.99	1.4571	0	0
176	94.9	150.5	0.068	7.77	1.0761	0	0
125	88.1	106.5	0.098	10.23	0.7891	0.001	0
88	78.3	75	0.122	13.68	0.5727	0.008	0.001
62	66.1	53	0.138	18.43	0.4147	0.043	0.006
44	52.3	37.5	0.140	25.05	0.2992	0.139	0.019
31	38.3	26.5	0.120	34.36	0.2148	0.329	0.039
22	26.3	19	0.107	46.80	0.1558	0.600	0.064
16	15.6	13.5	0.080	64.62	0.1118	0.942	0.075
11	7.6	9.4	0.041	91.39	0.0784	1.333	0.055
7.8	3.5	6.65	0.022	127.75	0.0558	1.669	0.037
5.5	1.3	4.7	0.013	179.24	0.0396	1.965	0.026
3.9	0	3.35	0	249.92	0.0283	2.222	0
2.8	0	1.4	0	592.31	0.0119	2.617	0
						$E_\infty = \sum E_{i\infty}$	**0.323**

E16 Choi *et al.* correlation

The correlation of Choi *et al.* (1999) is given in equation 2-151.

$$K^*_{i\infty} = \left(\frac{\mu}{d_{pi}}\right)(Ar)^{0.5}\exp\left(6.92 - 2.11F_g^{0.303} - \frac{13.1}{F_{da}^{0.902}}\right)$$

$$F_g = gd_{pi}\left(\rho_p - \rho_g\right) \text{ gravity force per projection area} \qquad (2\text{-}151)$$

$$F_{da} = \frac{C_D\rho_g U^2}{2} \text{ drag force per projection area}$$

The entrainment flux ($E_{i\infty}$) of d_{pi} is calculated as follows:

$$Ar = \frac{\rho_g d_{pi}^3 (\rho_p - \rho_g) g}{\mu^2} = \frac{(1.006)(26.5\times10^{-6})^3 (4600 - 1.006)(9.81)}{(1.8217\times10^{-5})^2}$$

$$Ar = 2.545$$

$$F_g = g d_{pi} (\rho_p - \rho_g) = (9.81)(26.5\times10^{-6})(4600 - 1.006)$$

$$F_g = 1.196$$

$$F_d = \frac{C_D \rho_g U^2}{2} = \frac{(34.34)(1.006)(0.5283)^2}{2}$$

$$F_d = 4.8209$$

$$K_{i\infty}^* = \left(\frac{\mu}{d_{pi}}\right)(Ar)^{0.5} \exp\left(6.92 - 2.11 F_g^{0.303} - \frac{13.1}{F_d^{0.902}}\right)$$

$$K_{i\infty}^* = \left(\frac{1.8217\times10^{-5}}{26.5\times10^{-6}}\right)(2.545)^{0.5} \exp\left(6.92 - 2.11(1.196)^{0.303} - \frac{13.1}{(4.8209)^{0.902}}\right)$$

$$\underline{K_{i\infty}^* = 5.022 \text{ kg/m}^2\text{.s}}$$

$$E_{i\infty} = K_{i\infty}^* X_{bi} = (5.022)(0.12)$$

$$\underline{E_{i\infty} = 0.603 \text{ kg/m}^2\text{.s}}$$

By repeating the above calculations for each d_{pi} in the particle size distribution, the elutriation rate constant and entrainment flux for each d_{pi} was calculated. The total entrainment flux (E_∞) was then calculated by summing the individual particle entrainment flux ($E_{i\infty}$). The results of these calculations are summarised in Table E17.

Table E17: Calculated entrainment flux for powder P3 at U = 0.5283 m/s using equation 2-151.

Size (μm)	% <	d_{pi} (μm)	X_{bi}	C_D	U_{ti} (m/s)	$K^*_{i\infty}$ (kg/m^2.s)	$E_{i\infty}$ (kg/m^2.s)
498	100	425	0.003	3.68	2.6267	0	0
352	99.7	300.5	0.010	4.67	1.9627	0	0
249	98.7	212.5	0.038	5.99	1.4571	0	0
176	94.9	150.5	0.068	7.77	1.0761	0	0
125	88.1	106.5	0.098	10.23	0.7891	0.006	0.001
88	78.3	75	0.122	13.68	0.5727	0.061	0.007
62	66.1	53	0.138	18.43	0.4147	0.387	0.053
44	52.3	37.5	0.140	25.05	0.2992	1.640	0.230
31	38.3	26.5	0.120	34.36	0.2148	5.022	0.603
22	26.3	19	0.107	46.80	0.1558	11.402	1.220
16	15.6	13.5	0.080	64.62	0.1118	21.426	1.714
11	7.6	9.4	0.041	91.39	0.0784	35.089	1.439
7.8	3.5	6.65	0.022	127.75	0.0558	48.591	1.069
5.5	1.3	4.7	0.013	179.24	0.0396	60.803	0.790
3.9	0	3.35	0	249.92	0.0283	69.657	0.000
2.8	0	1.4	0	592.31	0.0119	0.000	0.000
						$E_\infty = \sum E_{i\infty}$	**7.126**

E16 Summary of measured and calculated entrainment flux

Table E18: Entrainment flux for powder P1.

U (m/s)	E_∞ Measured (kg/m^2.s)	E_∞ Calculated, (kg/m^2.s)				
		Yagi and Aochi	Zenz and Weil	Wen and Hashinger	Tanaka *et al.*	Merrick and Highley
0.236	0.00771	0.0353	0.00464	0.00632	0.0139	1.175
0.342	0.0277	0.0671	0.0274	0.0322	0.0586	2.965
0.399	0.0437	0.105	0.0562	0.0609	0.102	4.195
0.449	0.0614	0.158	0.0991	0.0995	0.156	5.469
0.494	0.0800	0.222	0.156	0.145	0.218	6.726
0.525	0.122	0.282	0.212	0.187	0.273	7.784
0.572	0.136	0.382	0.314	0.257	0.360	9.224
0.610	0.172	0.483	0.424	0.327	0.444	10.525
0.670	0.260	0.683	0.657	0.466	0.607	12.792
0.732	0.349	0.933	0.975	0.644	0.803	15.183
0.789	0.468	1.212	1.345	0.842	1.015	17.529
U (m/s)	E_∞ Measured (kg/m^2.s)	E_∞ Calculated, (kg/m^2.s)				
		Geldart *et al.*	Lin *et al.*	Wen and Chen	Colakyan and Levenspiel	Kato *et al.*
0.236	0.00771	0.0831	0.499	0.0229	3.515	0.0199
0.342	0.0277	0.222	2.480	0.0731	2.808	0.0430
0.399	0.0437	0.327	4.739	0.116	3.106	0.0597
0.449	0.0614	0.439	7.907	0.165	3.504	0.0764
0.494	0.0800	0.552	11.885	0.216	3.882	0.0917
0.525	0.122	0.643	15.784	0.261	4.114	0.102
0.572	0.136	0.783	22.515	0.321	4.584	0.121
0.610	0.172	0.911	29.696	0.380	4.947	0.138
0.670	0.260	1.132	44.703	0.490	5.466	0.166
0.732	0.349	1.380	65.121	0.610	6.028	0.200
0.789	0.468	1.628	89.583	0.732	6.506	0.233
U (m/s)	E_∞ Measured (kg/m^2.s)	E_∞ Calculated, (kg/m^2.s)				
		Sciazko *et al.*	Baeyens *et al.*	Nakagawa *et al.*	Tasirin and Geldart	Choi *et al.*
0.236	0.00771	0.0848	0.0301	0.00319	0.00950	0.0155
0.342	0.0277	0.216	0.0851	0.0132	0.0443	0.116
0.399	0.0437	0.320	0.159	0.0248	0.0503	0.250
0.449	0.0614	0.426	0.270	0.0386	0.0809	0.430
0.494	0.0800	0.528	0.411	0.0530	0.117	0.634
0.525	0.122	0.610	0.536	0.0633	0.149	0.784
0.572	0.136	0.731	0.801	0.0850	0.207	1.121
0.610	0.172	0.844	1.079	0.106	0.266	1.435
0.670	0.260	1.040	1.636	0.142	0.380	1.980
0.732	0.349	1.253	2.442	0.189	0.529	2.693
0.789	0.468	1.464	3.397	0.238	0.698	3.423

Table E19: Entrainment flux for powder P3.

U (m/s)	E_∞ Measured ($kg/m^2.s$)	E_∞ Calculated, ($kg/m^2.s$)				
		Yagi and Aochi	Zenz and Weil	Wen and Hashinger	Tanaka *et al.*	Merrick and Highley
0.175	0.000271	0.567	0.000491	0.00802	0.0194	0.959
0.234	0.00105	0.758	0.00195	0.0215	0.0451	1.824
0.291	0.00525	0.939	0.00545	0.0449	0.0843	2.885
0.336	0.0160	1.140	0.0111	0.0739	0.130	3.953
0.387	0.0309	1.309	0.0217	0.117	0.193	5.239
0.439	0.0495	1.466	0.0391	0.176	0.272	6.658
0.486	0.0782	1.631	0.0629	0.245	0.360	8.066
0.528	0.120	1.797	0.0938	0.323	0.453	9.456
0.603	0.278	2.137	0.171	0.495	0.653	12.118
0.668	0.572	2.477	0.269	0.687	0.863	14.602
0.724	0.931	2.821	0.381	0.892	1.077	16.912
0.779	1.503	3.198	0.520	1.129	1.314	19.267
U (m/s)	E_∞ Measured ($kg/m^2.s$)	E_∞ Calculated, ($kg/m^2.s$)				
		Geldart *et al.*	Lin *et al.*	Wen and Chen	Colakyan and Levenspiel	Kato *et al.*
0.175	0.000271	0.185	0.600	0.0169	127.384	0.103
0.234	0.00105	0.320	2.084	0.0334	83.611	0.146
0.291	0.00525	0.475	5.282	0.0551	61.306	0.188
0.336	0.0160	0.625	10.091	0.0785	50.647	0.218
0.387	0.0309	0.803	18.443	0.108	41.882	0.256
0.439	0.0495	0.997	31.324	0.142	35.643	0.298
0.486	0.0782	1.187	48.131	0.177	31.694	0.335
0.528	0.120	1.372	69.098	0.213	28.972	0.369
0.603	0.278	1.726	122.198	0.284	25.658	0.431
0.668	0.572	2.053	189.261	0.355	23.777	0.487
0.724	0.931	2.356	268.024	0.425	22.641	0.535
0.779	1.503	2.665	366.830	0.499	21.852	0.587
U (m/s)	E_∞ Measured ($kg/m^2.s$)	E_∞ Calculated, ($kg/m^2.s$)				
		Sciazko *et al.*	Baeyens *et al.*	Nakagawa *et al.*	Tasirin and Geldart	Choi *et al.*
0.175	0.000271	0.162	0.399	0.0275	0.0136	0.651
0.234	0.00105	0.281	0.704	0.0610	0.0363	1.382
0.291	0.00525	0.419	1.078	0.107	0.0747	2.270
0.336	0.0160	0.551	1.457	0.151	0.122	3.015
0.387	0.0309	0.713	1.943	0.218	0.118	4.006
0.439	0.0495	0.891	2.534	0.304	0.177	5.121
0.486	0.0782	1.066	3.173	0.393	0.246	6.155
0.528	0.120	1.236	3.866	0.484	0.322	7.126
0.603	0.278	1.563	5.374	0.672	0.495	8.886
0.668	0.572	1.875	7.038	0.866	0.686	10.433
0.724	0.931	2.165	8.813	1.055	0.888	11.783
0.779	1.503	2.463	10.901	1.261	1.120	13.116

Table E20: Entrainment flux for powder P4.

U (m/s)	E_∞ Measured ($kg/m^2.s$)	E_∞ Calculated, ($kg/m^2.s$)				
		Yagi and Aochi	Zenz and Weil	Wen and Hashinger	Tanaka *et al.*	Merrick and Highley
0.227	0.000596	1.103	0.000391	0.00609	0.00980	0.149
0.282	0.00325	1.299	0.00110	0.0140	0.0198	0.282
0.335	0.0104	1.449	0.00248	0.0265	0.0342	0.460
0.385	0.0155	1.564	0.00480	0.0441	0.0528	0.677
0.432	0.0184	1.644	0.00837	0.0685	0.0765	0.931
0.477	0.0220	1.702	0.0134	0.0995	0.105	1.212
0.522	0.0238	1.729	0.0204	0.138	0.138	1.529
0.596	0.0336	1.797	0.0383	0.225	0.208	2.156
0.655	0.0412	1.846	0.0598	0.317	0.278	2.739
0.717	0.0509	1.901	0.0906	0.444	0.368	3.431
0.772	0.0823	1.955	0.128	0.588	0.465	4.121
U (m/s)	E_∞ Measured ($kg/m^2.s$)	E_∞ Calculated, ($kg/m^2.s$)				
		Geldart *et al.*	Lin *et al.*	Wen and Chen	Colakyan and Levenspiel	Kato *et al.*
0.227	0.000596	0.0606	0.504	0.00880	134.561	0.0206
0.282	0.00325	0.0965	1.277	0.0159	92.576	0.0282
0.335	0.0104	0.139	2.671	0.0246	67.590	0.0359
0.385	0.0155	0.185	4.849	0.0355	51.886	0.0436
0.432	0.0184	0.236	8.012	0.0490	41.130	0.0517
0.477	0.0220	0.290	12.243	0.0639	33.635	0.0599
0.522	0.0238	0.347	17.869	0.0801	27.886	0.0687
0.596	0.0336	0.455	31.623	0.112	21.238	0.0838
0.655	0.0412	0.551	47.389	0.143	17.580	0.0973
0.717	0.0509	0.661	69.752	0.184	14.794	0.114
0.772	0.0823	0.767	95.971	0.225	12.945	0.131
U (m/s)	E_∞ Measured ($kg/m^2.s$)	E_∞ Calculated, ($kg/m^2.s$)				
		Sciazko *et al.*	Baeyens *et al.*	Nakagawa *et al.*	Tasirin and Geldart	Choi *et al.*
0.227	0.000596	0.0545	1.015	0.00283	0.00655	0.154
0.282	0.00325	0.0862	1.458	0.00554	0.0144	0.298
0.335	0.0104	0.122	1.911	0.00913	0.0269	0.484
0.385	0.0155	0.164	2.351	0.0141	0.0271	0.699
0.432	0.0184	0.210	2.775	0.0204	0.0411	0.941
0.477	0.0220	0.258	3.178	0.0274	0.0585	1.198
0.522	0.0238	0.308	3.572	0.0358	0.0801	1.488
0.596	0.0336	0.400	4.273	0.0520	0.128	2.010
0.655	0.0412	0.487	4.870	0.0694	0.179	2.470
0.717	0.0509	0.589	5.563	0.0916	0.245	2.992
0.772	0.0823	0.687	6.273	0.115	0.318	3.499

Table E21: Entrainment flux for powder P5.

U (m/s)	E_∞ Measured ($kg/m^2.s$)	E_∞ Calculated, ($kg/m^2.s$)				
		Yagi and Aochi	Zenz and Weil	Wen and Hashinger	Tanaka *et al.*	Merrick and Highley
0.172	0.000180	0.267	0.00234	0.00663	0.0204	1.134
0.228	0.00123	0.357	0.00875	0.0172	0.0455	2.077
0.283	0.00357	0.444	0.0231	0.0348	0.0826	3.227
0.335	0.00664	0.534	0.0498	0.0613	0.133	4.530
0.380	0.00892	0.633	0.0884	0.0935	0.190	5.834
0.427	0.0157	0.733	0.146	0.137	0.261	7.290
0.472	0.0273	0.840	0.222	0.188	0.341	8.771
0.514	0.0444	0.955	0.317	0.248	0.429	10.269
0.589	0.108	1.203	0.547	0.386	0.619	13.133
0.652	0.338	1.466	0.818	0.538	0.814	15.755
0.709	0.637	1.747	1.124	0.705	1.019	18.258
0.764	0.937	2.062	1.492	0.895	1.241	20.777
U (m/s)	E_∞ Measured ($kg/m^2.s$)	E_∞ Calculated, ($kg/m^2.s$)				
		Geldart *et al.*	Lin *et al.*	Wen and Chen	Colakyan and Levenspiel	Kato *et al.*
0.172	0.000180	0.241	0.659	0.0200	55.034	0.200
0.228	0.00123	0.397	2.235	0.0380	36.483	0.268
0.283	0.00357	0.577	5.634	0.0613	27.063	0.334
0.335	0.00664	0.771	11.716	0.0901	21.766	0.398
0.380	0.00892	0.960	20.322	0.121	18.939	0.448
0.427	0.0157	1.168	33.568	0.156	16.827	0.505
0.472	0.0273	1.376	51.270	0.192	15.467	0.560
0.514	0.0444	1.584	74.052	0.232	14.555	0.613
0.589	0.108	1.978	132.56	0.313	13.576	0.708
0.652	0.338	2.336	205.061	0.391	13.155	0.788
0.709	0.637	2.676	293.902	0.467	12.977	0.862
0.764	0.937	3.017	404.542	0.546	12.932	0.935
U (m/s)	E_∞ Measured ($kg/m^2.s$)	E_∞ Calculated, ($kg/m^2.s$)				
		Sciazko *et al.*	Baeyens *et al.*	Nakagawa *et al.*	Tasirin and Geldart	Choi *et al.*
0.172	0.000180	0.224	0.161	0.0351	0.0171	0.732
0.228	0.00123	0.372	0.280	0.0708	0.0433	1.391
0.283	0.00357	0.545	0.431	0.120	0.0867	2.186
0.335	0.00664	0.736	0.619	0.183	0.150	3.062
0.380	0.00892	0.922	0.824	0.244	0.138	3.837
0.427	0.0157	1.128	1.090	0.324	0.199	4.751
0.472	0.0273	1.338	1.402	0.412	0.272	5.652
0.514	0.0444	1.554	1.769	0.510	0.357	6.552
0.589	0.108	1.965	2.622	0.711	0.547	8.187
0.652	0.338	2.341	3.588	0.907	0.752	9.588
0.709	0.637	2.702	4.710	1.110	0.978	10.890
0.764	0.937	3.067	6.052	1.328	1.233	12.154

Table E22: Entrainment flux for powder P6.

U (m/s)	E_∞ Measured (kg/m^2.s)	E_∞ Calculated, (kg/m^2.s)				
		Yagi and Aochi	Zenz and Weil	Wen and Hashinger	Tanaka *et al.*	Merrick and Highley
0.176	0.000271	0.355	0.000770	0.0100	0.0233	1.231
0.230	0.000686	0.470	0.00276	0.0246	0.0494	2.162
0.289	0.00217	0.607	0.00819	0.0531	0.0939	3.441
0.339	0.00285	0.742	0.0177	0.0907	0.148	4.751
0.391	0.00386	0.871	0.0345	0.144	0.216	6.211
0.440	0.00491	1.009	0.0606	0.212	0.299	7.754
0.485	0.00708	1.156	0.0958	0.294	0.391	9.300
0.526	0.0110	1.311	0.140	0.384	0.489	10.804
0.594	0.0253	1.631	0.238	0.576	0.688	13.564
0.659	0.0526	1.968	0.366	0.803	0.907	16.278
0.718	0.110	2.325	0.515	1.058	1.139	18.867
0.776	0.235	2.728	0.702	1.358	1.397	21.508
U (m/s)	E_∞ Measured (kg/m^2.s)	E_∞ Calculated, (kg/m^2.s)				
		Geldart *et al.*	Lin *et al.*	Wen and Chen	Colakyan and Levenspiel	Kato *et al.*
0.176	0.000271	0.255	0.873	0.0183	84.277	0.177
0.230	0.000686	0.406	2.763	0.0338	57.541	0.237
0.289	0.00217	0.600	7.391	0.0571	42.386	0.299
0.339	0.00285	0.790	14.866	0.0822	34.786	0.351
0.391	0.00386	0.997	27.114	0.112	29.555	0.407
0.440	0.00491	1.212	45.055	0.146	26.190	0.463
0.485	0.00708	1.424	68.746	0.182	24.037	0.514
0.526	0.0110	1.628	97.591	0.218	22.649	0.559
0.594	0.0253	1.998	166.037	0.288	21.118	0.631
0.659	0.0526	2.361	258.545	0.360	20.239	0.707
0.718	0.110	2.707	372.608	0.433	19.789	0.778
0.776	0.235	3.059	518.669	0.511	19.575	0.853
U (m/s)	E_∞ Measured (kg/m^2.s)	E_∞ Calculated, (kg/m^2.s)				
		Sciazko *et al.*	Baeyens *et al.*	Nakagawa *et al.*	Tasirin and Geldart	Choi *et al.*
0.176	0.000271	0.225	0.268	0.0511	0.0189	1.266
0.230	0.000686	0.366	0.457	0.101	0.0449	2.248
0.289	0.00217	0.549	0.729	0.176	0.0933	3.441
0.339	0.00285	0.730	1.030	0.255	0.156	4.519
0.391	0.00386	0.935	1.411	0.362	0.149	5.719
0.440	0.00491	1.150	1.874	0.485	0.216	6.916
0.485	0.00708	1.364	2.405	0.615	0.295	8.043
0.526	0.0110	1.570	2.986	0.745	0.380	9.060
0.594	0.0253	1.946	4.198	0.981	0.560	10.723
0.659	0.0526	2.326	5.718	1.257	0.772	12.376
0.718	0.110	2.693	7.484	1.546	1.007	13.893
0.776	0.235	3.072	9.655	1.867	1.279	15.393